

DRAFT

**GROUND-MOTION DATA FROM THE SMALL-SCALE EXPLOSIVE
EXPERIMENTS CONDUCTED
AT THE GREFCO PERLITE MINE NEAR SOCORRO, NEW MEXICO**

C.L. Edwards

D. Craig Pearson

Diane F. Baker

Geophysics Group, EES-3

Los Alamos National Laboratory

Los Alamos, New Mexico 87545

15 March 1994

DO NOT CIRCULATE

PERMANENT RETENTION

LOS ALAMOS NATIONAL LABORATORY



3 9338 00202 7554

**GROUND-MOTION DATA FROM THE SMALL-SCALE EXPLOSIVE
EXPERIMENTS CONDUCTED
AT THE GREFCO PERLITE MINE NEAR SOCORRO, NEW MEXICO**

C.L. Edwards
D. Craig Pearson
Diane F. Baker

Geophysics Group, EES-3
Los Alamos National Laboratory
Los Alamos, New Mexico 87545

15 March 1994

ABSTRACT

A series of small-scale explosive experiments were conducted in a perlite mine near Socorro, New Mexico. These experiments were a joint effort between Los Alamos National Laboratory, New Mexico Institute of Mining and Technology, Southern Methodist University, and Defense Nuclear Agency. The purpose of these tests was to measure the changes in the shock wave and seismic coupling as a function of depth of burial and structural setting. The size of the explosive charges ranged from 1 to 68 kg. Over 1150 measurements of velocity and acceleration were made on thirteen experiments using three-component sensors. The sensors were placed to maximize the azimuthal coverage as well as to provide data at a variety of ranges from ~1 to 130 m. A few far-field measurements were made at ranges of ~2 km. While the bulk of the measurements were made on the surface, high-g accelerometers were placed in one instrumentation borehole to provide some free-field measurements. Preliminary results indicate that significant differences in the amplitudes of signals can occur when the location of the explosive charges are changed by only meters. Part of the observed difference is attributed to variations in the rock immediately adjacent to the charge affecting the shock coupling; and part to the effects of the site characteristics. This report describes the acceleration, velocity, and displacement data for the sensors fielded. Most acceleration, velocity, and displacement records have had calibrations applied and have been deramped, offset corrected, deglitched, and band passed. Digital data for all of these records are stored at Los Alamos National laboratory.

Table of Contents

1. Introduction	1
2. Experiment Site	2
3. Preliminary Modeling	4
4. Measurement Types	4
5. Surface Motion Data	7
6. Preliminary Conclusions	29
7. Additional Information	29
8. Acknowledgements.....	29

Appendixes

A. Physical Property Measurements.....	A-1
B. Velocity Characterization of the Experiment Site.....	B-1
C. Two-Dimensional Calculations for Intermediate-Scale Source Experiments ..	C-1
D. Ground-Motion Data Plots.....	D-1
Ground-Motion Data Perlite #1	D-3
Ground-Motion Data Perlite #2	D-4
Ground-Motion Data Perlite #3	D-5
Ground-Motion Data Perlite #4	D-6
Ground-Motion Data Perlite #5	D-7
Ground-Motion Data Perlite #6	D-8
Ground-Motion Data Perlite #7	D-13
Ground-Motion Data Perlite #8	D-19
Ground-Motion Data Perlite #9	D-31
Ground-Motion Data Perlite #10	D-45
Ground-Motion Data Perlite #11.....	D-57
Ground Motion Data Perlite #12	D-71
Ground Motion Data Perlite #13	D-85

List of Figures

1. Fracture orientation at the site	2
2. An aerial photograph of the experiment site	5
3. Section plot of Perlite #1,2,3,4 data	9
4. Section plot of Perlite #5,6,7 data	10
5. Experiment layout Perlite #9, 10, 11	20
6. Experiment geometry Perlite #9, 10, 11	21
7. Record section plot of Perlite #9,10,11 data	22
8. Azimuthal variation Perlite #9 data	23
9. Azimuthal variation Perlite #10 data	24
10. Azimuthal variation Perlite #11 data.....	25
11. Experiment layout Perlite #8, 12, 13	26
12. Experiment geometry Perlite #8, 12, 13.....	27
13. Record section plot of Perlite #8,12, 13 data	28

List of Tables

1. Shot Description Data Summary Experiments P1-P13.....	6
2. Station Information for Experiments P1-P7.....	11
3. Station Survey Data for Experiments P1-P7.....	12
4. Station Information for Experiments P8-P13.....	14
5. Station Survey Data for Experiments P8-P13.....	16

1. Introduction

Ground-motion analysis has been a key part of the Los Alamos National Laboratory Source Region Program (SRP) for several reasons: near-source ground motion represents the up-going energy from an explosion, and that information is required to assess the total energy budget for an explosion. A large number of measurements both inside and outside the spall region is key to understanding the complexity of the signals and the effects on seismic waves. These data can be used to benchmark the numerical modeling of the nonlinear zone. Last, but not least, later time phenomena, such as spall closure, are believed to play significant roles in seismic and other signals used for detection, discrimination, and characterization of underground explosions. As a result, characterization of close-in ground motions in different media has been a major goal of the SRP.

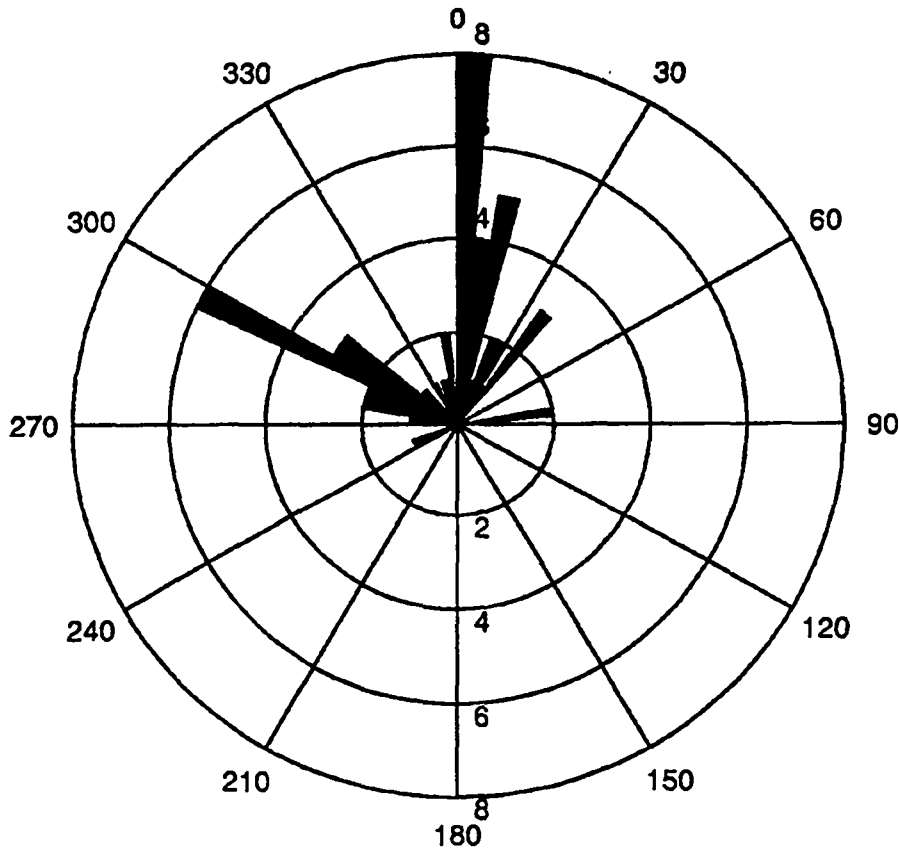
Effects of different explosion source processes on far-field seismic and atmospheric signals used for underground test monitoring are being evaluated through data analysis and modeling efforts. To address test ban issues in a nonproliferation environment, the project is being extended to investigate phenomenology in widely different geologic materials and emplacement conditions. One primary concern being addressed by the SRP is the three-dimensional characterization of the spall volume as a function of time (size, shape, volume, mass, ground motions, surface expression, and degree of damage). Surface observations of acceleration, velocity, and displacement provide constraints for spall and, when combined with the limited amount of subsurface ground-motion data, allow a three-dimensional model to be generated. This will be done through a series of intermediate-scale high-energy (HE) explosion-source experiments conducted in widely different geologic media. Candidate sites are alluvium, perlite, sandstone, limestone, and granite. Perlite was chosen for the first set of experiments because of its physical properties: low density, low strength, high porosity, and low compressional seismic velocity. This first in a series of experiments was also possible because of good working relationships with mining operators and New Mexico Institute of Mining and Technology (NM Tech).

Presented herein are the data and preliminary results from a variety of close-in ground-motion experiments conducted by Los Alamos National Laboratory and its collaborators, NM Tech, Southern Methodist University (SMU), and the Defense Nuclear Agency, Albuquerque (DNA/A) on 13 small-scale (1 to 68 kg) charges. These data are the acceleration and velocity records for the accelerometers and velocity sensors fielded. All acceleration and velocity records have had calibrations applied and have been deramped, offset corrected, deglitched, and band-pass filtered between 0-80 Hz.

2. Experiment Site

The experiments were conducted in the Dicaperl perlite mine located three miles southwest of Socorro, New Mexico, at the southeastern edge of the Socorro Mountains. Perlite is a hydrated volcanic glass that is heated and expanded to form a product used as a filter material. The silica content of this deposit is 76% with a 3.4% water content. Mine production is 240,000 tons of ore per year with estimated reserves of 12,000,000 tons.

The Dicaperl dome was formed 7.4 million years ago. The deposit has a domed shape, exhibits depositional flow banding, and is faulted on the east side and eroded on the top. Dominant joint sets trend in north-south and west northwest-east southeast directions. We also measured fracture orientations exposed at the surface of the mine floor where the experiments were performed (Figure 1). The major axis is parallel to the long axis of the instrumentation array (about 0°), with a secondary set striking about 300°. The dome's horizontal extent is 610 m wide by 790 m long and has an exposed vertical extent of 140 m with thickness ranging from 90 to more than 150 m.



r axis is the number of measurements

Figure 1. Fracture orientation at the site.

The perlite body was deposited as an extrusive, rhyolitic lava with a high silica content and hence, high viscosity. Crystallization did not occur, and obsidian was formed when the lava cooled rapidly by contact with the surrounding rocks. The interior of the dome cooled by vesiculation, leaving a solid core of obsidian. The Dicaperl dome has a surface layer of crystalline rock on the northeast edge that may have formed during an earlier period of slow cooling at depth before rising or being pushed to the surface.

The perlite formed through rapid and thorough hydration of the obsidian core. The elongated shape, a result of the north-south direction of the lava flow, and closely packed nature of the vesicles, provided paths for meteoric water to travel, resulting in hydration of the glass. The hydration of the glass occurred as a low-temperature diffusion process as water migrated inward through fractures and vesicles that provided the surface area for the hydration to progress.

Figure 2 shows an aerial photograph of the portion of the mine that was used for these experiments. The shotholes and sensor locations are superimposed on the photograph. The coordinate system used to identify locations of shots and stations is referenced to surface ground zero of shot 9. Northings and Eastings are in meters.

A seismic refraction survey was conducted to estimate the near-surface compressional seismic velocities in the perlite (Appendix A). The apparent velocities on either side of the central source location are slightly different, but both are higher than the near-surface apparent velocities measured from end shots, which are quite low at 350 m/s. Such low velocities are characteristic of dry, unconsolidated porous materials. The velocity of the refracting horizon is 1335 m/s; the depth to this refractor varies from 4 to 10 m below ground surface. We suspect that this refractor simply represents the "normal" (unweathered) velocity for the perlite or, alternatively, water saturation at this depth.

The physical and elastic properties of several core samples taken near-surface in the experiment area were measured. These results are summarized in Appendix B.

The first seven experiments (P1-P7) used small charges (1-3 kg) in order to minimize the damage to the surrounding test bed. We wanted to determine the cratering curve for this particular rock and to obtain preliminary measurements of seismic velocities and ground-motion amplitudes.

The size of the charges in following experiments needed to be large enough to produce significant ground motions. In addition, to model the results as a spherical explosion we wanted to have an aspect ratio less than 2.0. The final charge size was a cylinder 0.3 m in diameter and 0.6 m high, weighing 68 kg. Pertinent data about the individual experiments are summarized in Table 1.

3. Preliminary Modeling

Several aspects of numerical modeling have provided input to the design process of the intermediate source experiments. Both finite difference calculations and scaling analyses have been considered in the preliminary stages. These preliminary calculations are summarized in Appendix C.

4. Measurement Types

Three types of ground-motion measurements were performed on these experiments: (1) high-g (25 g and 100 g) measurements in and near the spall region on the surface and in boreholes; (2) extended range surface accelerometer measurements (to define and characterize the spall zone); and (3) velocity measurements well beyond spall. Not all types were used on each experiment. The first seven experiments were primarily designed to determine the cratering curve for perlite and to aid in the design of the heavily instrumented 68-kg charge experiments. All three types of measurements were made on experiments P8-P13.

High-g Surface and Borehole Accelerometer Measurements. These sensors were located within 15 m of surface ground zero for shots P9, P10, and P11. Each station typically recorded three components (vertical, radial, and tangential) of motion at ranges of 5, 10, 20, 30, and 40 m along seven different azimuths.

These sensors were also recorded on shots 8, 12, and 13, although they were located outside spall. The accelerometers used for these stations are Endevco 100-g or 25-g instruments (Endevco Model 2262), depending on the anticipated motions. The positive directions on the data plots presented herein are: vertical, up; radial, toward SGZ; and tangential, left of SGZ.

Extended Surface Accelerometer Measurements. For shots P11, P12, and P13 we acquired ground-motion data that straddled the edge of predicted spall and for all shots, data out to at least three times the predicted spall radius was recorded. To acquire these measurements, we installed portable stations consisting of accelerometers, portable power (batteries), and portable digital recorders. The accelerometers are Model SA-111 force-balanced accelerometers (built by Terra Technology).

All accelerometer data were recorded by 25 6-channel Reftek DAS (data acquisition subsystems, made by Refraction Technology). We have preprocessed the data, which may include corrections for timing, amplitude calibration, baseline offsets, integration ramps, noise, etc. The data were recorded at 500 samples/s.



Figure 2. Aerial photograph of the mine.

Table 1
Shot Description Data Summary Experiments P1-P13

Experiment	Easting	Northing	Elevation	Explosive	Charge (kg)	SDOB (m/kg ^{1/3})	Comments
P1	29.5	24.5	1528.7	Nitromethane	2.3	1.8	RETARC
P2	30.2	36.9	1528.5	Nitromethane	2.3	1.6	RETARC
P3	29.4	13.7	1528.6	Nitromethane	2.3	1.1	CRATER
P4	30.7	48.3	1527.8	Nitromethane	2.3	2.0	Radial Cracks
P5	30.4	59.5	1527.6	Nitromethane	2.3	2.3	No surface effects
P6	29.2	53.4	1527.6	Nitromethane	1.8	1.0	CRATER
P7	29.3	68.1	1527.4	Nitromethane	1.1	1.0	CRATER
P8	22.9	-49.0	1533.7	Petrogel	68.0	6.5	No surface effects
P9	0.0	0.0	1532.1	Petrogel	68.0	9.9	No surface effects
P10	0.0	0.0	1532.0	Petrogel	68.0	7.3	No surface effects
P11	0.0	0.0	1532.0	Petrogel	68.0	2.1	No surface effects
P12	30.0	5.3	1529.5	Petrogel	68.0	3.4	No surface effects
P13	-34.7	-14.8	1534.1	Petrogel	68.0	2.9	No surface effects

9

LAUR-94-
 Ground Motion Data collected from
 Small-Scale Explosive Experiments at Grafco Perlite Mine

Los Alamos National Laboratory
 EES-3 Source Region Program

Extended Surface Velocity Measurements. NM Tech personnel installed a linear array of velocity transducers beginning outside spall, interspersed with and extending to the edge of the linear portion of the accelerometer array. The sensors were strong motion, three-component Geospace velocity sensors. The digital recording system (NOMIS) records 33 channels in an 8-bit format. Data were recorded at 1024 samples/s.

5. Surface Motion Data

The accelerometer data presented herein are the vertical components of surface acceleration. At most ground-motion stations discussed in this report, three-component data (mainly vertical, radial and tangential) were collected and are shown in Appendix D. The data are also in available ground-motion databases at Los Alamos National Laboratory. The data are reported as acceleration, in units of ccm/s^2 for each gauge. Only those gauges with valid records are included in this report. Earlier experiments indicate that any ground-motion data of the type and density reported herein may be spatially aliased and probably do not represent more than a snapshot of outgoing wave generation (report in preparation). However, taken collectively, these data can be used to generate predictive curves for the average ground motion as a function of scaled range for contained underground explosions.

The following is an example of our file naming scheme:

gsnm-8fl-2z.a

Grefco, Socorro, New Mexico-Shot 8 FBA LANL-Station 2 vertical (z) component.Acceleration

The purpose of the first seven shots (P1-P7) was to confirm that the standard cratering curves were valid for this particular rock type, to determine the near-surface compressional wave velocities, and to determine the range dependence of peak ground motion. We fielded the NOMIS velocity array on each shot. On shots P6 and P7, in addition to the NOMIS array, we fielded accelerometers and sensitive velocity gauges to confirm our computer-determined sensitivities and gains for the fully instrumented experiments. The slant range/time record sections of the linear array for shots P1-P7 are shown in Figures 3 and 4.

The general purpose of experiments P8-P13 was to gather extensive ground-motion data from 68-kg high-explosive tests. A surface array provided extensive radial and azimuthal coverage from ground zero to well beyond the edge of spall. The shot data are summarized in Table 1.

The primary purpose of experiments P9, P10, and P11 was to provide an extensive set of ground-motion measurements on 68-kg explosive charges at three different scale depths. The experiment layout for P9, P10, and P11 is shown in Figure 5, and the shot

geometries are displayed in Figure 6. Table 2 and Table 3 give the details of the station locations and instruments. The explosive charges were fired at 40, 30, and 8.5 m in the same shot hole. We acquired ground-motion data at a variety of ranges and azimuths from ground zero to well beyond the edge of spall. The slant range/time record sections of the linear array for shots P9, P10, and P11 are shown in Figure 7. Constant range variable azimuth record sections for experiment P9, P10, and P11 are shown in Figures 8, 9, and 10 respectively.

The purpose of experiments P8, P12, and P13 was to provide a extensive set of ground-motion measurements on 68-kg explosive charges located at the southern, eastern and western edges of the mine floor. This provided additional data in the 40-150 m ranges with a different source locations as well as providing extensive azimuthal coverage of the experiment site. Experiment P8 was also to provide a comprehensive check of the complete instrumentation array at ground motion near what they would be in experiments P9, P10, P11, P12, and P13. Following the evaluation of the data from P8, the final instrument placement could be determined and the data acquisition parameters could be set with high confidence. The shot data are summarized in Table 1. The experiment layout for experiments P8, P12, and P13 is shown in Figure 11, and the shot geometries are displayed in Figure 12. Table 4 and Table 5 give the details of the station locations and instruments. Linear section plots along the main north-south line for each experiment are shown in Figure 13.

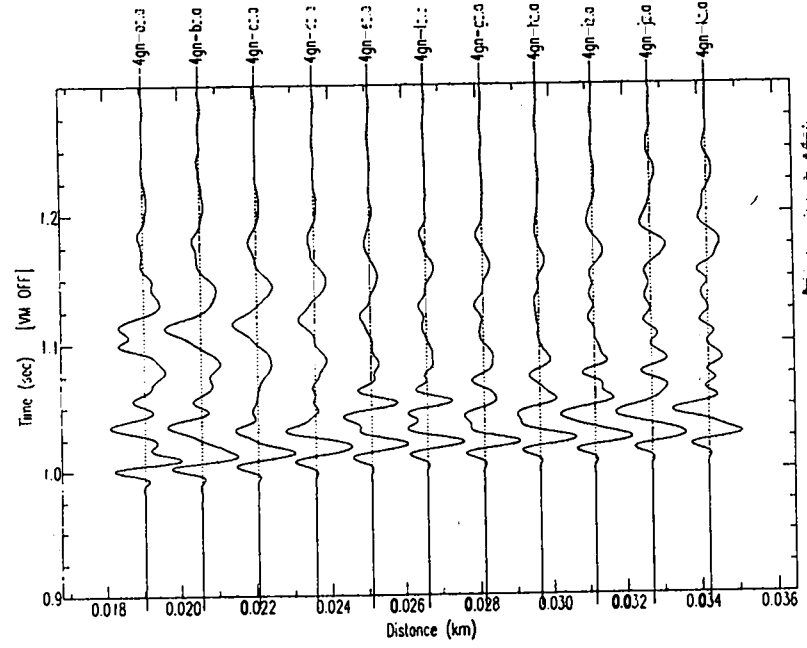
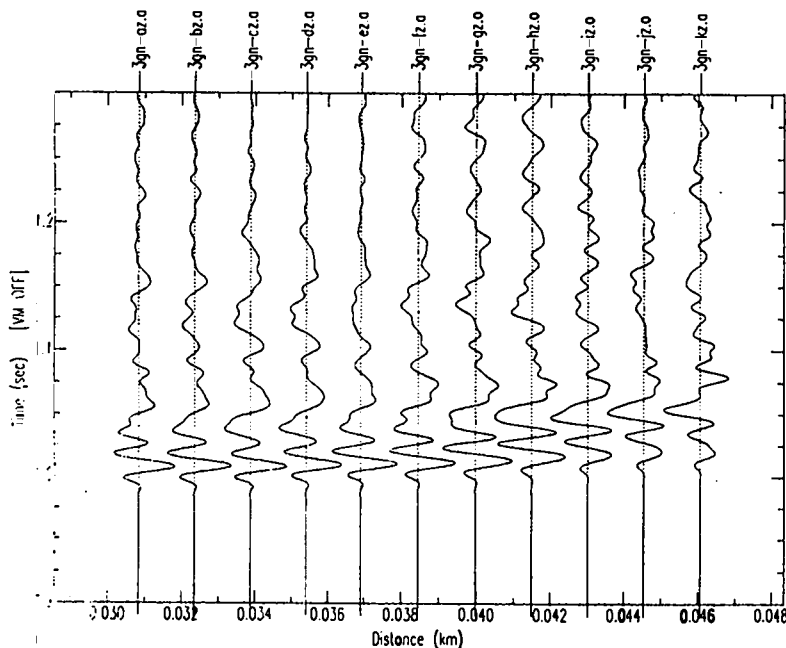
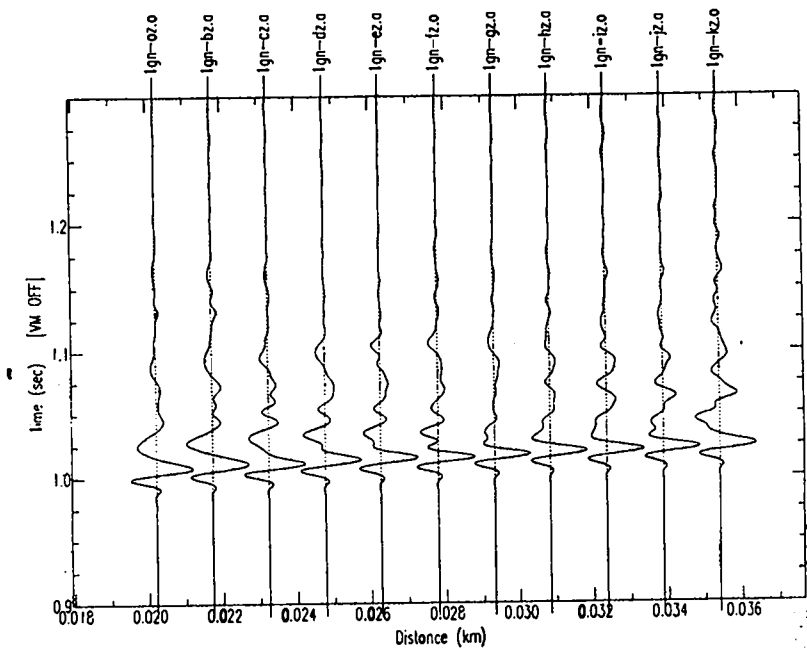
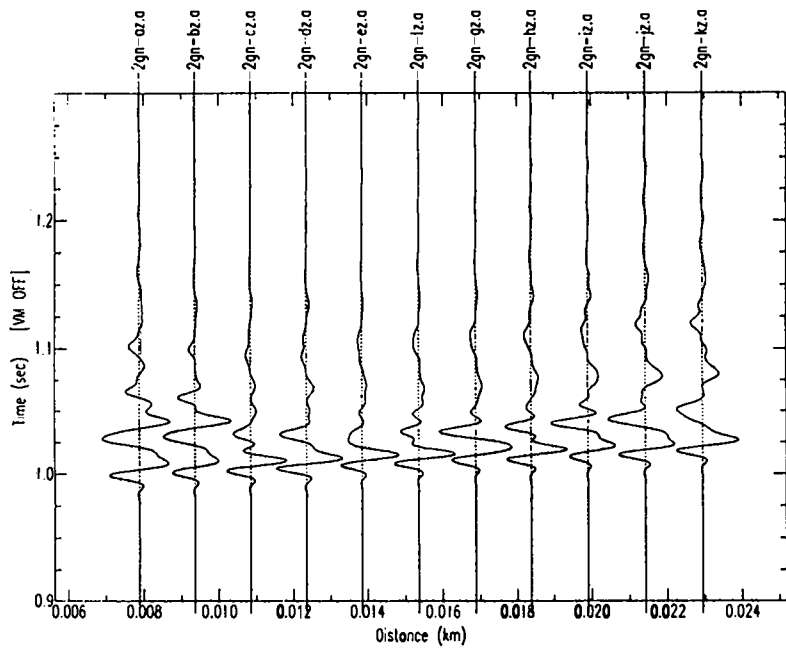


Figure 3. Section plot of Perlite #1, 2, 3, 4 data.

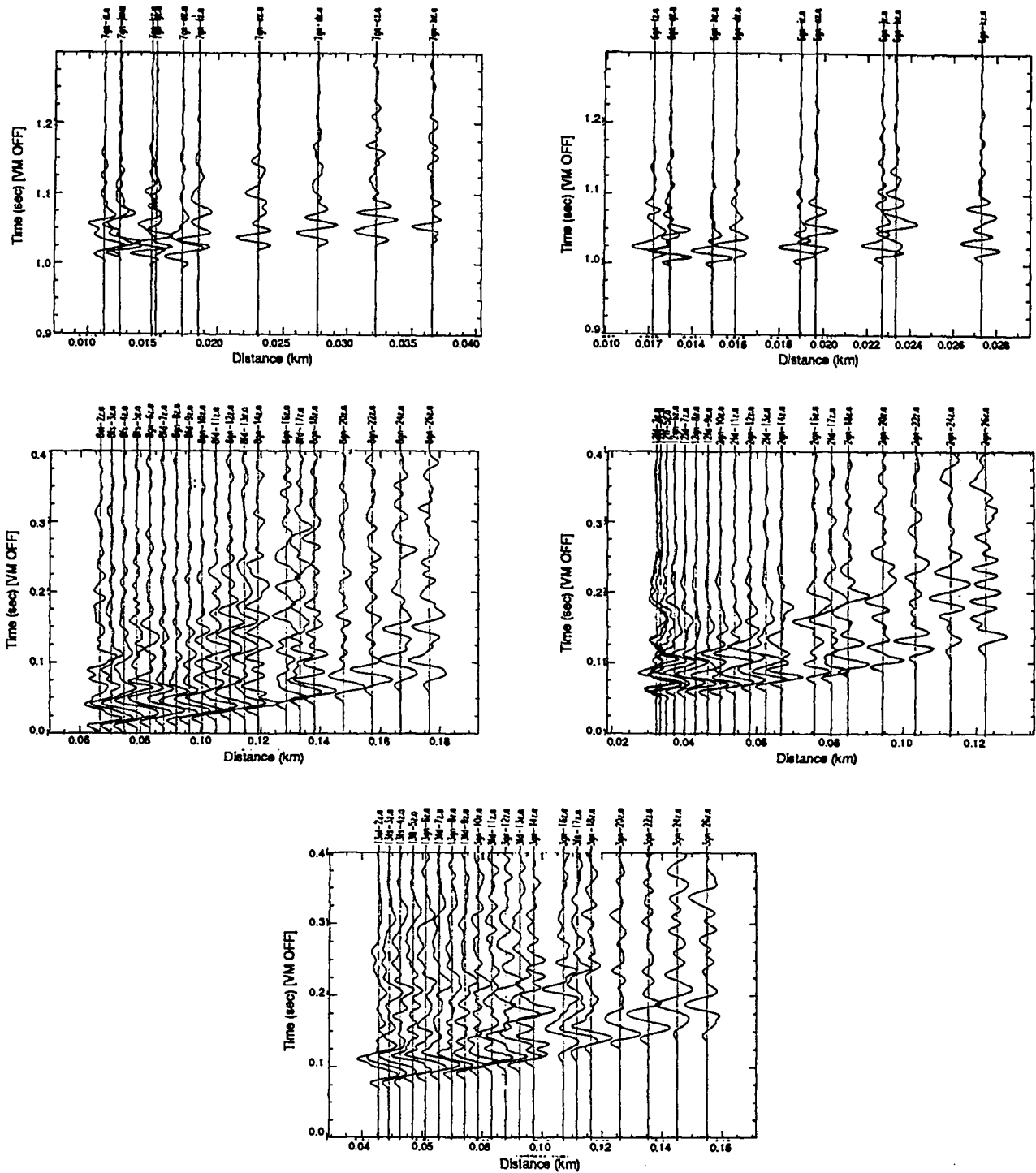


Figure 4. Section plot of perlite #5, 6, 7 data.

Table 2
Station Information for Experiments P1-P7

Station	Sensor	Sensor Ser #	Recorder type/ser #	Channel #
A	Geospace		NOMIS	1 2 3
B	Geospace		NOMIS	4 5 6
C	Geospace		NOMIS	7 8 9
D	Geospace		NOMIS	10 11 12
E	Geospace		NOMIS	13 14 15
F	Geospace		NOMIS	16 17 18
G	Geospace		NOMIS	19 20 21
H	Geospace		NOMIS	22 23 24
I	Geospace		NOMIS	25 26 27
J	Geospace		NOMIS	28 29 30
K	Geospace		NOMIS	31 32 33
L	Terra Tek FBA	SMU 508	Reftek LANL 37	1 2 3
M	Terra Tek FBA	DNA 338	Reftek LANL 410	1 2 3
N	Terra Tek FBA	LANL 14	Reftek LANL 410	4 5 6
O	Terra Tek FBA	SMU 509	Reftek LANL 37	4 5 6
P	Terra Tek FBA	LANL 11	Reftek LANL 412	1 2 3
Q	Terra Tek FBA	LANL 12	Reftek LANL 412	4 5 6
R	Terra Tek FBA	SMU 503	Reftek LANL 38	4 5 6

Table 3
 Station Survey Data for Experiments P1-P7

Station	Easting	Northing	Range		Station	Easting	Northing	Range
P1	29.5	24.5	0.0		P4	30.7	48.3	0.0
1A	30.4	44.5	20.1		4A	31.0	67.1	18.9
1B	30.5	46.0	21.6		4B	31.1	68.6	20.4
1C	30.5	47.6	23.1		4C	31.1	70.2	21.9
1D	30.6	49.1	24.6		4D	31.2	71.7	23.4
1E	30.7	50.6	26.2		4E	31.2	73.2	24.9
1F	30.7	52.1	27.7		4F	31.3	74.7	26.5
1G	30.8	53.7	29.2		4G	31.4	76.3	28.0
1H	30.8	55.2	30.7		4H	31.4	77.8	29.5
1I	30.9	56.7	32.3		4I	31.5	79.3	31.0
1J	30.9	58.2	33.8		4J	31.5	80.8	32.6
1K	31.0	59.7	35.3		4K	31.6	82.4	34.1
Station	Easting	Northing	Range		Station	Easting	Northing	Range
P2	30.2	36.9	0.0		P5	30.4	59.5	0.0
2A	30.4	44.5	7.65		5A	31.0	67.1	7.7
2B	30.5	46.0	9.1		5B	31.1	68.6	9.2
2C	30.5	47.6	10.7		5C	31.1	70.2	10.7
2D	30.6	49.1	12.2		5D	31.2	71.7	12.3
2E	30.7	50.6	13.7		5E	31.2	73.2	13.8
2F	30.7	52.1	15.2		5F	31.3	74.7	15.3
2G	30.8	53.7	16.8		5G	31.4	76.3	16.8
2H	30.8	55.2	18.3		5H	31.4	77.8	18.3
2I	30.9	56.7	19.8		5I	31.5	79.3	19.9
2J	30.9	58.2	21.3		5J	31.5	80.8	21.4
2K	31.0	59.7	22.8		5K	31.6	82.4	22.9
Station	Easting	Northing	Range					
P3	29.4	13.7	0.0					
3A	30.4	44.5	30.8					
3B	30.5	46.0	32.3					
3C	30.5	47.6	33.8					
3D	30.6	49.1	35.4					
3E	30.7	50.6	36.9					
3F	30.7	52.1	38.4					
3G	30.8	53.7	39.9					
3H	30.8	55.2	41.5					
3I	30.9	56.7	43.0					
3J	30.9	58.2	44.5					
3K	31.0	59.7	46.0					

Table 3
Station Survey Data for Experiments P1-P7, concluded

Station	Easting	Northing	Range
P6	29.2	53.4	0.0
6A	19.6	53.8	9.6
6B	16.5	33.9	23.3
6C	16.1	38.8	19.6
6D	16.7	43.5	15.9
6E	17.3	48.4	12.9
6F	17.1	54.2	12.1
6G	17.4	58.6	12.9
6H	17.9	63.1	14.9
6I	18.1	68.7	18.9
6J	17.9	73.0	22.7
6K	18.6	78.5	27.3
6L	27.5	52.3	2.0
6M	25.1	50.6	5.0
6N	18.8	46.4	12.5
6O	8.0	39.8	25.1
6P	-10.0	28.8	46.3
6Q	-26.9	14.2	68.4
6R	-40.5	0.7	87.3
Station	Easting	Northing	Range
P7	29.3	68.1	0.0
7A	19.6	53.8	17.3
7B	16.5	33.9	36.6
7C	16.1	38.8	32.2
7D	16.7	43.5	27.7
7E	17.3	48.4	23.1
7F	17.1	54.2	18.5
7G	17.4	58.6	15.2
7H	17.9	63.1	12.4
7I	18.1	68.7	11.2
7J	17.9	73.0	12.4
7K	18.6	78.5	14.9
7L	26.6	65.5	3.8
7M	22.7	61.6	9.3
7N	20.5	59.3	12.5
7O	8.0	39.8	35.4
7P	-10.0	28.8	55.6
7Q	-26.9	14.2	77.9
7R	-40.5	0.7	97.0

**Table 4
 Station Information for Experiments P8-P13**

Station	Sensor	Sensor Ser #	Recorder type/ser #	Channel #
2	Endevco 25 g	E25-2	Reftek LANL 409	123
3	Terra Tek FBA	SMU 506	Reftek SMU 35	456
4	Terra Tek FBA	SMU 507	Reftek SMU 35	123
5	Terra Tek FBA	LANL 8	Reftek LANL 409	456
6	Geospace		NOMIS	1
7	Terra Tek FBA	DNA 301	Reftek SMU 41	123
8	Geospace		NOMIS	2
9	Terra Tek FBA	DNA 302	Reftek SMU 42	123
10	Geospace		NOMIS	3
11	Terra Tek FBA	DNA 303	Reftek SMU 41	456
12	Geospace		NOMIS	4
13	Terra Tek FBA	DNA 304	Reftek SMU 42	456
14	Geospace		NOMIS	5
15	Terra Tek FBA	DNA 305	Reftek SMU 43	123
16	Geospace		NOMIS	6
17	Terra Tek FBA	DNA 306	Reftek SMU 44	123
18	Geospace		NOMIS	7
19	Terra Tek FBA	DNA 307	Reftek SMU 43	456
20	Geospace		NOMIS	8
21	Terra Tek FBA	DNA 308	Reftek SMU 45	123
22	Geospace		NOMIS	9
23	Terra Tek FBA	DNA 336	Reftek SMU 44	456
24	Geospace		NOMIS	10
25	Terra Tek FBA	DNA 337	Reftek SMU 45	456
26	Geospace		NOMIS	11
27	Endevco 100 g	E100-12	Reftek LANL 566	123
28	Endevco 25 g	E25-6	Reftek LANL 470	123
29	Terra Tek FBA	SMU 508	Reftek SMU 37	123
30	Terra Tek FBA	DNA 338	Reftek LANL 410	123
31	Terra Tek FBA	LANL 14	Reftek LANL 410	456
32	Endevco 100 g	E100-11	Reftek LANL 566	456
33	Endevco 25g	E25-4	Reftek LANL 470	456
34	Terra Tek FBA	SMU 509	Reftek SMU 37	456
35	Terra Tek FBA	LANL 11	Reftek LANL 412	123
36	Terra Tek FBA	LANL 12	Reftek LANL 412	456
37	Endevco 25g	E25-7	Reftek LANL 415	123
38	Terra Tek FBA	SMU 503	Reftek SMU 38	456
39	Terra Tek FBA	SMU 510	Reftek SMU 38	123
40	Terra Tek FBA	LANL 9	Reftek LANL 414	123
41	Terra Tek FBA	LANL 10	Reftek LANL 414	456
42	Terra Tek FBA	SMU 502	Reftek SMU 36	456

Table 4
Station Information for Experiments P8-P13

Station	Sensor	Sensor Ser #	Recorder type/ser #	Channel #
43	Terra Tek FBA	SMU 505	Reftex SMU 36	123
44	Terra Tek FBA	LANL 1	Reftex LANL 473	123
45	Terra Tek FBA	LANL 3	Reftex LANL 473	456
46	Terra Tek FBA	LANL 5	Reftex LANL 565	123
47	Endevco 25 g	E25-3	Reftex LANL 509	123
48	Endevco 25 g	E25-1	Reftex LANL 509	456
49	Terra Tek FBA	LANL 2	Reftex LANL 510	123
50	Terra Tek FBA	LANL 4	Reftex LANL 510	456
51	Terra Tek FBA	LANL 6	Reftex LANL 565	456
52	Endevco 25g	E25-5	Reftex LANL 459	456
53	Terra Tek FBA	SMU 504	Reftex SMU 39	456
54	Terra Tek FBA	SMU 511	Reftex SMU 39	123
55	Terra Tek FBA	LANL 7	Reftex LANL 459	123
56	Endevco 100 g	E100-8	Reftex LANL 415	456
57	Endevco 100 g	E100-9	Reftex LANL 469	123
58	Endevco 100 g	E100-10	Reftex LANL 469	456
59	Mark Pro L4-3D		Reftex LANL 508	123
60	Kinematics sv sh		Reftex LANL 508	456
P08-0	Endevco 100 g	E100 -15	Reftex LANL 405	2
P08-2.5	Endevco 100 g	E100 -14	Reftex LANL 405	3
P08-5	Endevco 100 g	E100 -13	Reftex LANL 405	456
P08-SB	Mark Products L22	-	Reftex LANL 405	1
P09-0	Endevco 100 g	E100 -15	Reftex LANL 405	2
P09-2.5	Endevco 100 g	E100 -14	Reftex LANL 405	3
P09-5	Endevco 100 g	E100 -13	Reftex LANL 405	456
P09-SB	Mark Products L22	-	Reftex LANL 405	1
P10-0	Endevco 100 g	E100 -15	Reftex LANL 405	2
P10-2.5	Endevco 100 g	E100 -14	Reftex LANL 405	3
P10-5	Endevco 100 g	E100 -13	Reftex LANL 405	456
P10-SB	Mark Products L22	-	Reftex LANL 405	1
P11-0	Endevco 100 g	E100 -15	Reftex LANL 405	2
P11-2.5	Endevco 100 g	E100 -14	Reftex LANL 405	3
P11-5	Endevco 100 g	E100 -13	Reftex LANL 405	456
P11-SB	Mark Products L22	-	Reftex LANL 405	1
P12-0	Endevco 100 g	E100 -15	Reftex LANL 405	2
P12-2.5	Endevco 100 g	E100 -14	Reftex LANL 405	3
P12-5	Endevco 100 g	E100 -13	Reftex LANL 405	456
P12-SB	Mark Products L22	-	Reftex LANL 405	1
P13-0	Endevco 100 g	E100 -15	Reftex LANL 405	2
P13-2.5	Endevco 100 g	E100 -14	Reftex LANL 405	3
P13-5	Endevco 100 g	E100 -13	Reftex LANL 405	456
P13-SB	Mark Products L22	-	Reftex LANL 405	1

Table 5
Station Survey Data for Experiments P8-P13

Station	Eastng (m)	Northng (m)	Elevation (m)	P8 Slant Range (m)	P9 Slant Range (m)
1.0	2.1	18.8	1531.5	63.1	40.0
2.0	6.8	34.4	1531.0	66.6	40.5
3.0	9.8	50.2	1530.4	70.4	41.5
4.0	12.6	66.0	1530.1	74.5	43.4
5.0	16.0	82.5	1530.0	78.8	46.0
6.0	19.3	98.6	1529.7	83.1	48.7
7.0	22.6	115.3	1529.4	87.6	51.9
8.0	26.2	130.7	1529.2	91.9	55.2
9.0	29.7	146.5	1528.8	96.2	58.7
10.0	33.3	161.7	1528.4	100.5	62.2
11.0	37.0	178.1	1528.0	105.1	66.2
12.0	39.9	194.3	1527.7	109.8	70.3
13.0	43.2	210.8	1527.6	114.6	74.7
14.0	46.7	226.1	1528.0	119.1	79.1
15.0	50.6	242.3	1527.2	123.8	83.3
16.0	54.4	258.7	1527.0	128.6	87.9
17.0	57.6	274.4	1526.9	133.3	92.4
18.0	60.6	290.4	1526.9	138.1	97.0
19.0	64.5	306.8	1526.7	143.0	101.7
20.0	67.4	323.1	1526.5	147.8	106.4
21.0	71.0	337.8	1526.4	152.2	110.7
22.0	74.2	354.1	1526.3	157.2	115.5
23.0	77.2	370.3	1526.3	162.1	120.3
24.0	81.0	385.7	1526.2	166.7	125.0
25.0	84.2	401.0	1526.1	171.4	129.5
26.0	87.9	417.9	1526.0	176.5	134.6
27.0	-5.4	16.7	1531.8	63.5	40.3
28.0	-10.5	33.1	1531.7	68.3	41.2
29.0	-22.5	63.1	1531.7	77.6	44.8
30.0	-32.8	94.4	1531.2	87.0	49.7
31.0	-44.9	125.6	1530.8	96.7	56.3
32.0	-13.8	9.0	1531.9	62.7	40.4
33.0	-28.7	17.6	1532.2	67.0	41.7
34.0	-58.9	31.9	1532.1	75.1	45.2
35.0	-88.2	46.6	1532.0	83.5	50.4
36.0	-117.5	63.6	1532.2	92.9	57.3
37.0	-17.6	1.7	1532.2	61.6	40.7
38.0	-33.4	2.1	1532.5	64.1	41.9
39.0	-66.3	2.5	1532.7	70.0	45.5
40.0	-98.1	1.2	1532.6	76.1	50.5
41.0	-132.8	2.4	1533.3	84.2	57.9
42.0	14.7	10.4	1531.3	59.6	39.8
43.0	30.3	17.9	1530.4	59.9	40.0

P10 Slant Range (m)	P11 Slant Range (m)	P12 Slant Range (m)	P13 Slant Range (m)
29.9	9.9	33.4	41.9
30.7	13.1	32.3	45.5
32.2	17.1	32.3	48.9
34.7	21.6	33.4	52.6
37.9	26.5	35.1	56.8
41.2	31.3	37.3	61.0
45.0	36.3	40.2	65.4
48.8	41.1	43.1	69.7
52.8	45.9	46.5	74.1
56.8	50.6	49.9	78.5
61.2	55.6	53.9	83.2
65.7	60.6	58.1	87.8
70.4	65.7	62.5	92.6
75.0	70.5	66.7	97.1
79.5	75.5	71.0	102.0
84.3	80.7	75.6	106.9
89.0	85.5	80.1	111.5
93.8	90.5	84.7	116.3
98.7	95.6	89.5	121.3
103.5	100.6	94.3	126.1
108.0	105.2	98.6	130.6
112.9	110.3	103.4	135.5
117.8	115.3	108.3	140.4
122.5	120.2	112.9	145.1
127.2	124.9	117.5	149.8
132.3	130.2	122.5	154.9
30.1	10.0	35.5	39.8
31.4	13.5	37.2	41.3
36.0	22.1	42.6	45.0
42.1	31.5	48.9	50.9
49.8	41.3	56.8	57.7
30.2	9.9	38.0	36.5
31.8	13.6	42.2	34.4
36.3	22.2	50.9	31.3
42.6	31.6	59.9	31.6
50.6	41.7	69.3	35.6
30.5	10.3	39.4	34.6
32.0	13.7	43.8	30.8
36.6	22.3	53.2	23.7
42.7	31.3	62.4	19.0
51.1	41.7	72.8	20.0
29.7	9.6	30.0	44.1
30.2	12.8	25.5	49.1

Table 5 (concluded)
Station Survey Data for Experiments P8-P13

Station	Easting (m)	Northing (m)	Elevation (m)	P8 Slant Range (m)	P9 Slant Range (m)
44.0	56.5	34.7	1529.6	63.1	42.8
45.0	85.1	49.8	1528.9	66.9	47.7
46.0	113.8	66.4	1528.9	72.6	54.6
47.0	10.8	16.4	1531.3	61.5	39.9
48.0	20.4	28.6	1530.4	63.6	39.9
49.0	38.3	53.6	1529.6	69.2	42.8
50.0	60.3	81.1	1529.3	76.2	48.5
51.0	78.0	107.7	1528.5	83.7	54.6
52.0	13.9	-6.4	1531.9	55.6	40.3
53.0	33.2	-14.1	1531.3	51.6	40.9
54.0	57.9	-31.2	1531.1	45.7	44.1
55.0	85.4	-48.3	1532.2	41.9	50.2
p1	96.8	80.3	1528.7	76.0	53.2
p2	99.0	121.1	1528.5	87.9	60.1
p3	96.3	45.1	1528.6	65.8	49.0
p4	100.7	158.4	1527.8	98.8	67.6
p5	99.9	195.1	1527.6	109.7	75.7
p6	95.8	175.1	1527.6	103.7	70.6
p7	96.1	223.6	1527.4	118.1	82.2
p8	75.2	-160.6	1533.7	26.6	68.4
p9	0.0	0.0	1532.1	58.8	40.2
p12	98.4	17.5	1529.5	58.3	48.4
p13	-113.9	-48.5	1534.1	71.8	56.6
p8-0	74.0	-157.7	1533.6	26.5	67.5
p8-2.5	71.3	-152.4	1533.4	26.3	66.0
p8-5	66.9	-144.1	1533.5	26.8	63.9
p9-0	3.4	0.6	1532.0	58.5	40.1
p9-2.5	6.2	-2.9	1531.9	57.3	40.1
p12-0	96.2	19.1	1529.4	58.7	48.0
p12-2.5	91.0	21.0	1529.0	58.9	46.8
p12-5	79.8	26.0	1529.3	60.2	45.4
p13-0	-119.9	-49.6	1534.1	73.2	57.9
p13-2.5	-123.7	-48.0	1534.1	74.3	58.5
p13-5	-132.8	-48.7	1534.3	76.6	60.5

P10 Slant Range (m)	P11 Slant Range (m)	P12 Slant Range (m)	P13 Slant Range (m)
34.1	21.1	19.7	58.3
40.2	30.6	17.0	68.0
48.2	40.5	20.5	78.0
29.8	9.9	31.0	43.8
30.2	12.8	28.2	47.9
34.1	21.0	25.6	56.4
41.1	31.4	26.4	66.6
48.4	40.9	31.0	75.7
30.1	9.7	31.3	42.1
31.1	13.5	27.1	46.9
35.2	21.5	24.8	53.4
42.4	31.2	26.4	61.6
46.7	38.7	23.2	75.6
54.5	47.9	34.1	83.2
41.9	32.8	15.6	70.4
62.7	57.4	44.7	91.0
71.5	66.9	55.5	98.9
66.0	61.0	49.6	93.6
78.4	74.3	63.9	104.9
62.6	55.0	57.7	68.0
30.0	8.7	34.6	39.0
40.9	31.1	13.9	68.2
49.5	39.2	70.2	12.0
61.7	54.1	56.8	67.2
60.1	52.3	55.4	65.7
57.7	49.5	53.3	63.4
29.9	8.7	33.7	40.0
29.8	8.8	33.1	40.4
40.5	30.5	13.8	67.7
39.2	29.0	13.7	66.3
37.3	26.3	15.1	63.7
50.9	41.0	72.0	12.1
51.6	41.8	73.0	12.4
53.8	44.5	75.6	13.5

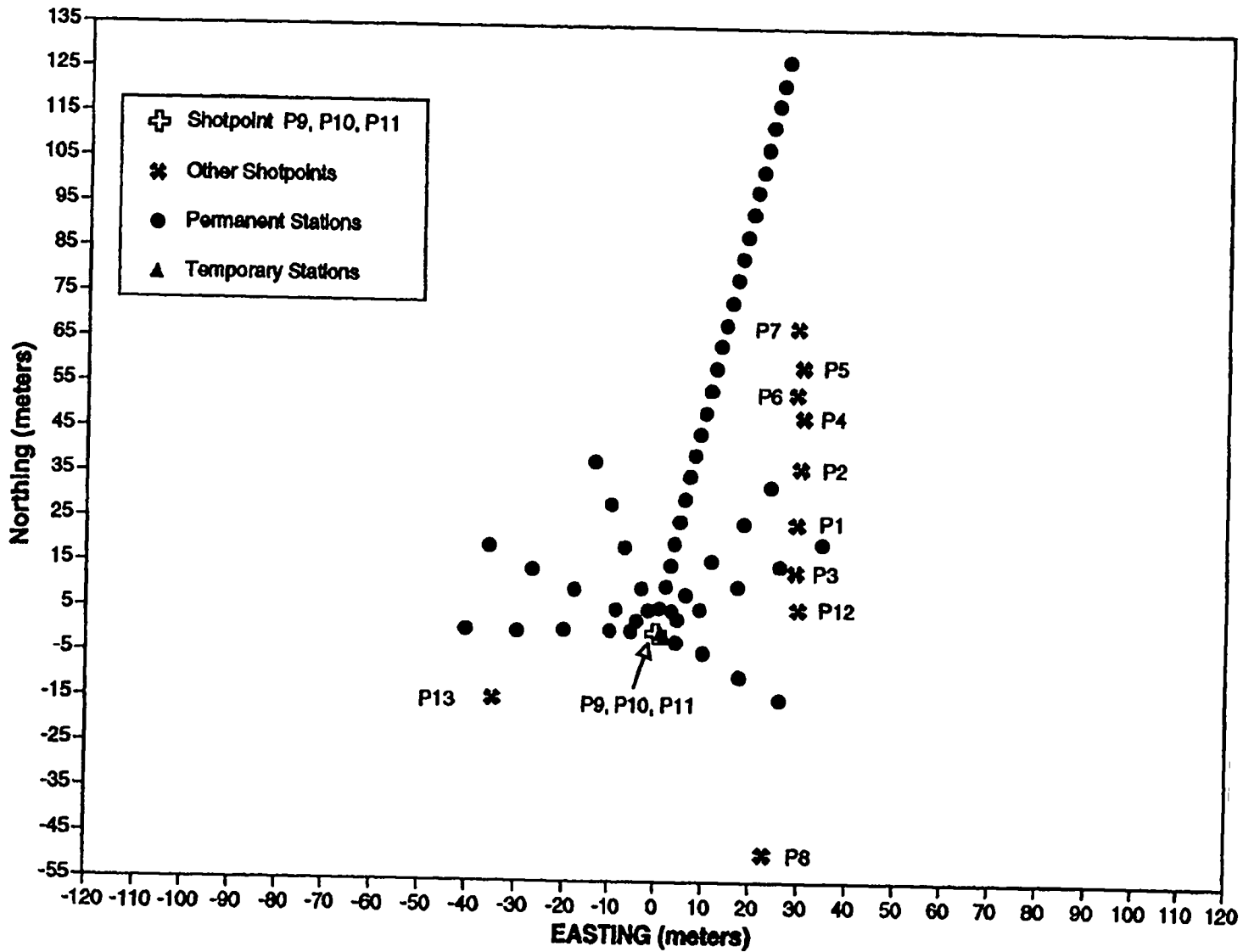


Figure 5. Experiment layout P9, P10, P11.

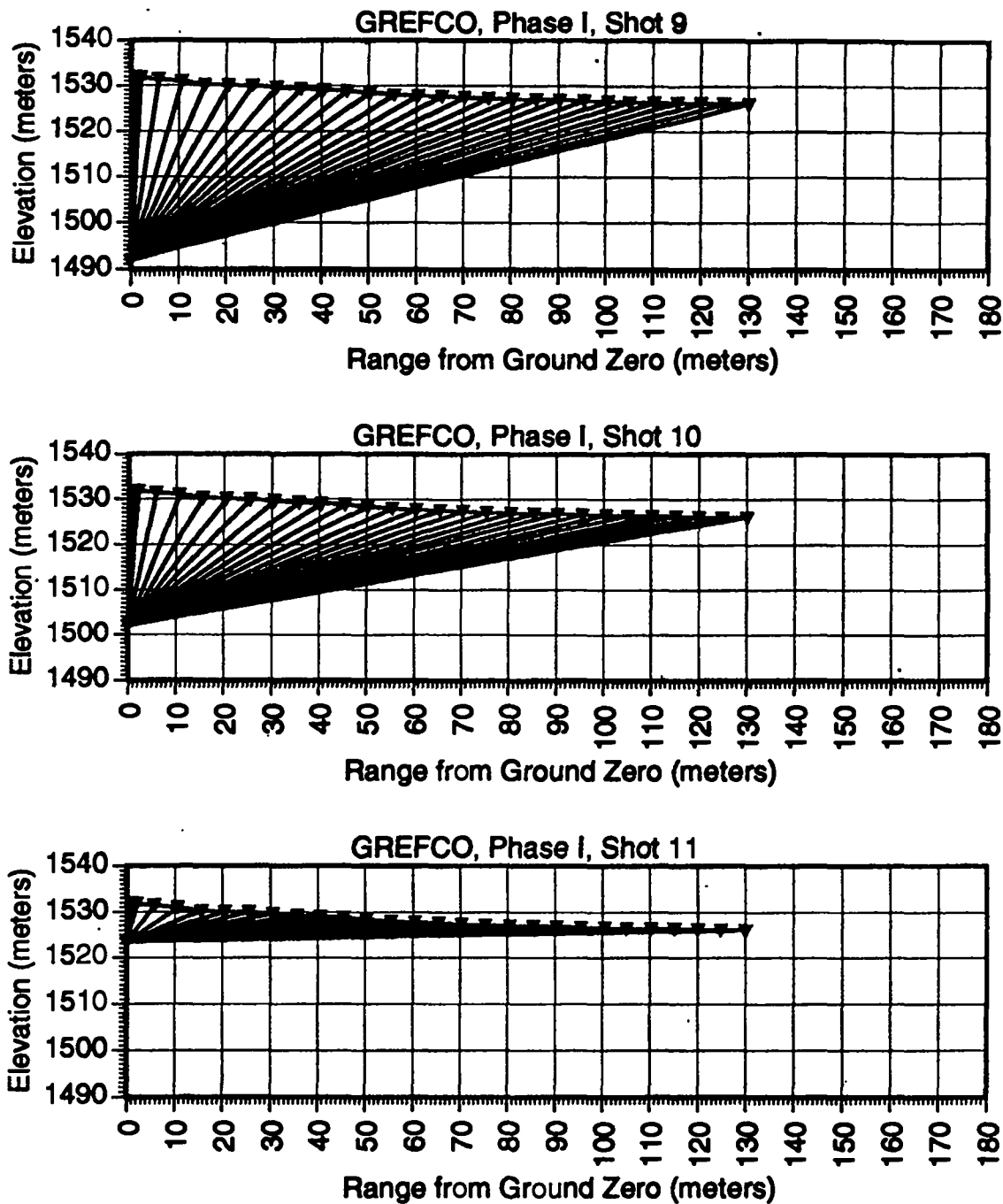


Figure 6. Ray path geometry for shots P9 (a), P-10 (b), and P11 (c). The shot depth of burial (DOB) strongly affects the incidence angle of the wave front at the stations composing the long linear array (see Figure 1).

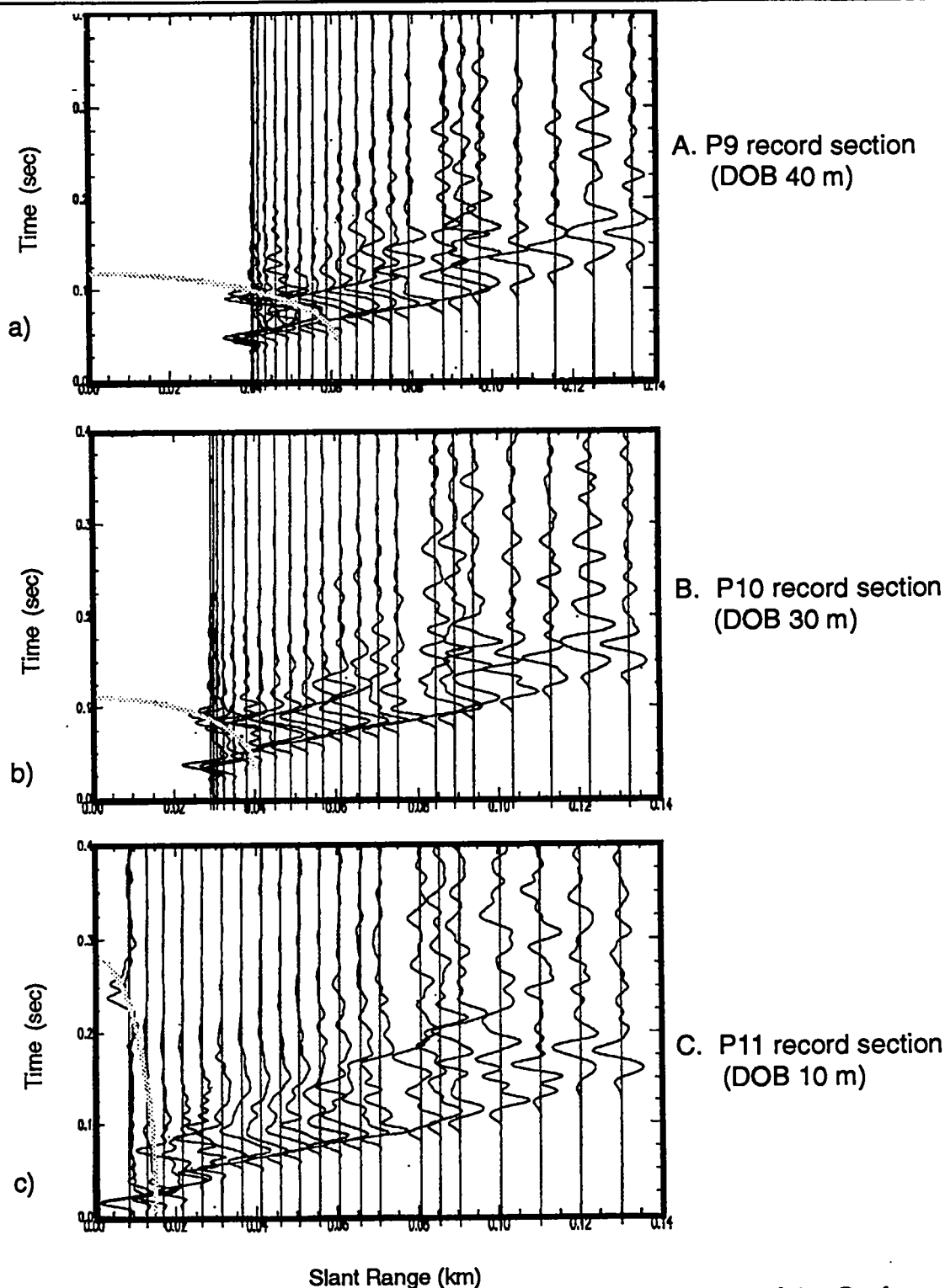


Figure 7. Record section plots of surface acceleration along the length of the Grefco Dicapperl test best (see the long linear array in Figure 1). The data are presented as a function of slant range to facilitate determination of seismic velocities. The observed extent of surface spall is denoted by the hatched line.

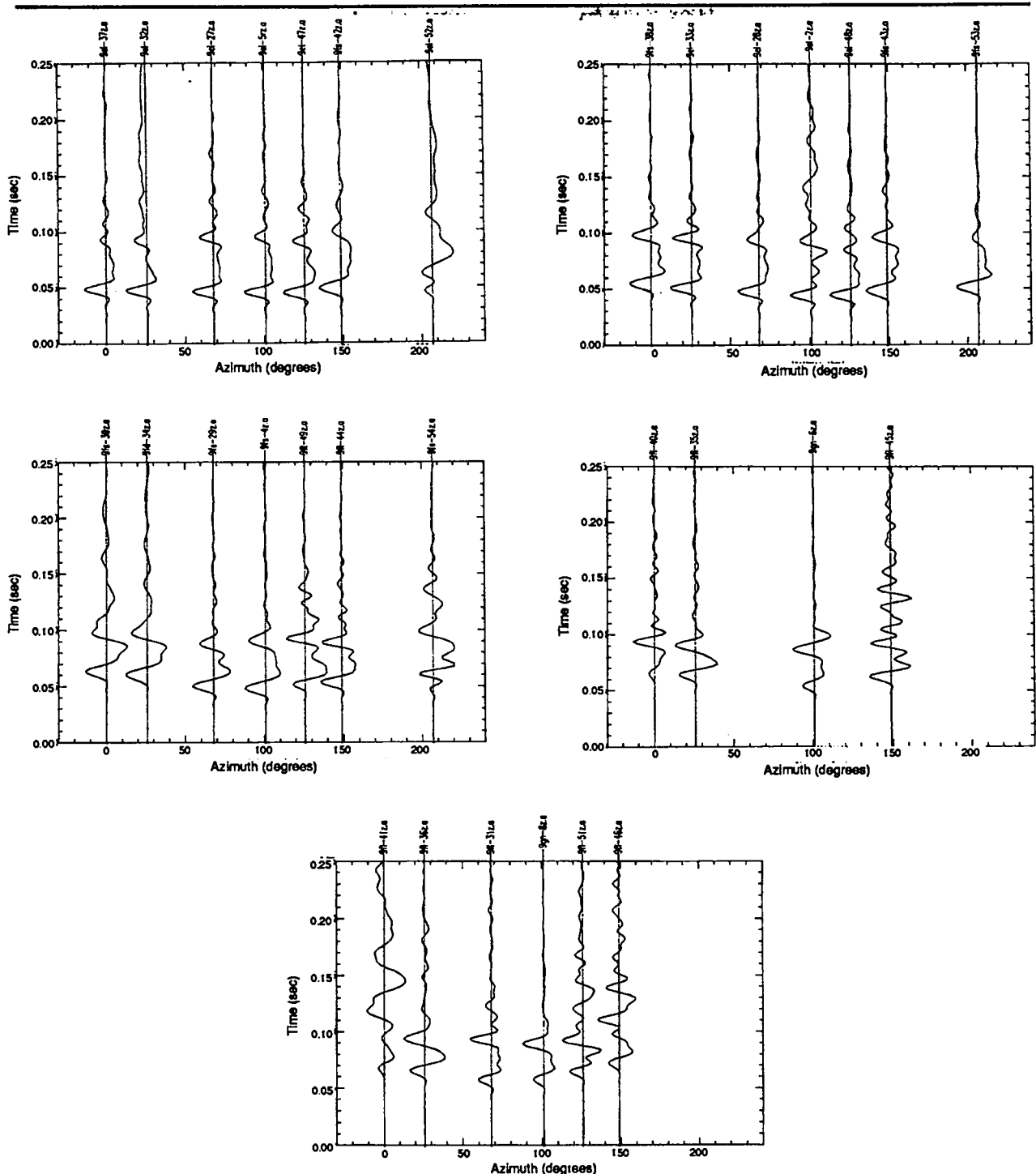


Figure 8. The azimuthal variation of the waveforms is shown for a) 5-m range, b) 10-m range, c) 20-m range, d) 30-m range, and e) 40-m range. At 5 m, the spall initiation time is nearly identical at all azimuths. At increasing ranges, the first motion is delayed in time at increasing and decreasing angles away from the major joint orientation near 0 deg. (see Figure 1). Spall dwell time decreases both with increasing range and increasing azimuth away from the major joint orientation.

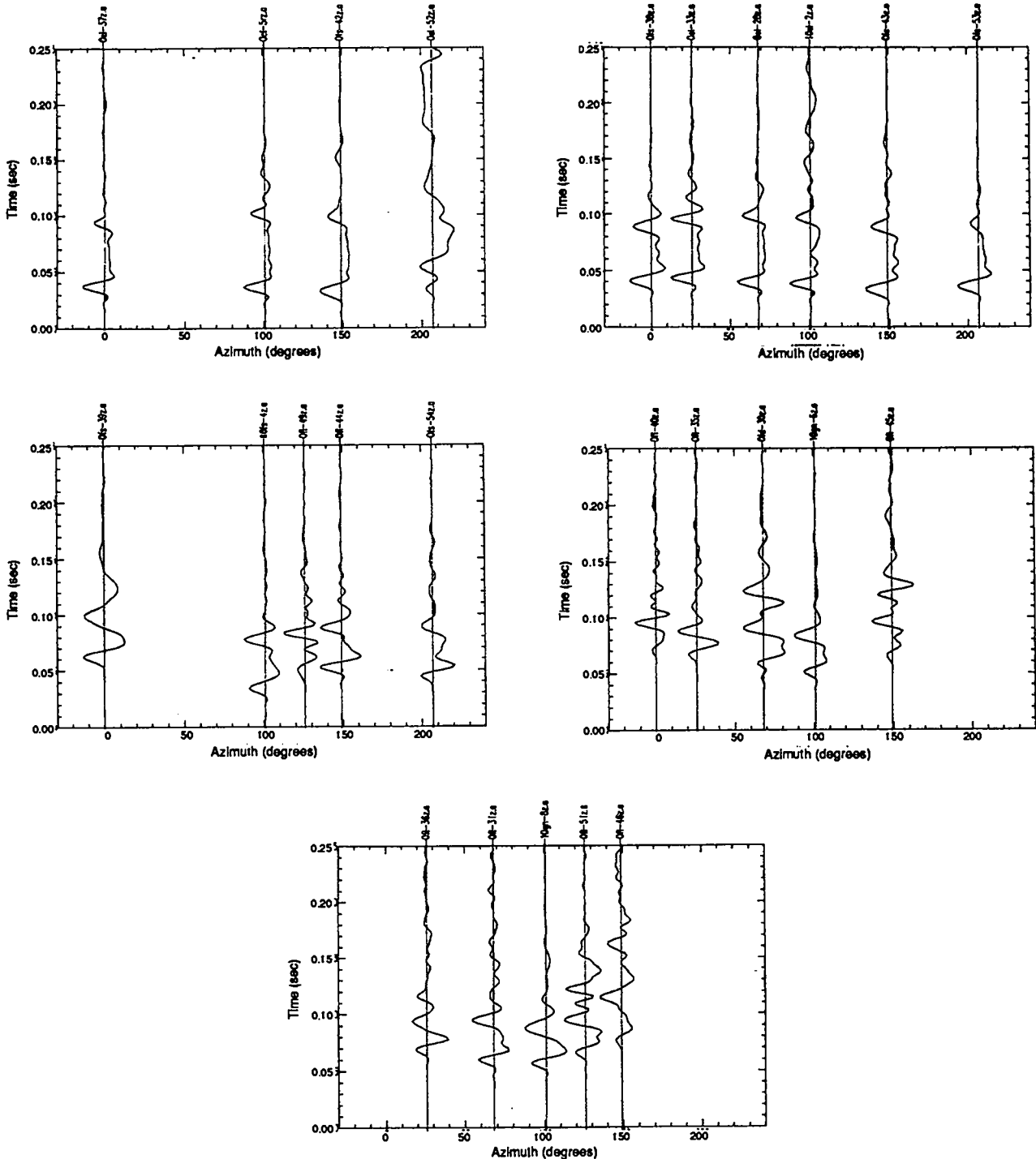


Figure 9. The azimuthal variation of the waveforms is shown for a) 5-m range, b) 10-m range, c) 20-m range, d) 30-m range, and E) 40-m range. At 5 m, the spall initiation time is nearly identical at all azimuths. At increasing ranges, the first motion is delayed in time at increasing and decreasing angles away from the major joint orientation near 0 deg. (see Figure 1). Spall dwell time decreases both increasing range and increasing azimuth away from the major joint orientation.

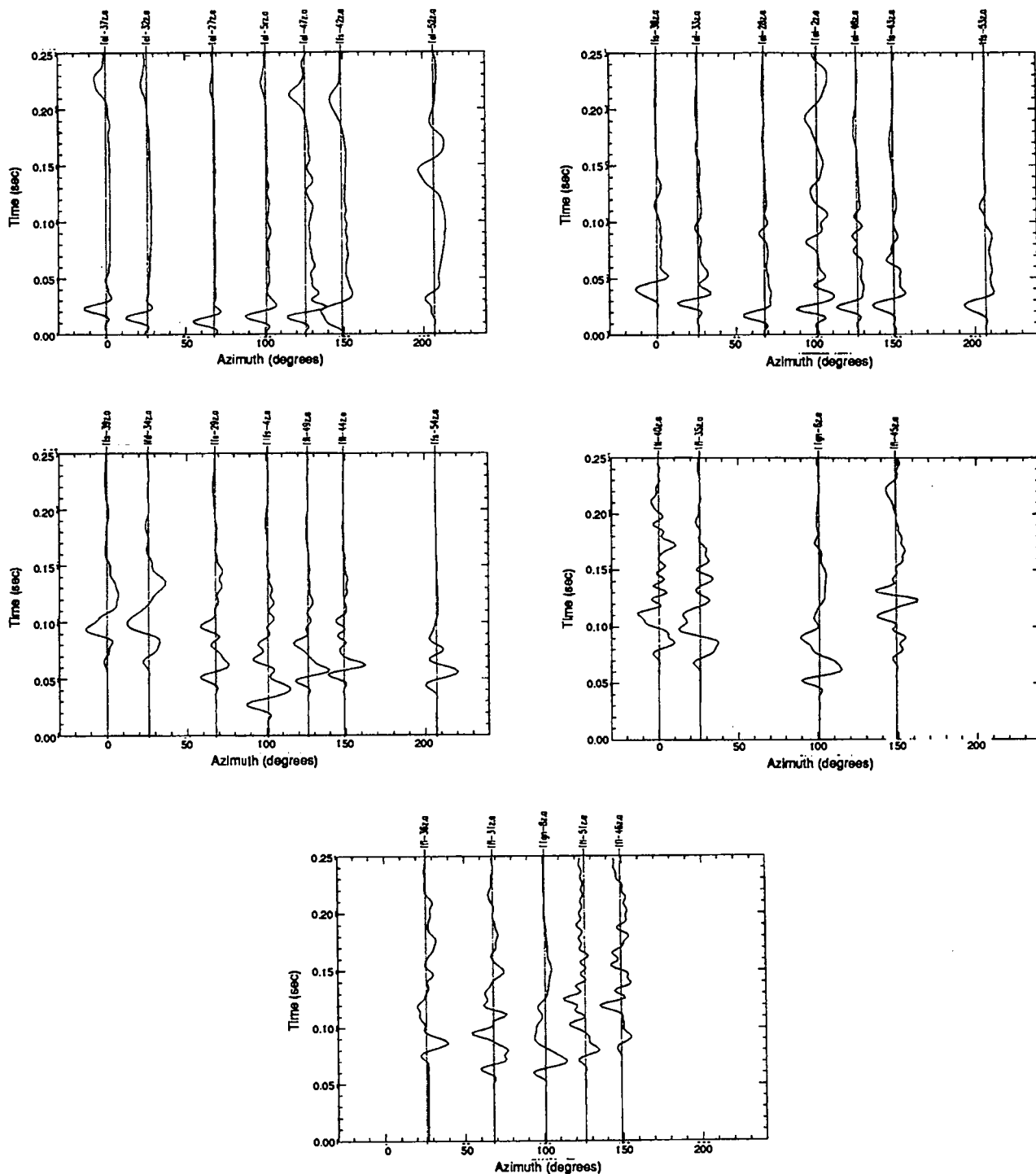


Figure 10. The azimuthal variation of the waveforms is shown for a) 5-m range, b) 10-m range, c) 20-m range, d) 30-m range, and E) 40-m range. At 5 m, the spall initiation time is nearly identical at all azimuths. At increasing ranges, the first motion is delayed in time at increasing and decreasing angles away from the major joint orientation near 0 deg. (see Figure 1). Spall dwell time decreases both increasing range and increasing azimuth away from the major joint orientation.

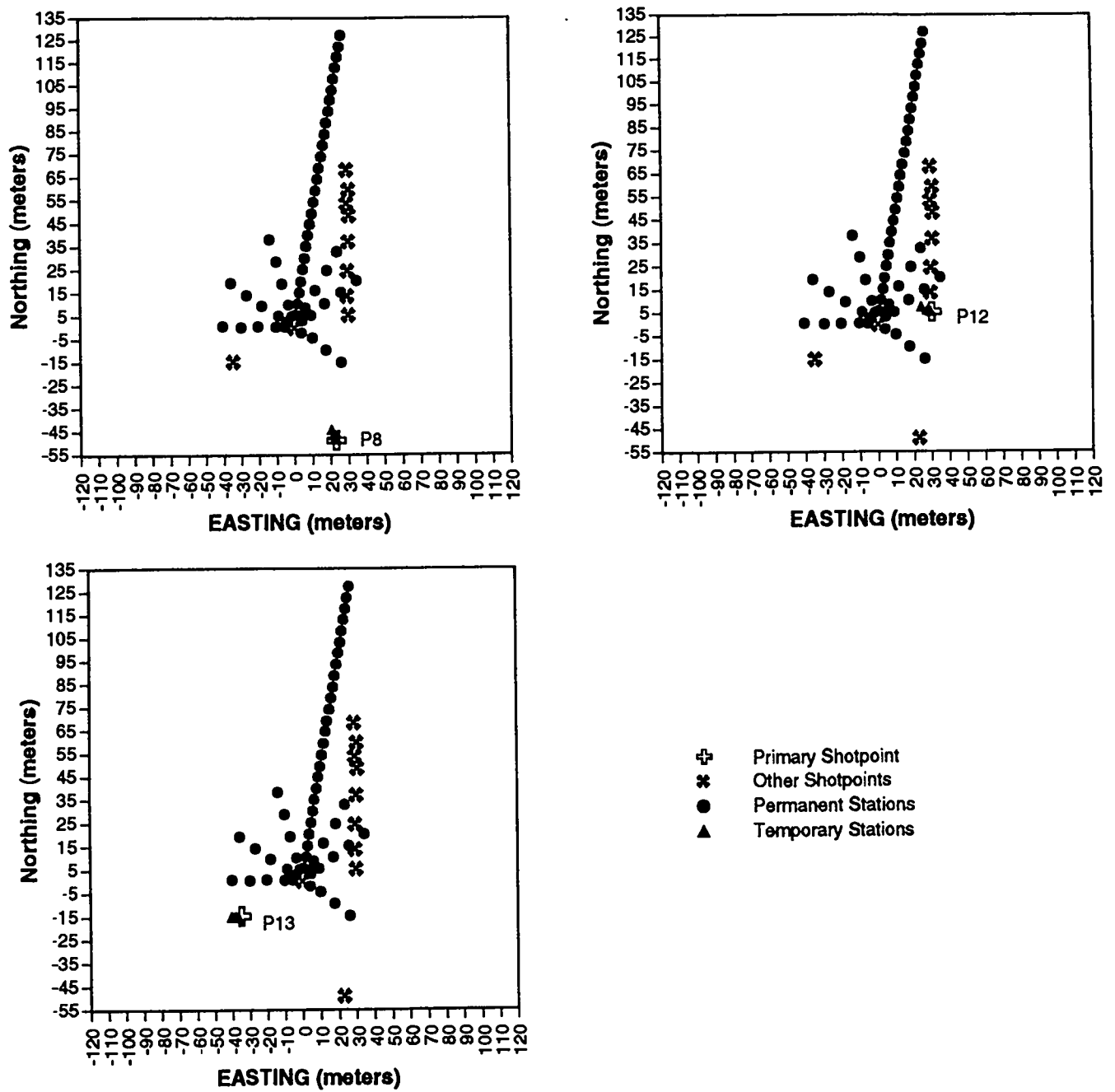


Figure 11. Experiment Layout Perlite #8, 12, 13.

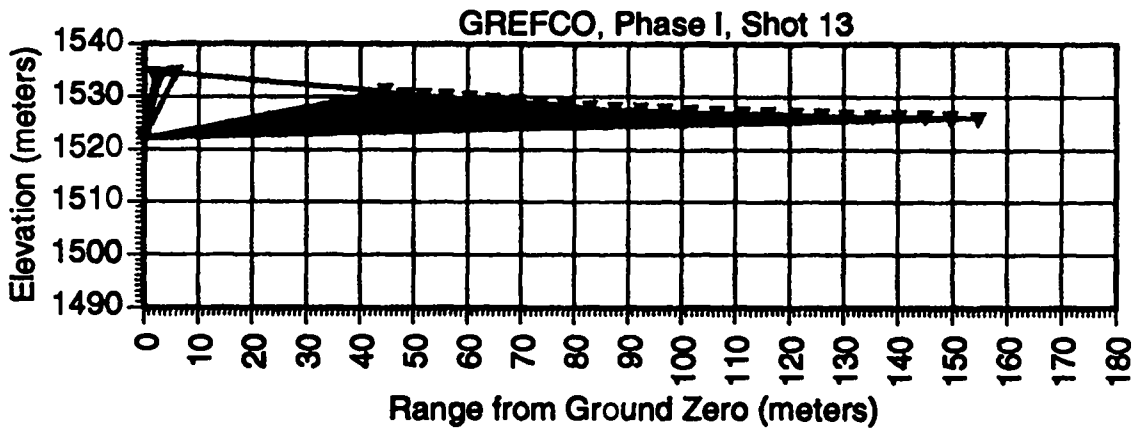
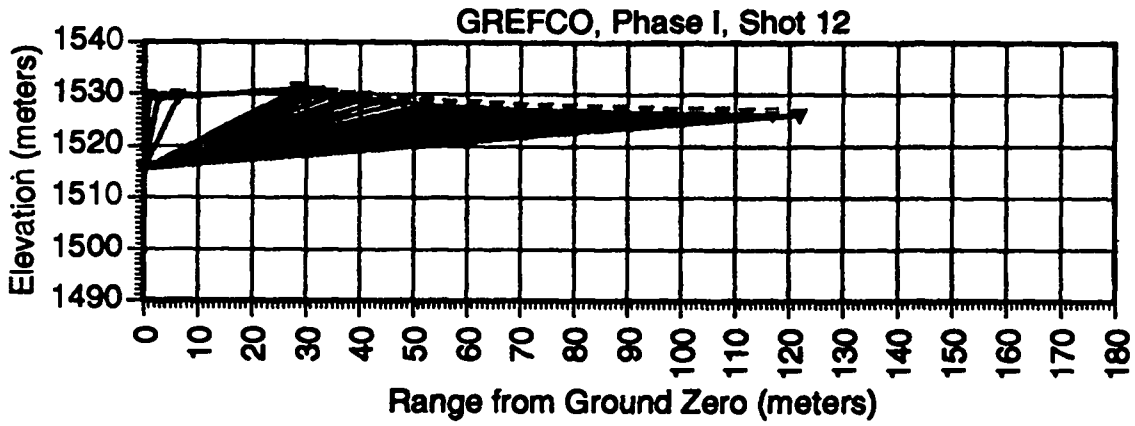
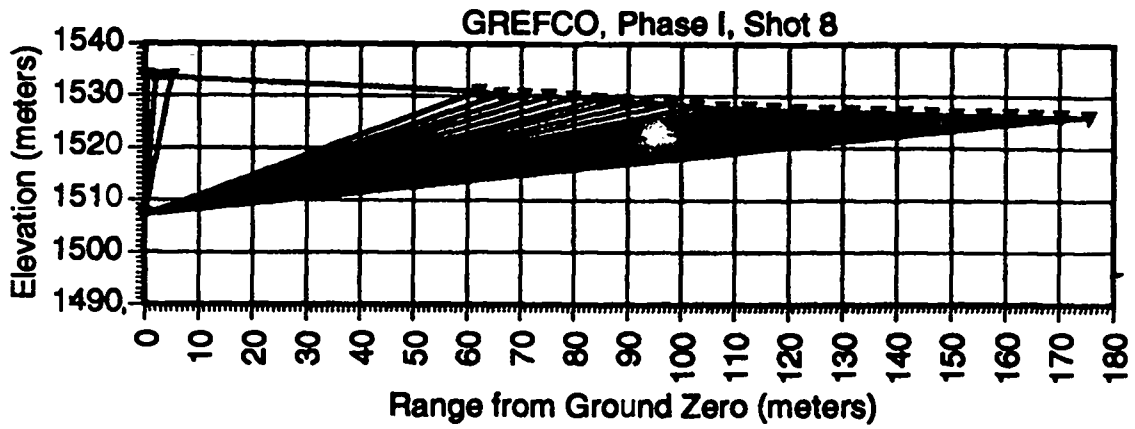


Figure 12. Experiment Geometry Perlite #8, 12, 13.

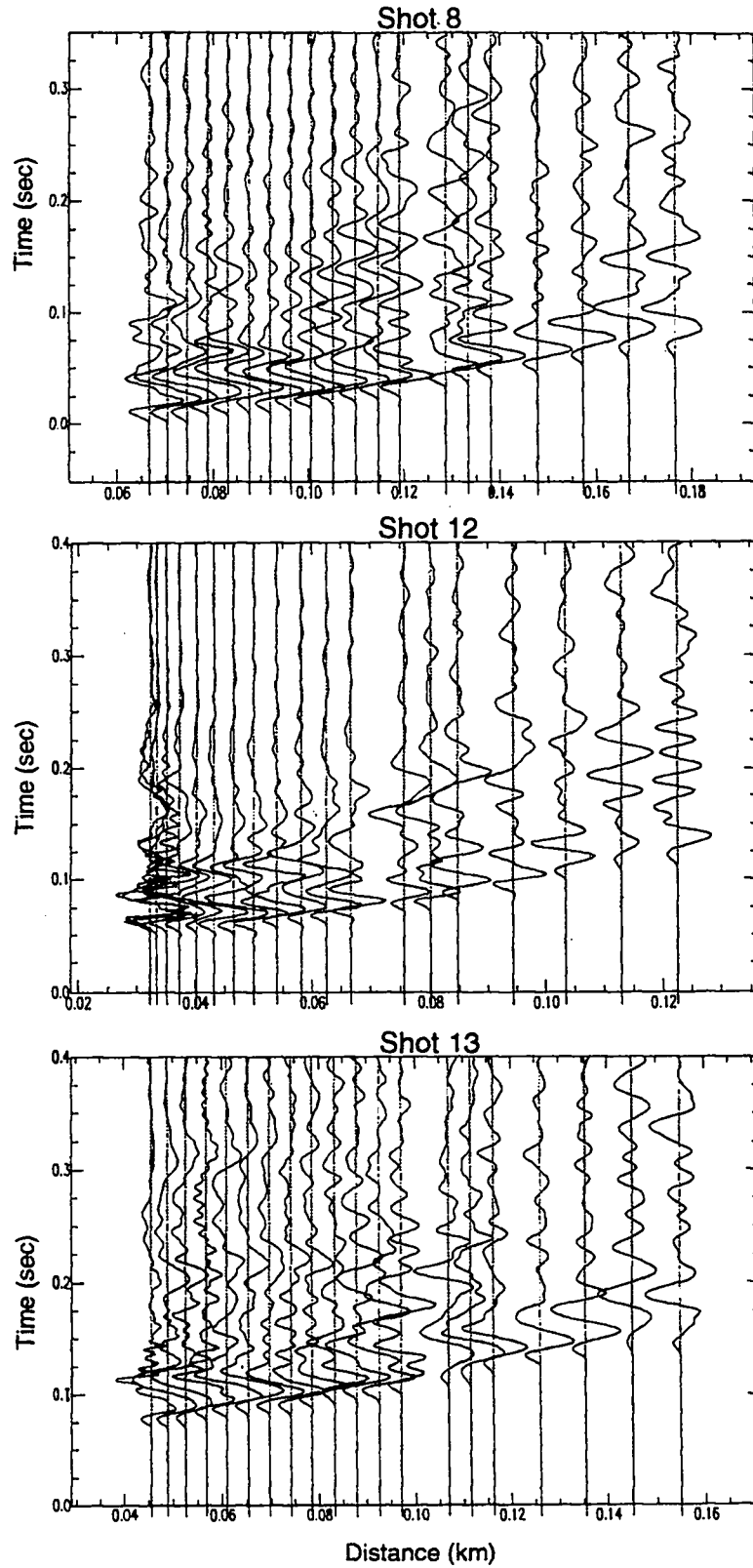


Figure 13. Record Section Plot of Perlite #8, 12, 13.

6. Preliminary Conclusions

Experiments P1 scaled depth of burial (SDOB 1.8 m/kg^{1/3}) and P2 (SDOB 1.6m/kg^{1/3}) produced RETARCs. A RETARC is a noncratering of surface materials by bulking of the material to form a convex dome at the surface (crater spelled backwards). Experiments P3 (SDOB 1.1m/kg^{1/3}), P6 (SDOB 1.0m/kg^{1/3}), and P7 (SDOB 1.0m/kg^{1/3}) all produced throw-out craters. P4 (SDOB 2.0m/kg^{1/3}) did not produce a RETARC, but several fractures were produced, radiating out from the borehole. P5 (SDOB 2.3m/kg^{1/3}) was the most deeply buried shot and produced no visible surface effects. These lightly instrumented shots allowed us to develop realistic recording parameters for the following shots.

Shots P8-P13 produced ground motions at all stations with good signal-to-noise ratios. The geometry imposed by the various source depth-of-burials complicates the interpretation of single-component data shown in this study. Further analysis, including all three components of ground motion, is necessary to separate the geometric effects from the structural effects. There is a strong indication of azimuthal variation in rock properties at the Grefco Dicaperl Mine. Spall initiation, dwell time, and range vary strongly as a function of azimuth. Future experiments at this site will be designed to address the full range of azimuthal effects imposed by the local geology and to collect additional free-field data.

7. Additional Information

These data reside, as digital time-series files, in the Ground-Motion Database (a GEODES DBMS database on a VAX VMS minicomputer) and also as SAC (Seismic Analysis Code, from Tull (19__)), files on a SUN workstation. For additional information regarding these data sets you may contact:

For general information:
C. L. Edwards or Craig Pearson
Los Alamos National Laboratory
EES-3, MS C335
Los Alamos, New Mexico 87545
Telephone: (505) 667-8464
Fax: (505) 667-4739

For SAC file information:
Diane F. Baker
Los Alamos National Laboratory
EES-3, MS C335
Los Alamos, New Mexico 87545
Telephone: (505) 667-3776
Fax: (505) 667-4739

8. Acknowledgments

This work is sponsored by the Department of Energy, Office of Arms Control and Non-Proliferation (DOE/AN). We gratefully acknowledge the contribution of Tim Hall, the manager of the Grefco Dicaperl Mine, without whose help and cooperation these experiments could never have taken place. We would also like to thank Catherine

Martin and the many students and staff at New Mexico Tech who helped prepare the experiment site, install sensors, and collect velocity data for all of the experiments. We appreciate the help of Meredith Ness and David Anderson of Southern Methodist University for their help in fielding the Reftec data acquisition systems. We also appreciate the help of Steve Woodard of Woodard Explosives for his help in the setup and detonation of the explosive charges. We also appreciate the contributions of Harry Plannerer for the physical properties characterization, Jim Kamm for the modeling to help design the experiments, and Allen Cogbill for the seismic refraction surveys (all in the Geophysics Group at Los Alamos National Laboratory). The efforts of Al Leverett (DNA/A) in the collection of the data for several of the experiments is gratefully acknowledged.

APPENDIX A Physical Property Measurements

Harry Plannerer

Appendix A is a data compilation of physical properties for Grefco's Socorro mine perlite and the mechanical response of the perlite to uniaxial compression. It is a compilation of available data for the three individual perlite blocks that were supplied to the Los Alamos National Laboratory in April.

Table A-1 of the attachment is a listing of perlite physical properties. Moisture for both crushed and bulk specimens, and the dry bulk and grain densities, are measured properties. The total porosity value is a calculated value. The values reported in Table A-1 are "as-received" perlite. Moisture determinations in Table A-2 are the posttest moisture contents for air-dried specimens after a preparation process that involved the use of water.

Table A-1.
Physical Property Determinations for the Dicaperl Perlite

Physical Property	Mean	Range	Comments
Moisture (ASTM D2216)	0.27%	0.23% - 0.29%	crushed specimen
Moisture (ASTM D2216)	0.25%	0.16% - 0.37%	bulk specimen
Dry Bulk Density (ASTM C20)	1.86 g/cm ³	1.83 - 1.93 g/cm ³	
Grain Density (He pycnometer)	2.350 g/cm ³	2.341 - 2.359 g/cm ³	
Total Porosity (Calc.)	20.9%		

Results for uniaxial compression tests (Table A-2) are segregated as to orientation of the maximum principal stress to the characteristic flow-banding structure of the perlite. These tests were conducted with the maximum principal stress either perpendicular to the flow-banding ($s_{1\perp}$) or in the plane of flow banding ($s_{1\parallel}$). Table A-2 shows that the perlite is anisotropic in its mechanical response, having greater strength and larger values for Young's modulus and Poisson's ratio in the orientation ($s_{1\parallel}$) than for ($s_{1\perp}$). The table also shows that an unconfined compressive strength of 264 bars in the ($s_{1\perp}$) orientation is reproducible within a standard deviation of approximately 18 bars. On the other hand, the unconfined compressive strength in the ($s_{1\parallel}$) orientation varies by a magnitude of 240+ bars from 311 bars to 554 bars. From the current suite of specimens, it cannot be ascertained whether this broad spread in ($s_{1\parallel}$) strength values corresponds to spatial inhomogeneities in the rock fabric or to preferred regional orientations.

Table A-2.
 Elastic Properties and Compression Test Parameters for the Dicaperl Perlite
 (ASTM D3148; D2216)

Specimen	$\Delta\sigma$ (kbars)	σ_3 (kbars)	E(kbars)	ν	Moisture (% total mass)
σ_1 perpendicular to flow banding ($\sigma_{1\perp}$):					
Perlit1S	0.249	0.0	174.3	0.13	0.19
Perlit2S	0.280	0.0	171.3	0.18	0.16
Perlit4S	0.280	0.0	119.3	0.07	0.68
Perlit6S	0.247	0.0	123.3	0.08	0.40
σ_1 in the plane of the flow banding ($\sigma_{1\parallel}$):					
Perlit3S	0.311	0.0	246.9	0.32	0.20
Perlit5S	[0.470]	0.0	240.0	0.20	2.90
Perlit5S#2	0.554	0.0	280.4	0.29	2.90
Perlit7S	0.367	0.0	nd	nd	0.86
$\Delta\sigma$	maximum differential stress.			ν	Poisson's ratio.
σ_3	confining stress.			nd	not determined.
E	Young's modulus.				
[]	maximum stress in a load/unload cycle without failure.				

Compressional (longitudinal) wave velocities through Grefco's Socorro mine perlite were determined by laboratory measurement. The determinations were conducted using three each NX-size core segments oriented perpendicular and parallel to the flow-banding structure that is visible in the tested specimens. The measurements were made on laboratory air-dried specimens at room temperature and at atmospheric pressure. Please be advised that these measurements were conducted with uncalibrated laboratory instrumentation. Therefore, we cannot confidently express the accuracy associated with these values. Measurements made on materials with published V_p values suggest they are accurate to $\pm 6\%$.

The compressional wave velocities are found to be highly dependent on path orientation through the perlite. The wave velocity, $V_{p\perp}$, perpendicular to flow banding was determined as 2.94-3.14 km/s and, $V_{p\parallel}$, parallel to the flow banding, was determined as 5.24-5.27 km/s. These values compare with a single value of 3.60 km/s obtained for Grefco's No Agua mine perlite for which a path orientation with respect to flow structure could not be determined. The individual velocity measurements are shown in Table A-3.

Table A-3.
Laboratory Determinations for the Perlite Compressional Wave Velocity

Specimen	Path Orientation	Velocity (km/s)
P4-1	$V_{p\perp}$	3.08
P4-2	$V_{p\perp}$	3.14
P4-3	$V_{p\perp}$	2.94
P8-1	$V_{p\parallel}$	5.24
P8-2	$V_{p\parallel}$	5.25
P8-3	$V_{p\parallel}$	5.27

Path orientations:
 $V_{p\perp}$ perpendicular to flow banding
 $V_{p\parallel}$ parallel to flow banding

APPENDIX B
Results of Seismic Refraction Survey in Perlite Mine

Allen Cogbill

On May 21, 1993, we conducted a short seismic refraction survey in a perlite mine near Socorro. The purpose of the refraction survey was to estimate the near-surface seismic velocities in the perlite, which was to be the host medium for a series of spall experiments to be conducted later in the summer. The survey was performed along a portion of main line that extends north of the planned shot-point for the spall experiment (Figure B-1). Three source locations were used: one on each end of the line, and one in the middle, with the EES-3 elastic wave generator being used as the source. Data quality was fair to good. No evidence of reflecting horizons was observed on the shot gathers.

The interpretation was performed using first-arrival travel times only. The times from all the source locations used are shown in Figure B-2. Note that distance zero on Figure B-2 is coincident with the planned shot point. A commercial refraction interpretation package called GREMIX was used to assist in the interpretation. This software is basically an implementation of the generalized reciprocal method (GRM). It provides a reasonably good estimate of the depth to a refracting horizon, but does not attempt to model vertical variations in velocity except for those due to layering (that is, vertical velocity variations within a layer are not modeled).

The apparent velocities on either side of the central source location (shot 2) are slightly different, but both are higher than the near-surface apparent velocities measured from end shots (shots 1 and 3), which are quite low at 350 m/s. Such low velocities are characteristic of dry, unconsolidated porous materials. Figure B-3 shows the overall interpretation. The upper plot of Figure B-3 shows the measured first arrivals, the middle plot shows the interpreted refractor elevations, and the bottom plot shows the inferred variation in velocity. The upper layer in this interpretation is shown as having a very simple, linear variation in velocity. The simplicity is due to the fact that the GRM is not tuned to measuring vertical velocity variations within a given layer. The velocity of the refracting horizon is 1335 m/s; the depth to this refractor varies from 4 to 10 m below ground surface. It is possible that this refractor simply represents the "normal" (that is, unweathered) velocity for the perlite. Alternatively, the water saturation at this depth may approach 100%, with dryer materials above the refractor.

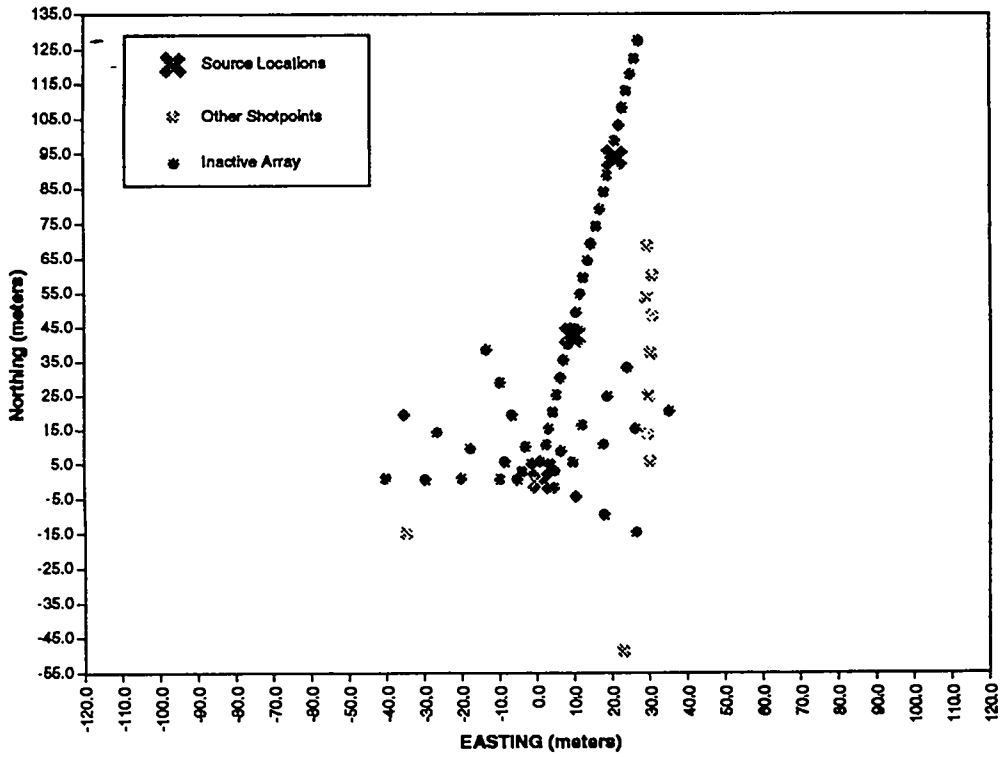
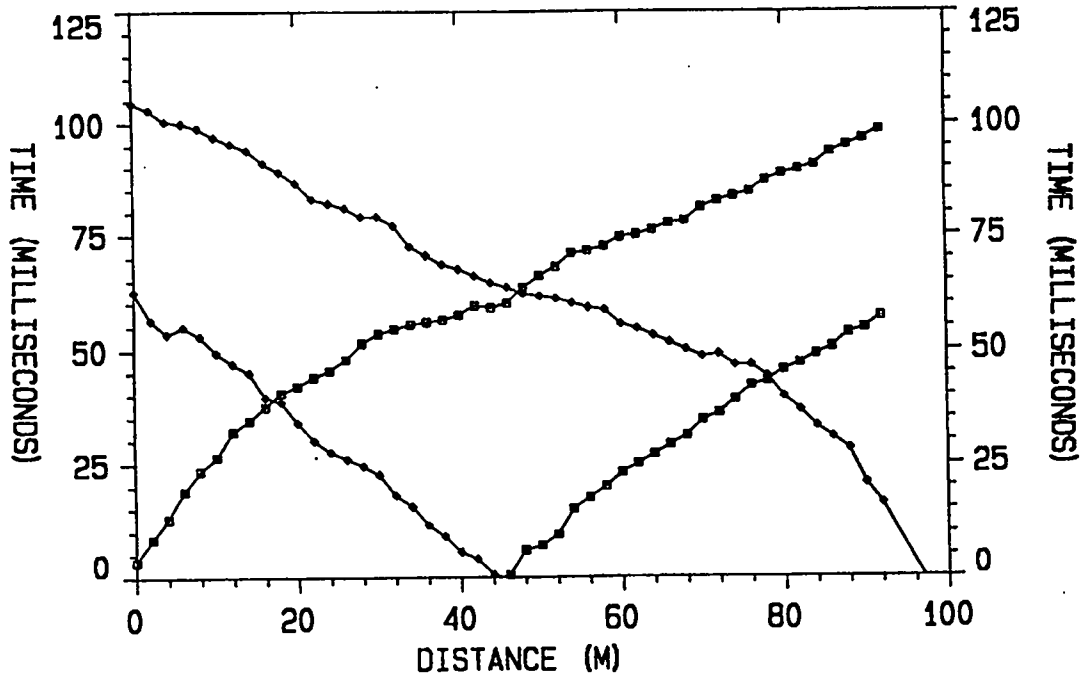


Figure B-1. Refraction survey layout



REFRACTION DATA
Figure B-2. Refraction data.

B-2

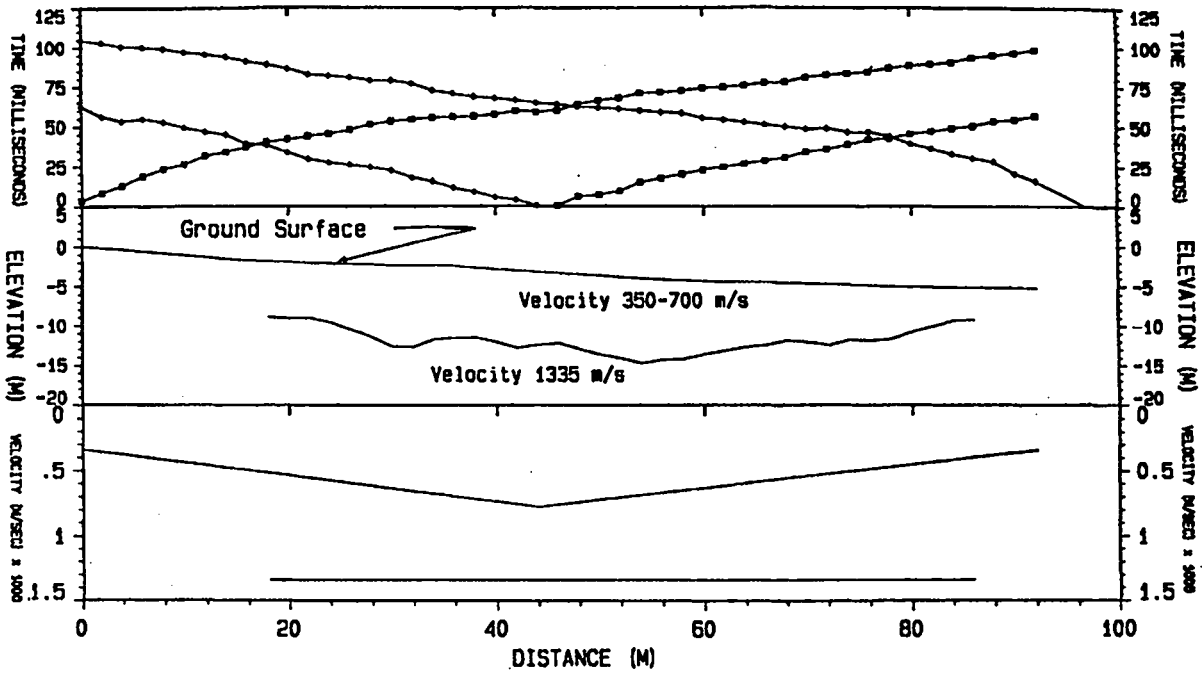


Figure B-3. Velocity model.

APPENDIX C Two-Dimensional Calculations for Intermediate-Scale Source Experiments

James Kamm

Introduction

This appendix contains a discussion of calculations performed with SMC-2D in support of the intermediate-scale explosion source experiments to be conducted in the Grefco perlite mine starting in summer 1993. We describe the first two-dimensional calculations that approximate these experiments.

In the previous numerical simulations [1], the lack of information about perlite and the uncertainty regarding the specific explosive to be used resulted in the somewhat arbitrary choices of alluvium as a "convenient" computational simulant for perlite and of C-4 for the explosive. Since those calculations, preliminary physical properties data for the Grefco perlite have been obtained [2], and mechanical properties for perlite at the Grefco No Agua mine have been located [3]. Furthermore, a candidate explosive has been chosen (ICI Power Primer™) and characterization of a similar explosive has been obtained [4]. This appendix contains a discussion of preliminary results from two-dimensional calculations using these more realistic properties.

Material Properties of Perlite

The material properties collected by H. Plannerer [2] for surface samples of the Grefco Socorro perlite are given in Table C-1 on the following page. For this material, the grain density, dry bulk density, and water mass-fraction were measured; the other values are derived. Also included in this table are values for the MERLIN alluvium [5] used in the previous calculations, and "typical" values given by Perret and Bass [6] for NTS alluvium and NTS dry tuff used in previous scaling analyses [7,8].

In addition to the values of the bulk density, grain density, and mass-fraction of water, three additional parameters are needed to compute an equation of state (i.e., pressure-volume relation) using Butkovich's method [9]: an elastic wave speed, and values of the incipient crush pressure and total crush pressure. The data provided by A. Cogbill [10] resulting from the seismic survey performed in the Grefco Socorro mine include values for the elastic wave speed. In addition, the seismic survey indicated that a two-layer structure exists in the perlite bed: the upper layer consists of low-velocity material ($c_p \approx 350\text{--}700$ m/s) to a depth of between 4 m and 10 m below the surface, and the lower layer consists of higher-velocity material ($c_p \approx 1335$ m/s). Results of material tests done on the Grefco No Agua mine perlite provided by H. Plannerer [3] suggest that the incipient crush pressure (i.e., the pressure at which pore reduction commences) is at least 0.5 kbar (50 MPa). On the basis of this information, we have somewhat arbitrarily chosen the incipient crush pressure to be 0.5 kbar (50 MPa) and

Table C-1.
 Physical Properties of Perlite

Material	ρ_B (g/cm ³)	ρ_G (g/cm ³)	ρ_S (g/cm ³)	W	S	ϕ	ψ
Perlite	1.86	2.35	2.35	2.5×10^{-3}	2.2×10^{-2}	0.21	0.21
Qal	1.71	2.52	2.13	0.12	0.51	0.40	0.20
P&B All./Tuff	1.78	1.84	2.07	0.34	0.61	0.36	0.14

Table C-1. Listed are the material, the bulk density (ρ_B), the grain density (ρ_G), the solid density (ρ_S), the mass-fraction of water (W), the saturation (S), the total porosity (ϕ), and the gas-filled porosity (ψ) for the experimental Grefco perlite [2], for the MERLIN alluvium used in the previous calculations [1], and for the NTS alluvium and NTS dry tuff materials of Perret and Bass [6].

the total crush pressure (i.e., the pressure at which pore reduction ceases) to be 1 kbar (100 MPa); these values may be incorrect for the Grefco Socorro perlite, and, consequently, certain computed values may be erroneous. The EOSs computed using these data are depicted in Figure C-1; also shown in that diagram is the MERLIN alluvium EOS used in the previous calculations. In this log-log plot, the pressure P is plotted against the nondimensional compression μ (defined as $(\rho/\rho_0)-1$). The solid lines originating at $\mu=0$ represent elastic behavior of the materials up to the "knee" at the incipient crush pressure, at which point pore reduction begins and continues up to the total crush pressure; the dotted lines represent the unloading behavior of the fully crushed material.

In addition to the volumetric material response given by the EOS, a description of the shear material response is required for the numerical simulation. The only available data on the shear response of perlite are contained in the description of the Grefco No Agua perlite given by H. Plannerer [4]. That memo contains two data sets giving unconfined shear strength and shear strength at a confining pressure of 0.5 kbar (50 MPa); a shear envelope was fitted to those values. Those data, as well as the shear envelope for MERLIN alluvium, are shown in Figure C-2, which depicts the shear stress as a function of confining pressure. The failure surface for perlite is modeled in the code by the equation

$$Y = Y_0 - Y_1 \exp(-P/Y_2) \quad (1)$$

where values of Y_0 , Y_1 , and Y_2 were "eyeballed" to approximate the No Agua perlite data shown in Figure C-2. These values are given in Table C-2, along with the elastic wave speed and the value of Poisson's ratio, from which the value of perlite was inferred [4]. Typically, a "damaged" shear failure surface is also used in calculations;

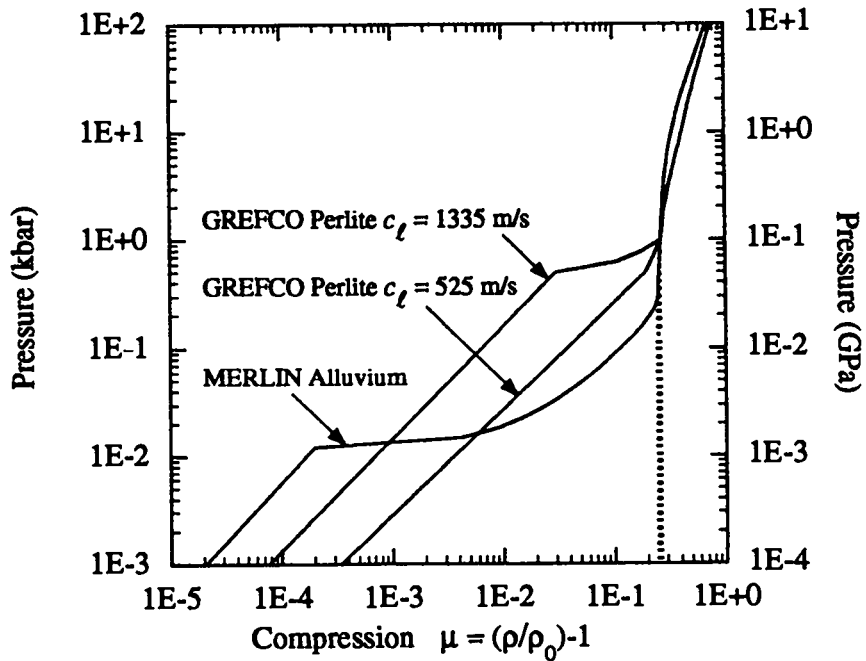


Figure C-1. Pressure (kbar) vs nondimensional compression, defined as $(\rho/\rho_0)-1$, for MERLIN alluvium and for the Butkovich [9] fits to the Grefco perlite data [2]. The solid lines depict the (porous) loading curves, and the dotted lines depict the unloading curves of the fully crushed materials. The alluvium has an incipient crush pressure of 12 bar; the perlite is assumed to have a crush pressure of 0.5 kbar based on the Grefco No Agua perlite data [3]. The loading and unloading curves merge at the complete crush pressures of 0.3 kbar for the alluvium, and the assumed value of 1 kbar for perlite.

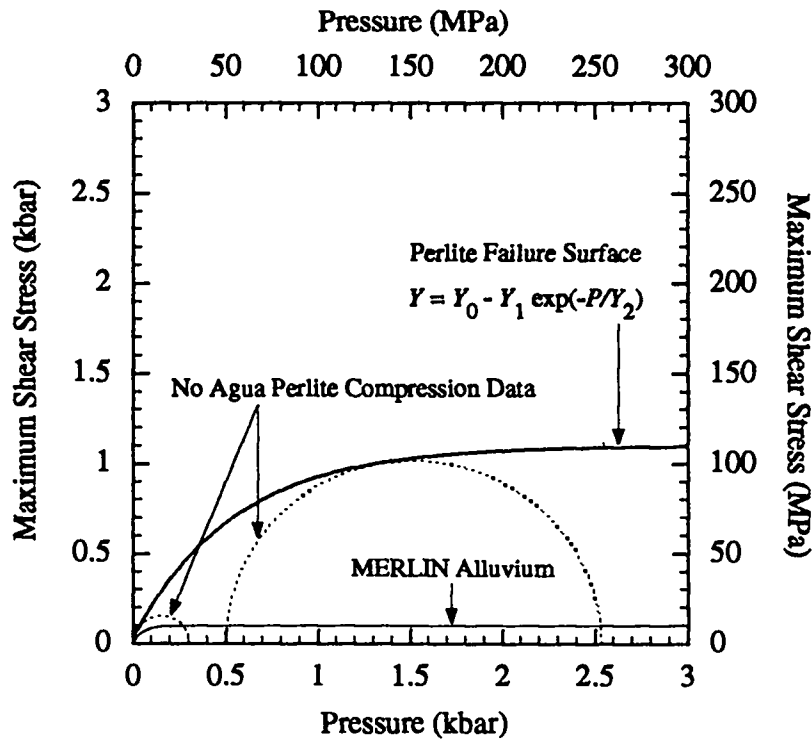


Figure C-2. Maximum shear stress (kbar) versus confining pressure (kbar) for the Grefco No Agua perlite data [2] and for MERLIN alluvium [5]. A failure surface of the form given in Equation 1 was "eyeballed" to fit the perlite data. The shear behavior of the No Agua perlite may differ from that of the Socorro perlite. According to this model, the maximum shear stress (at a given confining pressure) is notably greater for perlite than for alluvium.

the damaged surface models the reduction of shear strength due to inelastic processing of the material. Due to our lack of knowledge about perlite, however, no damage model was included in these initial calculations; since field evidence suggests that the perlite becomes "pulverized" under high-pressure loading, the lack of a damage model may be a significant modeling misjudgment. In the calculation, the accumulated inelastic shear strain was not computed, so no estimate of the elastic radius is provided by these calculations. One further modeling assumption regarding perlite material strength, which affects the computed spall region, for example, is that the tensile strength of perlite is zero.

Table C-2.
Selected Mechanical Properties Used in the Numerical Simulations

Material	ν	c_ℓ (m/s)	Y_0 (kbar)	Y_1 (kbar)	Y_2 (kbar)
Perlite	0.20	1335/525	1.100	1.070	0.55
Qal	0.33	1599	0.100	0.0999	50.28

Table C-2. Listed are the material, Poisson's ratio (ν), the elastic sound speed (c_ℓ), the maximum stress difference supported by the material (i.e., the flow stress) (Y_0), the flow stress decrement (Y_1), and the pressure-softening exponent (Y_2) used in the modeling of the Grefco perlite and MERLIN alluvium.

Properties of the Explosive

To describe HE materials, SMC-2D uses the JWL EOS [11], which is an analytic expression for the pressure as a function of normalized specific volume and internal energy of the material. The analytic form of the JWL EOS is as follows:

$$P(V, E) = A \left(1 - \frac{\omega}{R_1 V} \right) \exp(-R_1 V) + B \left(1 - \frac{\omega}{R_2 V} \right) \exp(-R_2 V) + \frac{\omega E}{V}, \quad (2)$$

where P is the pressure, V is the normalized specific volume (i.e., $V = v/v_0$, where v is the specific volume and v_0 is the initial specific volume) and E is the normalized specific energy (i.e., $E = e/v_0$, where e is the specific internal energy). ICI Explosives, the manufacturer of the candidate explosive (Power Primer™), does not have the JWL parameters for this explosive; however, in discussions with ICI [12], they suggested that the Hercules product Unigel™, for which JWL coefficients are available [4], is essentially the same as Power Primer™. Values of parameters characterizing each of these explosives are cataloged in Table C-3. In the numerical simulations, the cylinder of HE is point-initiated at the center, with the detonation proceeding according to the C-J volume burn model, where the C-J volume is computed according to standard detonation theory [13].

Table C-3.
 Explosives Parameters

Explosive	ρ_0 (g/cm ³)	P_{CJ}	D (kbar)	E_0 (km/s)	Γ (erg/g)	A	B (kbar)	R_1 (kbar)	R_2	ω
Power Primer™	1.38	135	≈5.60	≈4.24×10 ¹⁰	N/A	N/A	N/A	N/A	N/A	N/A
Unigel™	1.26	128	5.76	4.04×10 ¹⁰	2.49	1097.0	75.8	4.4	1.4	0.23

Listed are the explosive, the reference density (ρ_0), C-J pressure (P_{CJ}), the detonation velocity (D), the initial energy density (E_0), the G \ddot{u} neisen gamma (Γ), and the exponential fit JWL EOS parameters (A, B, R_1 , R_2 , ω ; see Eq. 2) used in the numerical simulation of the explosive. The value of the energy density of Power Primer™ is an estimate based on the Relative Weight Strength (see [14]) value of 111 provided by ICI, with the assumption that the energy density of "standard" ANFO is 3.82×10¹⁰ erg/g (obtained from [4]).

Setup of the Two-Dimensional Simulations

The calculations performed were run in cylindrically symmetric geometry with the axis of symmetry through the center of the explosive charge. The shot to be simulated was approximately 150 lb of Power Primer™ buried at a depth of 40 ft, in a cylinder with aspect ratio of 2:1 (L:D). Details of the initial configuration of the simulation are discussed in this section.

In the experimental configuration, the explosive is to be packed into a cylinder of radius 6.3125 in (16.034 cm) and length 25.25 in (64.135 cm), corresponding (ideally) to 158 lb of Power Primer™; given the inferred energy density of this explosive (see Table C-3), this corresponds to 7.25×10⁻⁵ kt and a SDOB of 292 m/kt^{1/3}. In the numerical simulation, we assign the depth of burial of the center of the explosive to be exactly 12 m (39.37 ft), slightly less than the 40 ft DOB of the experiment. Furthermore, we ascribe to the cylinder of explosive a radius of exactly 16 cm and length of exactly 64 cm, which contains 143 lb of Unigel™ explosive; this corresponds to 6.28×10⁻⁵ kt for an SDOB of 302 m/kt^{1/3}. The initial computational grid contains uniform zones of size $\Delta r = \Delta z = 4$ cm throughout the explosive and extending one cylinder radius into the surrounding perlite. A geometric grid of zone size ratio $\sigma = 1.05$ is used out to $r = 100$ m and down to $z = -112$ m, with a maximum allowed zone size of 2 m; the same geometric ratio, with a maximum zone size of $\Delta z = 0.5$ m, is used to the free surface. The initial grid contains ~100 radial zones and ~200 axial zones, for a total of ~2×10⁴ zones. This number of zones through the explosive probably does not model the radial detonation velocity accurately; however, a more finely zoned calculation (with $\Delta r = \Delta z = 1$ cm) was found to run extremely slowly, so the aforementioned zoning was chosen. The initial overburden pressure is assigned according to the depth and density of the overburden material. As in the previous one-

aforementioned zoning was chosen. The initial overburden pressure is assigned according to the depth and density of the overburden material. As in the previous one-dimensional calculations, the initial stress state is *not* in equilibrium, so the long-time, far-field data from such a simulation are not reliable.

Preliminary Results of the Two-Dimensional Simulations

Results for various material response properties at various scaled ranges are provided in this section. Specifically, peak stresses and velocities at shot depth are given, as are acceleration and velocity records at selected surface and free-field locations.

The simulation was run out to 130 ms; given the extent of the calculational grid described above, the initial outgoing signal reaches the computational boundary at time $\approx 100 \text{ m} \div 1335 \text{ m/s} \approx 75 \text{ ms}$, after which the information is unphysically reflected back onto the grid at approximately the same speed. Values for material response properties near the axis of symmetry (e.g., near the shot point and SGZ) are unaffected by this numerical artifice until the latest times of the calculation.

Figure C-3 gives the computed values of peak stresses as functions of range at shot depth; in this plot, the solid line depicts the mean stress p , the coarsely dashed line denotes the radial stress σ_{rr} , the finely dashed line denotes the axial stress σ_{zz} , and the dotted line indicates the hoop stress $\sigma_{\theta\theta}$. Figure C-4 shows the peak velocity as a function of range from the shot point; in this plot, the solid line depicts the radial velocity u_r as a function of horizontal range at shot level, the dotted line denotes the axial velocity u_z as a function of vertical range to the surface, and the dashed lines represent the Perret and Bass [6] free-field peak velocity scaling results for alluvium and dry tuff. This figure suggests that the material response of perlite may be approximately bounded by the response of alluvium and tuff.

Figure C-5 shows vertical acceleration records at 5-cm depth (i.e., essentially the free surface) at 0, 10, 20, 30, 40, and 50 m from SGZ. The clear -1 g signal, indicative of ballistic free-fall associated with spallation of the surface layer, is apparent in the waveforms out to approximately 20 m ($\sim 500 \text{ m/kt}^{1/3}$) range from SGZ. In addition, a distinctive double spall signature, similar to that described by Jones, App, and Whitaker [15], is apparent in the acceleration data at the near-SGZ station. Given the uncertainty in the material strength description used in this calculation, it is unclear if this feature is realistic, much less if it is related to the cavity rebound mechanism posited in [15]. Figure C-6 shows vertical velocity records at 5-cm depth at the same locations; in these plots, the -1 g accelerations of Figure C-5 are manifest as the regions of constant negative slope in the velocity data at the three closest stations shown. Figure C-7 gives the peak vertical velocity at 5 cm depth as a function of horizontal range from SGZ; as shown in this plot, the peak vertical velocity near SGZ is positive (i.e., upward), while beyond approximately 2-m range the peak vertical velocity becomes

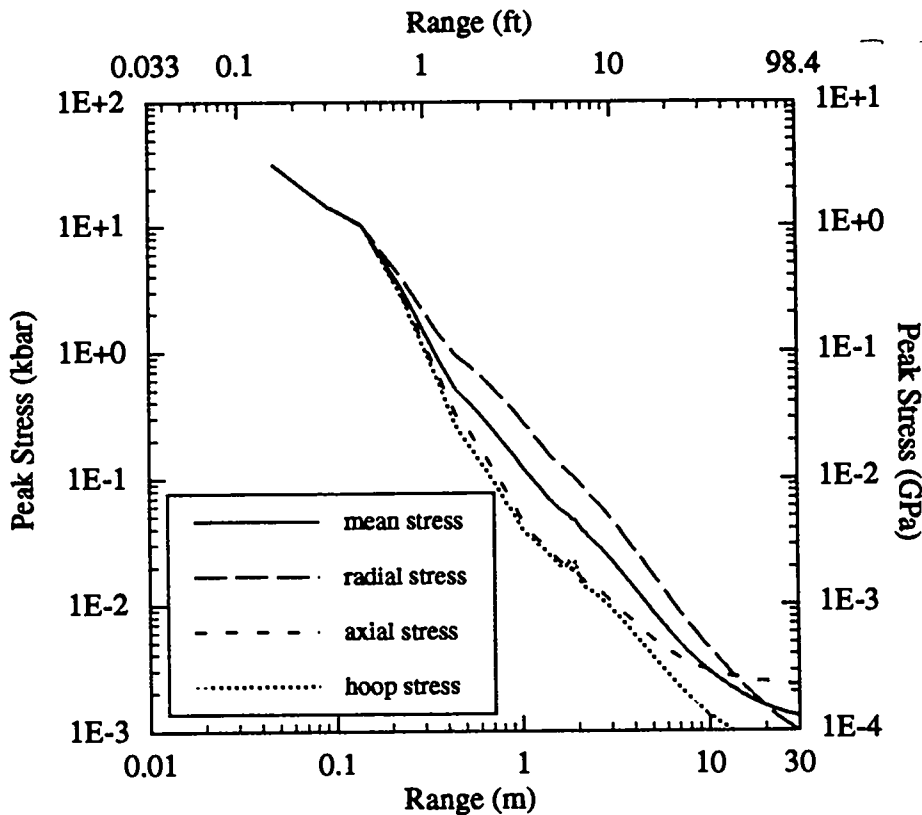


Figure C-3. Computed peak stress (kbar) vs range (m) at shot depth for two-dimensional numerical simulation of 143 lb of Unigel™ explosive buried at 12 m in perlite. The solid line depicts the mean stress p , the coarsely dashed line denotes the radial stress σ_r , the finely dashed line denotes the axial stress σ_{zz} , and the dotted line indicates the hoop stress $\sigma_{\theta\theta}$.

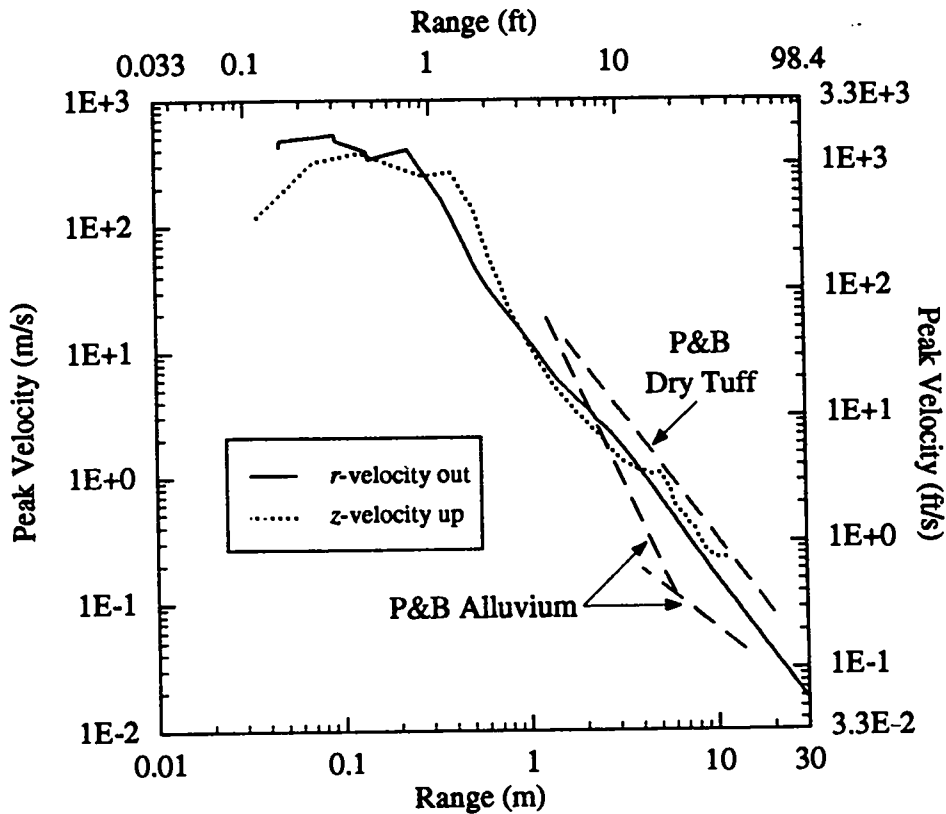
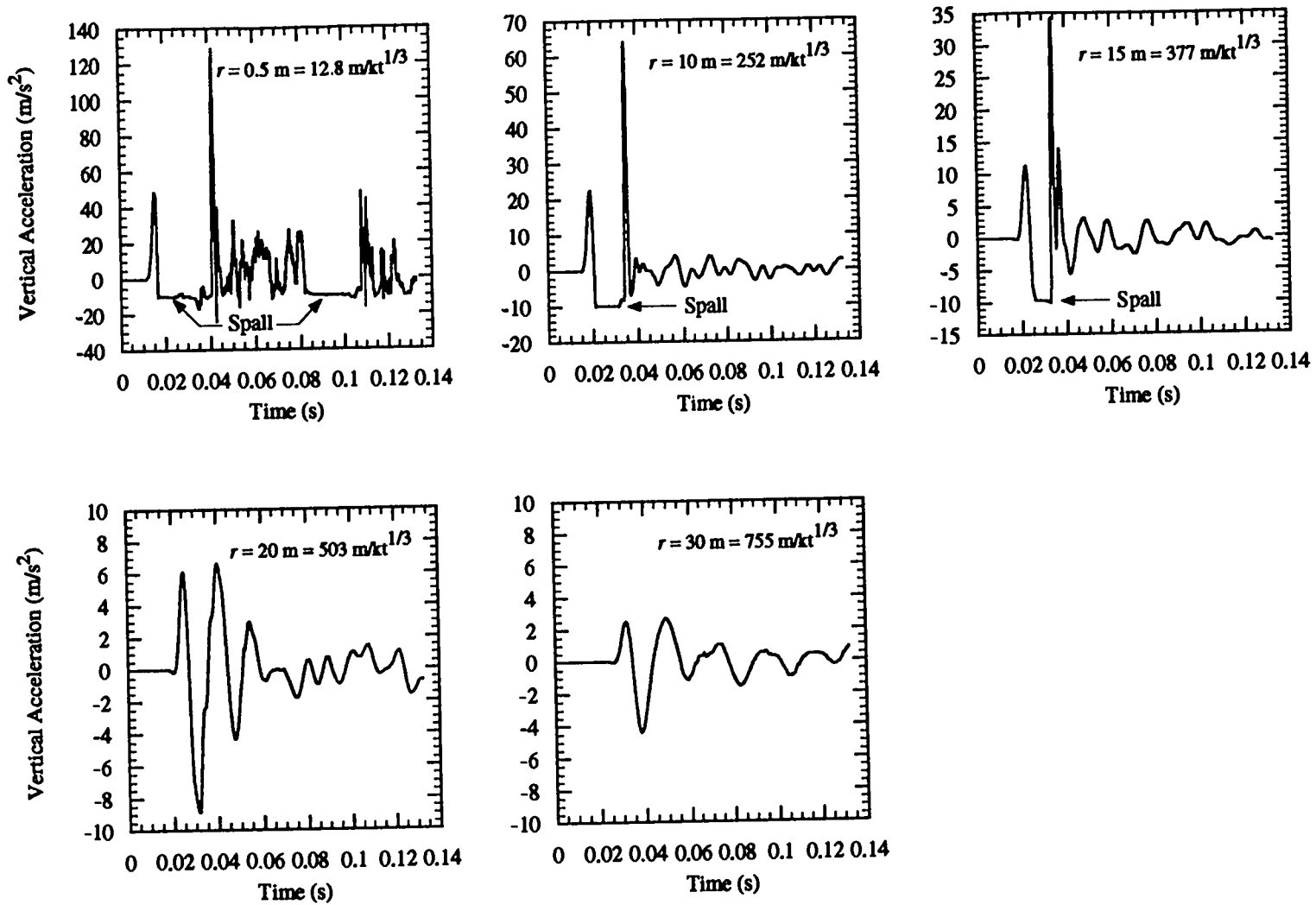


Figure C-4. Computed peak radial velocity (m/s) vs horizontal range (m) from the shot point for two-dimensional numerical simulation of 143 lb of Unigel™ explosive buried at 12 m in perlite. The solid line depicts the radial velocity u_r vs horizontal range at shot level, and the dashed line denotes the axial velocity u_z as a function of vertical range to the surface. The dashed lines represent the Perret and Bass [6] free-field peak velocity scaling results for alluvium and dry tuff. The computational results suggest that the response of perlite may be approximately bounded by the response of those materials.



C-10

Figure C-5. Computed vertical acceleration (m/s²) at 5-cm depth as a function of time at 0.5, 10, 15, 20, and 30 m from SGZ in the two-dimensional calculation of 143 lb Unigel™ at 12 m DOB. The clear -1 g spall signal is apparent in the stations out to ~20 m (~500 m/kt^{1/3}) range.

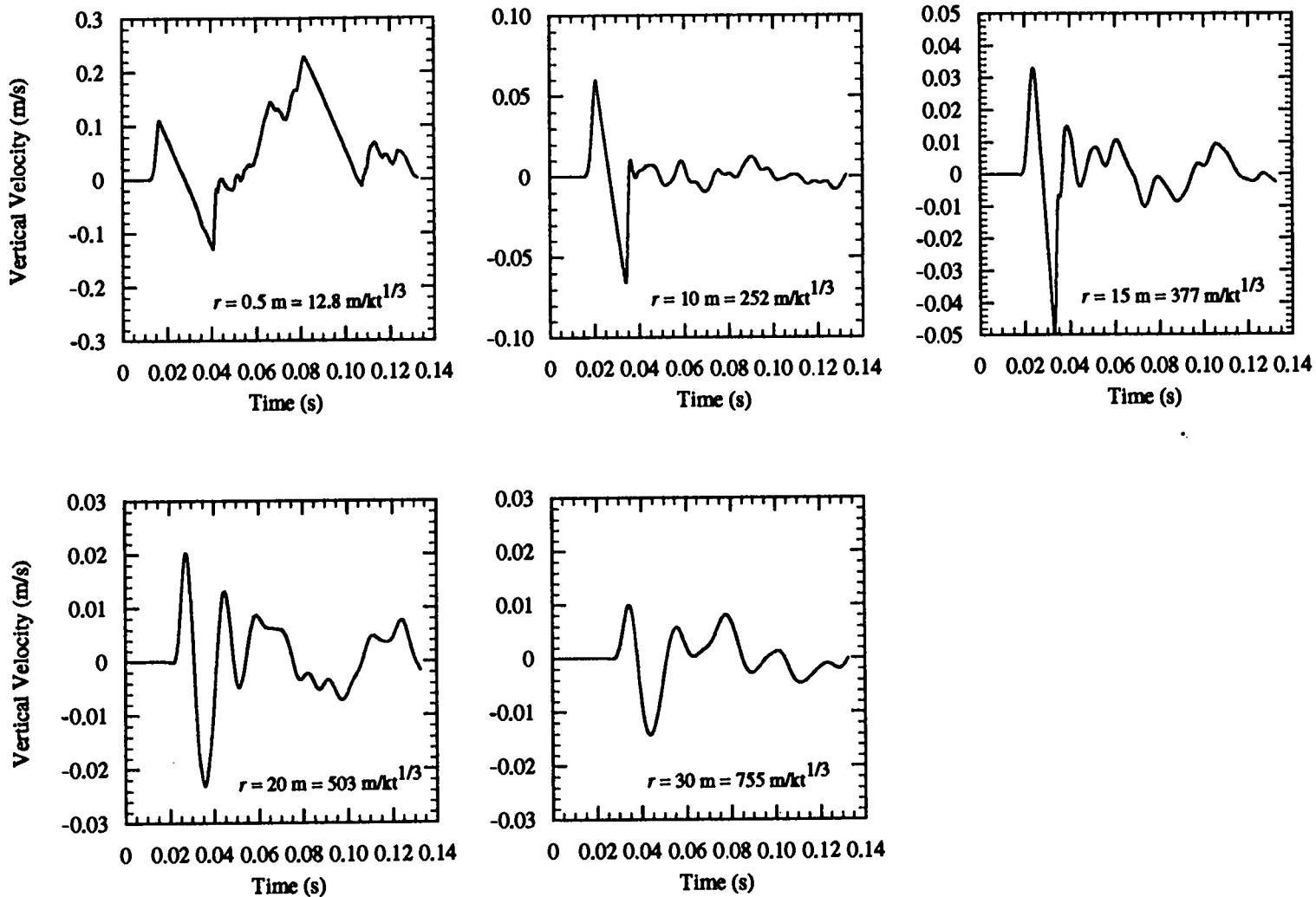


Figure C-6. Computed vertical velocity records at 5-cm depth at 0.5, 10, 15, 20, and 30 m from SGZ in the two-dimensional calculation of 143 lb Unigel™ explosive buried at 12 m in perlite. The regions of constant negative slope in the top three plots correspond to a ballistic free-fall phase associated with the surface spall.

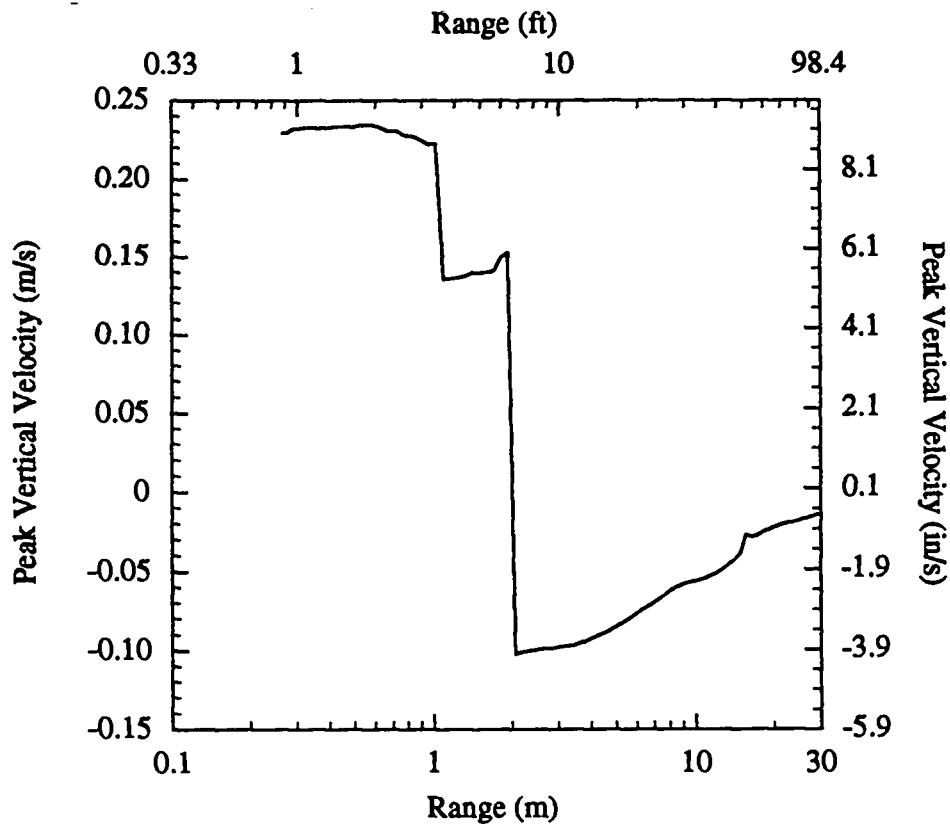


Figure C-7. Computer peak vertical velocity (m/s) at 5-cm depth vs horizontal range (m) from SGZ for two-dimensional simulation of 143 lb of Unigel™ explosive buried at 12 m in perlite. Near SZG, the peak vertical velocity is positive (i.e., upward), while at and beyond approximately 2-m surface range from SGZ, the peak velocity becomes negative (i.e., downward).

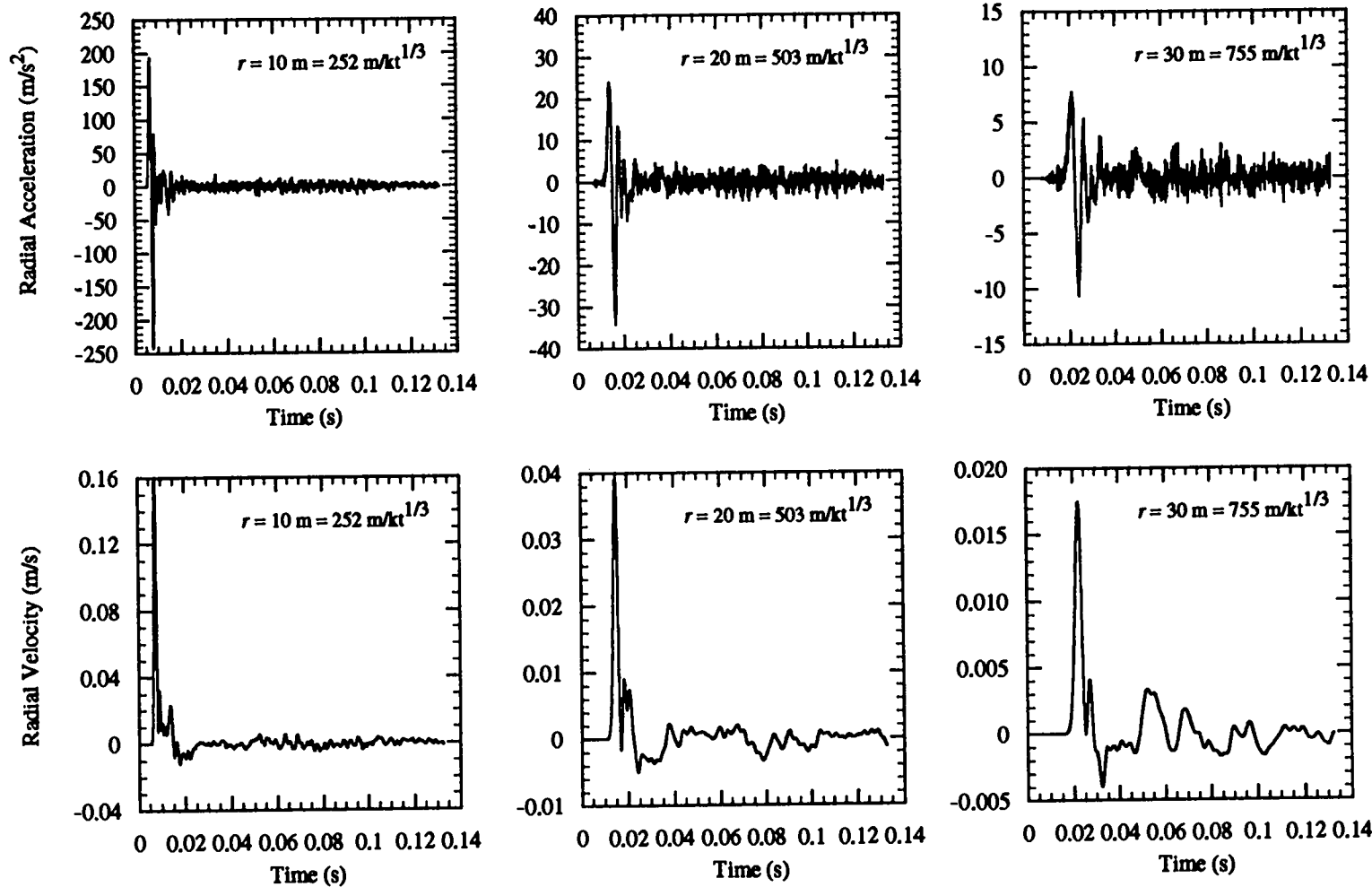


Figure C-8. Computed free-field radial acceleration (m/s²) at shot level as a function of time at 10, 20, and 30 m from the shot point (top row), and free-field radial velocity (m/s) at shot level at the same ranges (bottom row) in the two dimensional calculation of 143 lb Unigel™ at 12-m DOB in perlite.

Conclusions

In this memo we have provided preliminary results of two-dimensional cylindrically symmetric calculations simulating the explosion of approximately 150 lb of Power Primer™ explosive of aspect ratio 2:1 (L:D) at 40 ft DOB in perlite. The main conclusions of this study are the following:

- The region of spall along the surface extends out to ~20 m ($\sim 500 \text{ m/kt}^{1/3}$).
- The material response of perlite might be approximately bounded by the material response of alluvium and dry tuff.

Caveat: Several assumptions have been made regarding the strength properties of perlite; these assumptions, which may prove to be erroneous, greatly influence the computed material response. Therefore, we caution that details of the computed waveforms are not likely to be reflected in the field data.

The results of these calculations, particularly the surface acceleration as a function of range, are intended to provide (admittedly crude) input to the experimental planning process for the series of experiments to be conducted in perlite this summer. The results of these calculations will assist in the experimental design process and subsequent analysis plan.

References

1. J. R. Kamm, "Preliminary Calculations for Intermediate Scale Source Experiments," Los Alamos National Laboratory Memo of 13 April 1993.
2. H. N. Plannerer, private communication, 7 May 1993.
3. H. N. Plannerer, "Perlite Mechanical Properties," Los Alamos National Laboratory Memo of 19 May 1993.
4. M. Finger, F. Helm, E. Lee, R. Boat, H. Cheung, J. Walton, B. Hayes and L. Penn, "Characterization of Commercial, Composite Explosives," Sixth Symposium (International) on Detonation, pp. 729-739, Office of Naval Research (1976).
5. F. N. App and W. M. Brunish, "Modelling Surface Motion and Spall at the Nevada Test Site," Los Alamos National Laboratory Report LAUR-92-500 (1992).
6. W. R. Perret and R. C. Bass, "Free-Field Ground Motion Induced by Underground Explosions," Sandia National Laboratories Report SAND74-0252 (1975).
7. J. R. Kamm, "Peak Acceleration Estimates for Intermediate Scale Source Experiments," Los Alamos National Laboratory Memo of 13 May 1993.
8. J. R. Kamm, "Peak Acceleration Estimates for Intermediate Scale Source Experiments-Cont'd," Los Alamos National Laboratory Memo of 26 May 1993.
9. T. R. Butkovich, "A Technique for Generating Pressure-Volume Relationships and Failure Envelopes for Rocks," Lawrence Livermore National Laboratory Report UCRL-51441 (1973).
10. A. H. Cogbill, "Results of Seismic Refraction Survey in Perlite Mine," Los Alamos National Laboratory Memo of 7 June 1993.
11. E. L. Lee, H. C. Hornig and J. W. Kury, "Adiabatic Expansion of High Explosive Detonation Products," Lawrence Livermore National Laboratory Report UCRL-50422 (1968).
12. B. Mohanty (ICI Explosives), private communication, 14 June 1993.

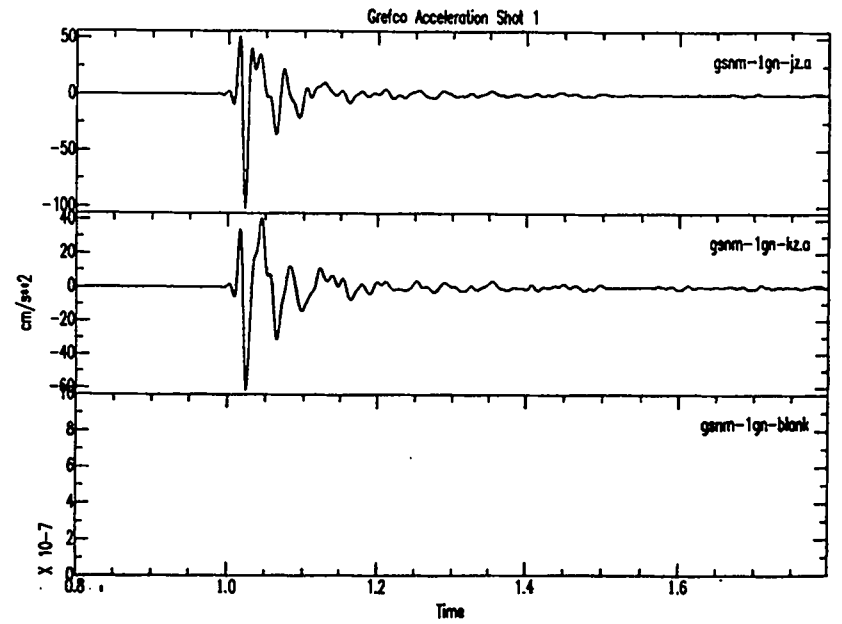
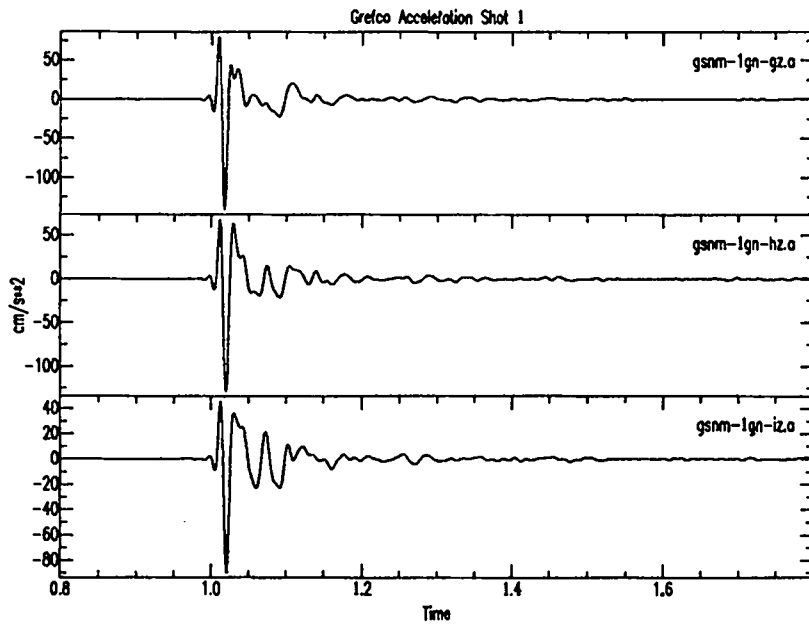
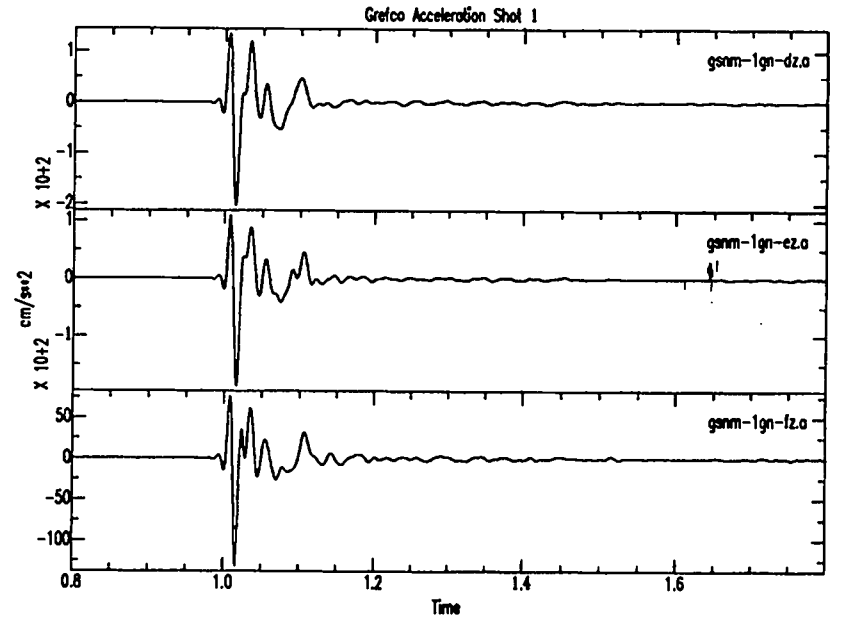
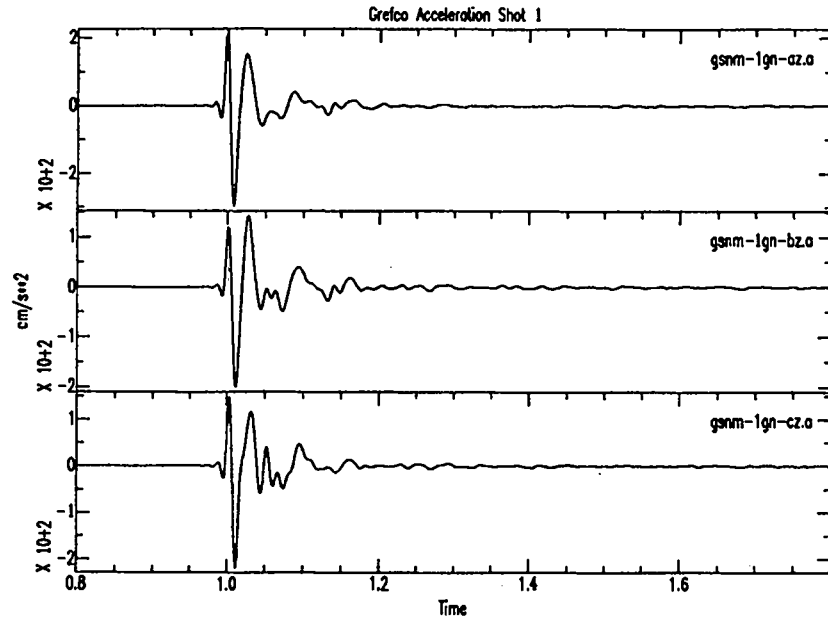
13. C. L. Mader, "Numerical Modeling of Detonations," University of California Press, 1979.
14. R. Meyer, "Explosives," VCH Verlagsgesellschaft mBH, 1987.
15. E. M. Jones, F. N. App and R. W. Whitaker," Ground Motions and the Infrasonic Signal: A New Model and the Discovery of a Significant Cavity Rebound Signal," Los Alamos National Laboratory Report LAUR-93-861 (1993).

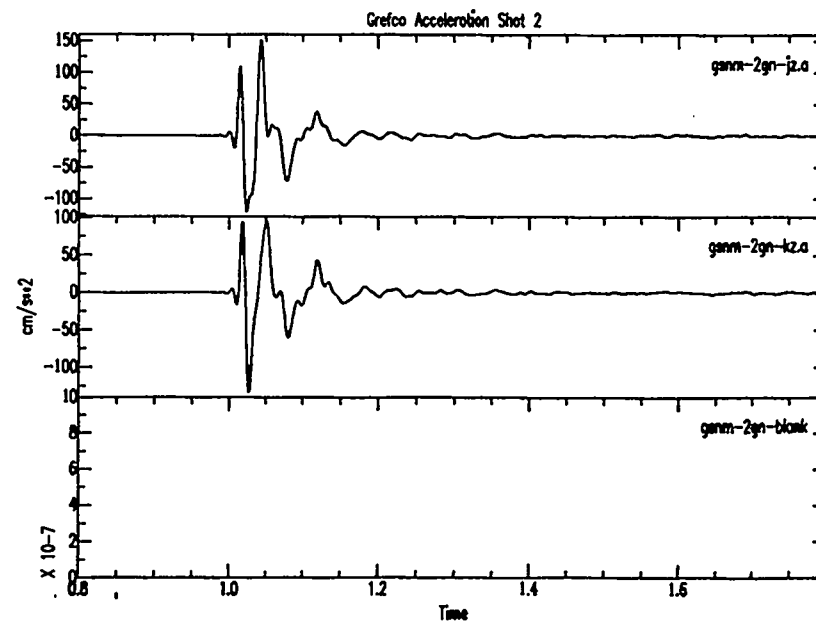
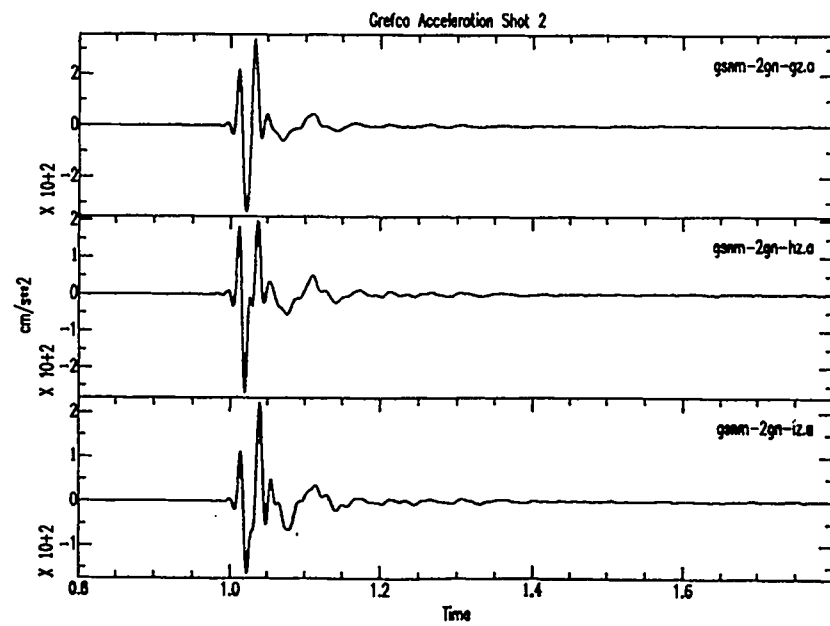
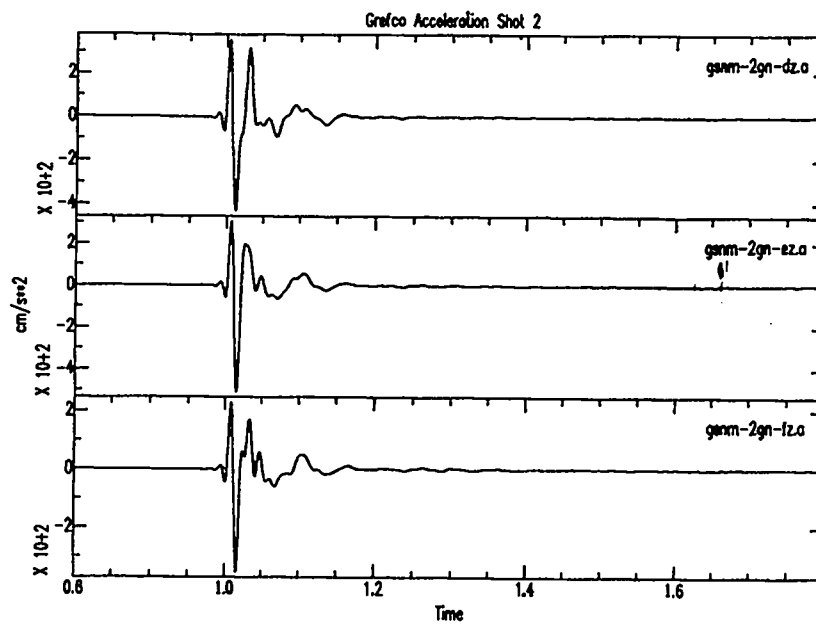
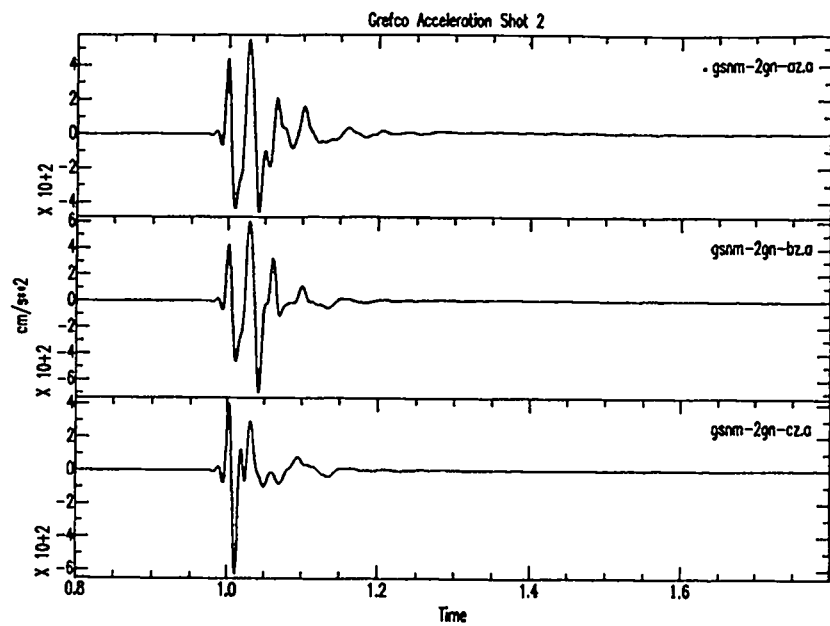
APPENDIX D
Ground-Motion Data Plots

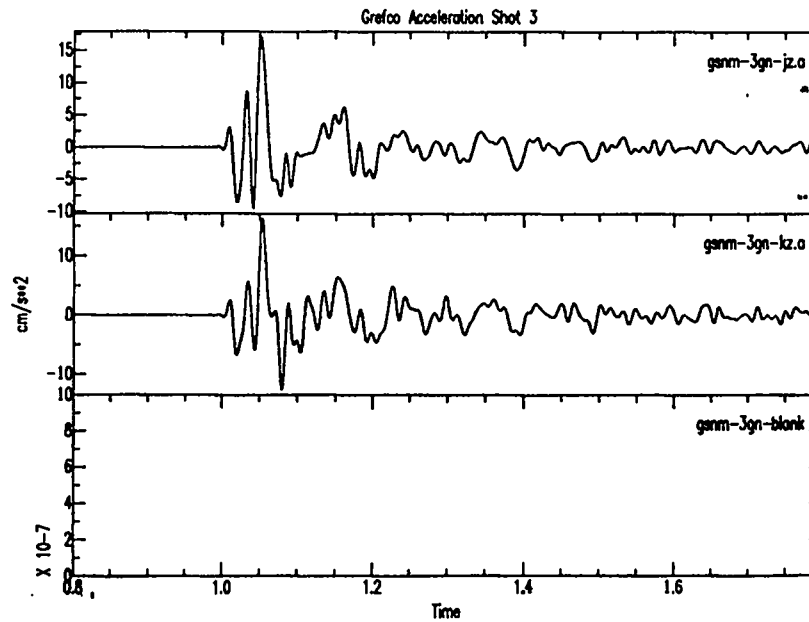
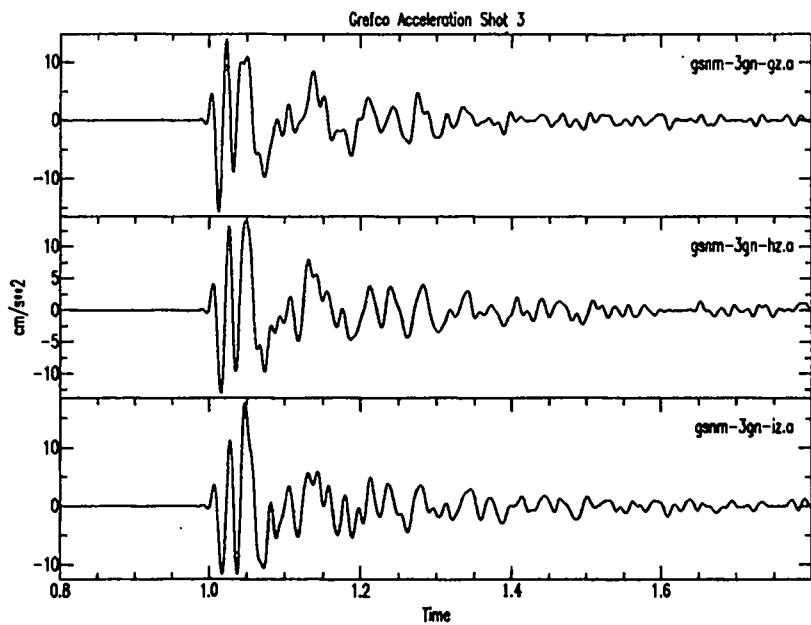
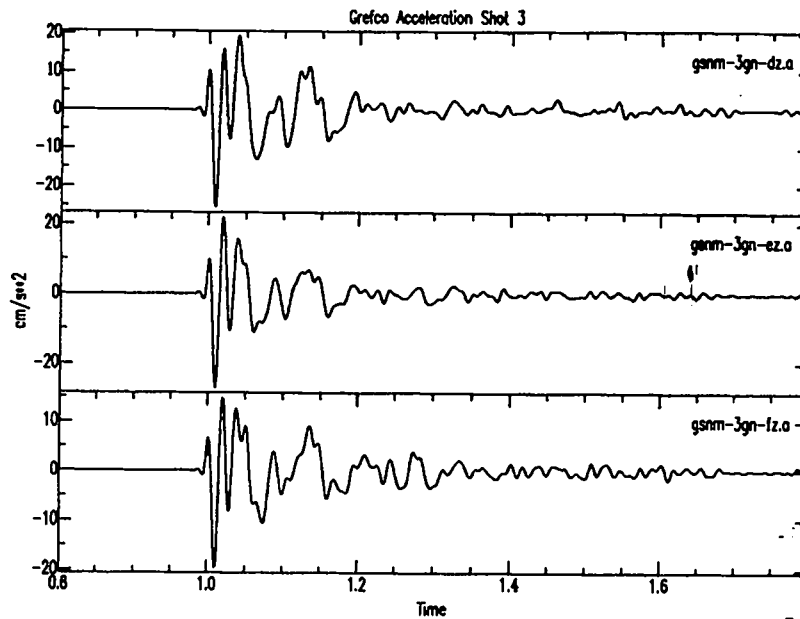
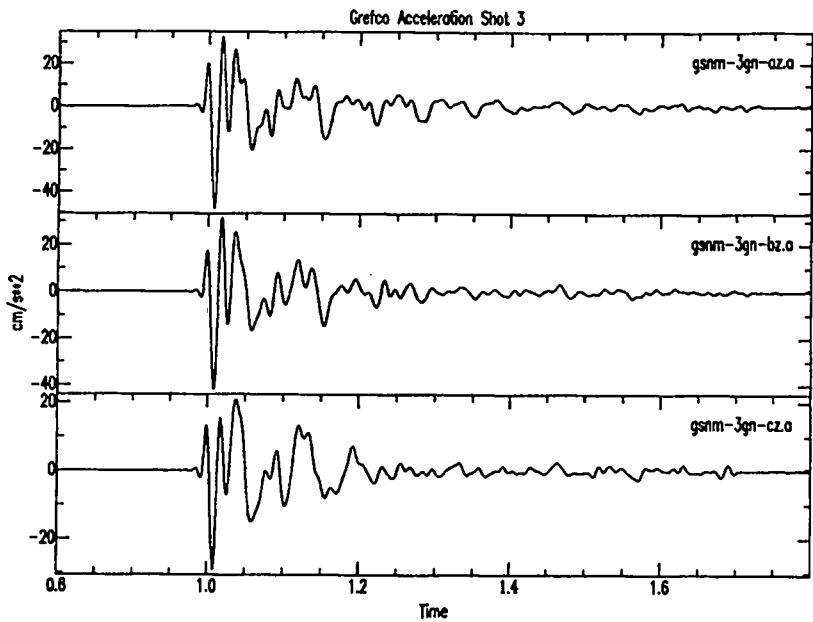
The following is an example of our file naming scheme:

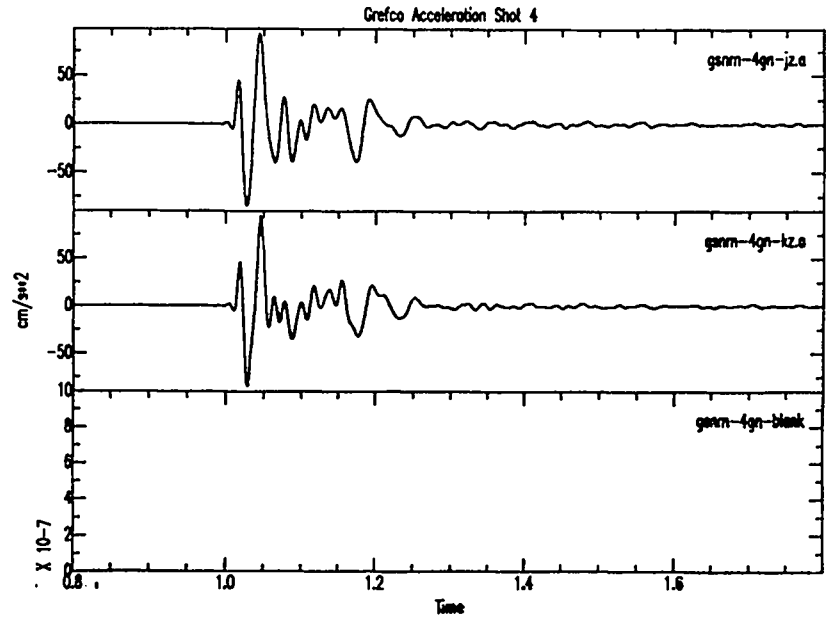
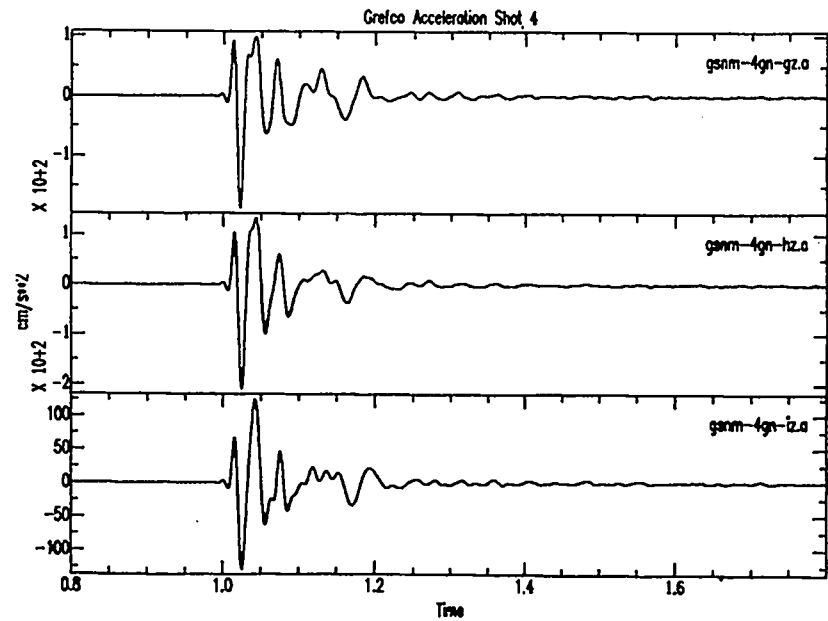
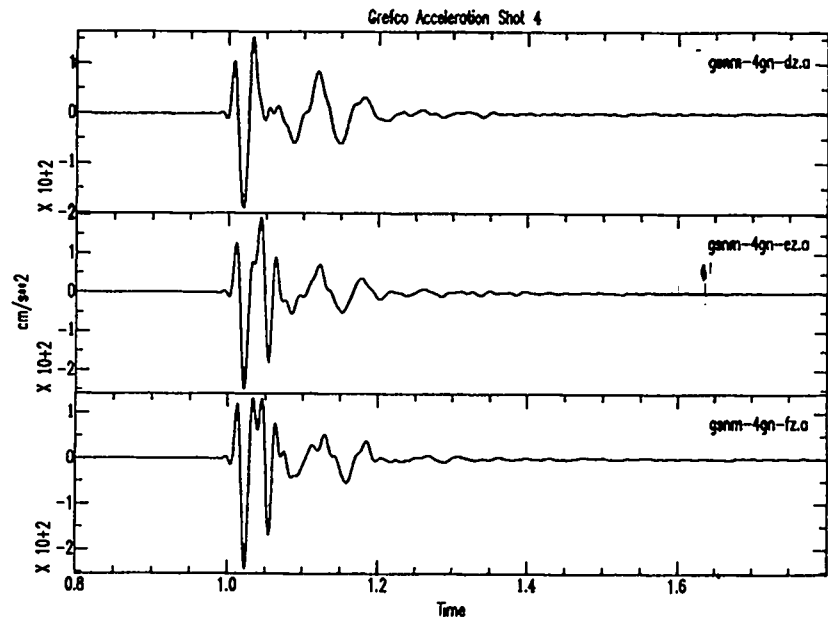
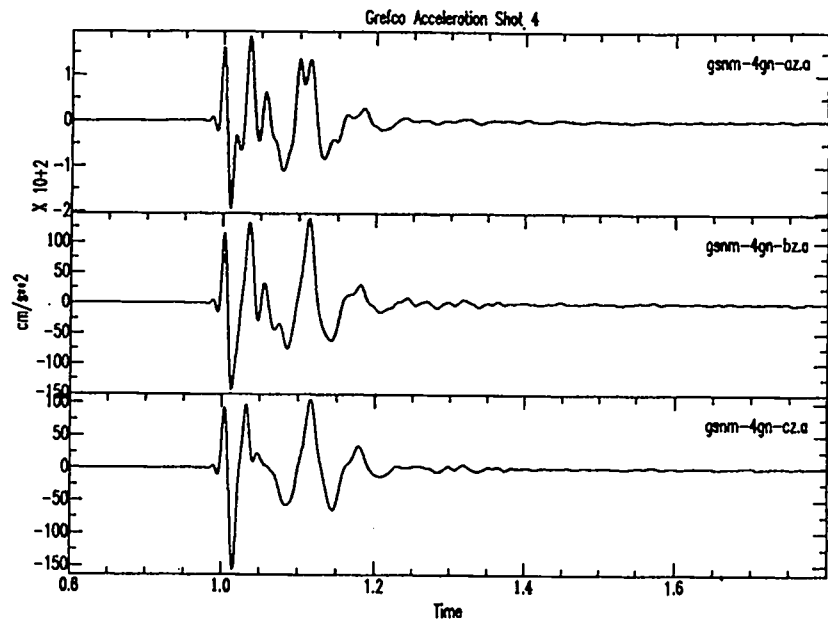
gsnm-8fl-2z.a

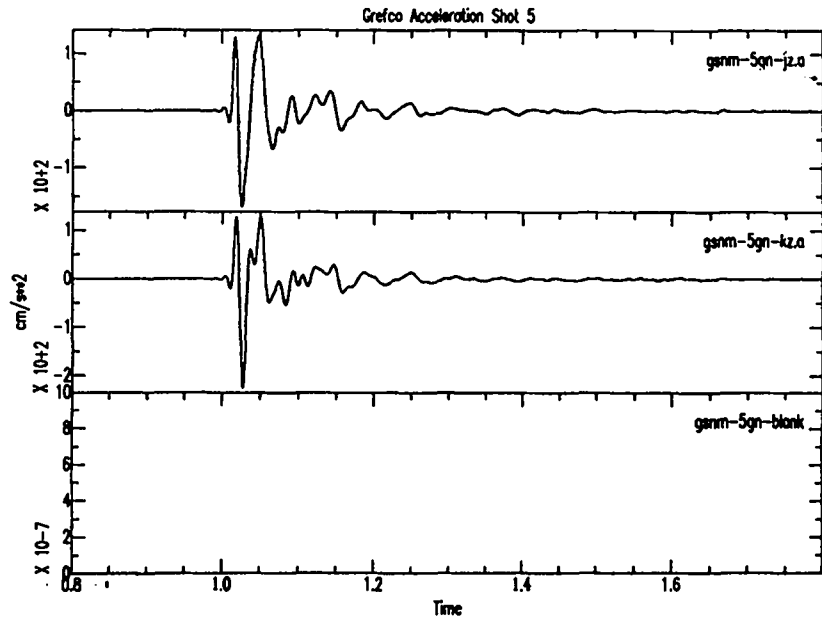
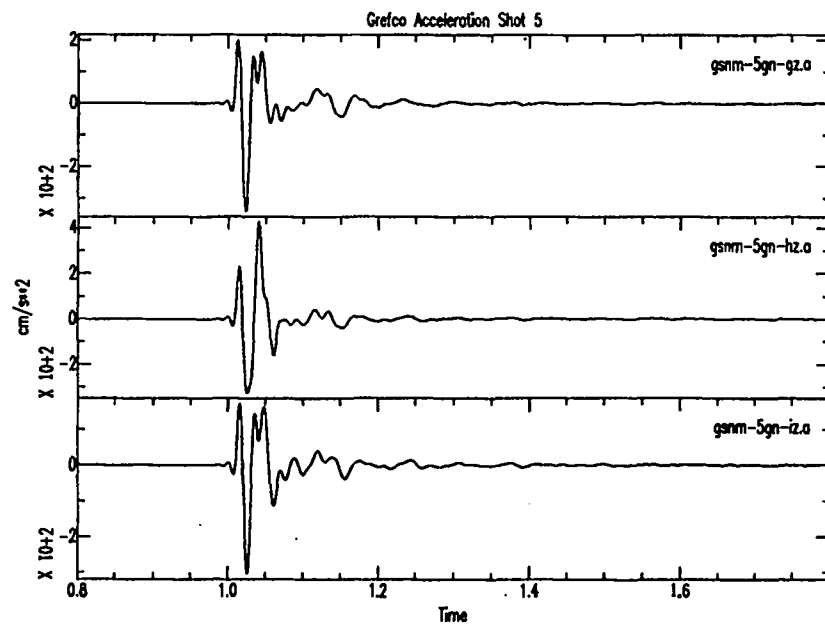
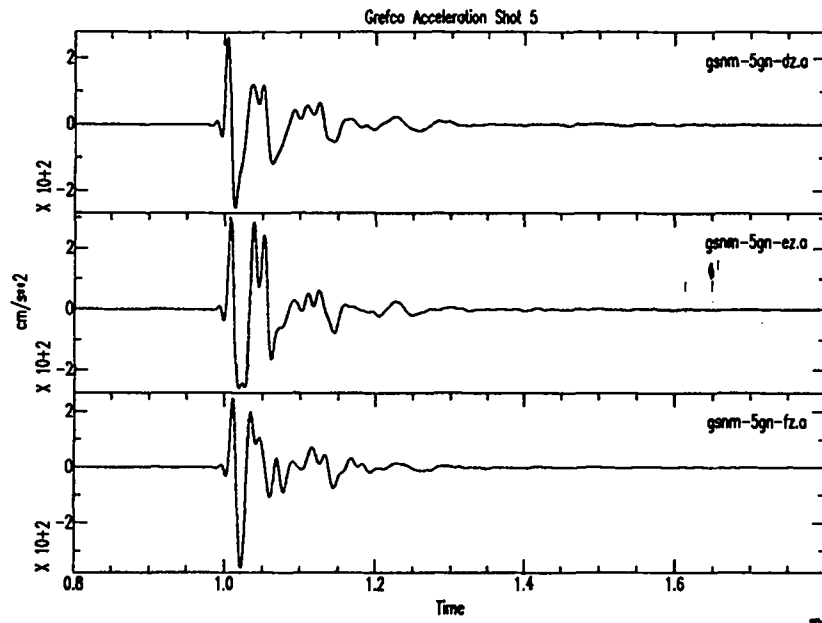
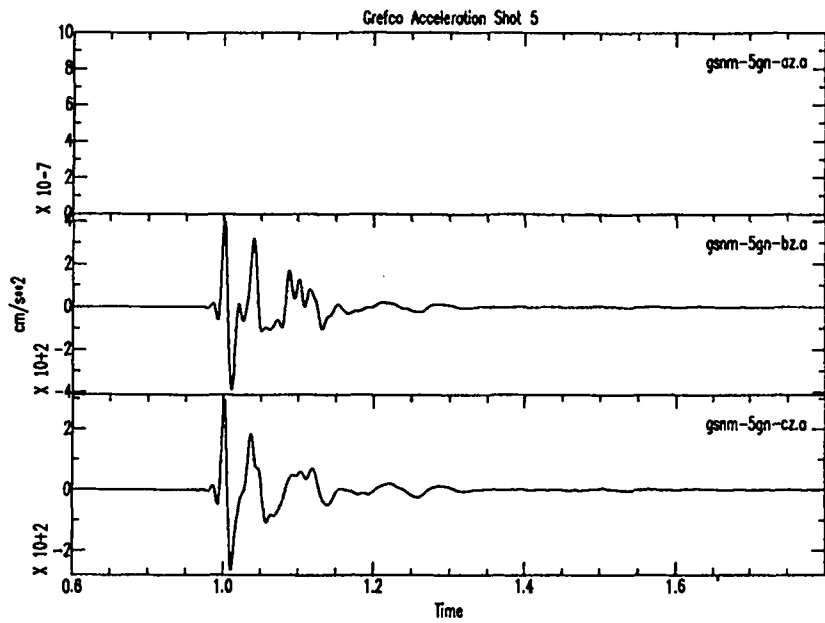
Grefco, Socorro, New Mexico-Shot 8 FBA LANL-Station 2 vertical (z) component.Acceleration

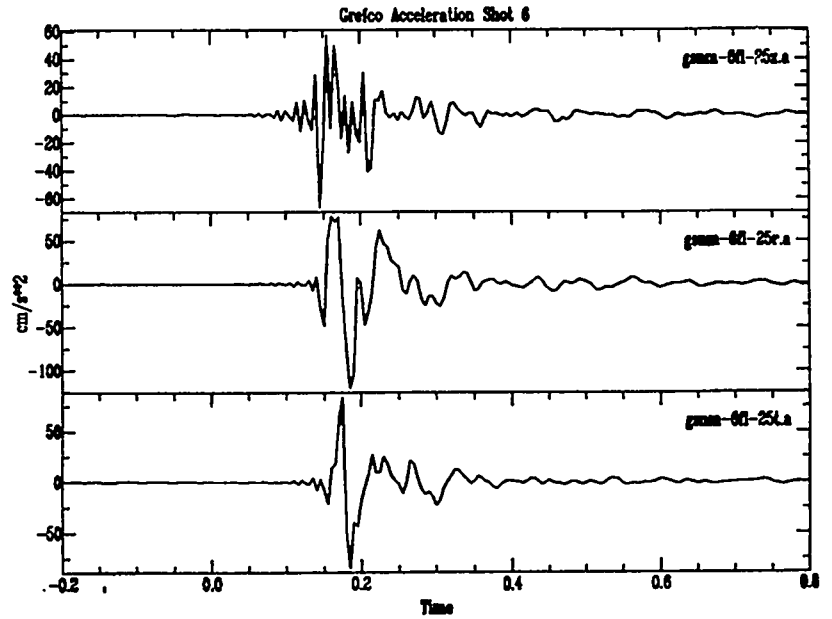
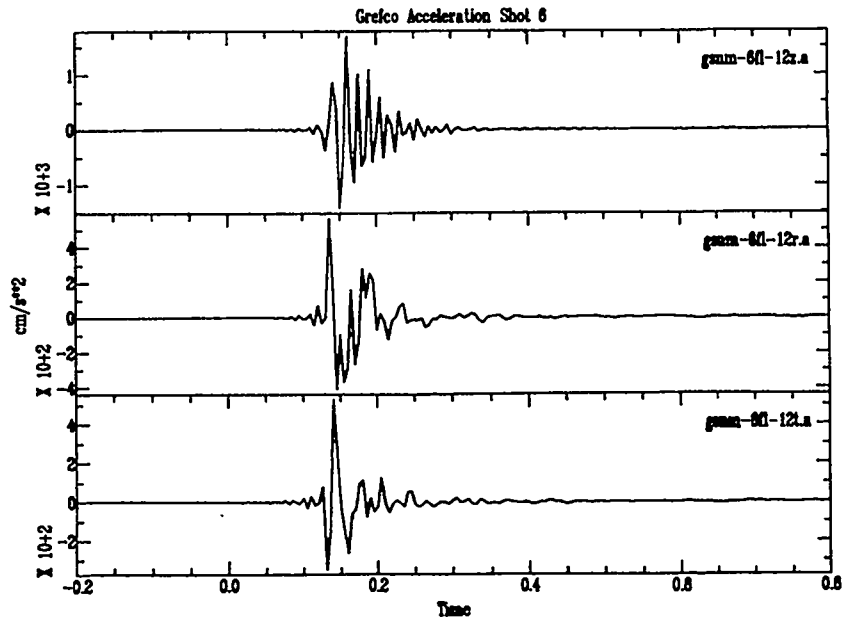
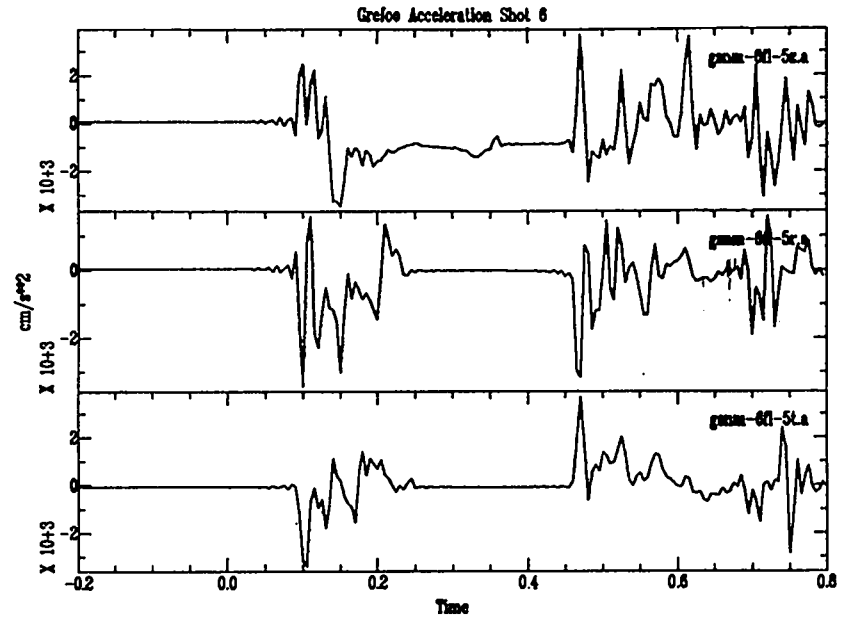
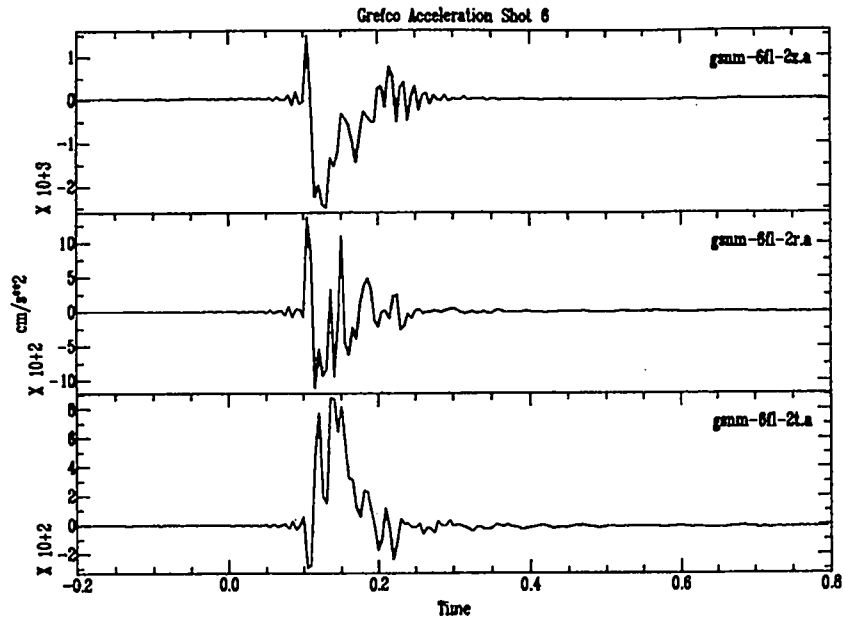




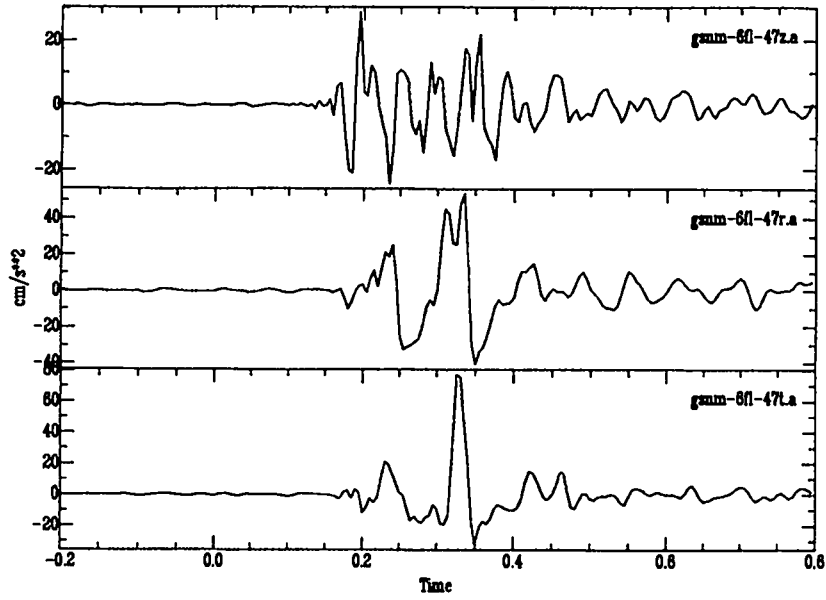




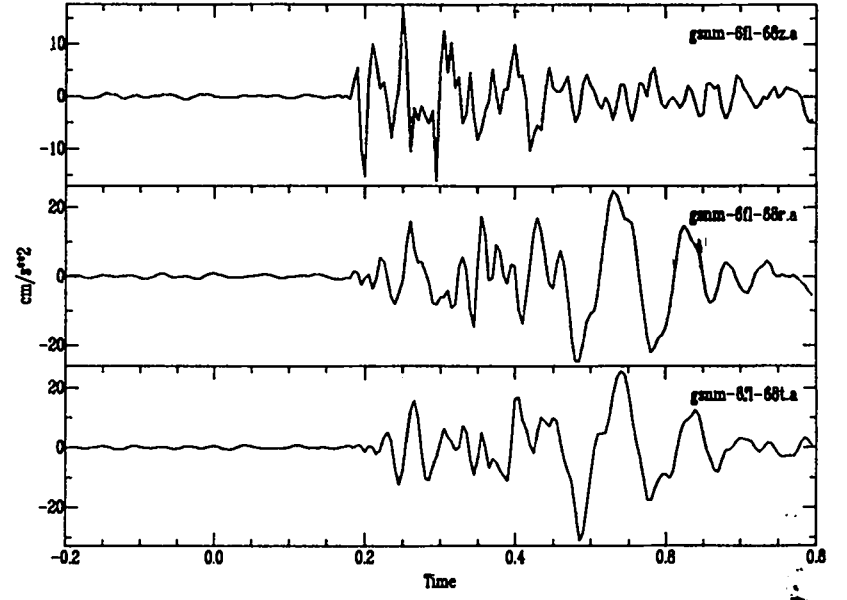




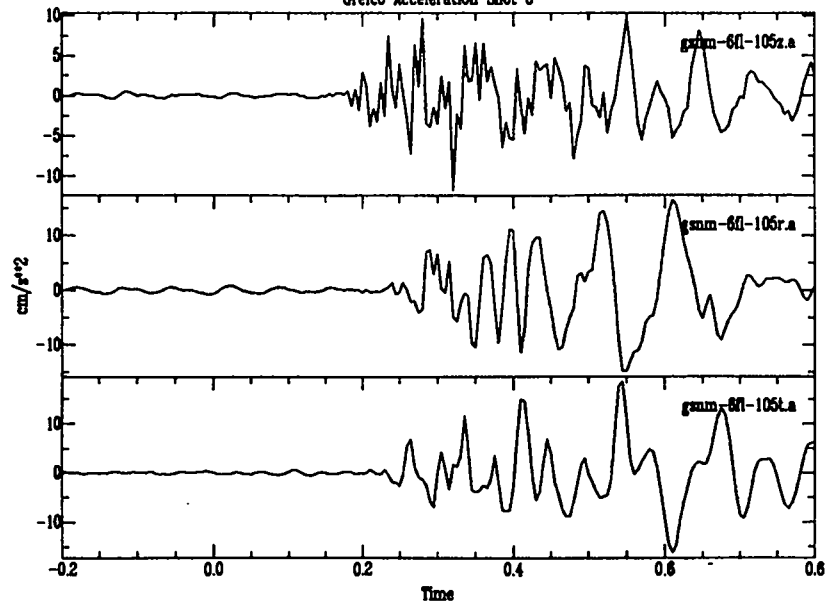
Grefco Acceleration Shot 8



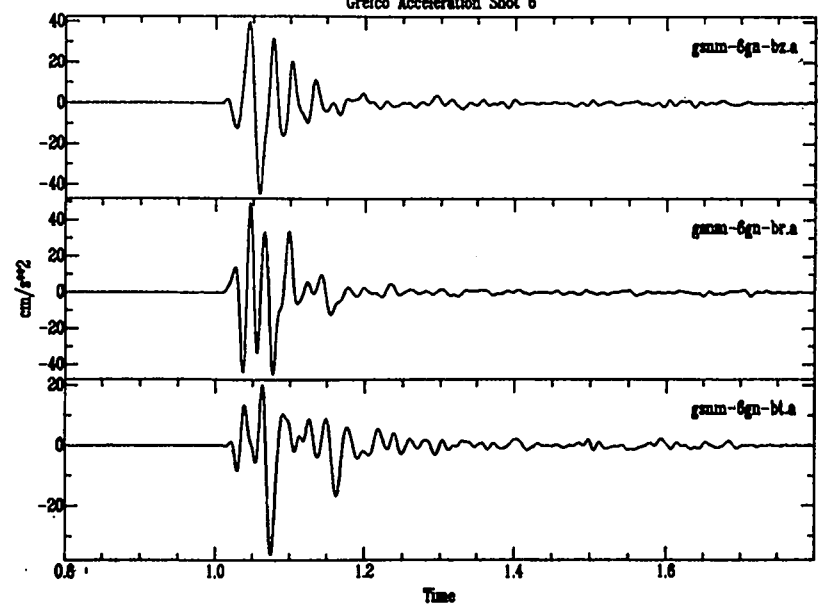
Grefco Acceleration Shot 8

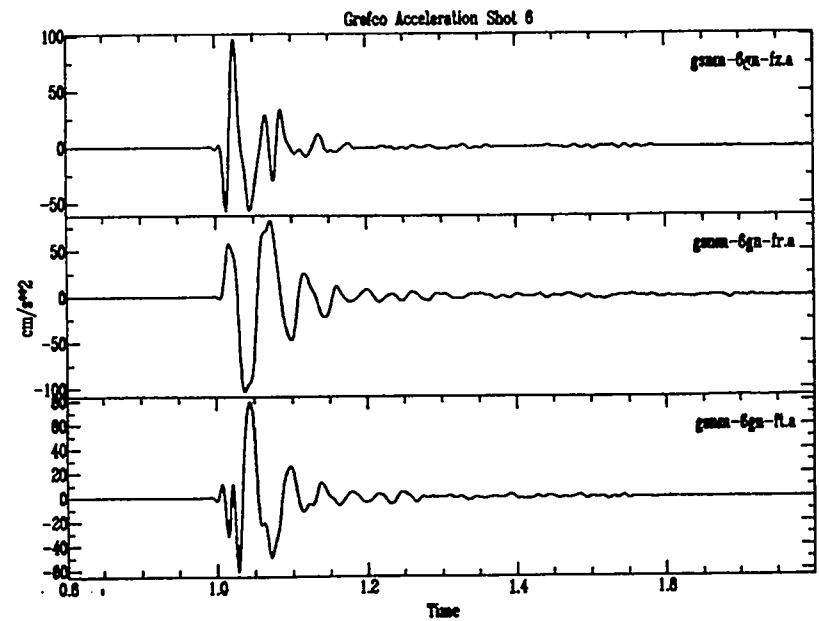
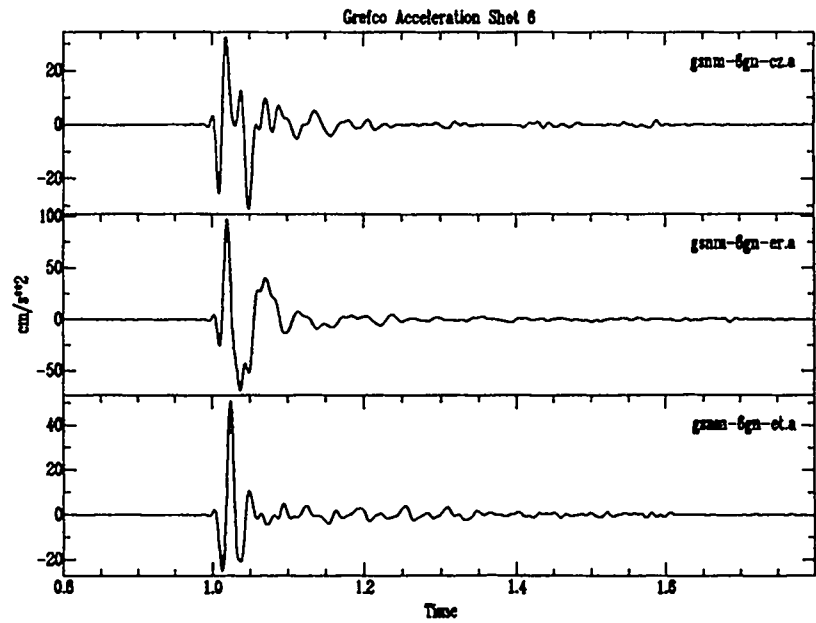
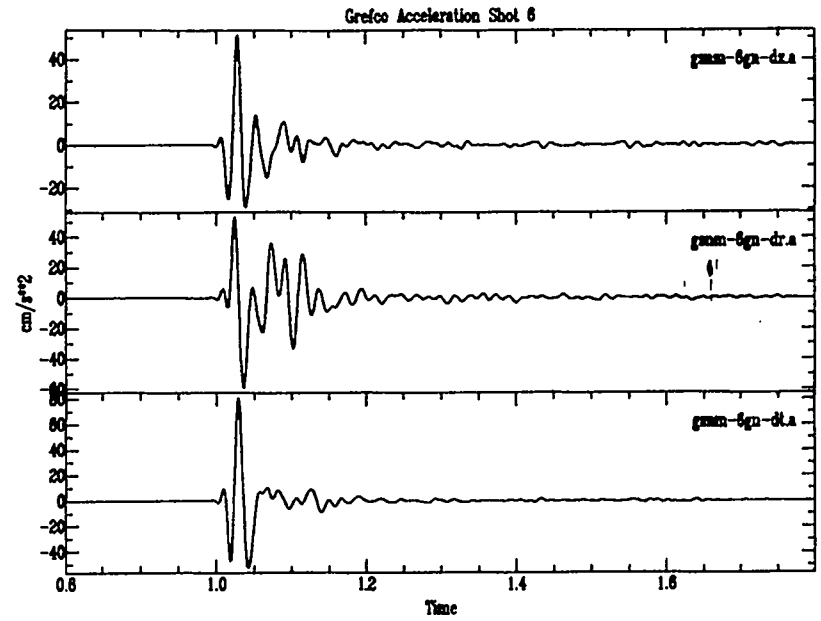
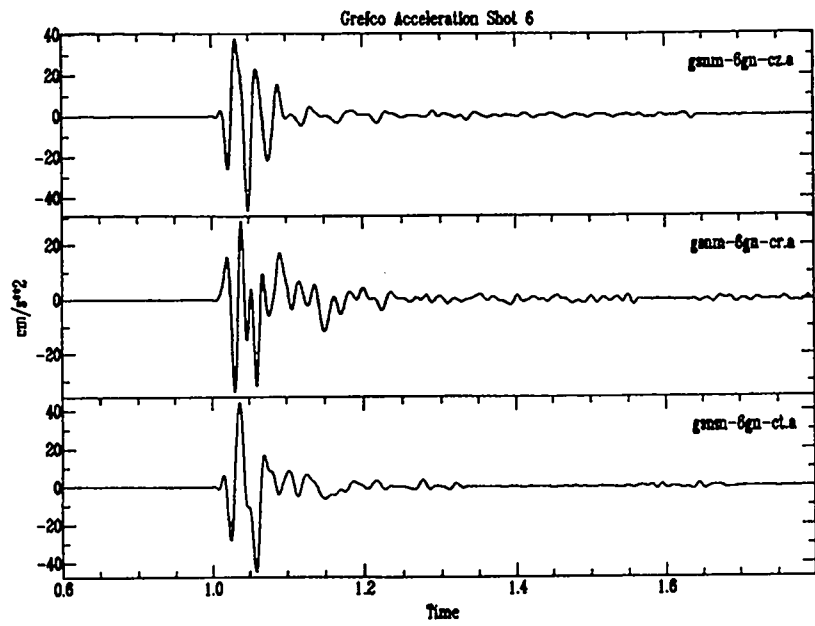


Grefco Acceleration Shot 8

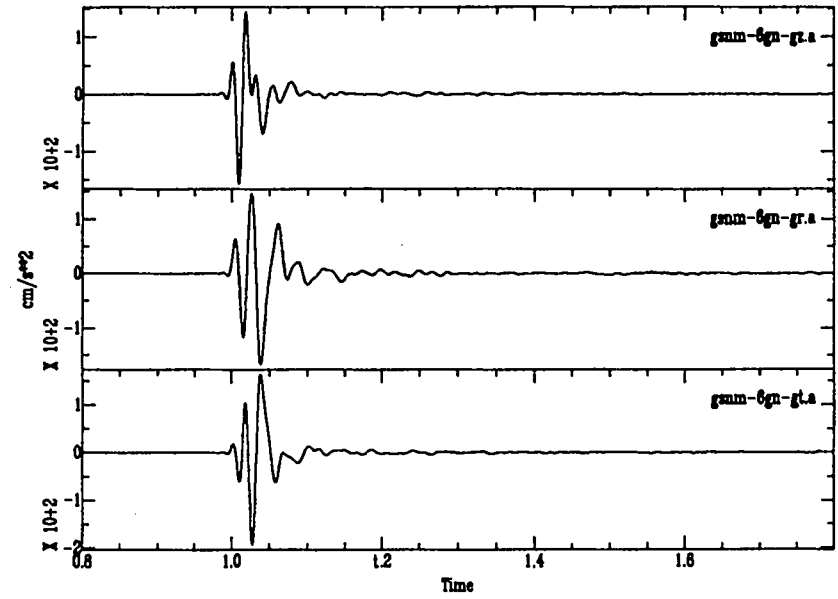


Grefco Acceleration Shot 8

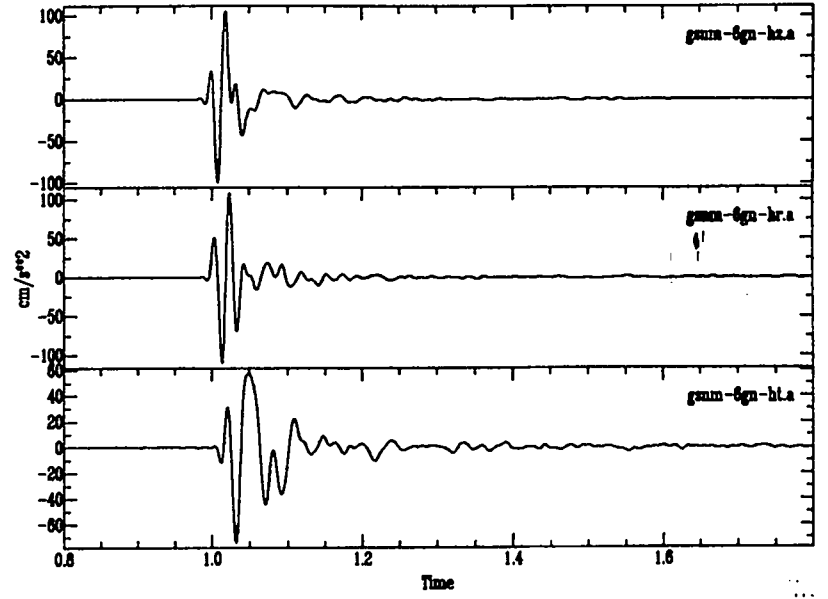




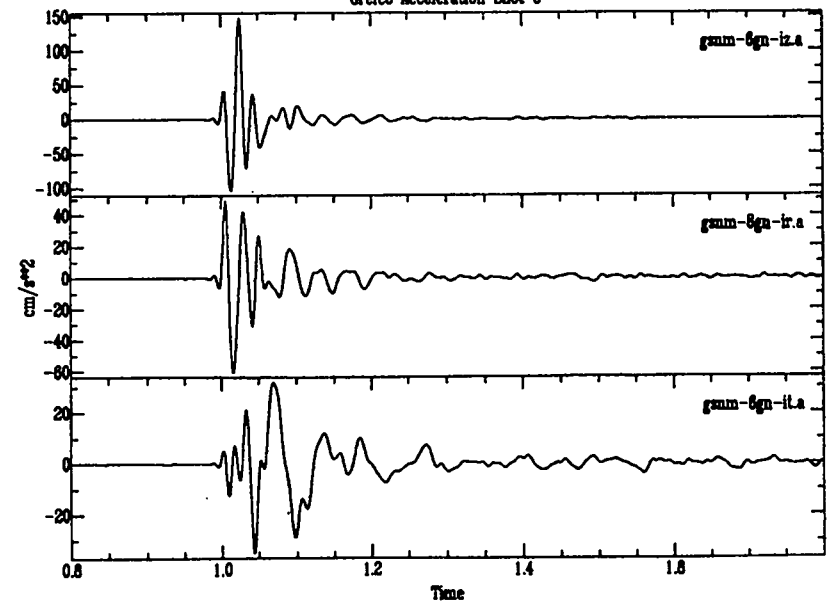
Grefco Acceleration Shot 6



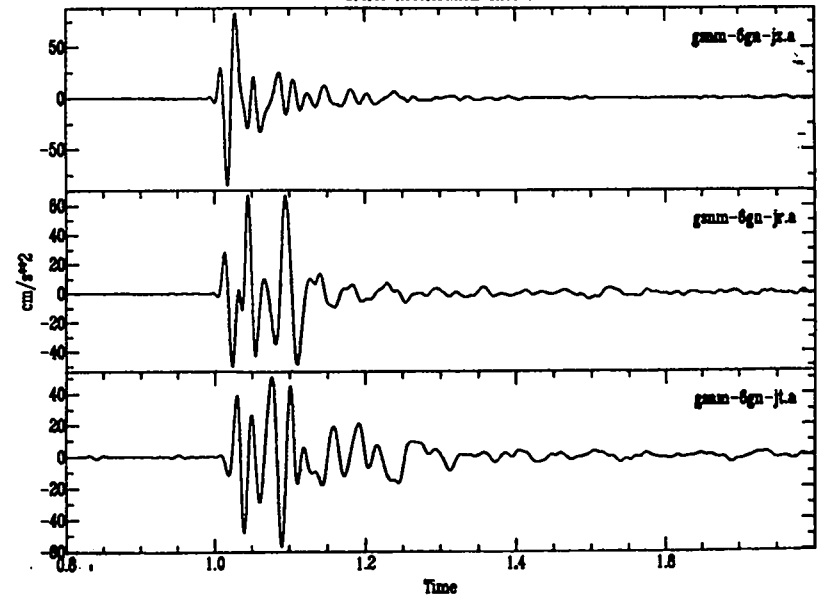
Grefco Acceleration Shot 6



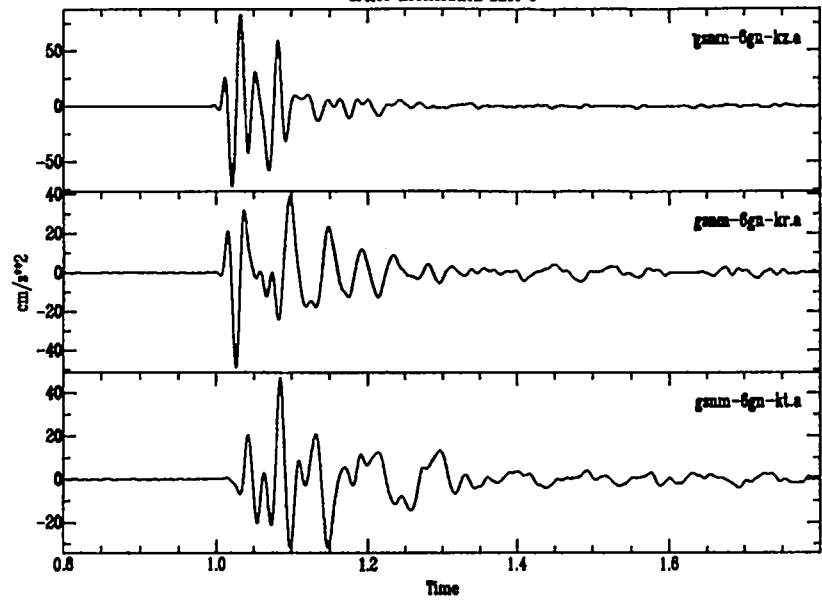
Grefco Acceleration Shot 6



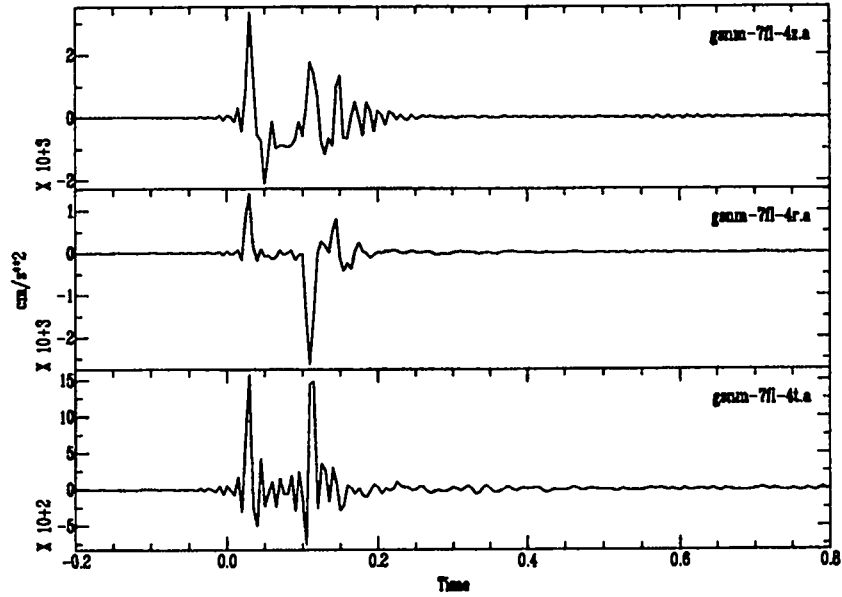
Grefco Acceleration Shot 6



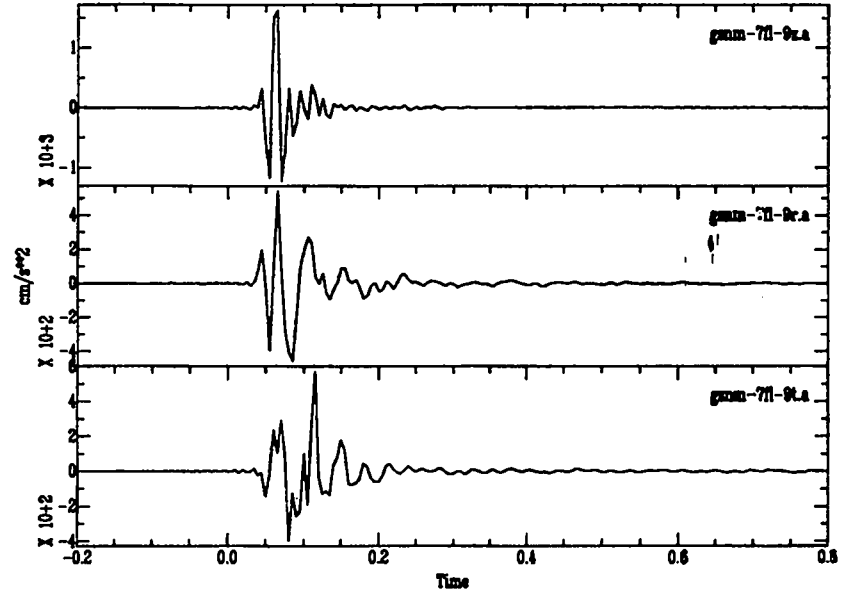
Greco Acceleration Shot 6



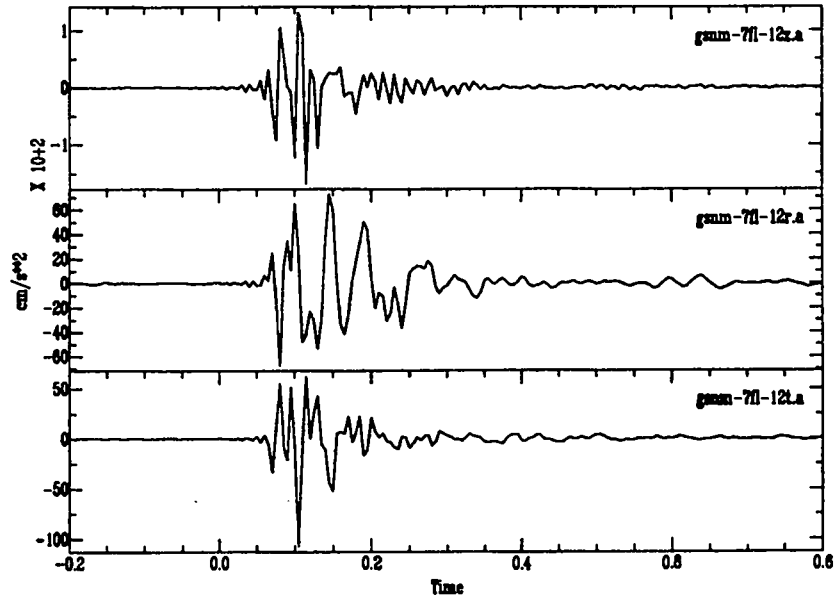
Grefco Acceleration Shot 7



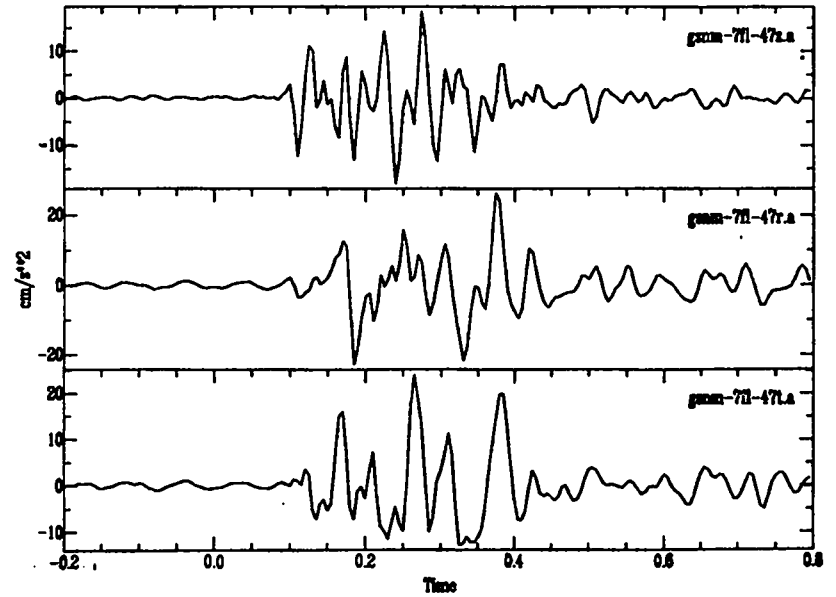
Grefco Acceleration Shot 7

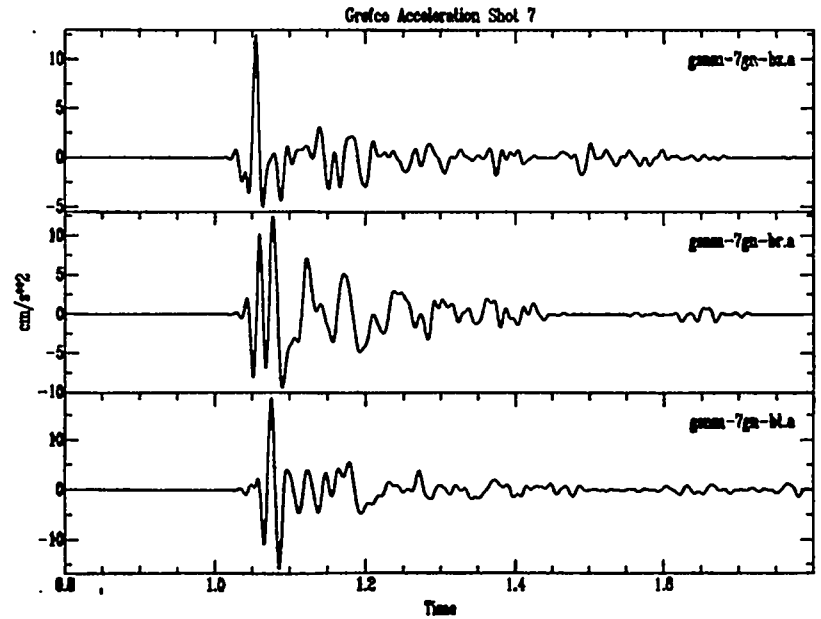
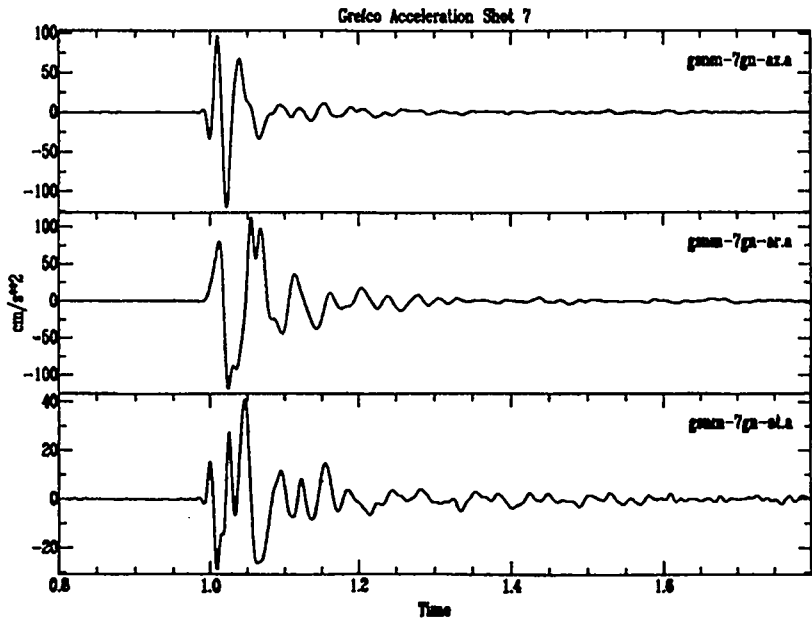
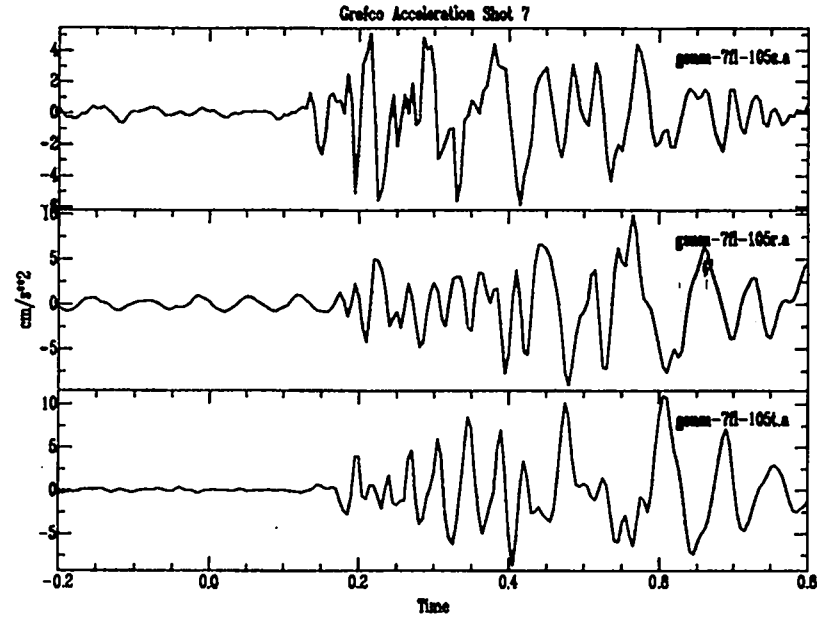
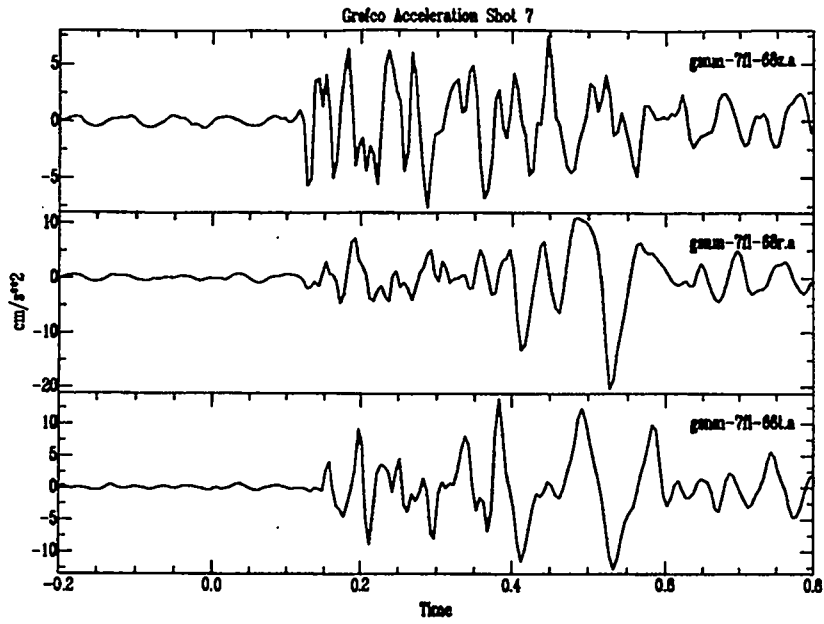


Grefco Acceleration Shot 7

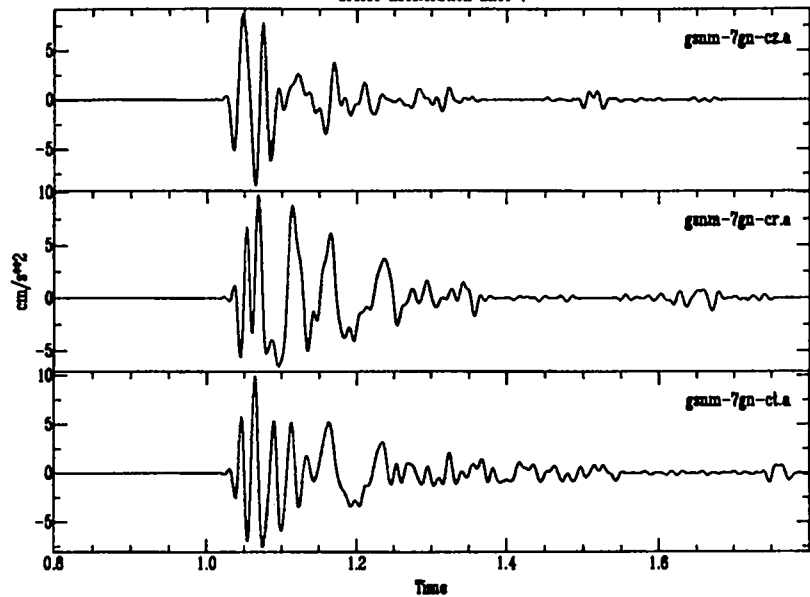


Grefco Acceleration Shot 7

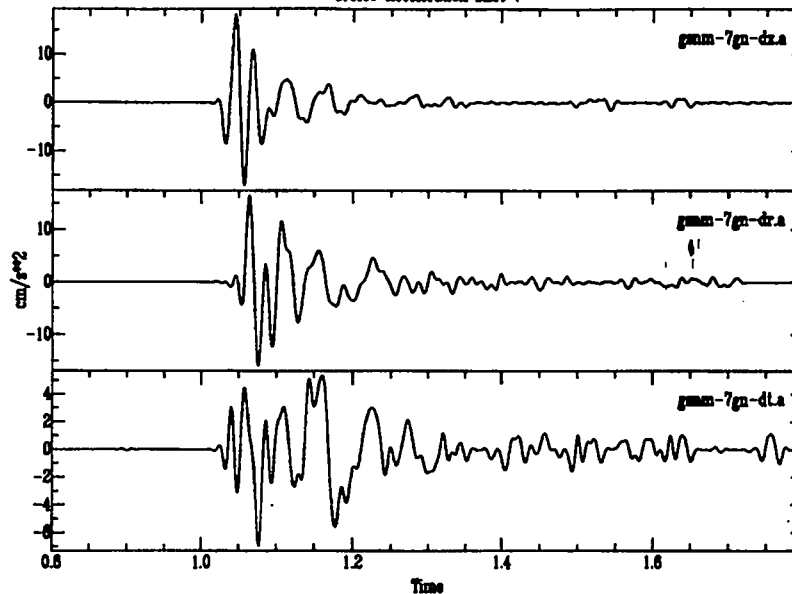




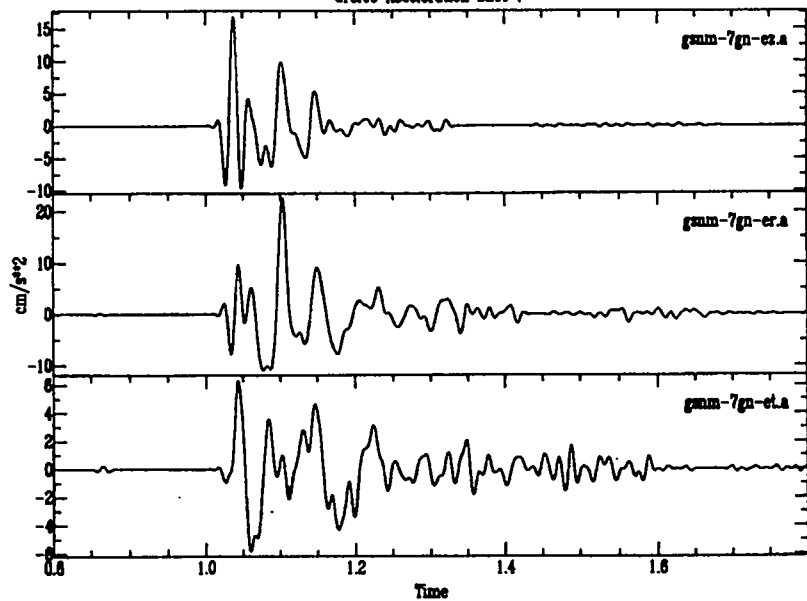
Grefco Acceleration Shot 7



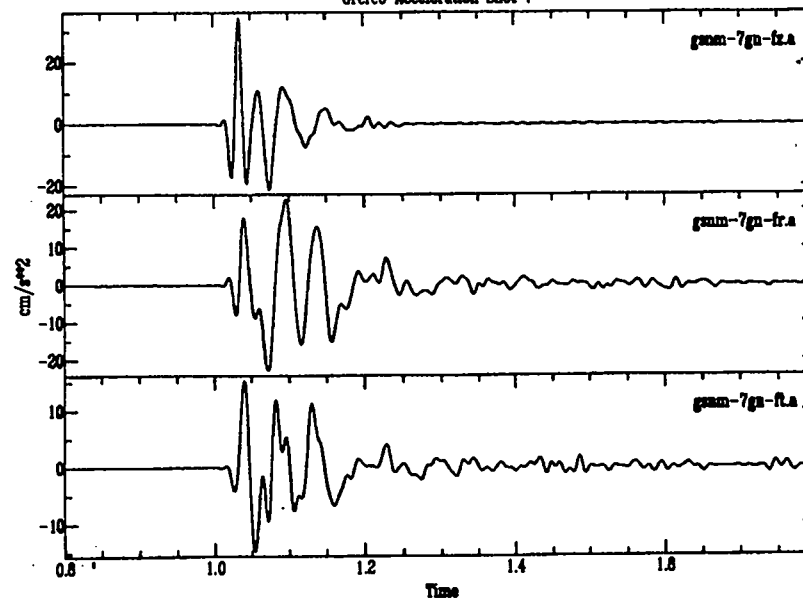
Grefco Acceleration Shot 7



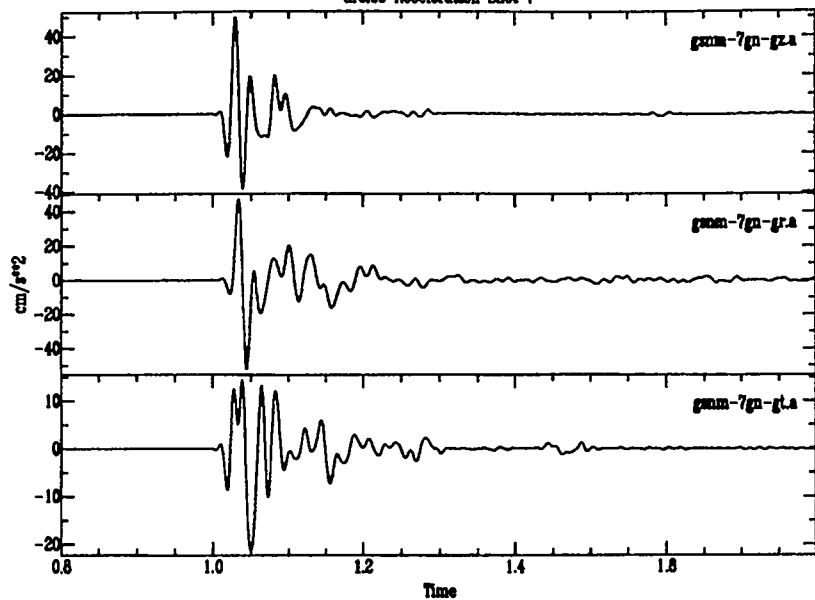
Grefco Acceleration Shot 7



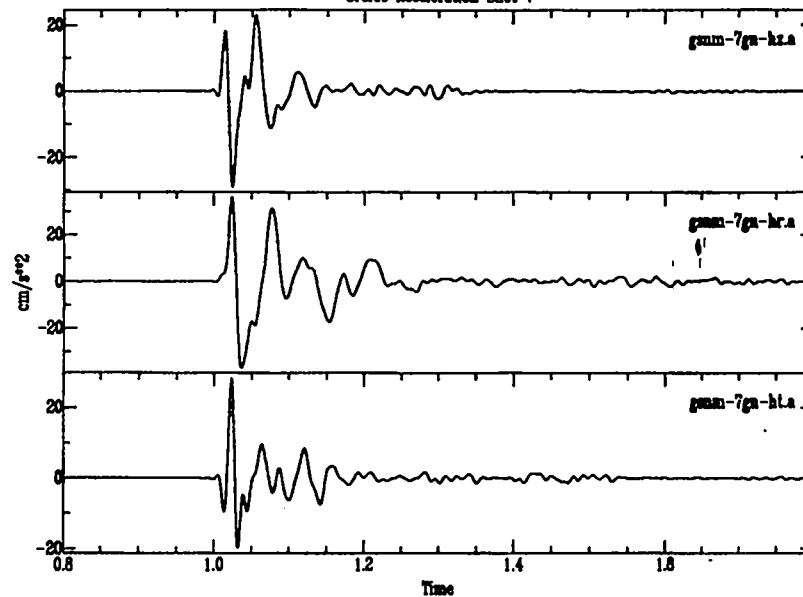
Grefco Acceleration Shot 7



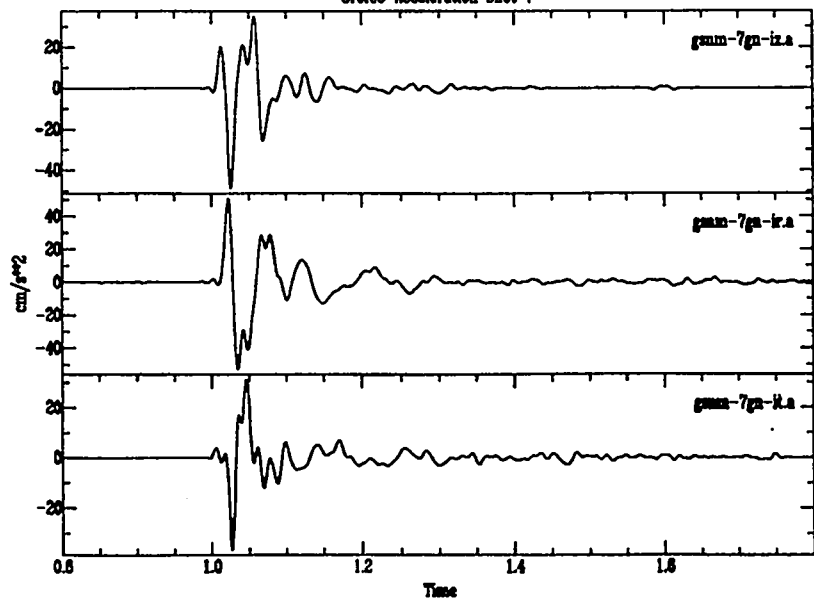
Grefco Acceleration Shot 7



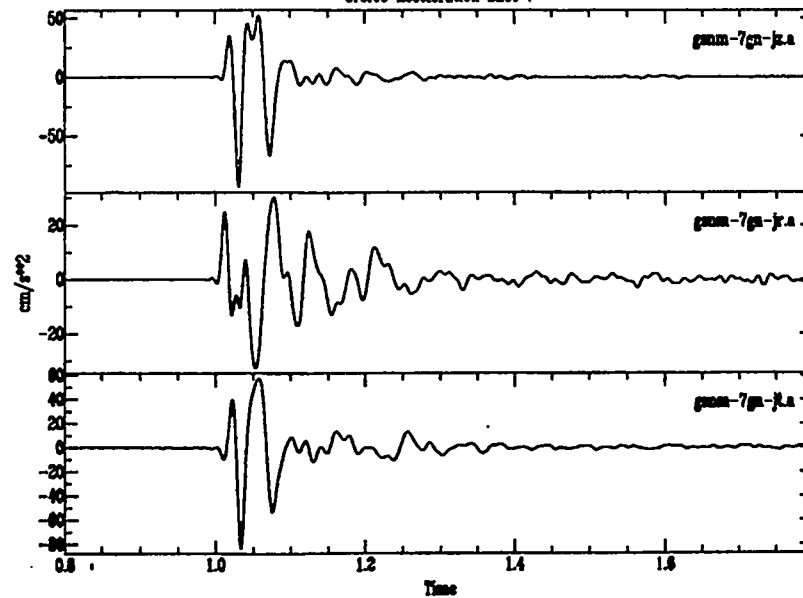
Grefco Acceleration Shot 7



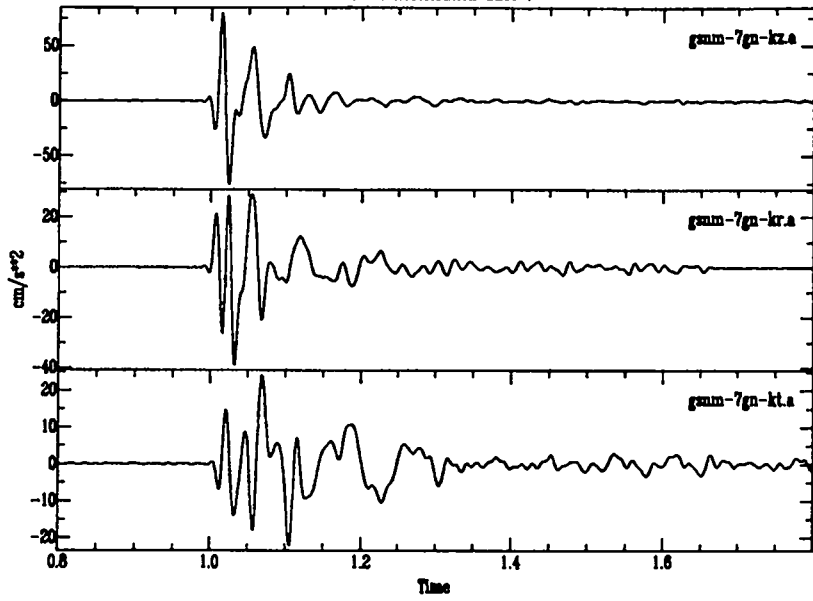
Grefco Acceleration Shot 7

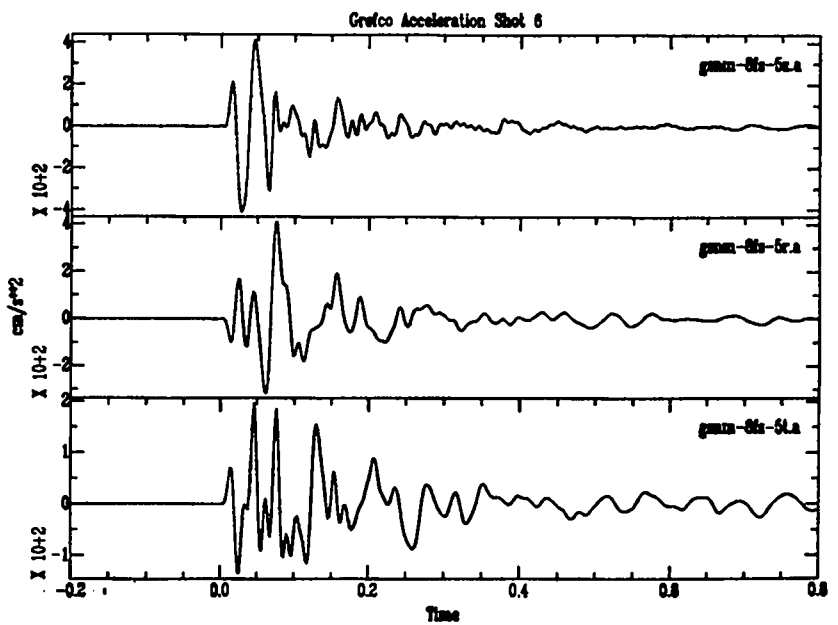
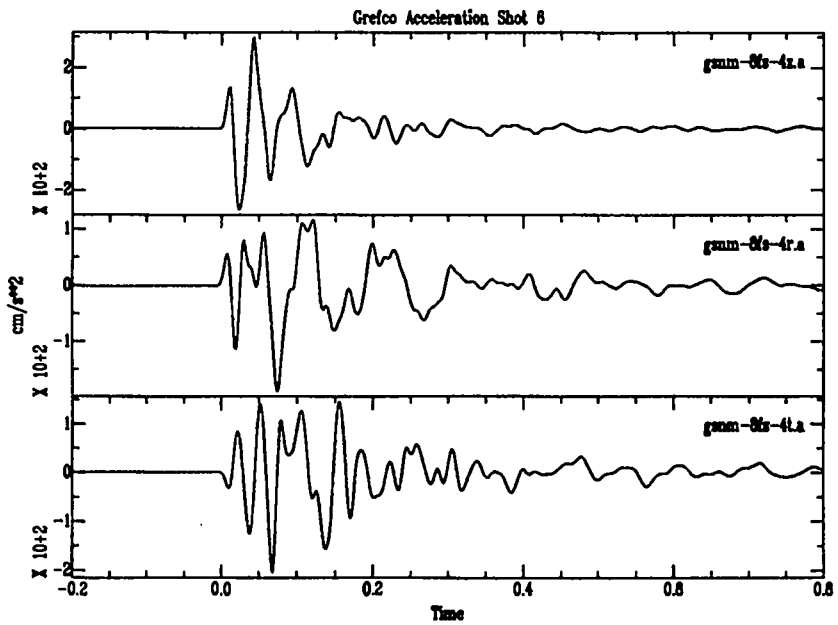
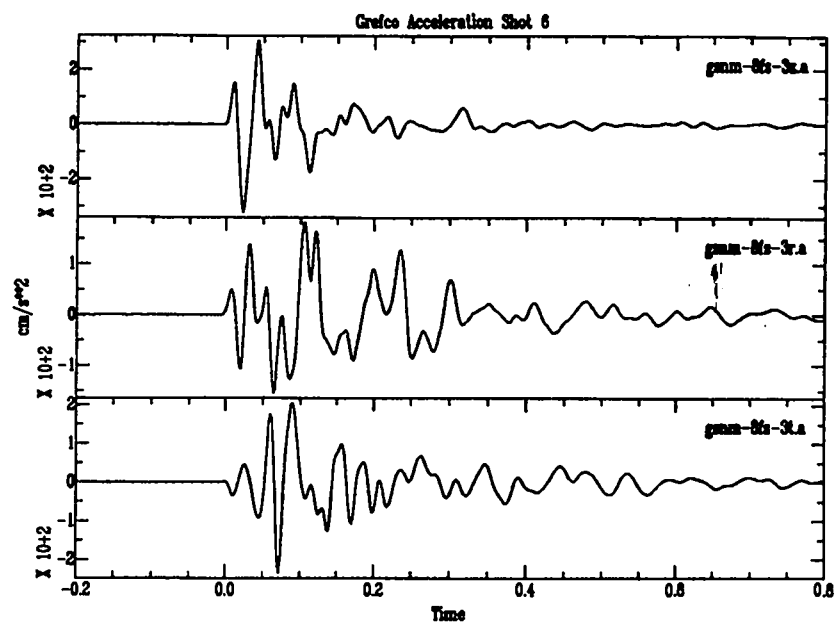
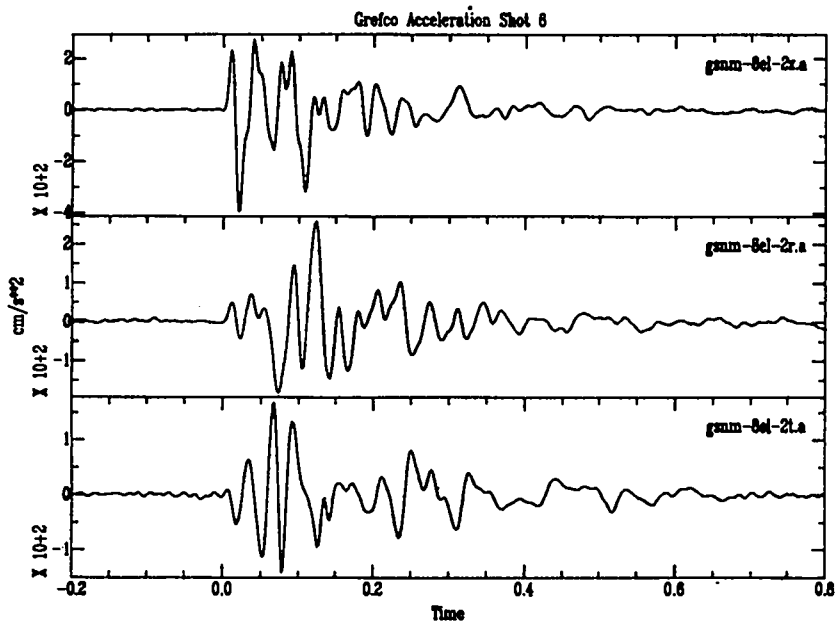


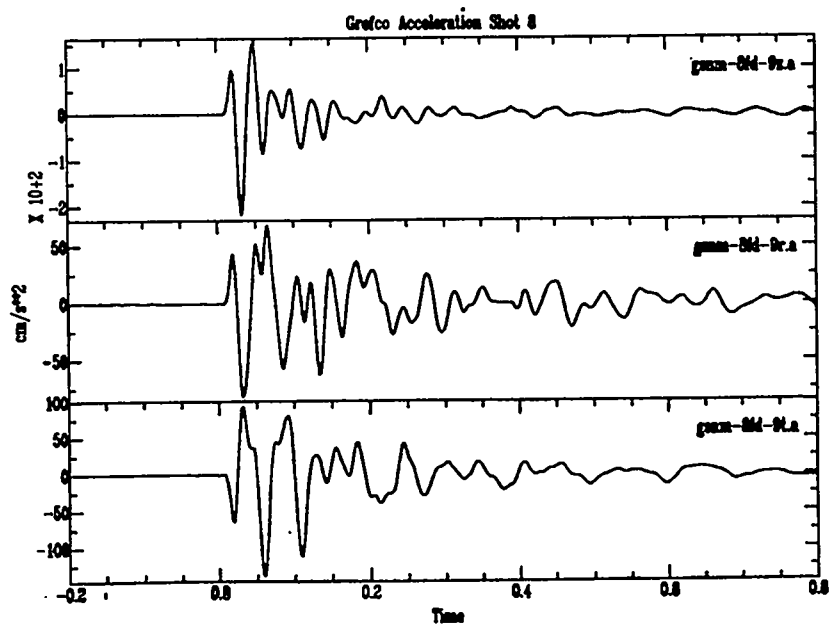
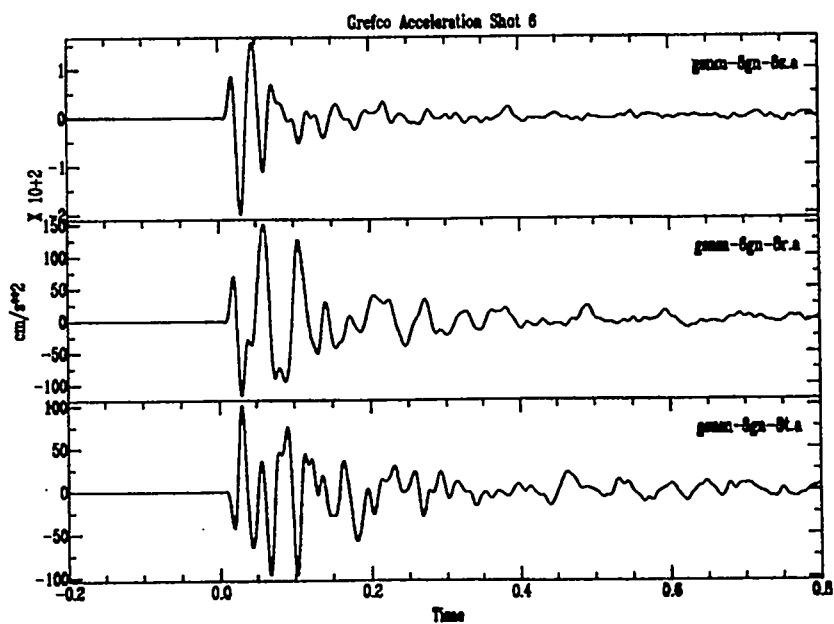
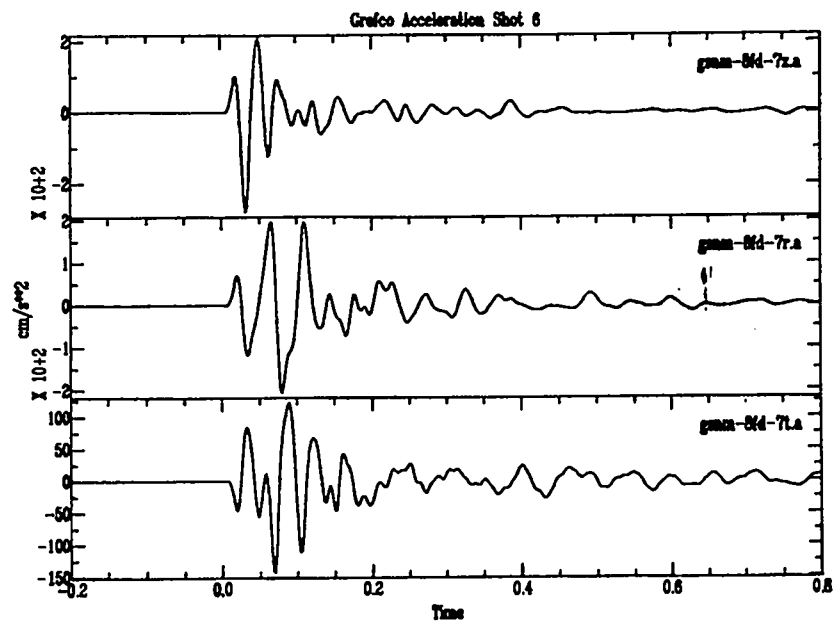
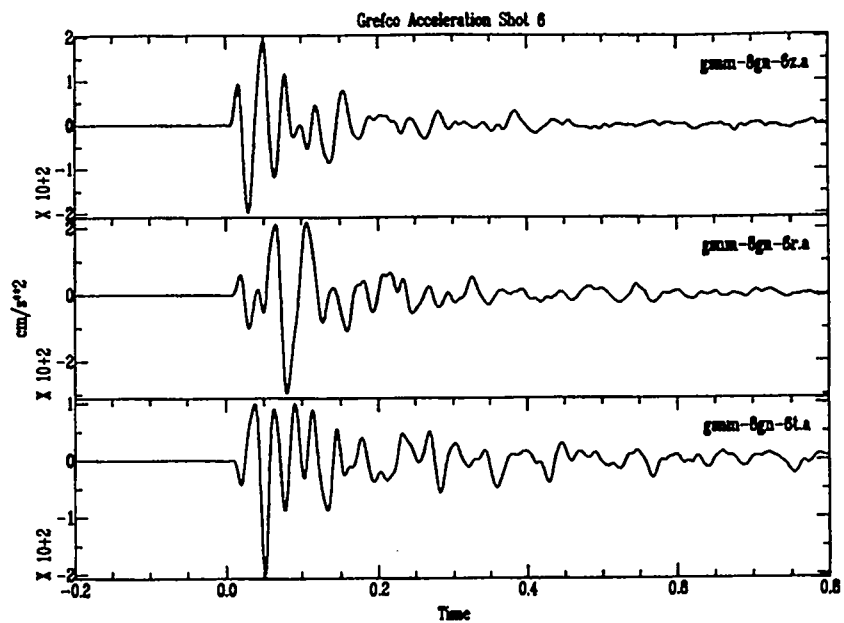
Grefco Acceleration Shot 7

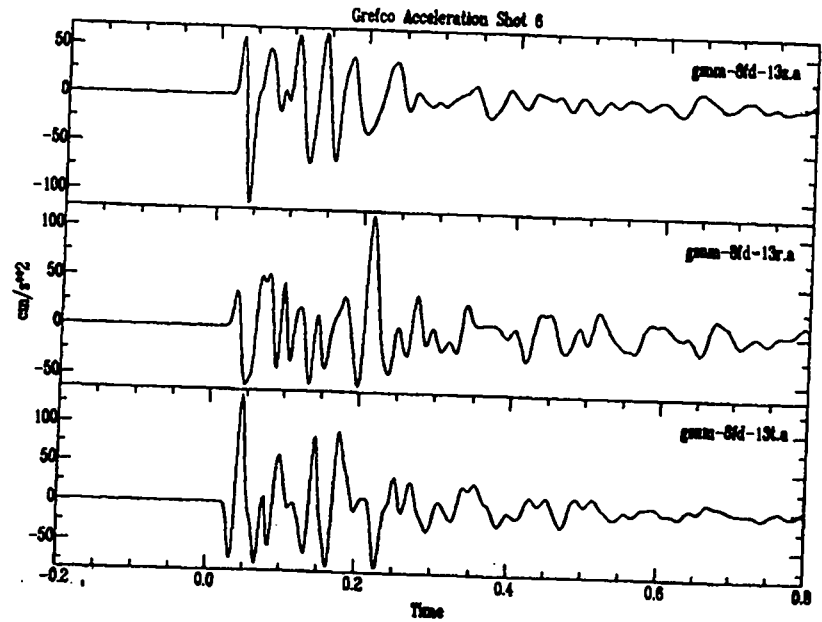
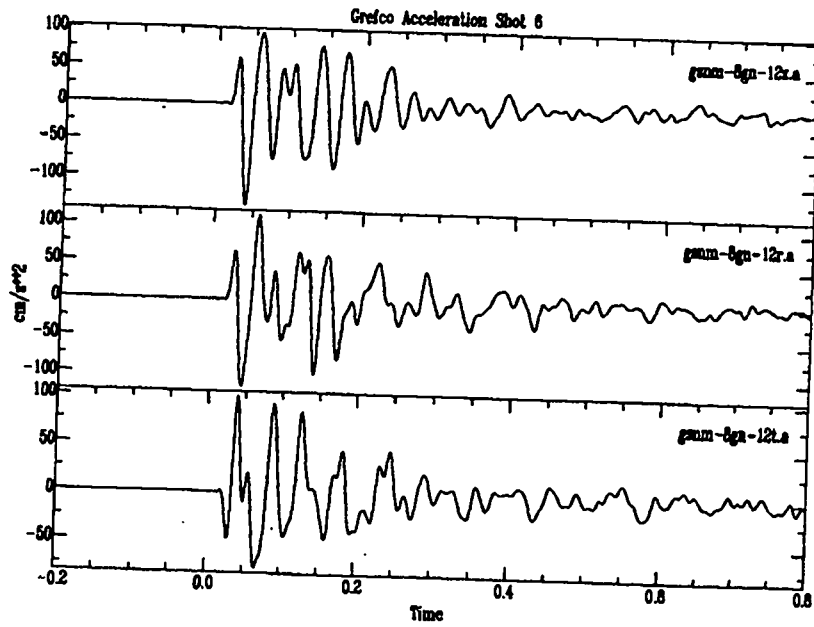
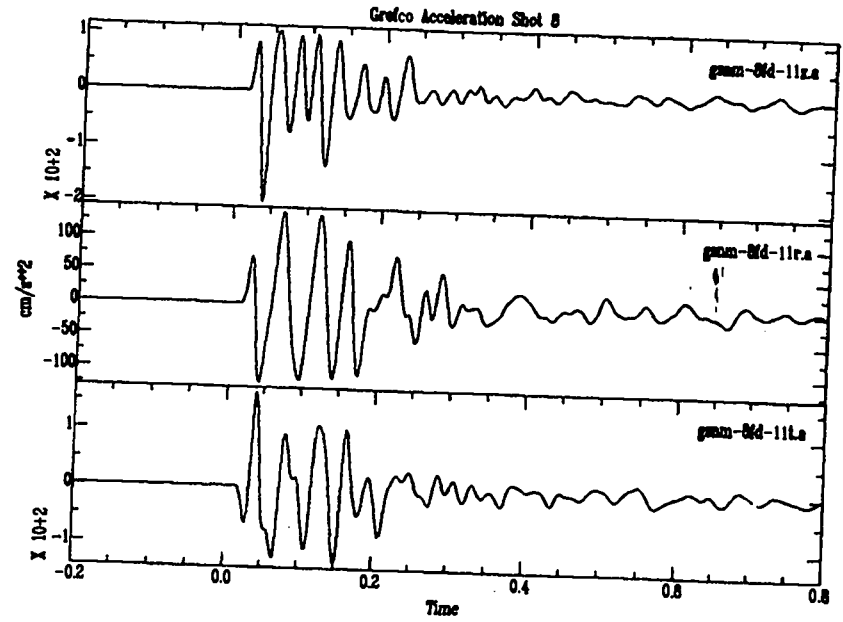
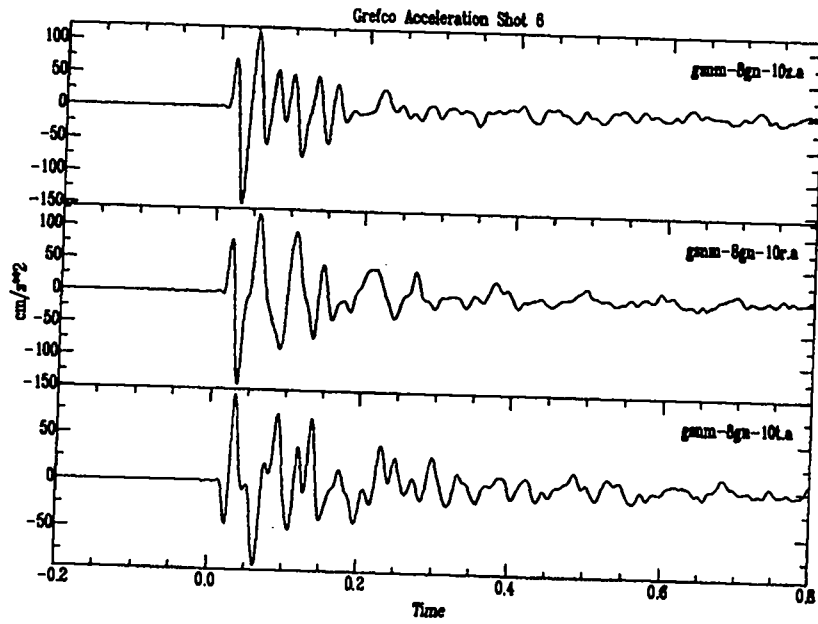


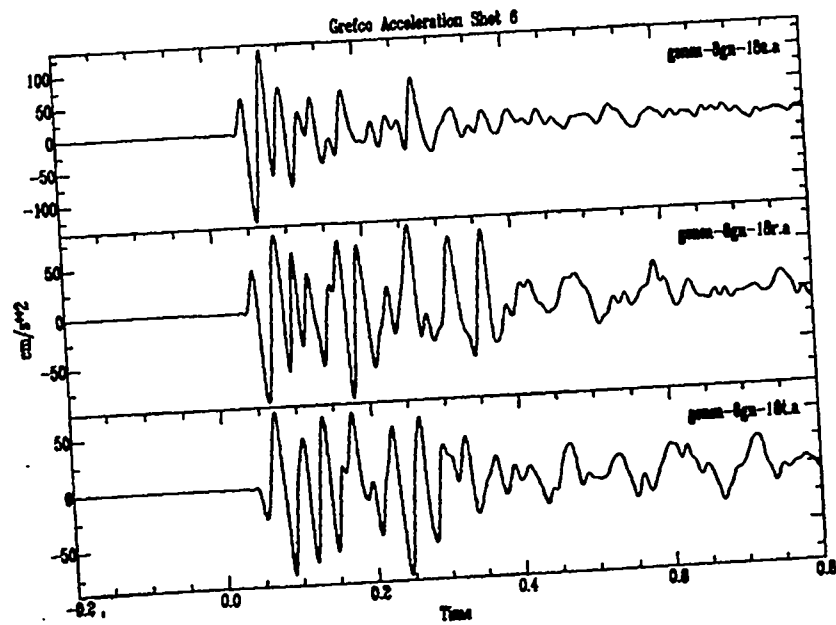
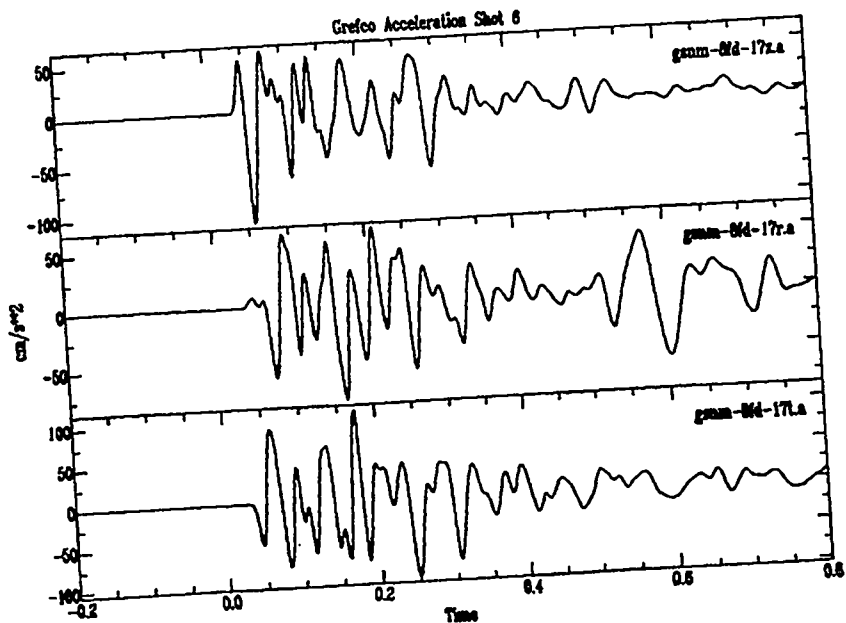
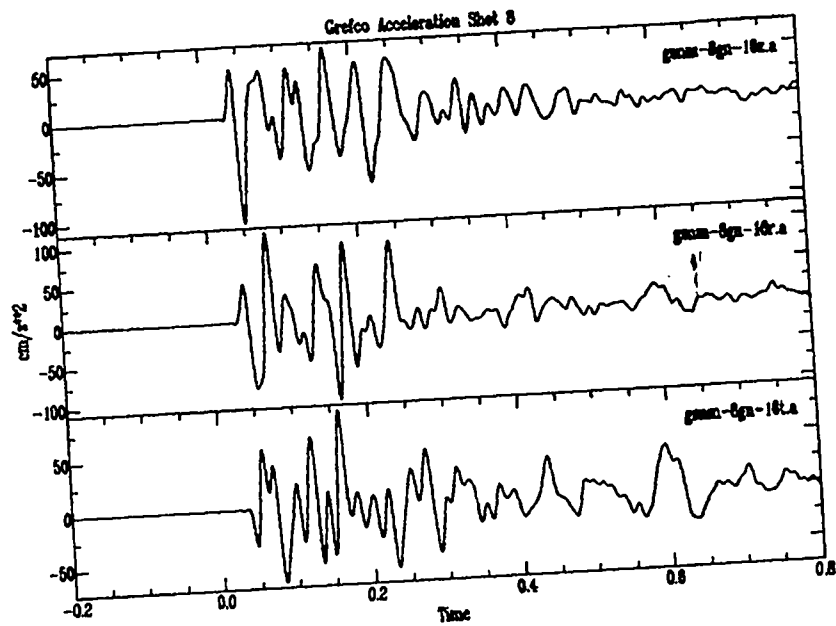
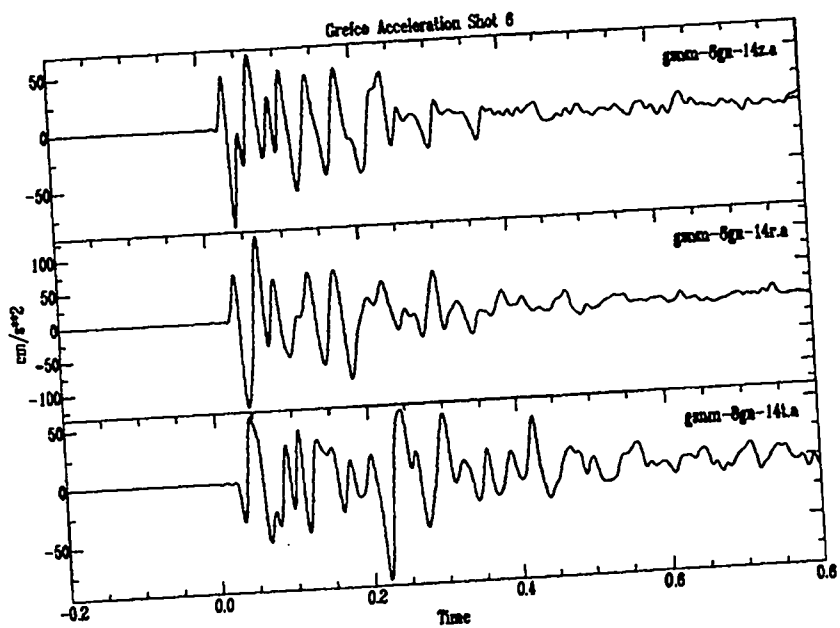
Greco Acceleration Shot 7



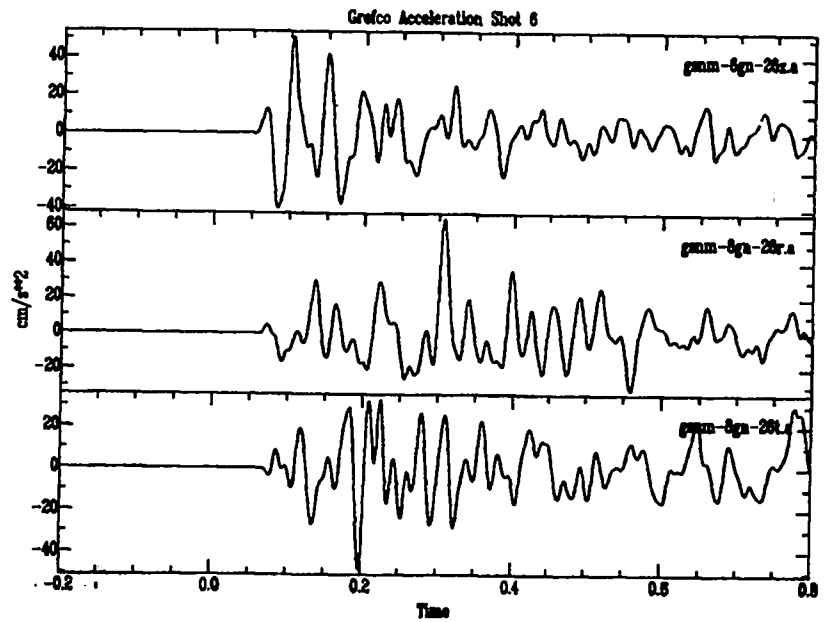
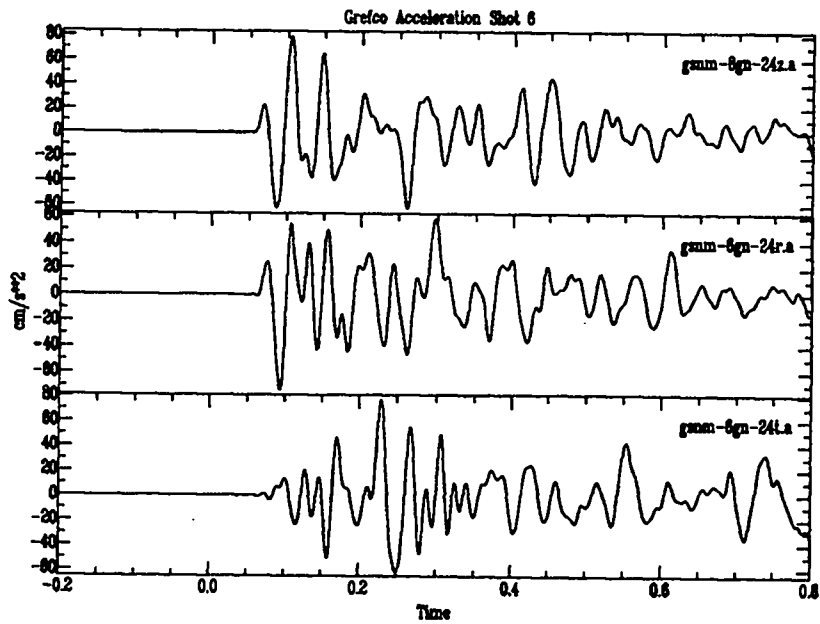
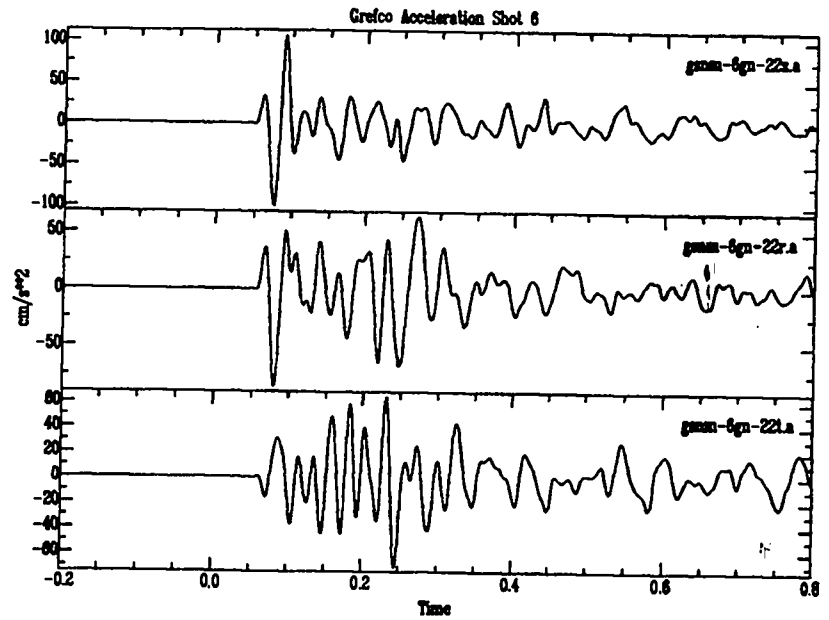
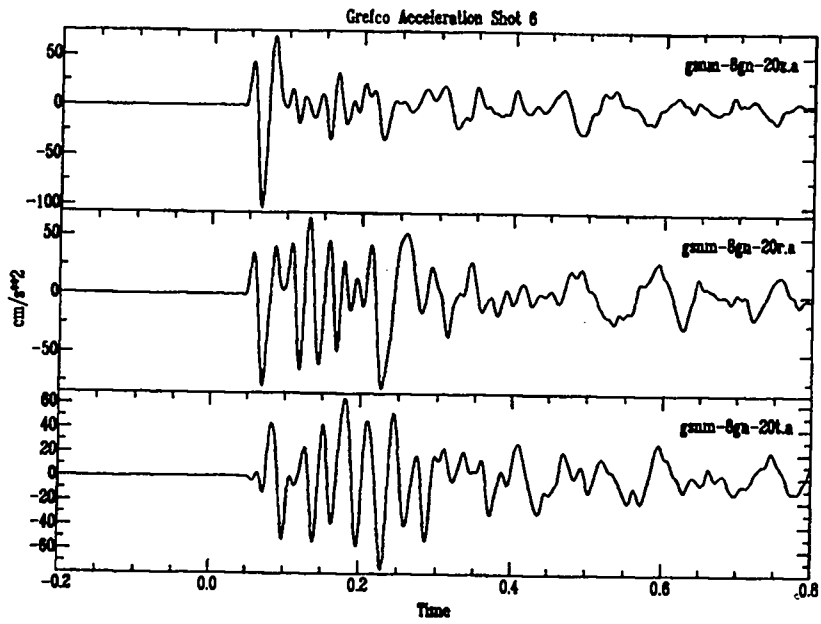


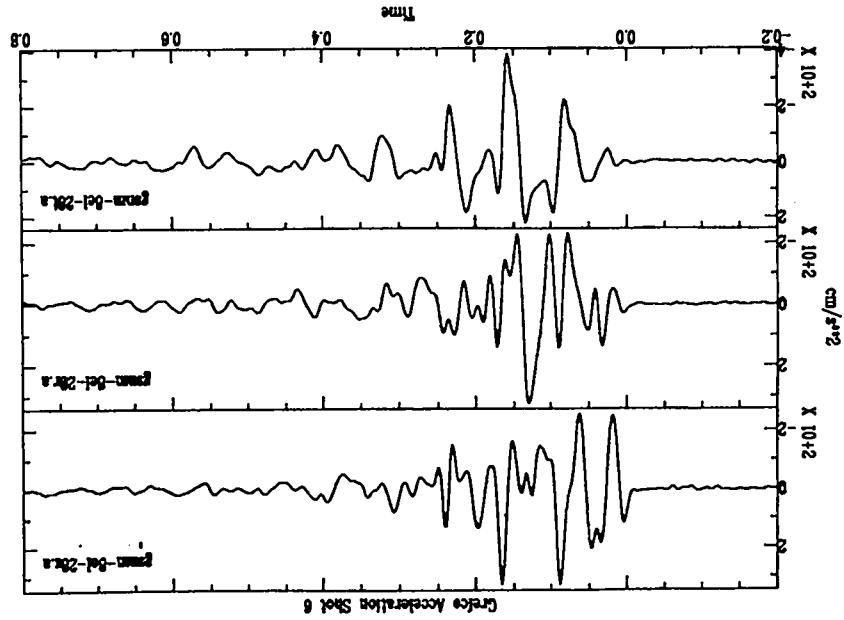
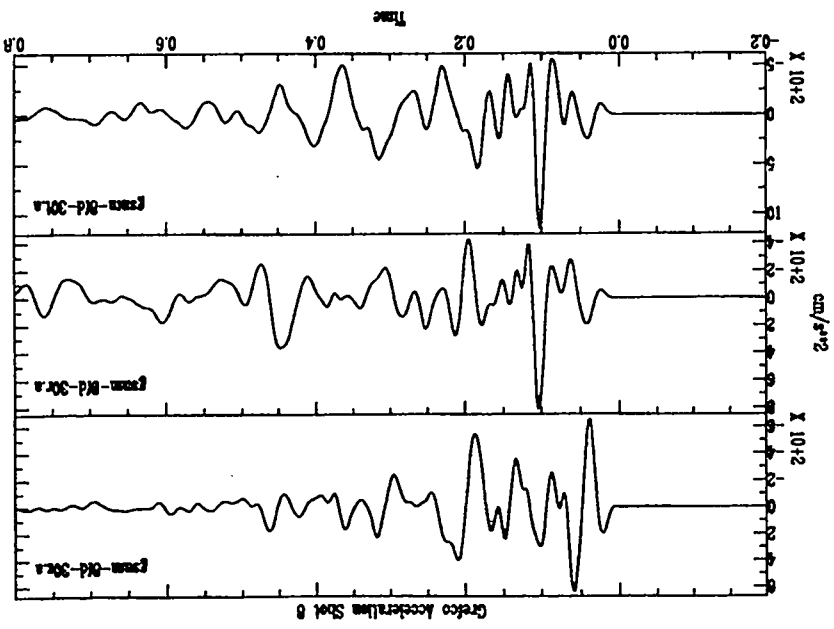
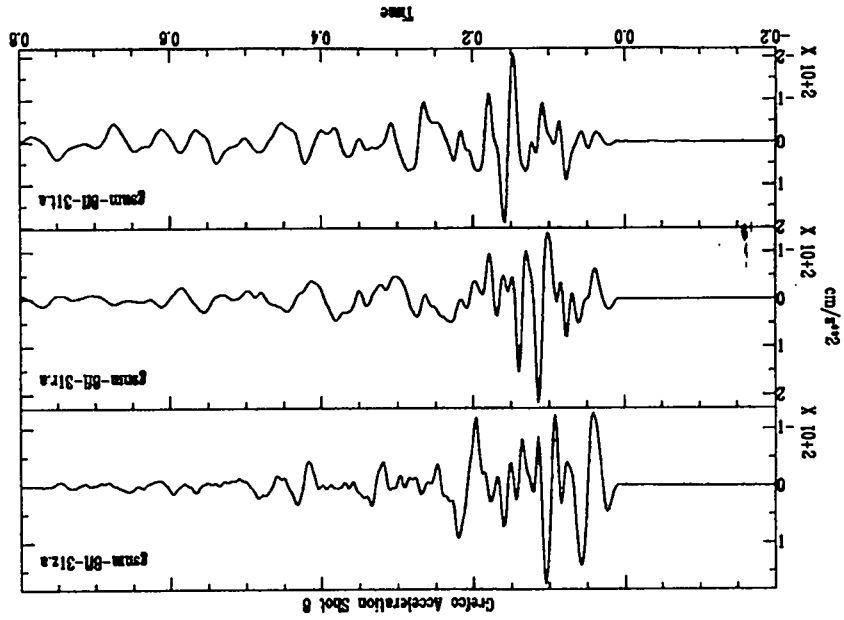
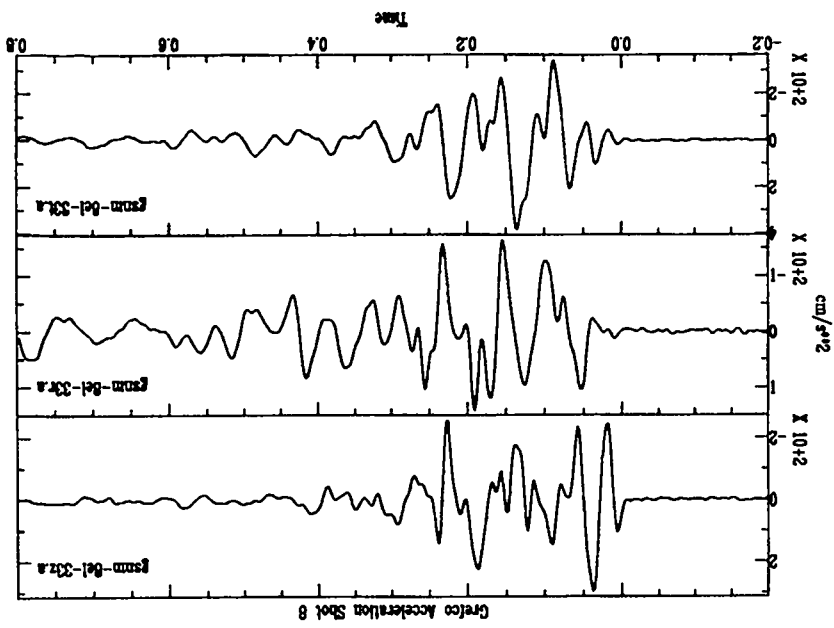


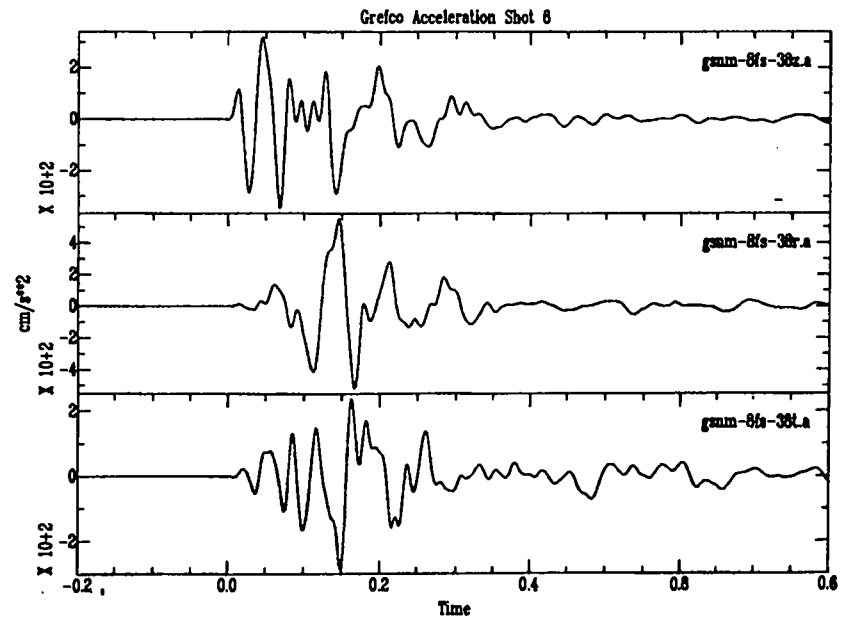
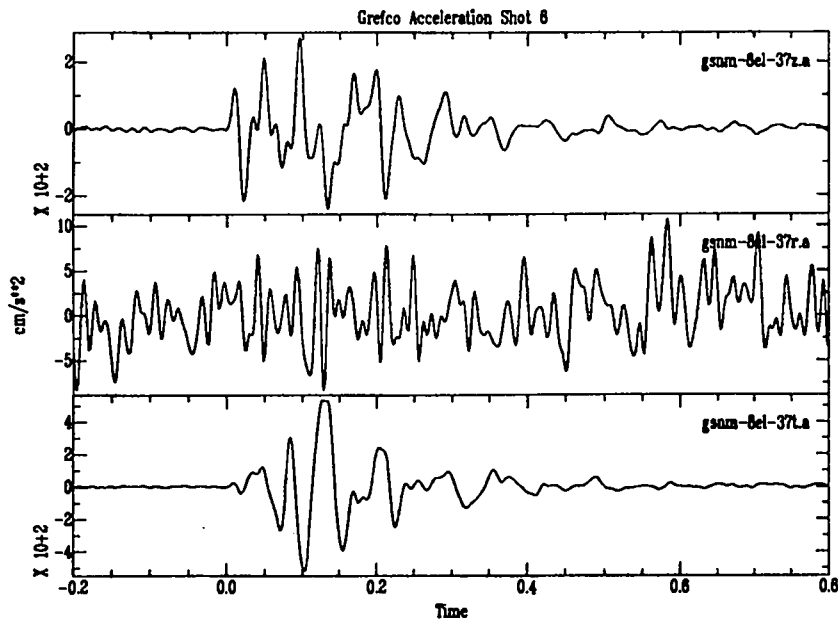
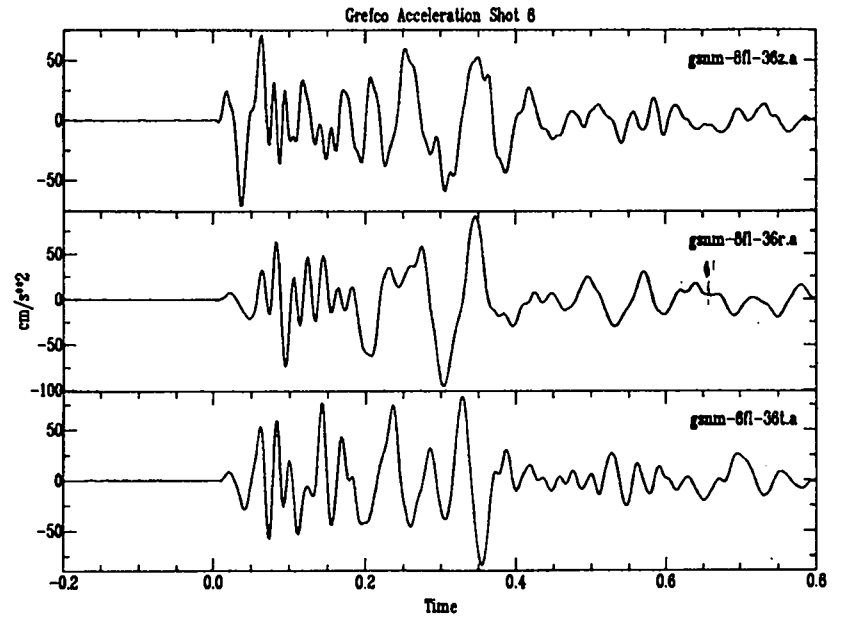
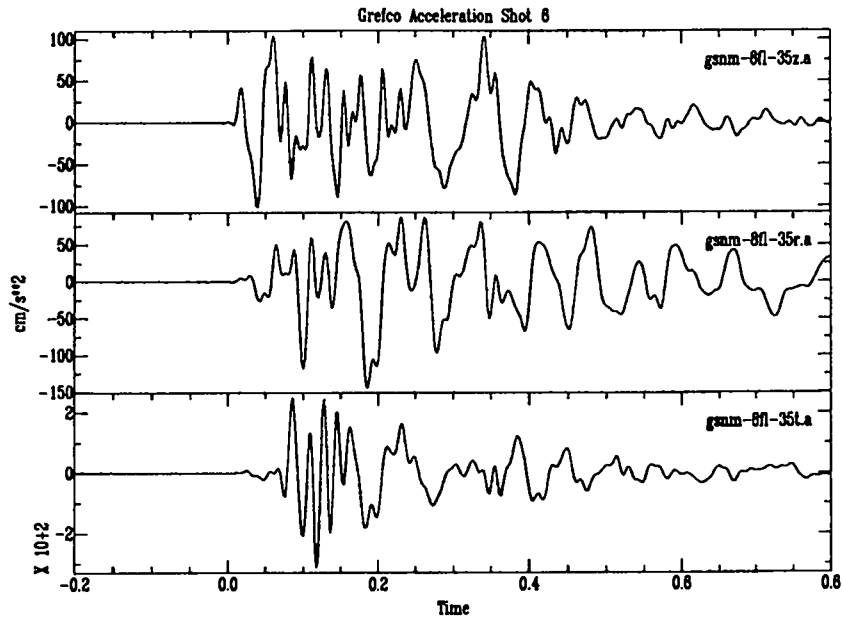


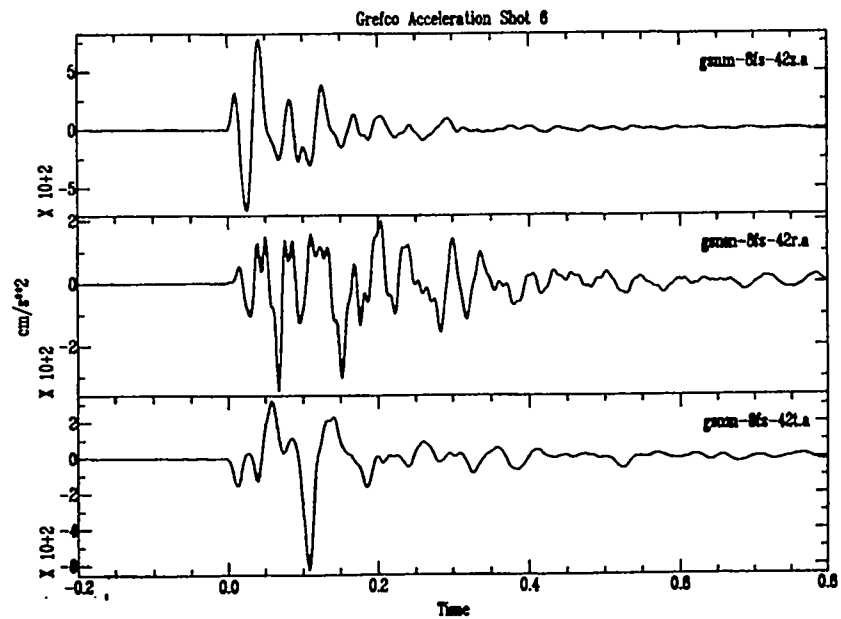
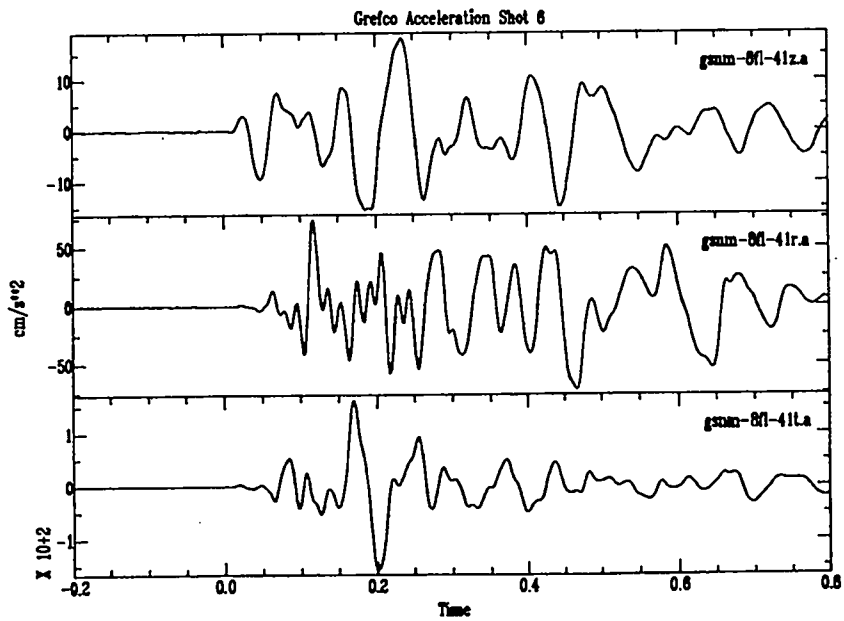
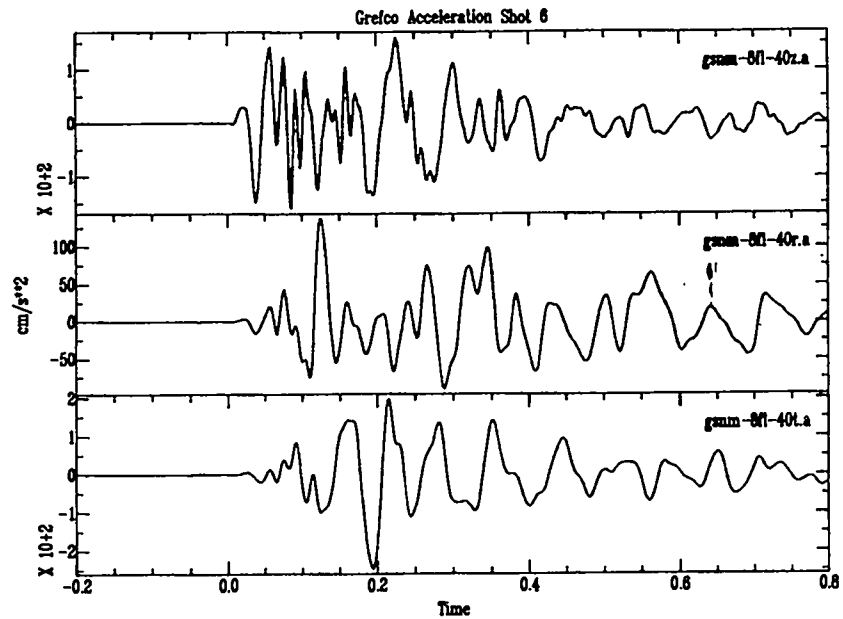
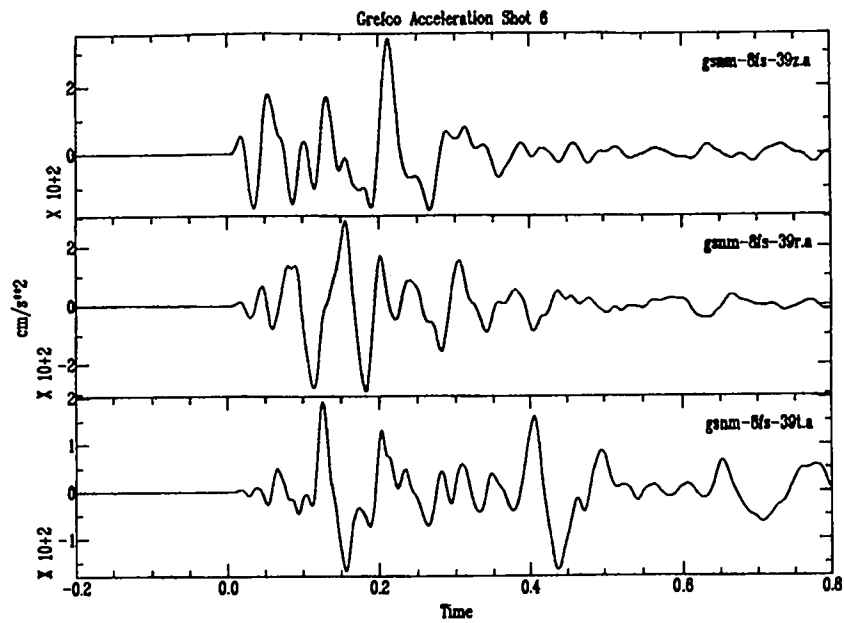


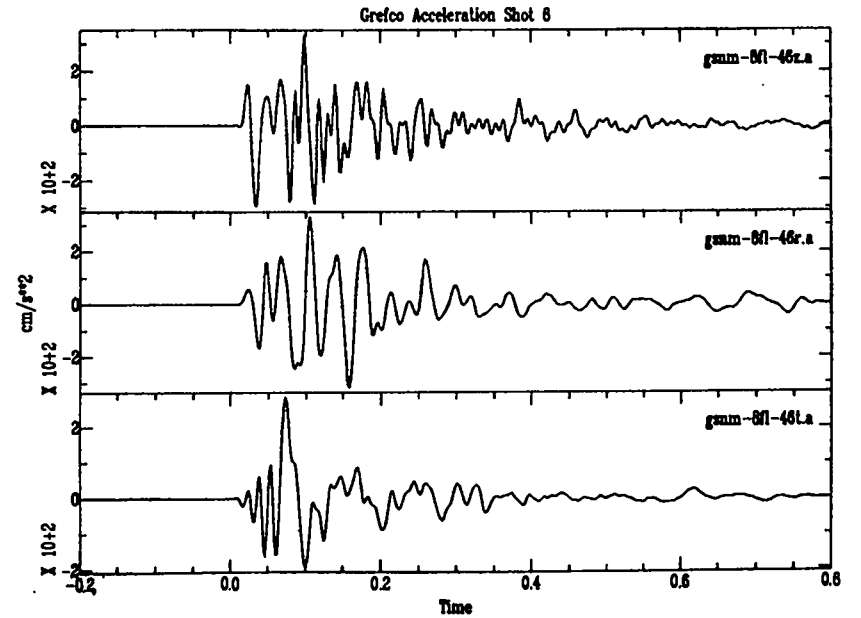
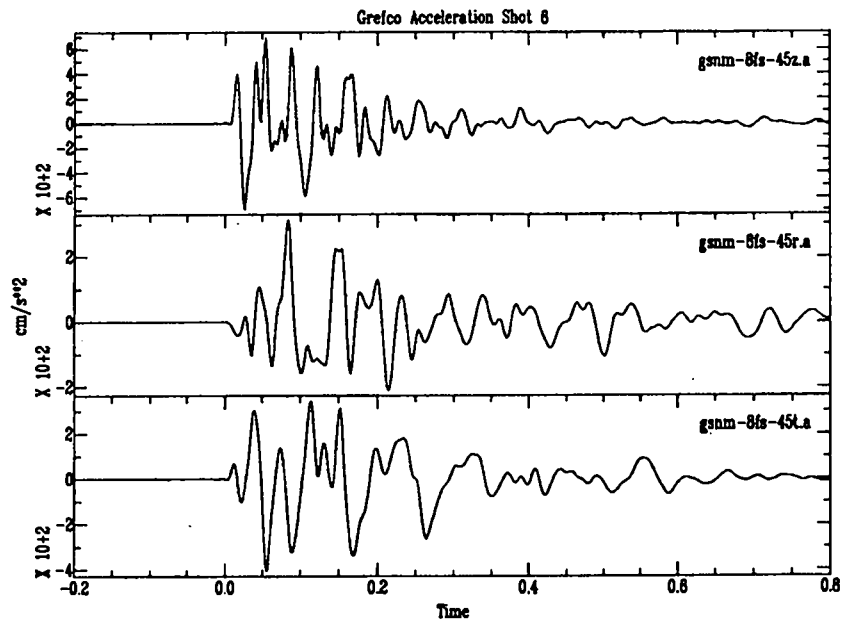
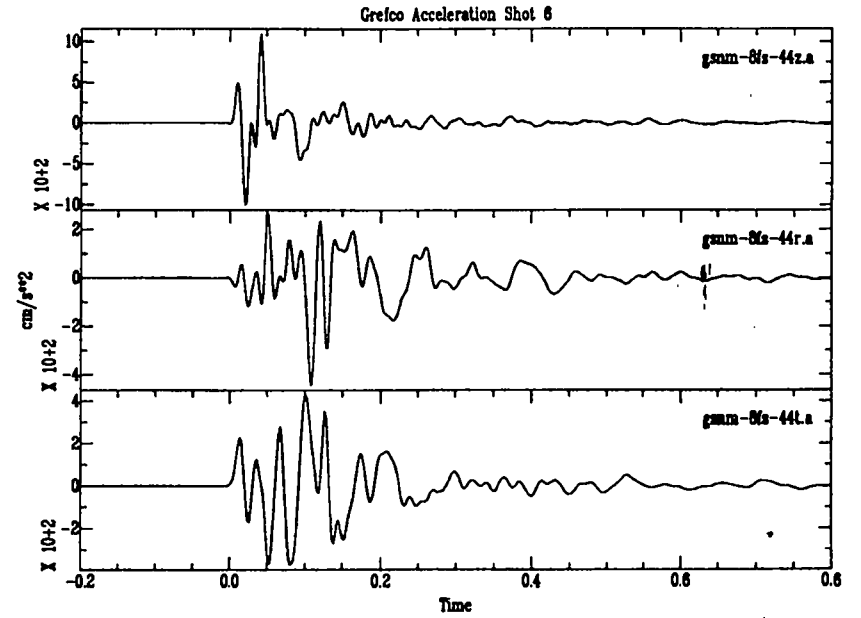
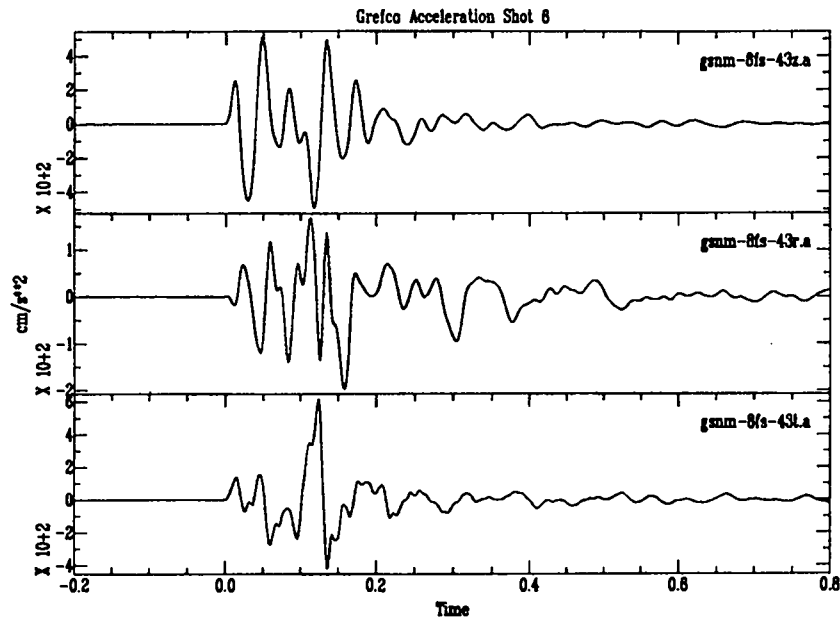
D-22

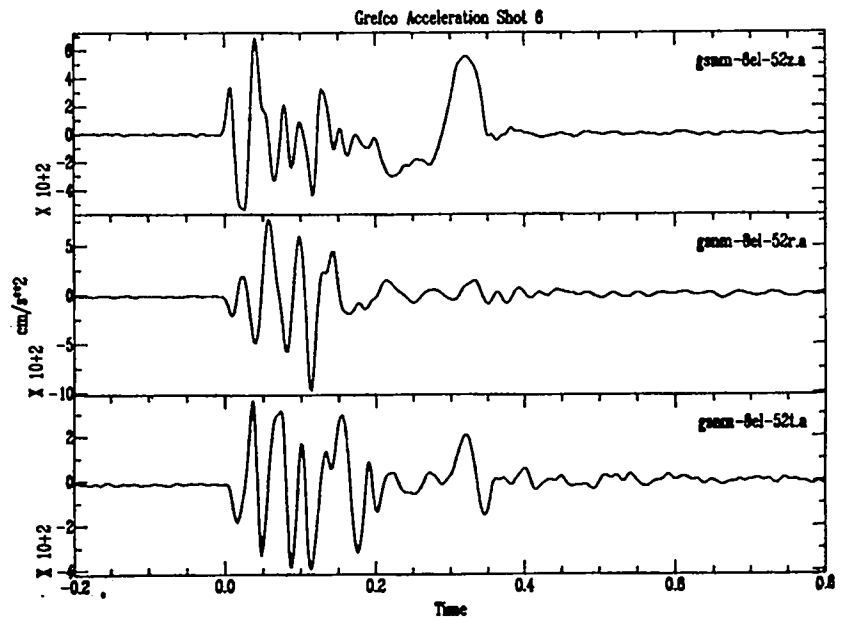
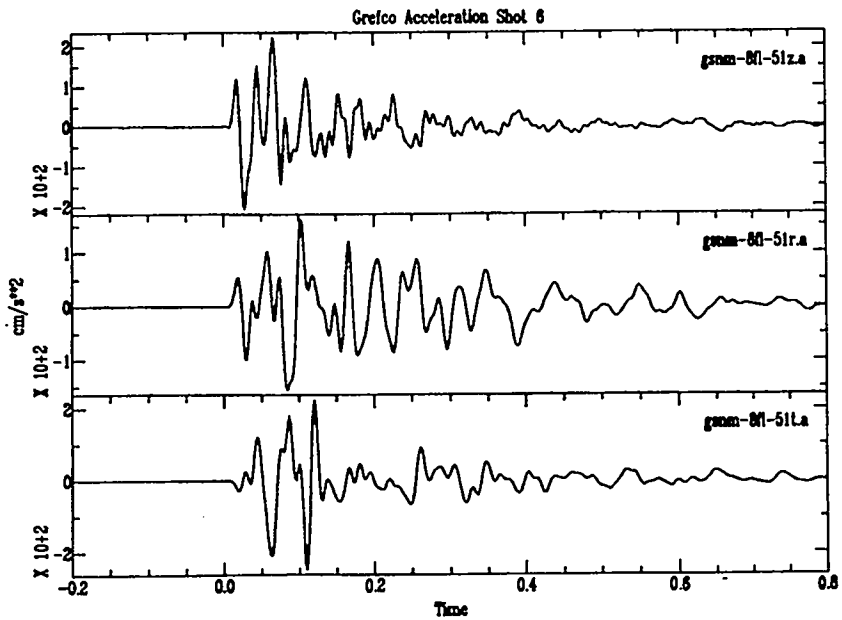
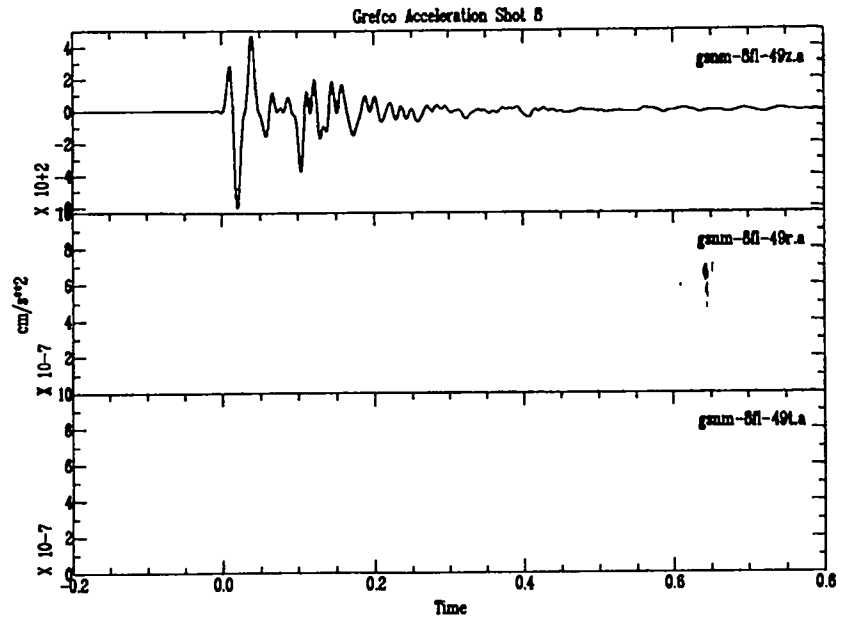
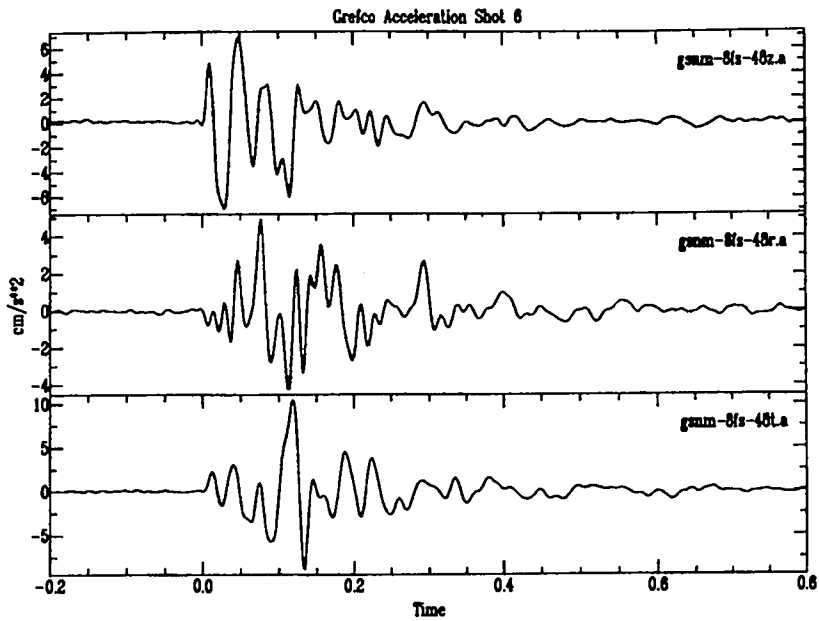




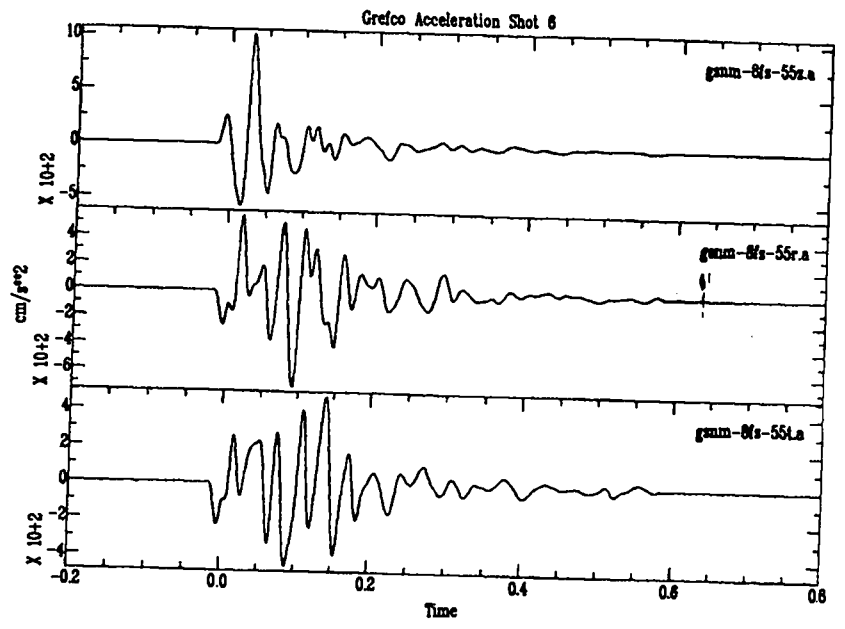
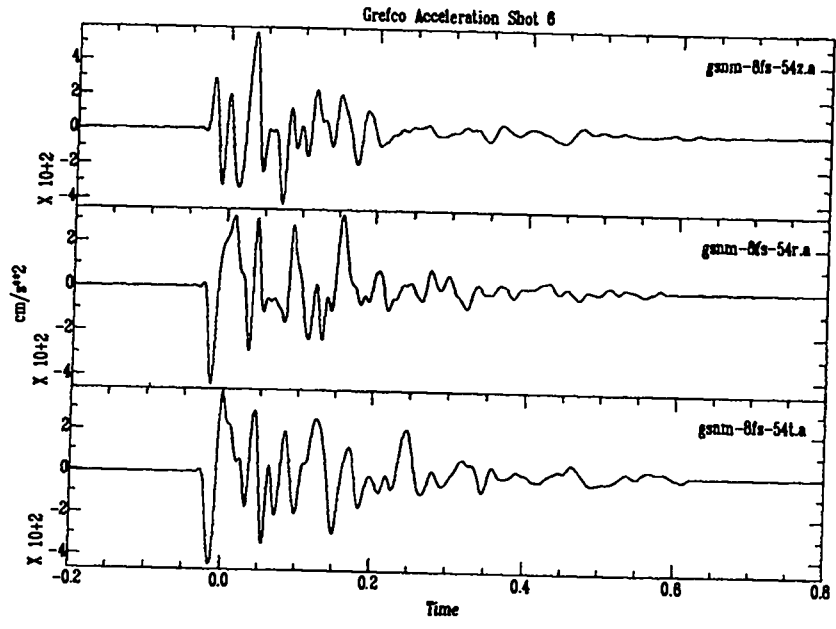






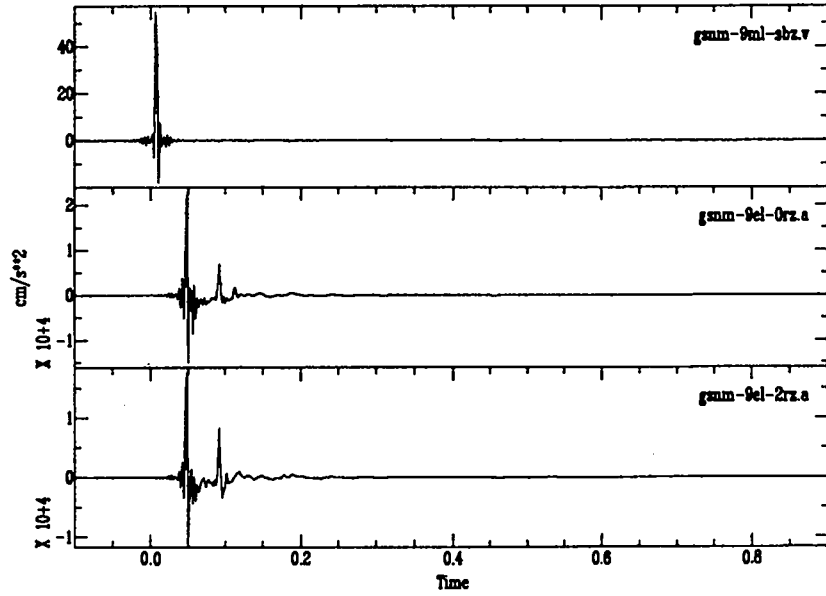


D-29

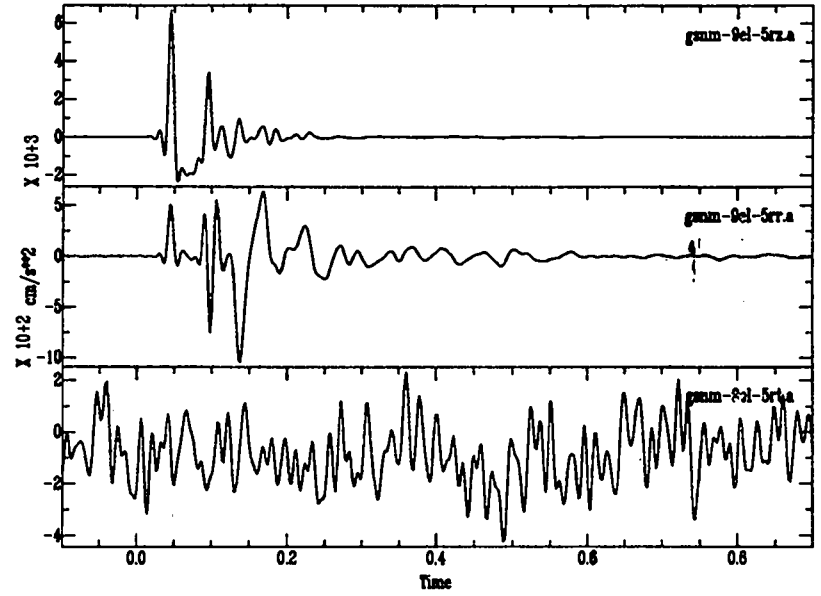


D-30

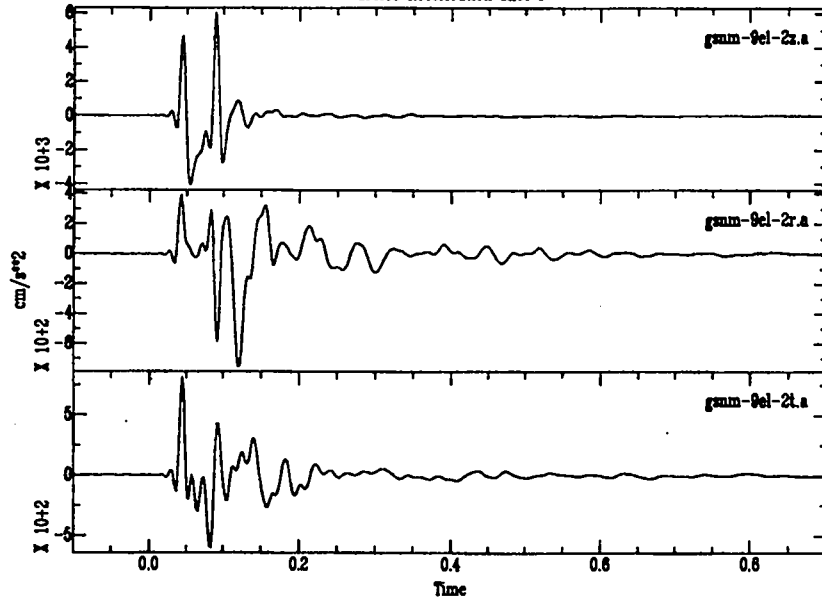
Grefco Acceleration Shot 9



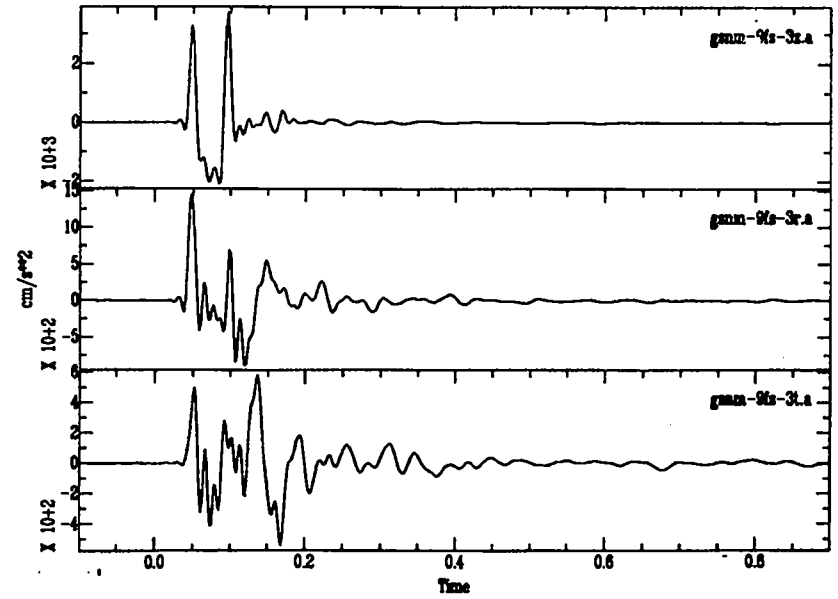
Grefco Acceleration Shot 9

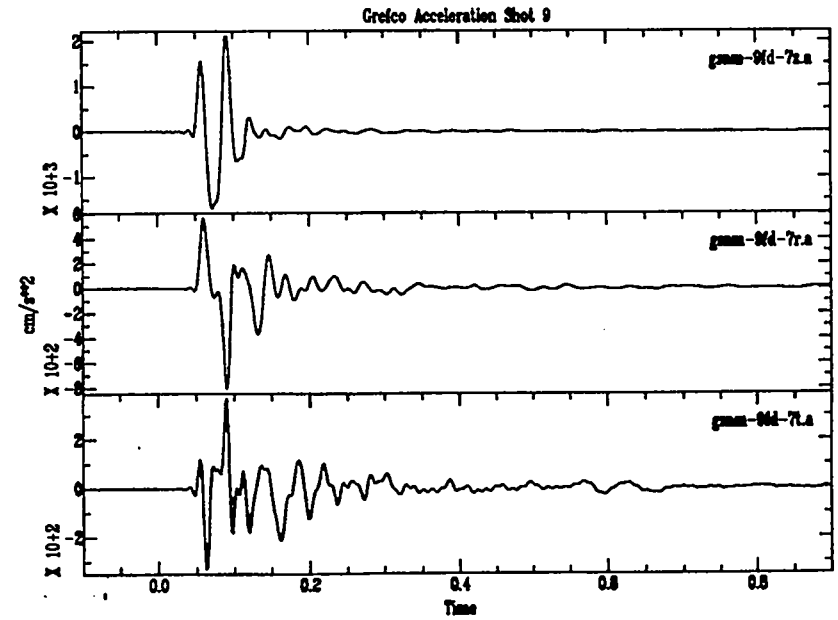
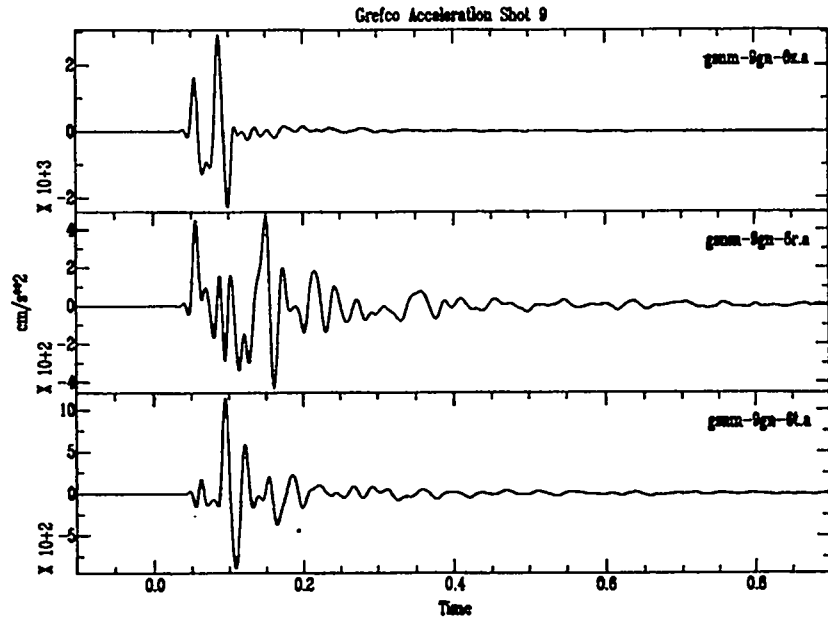
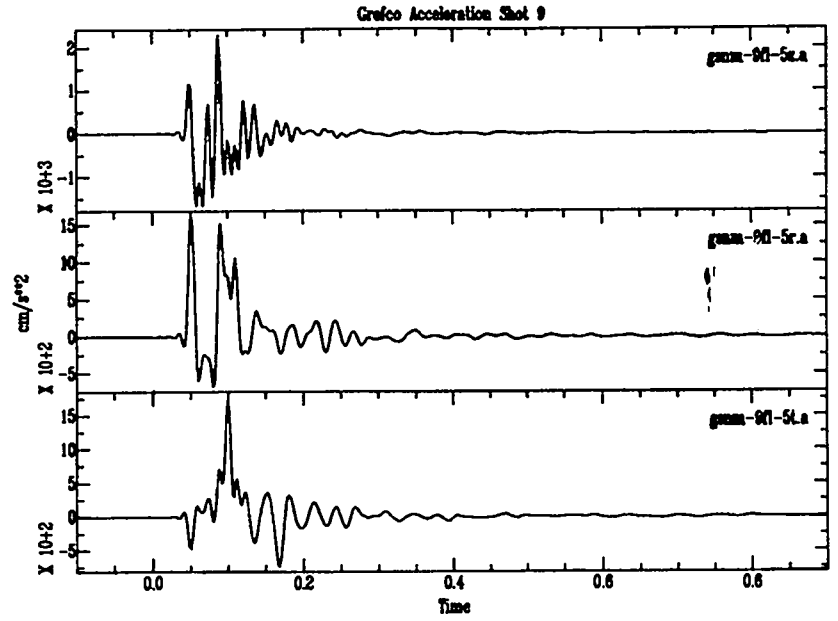
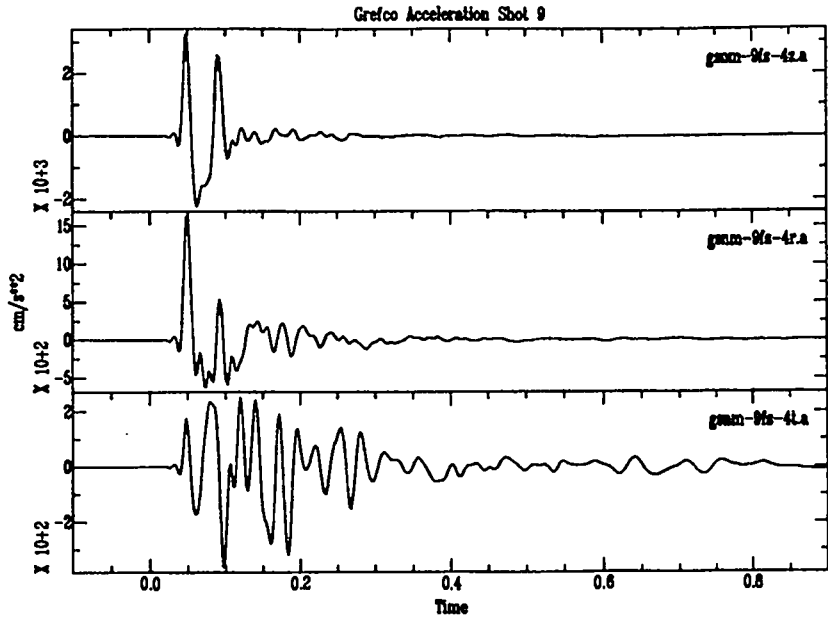


Grefco Acceleration Shot 9

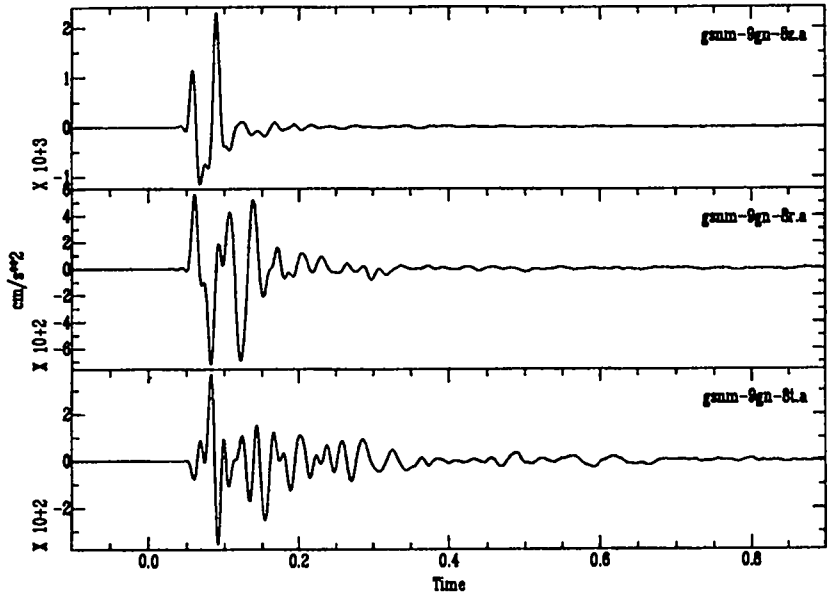


Grefco Acceleration Shot 9

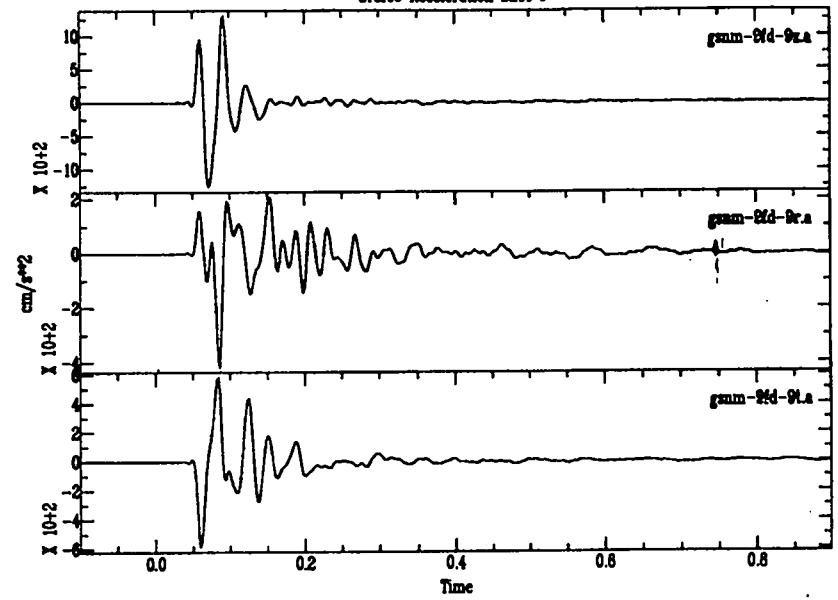




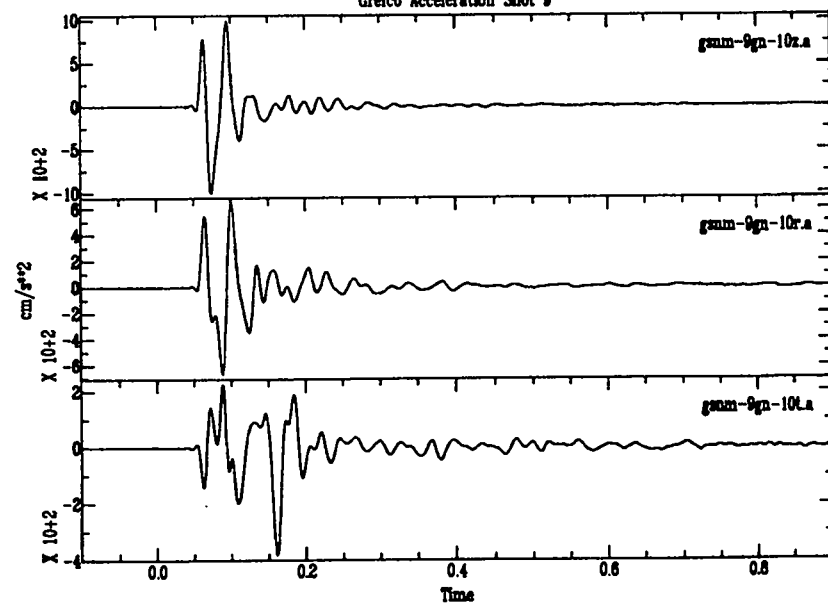
Grefco Acceleration Shot 9



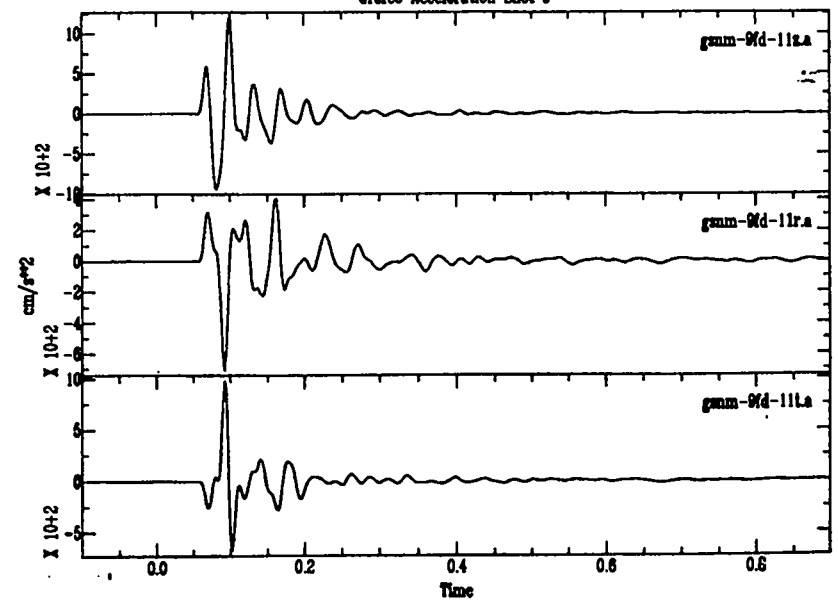
Grefco Acceleration Shot 9



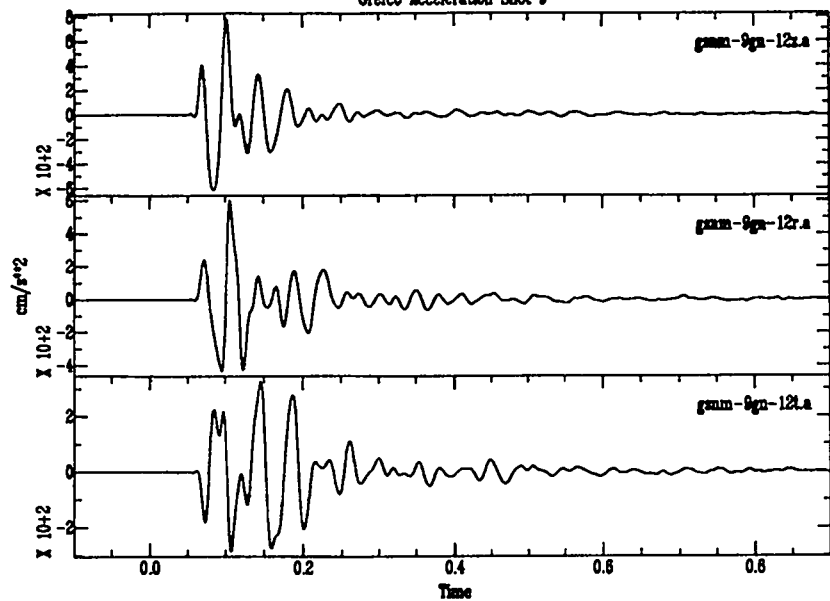
Grefco Acceleration Shot 9



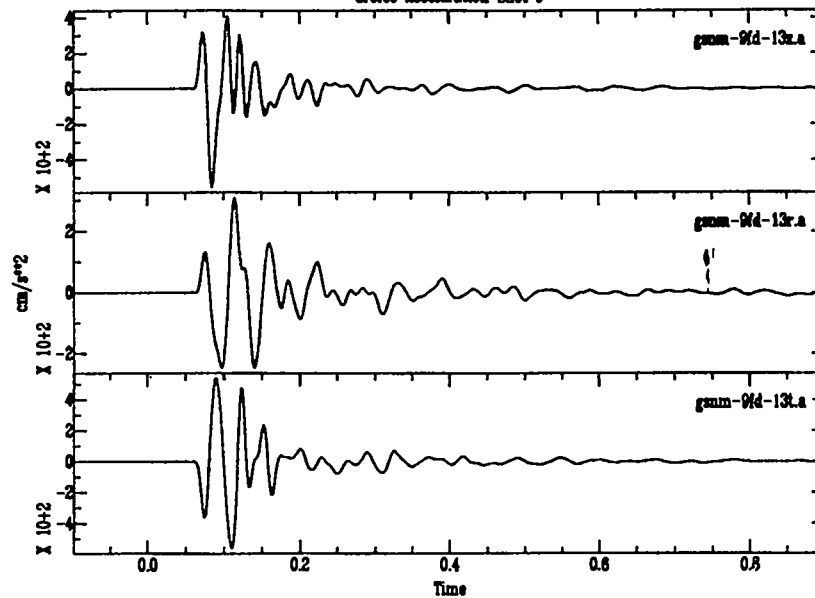
Grefco Acceleration Shot 9



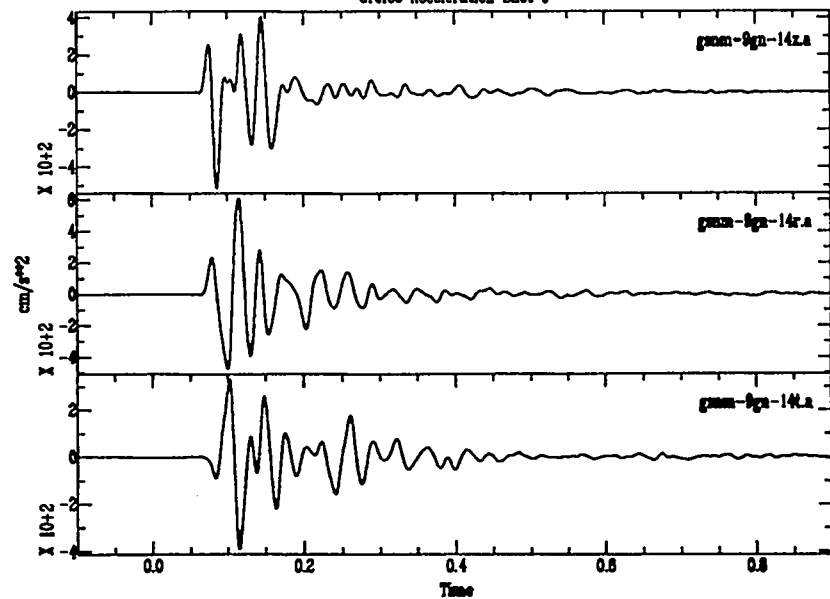
Grefco Acceleration Shot 9



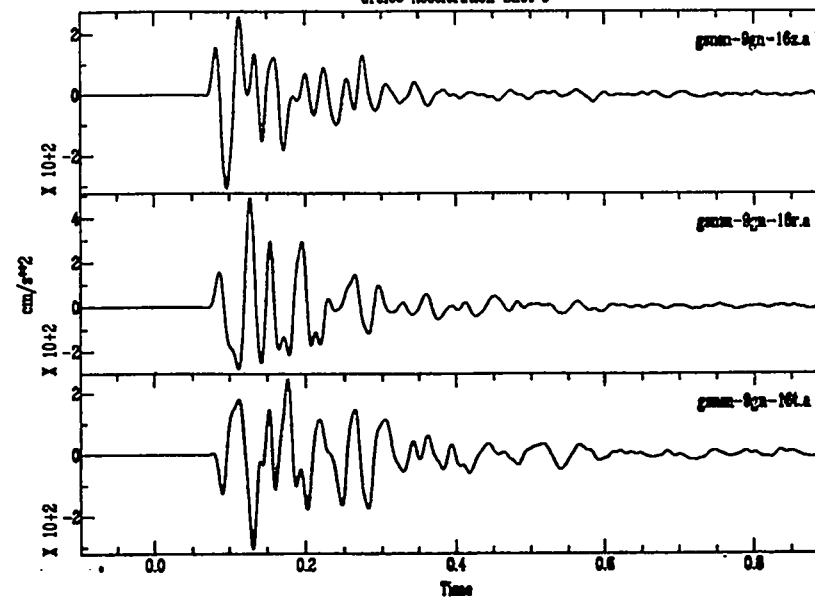
Grefco Acceleration Shot 9

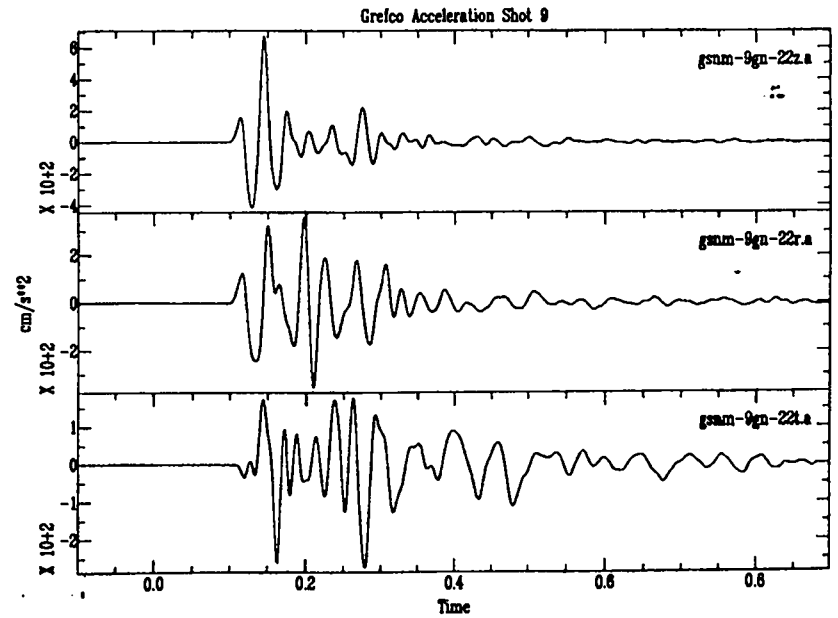
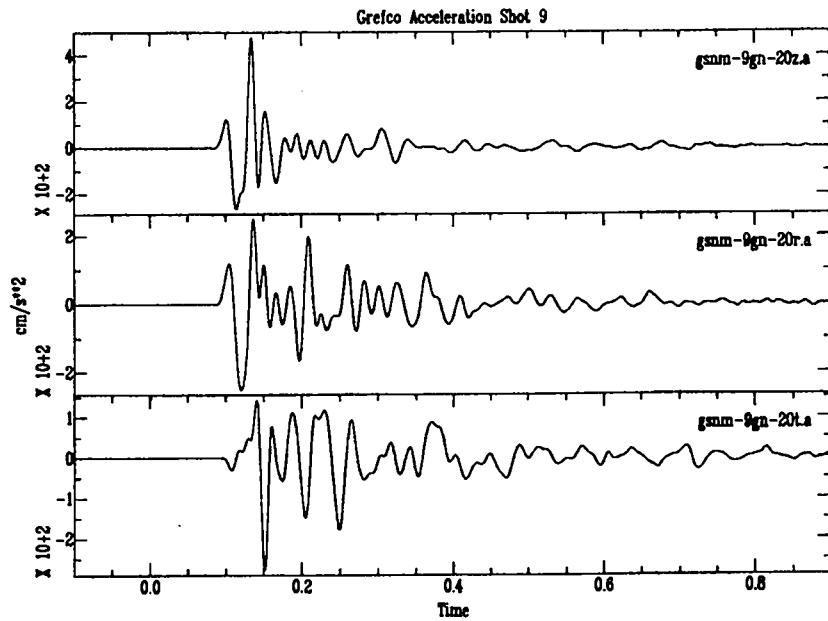
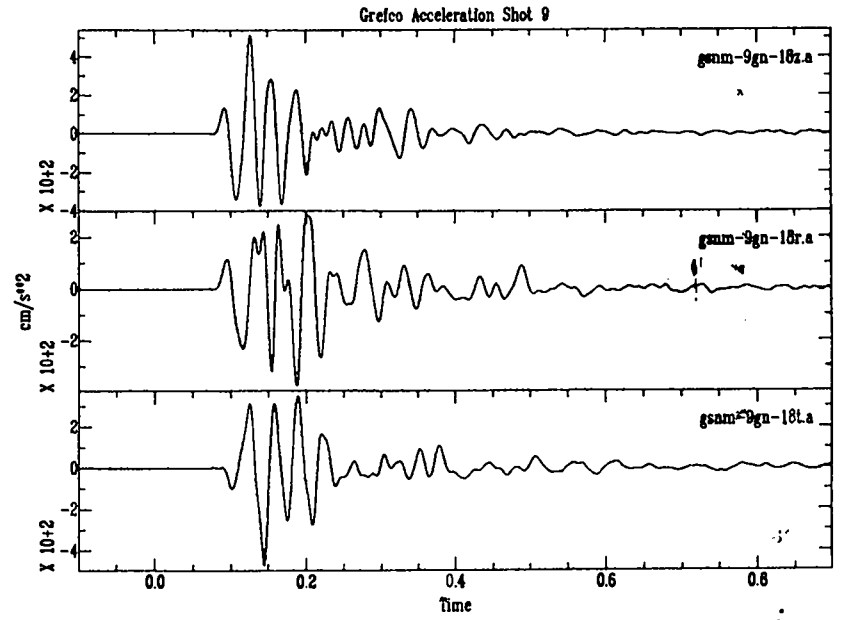
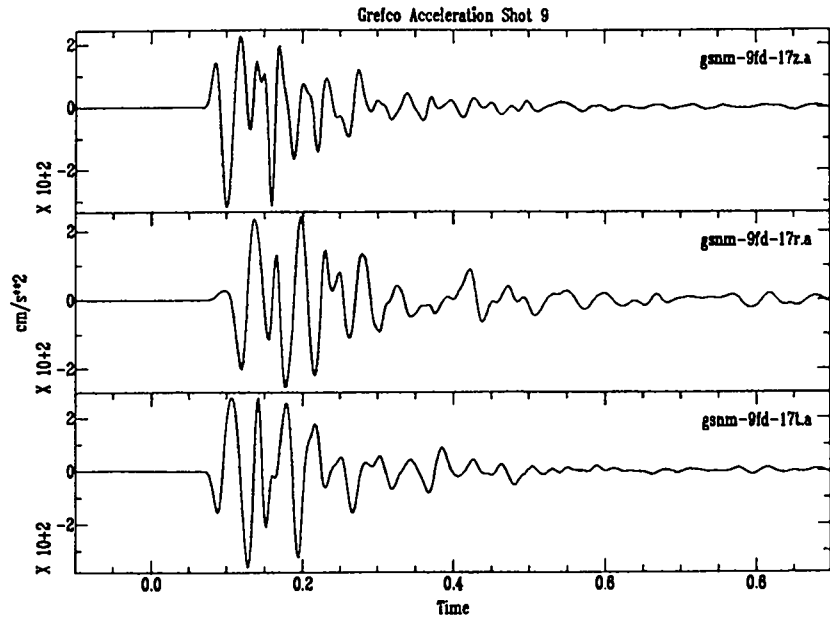


Grefco Acceleration Shot 9

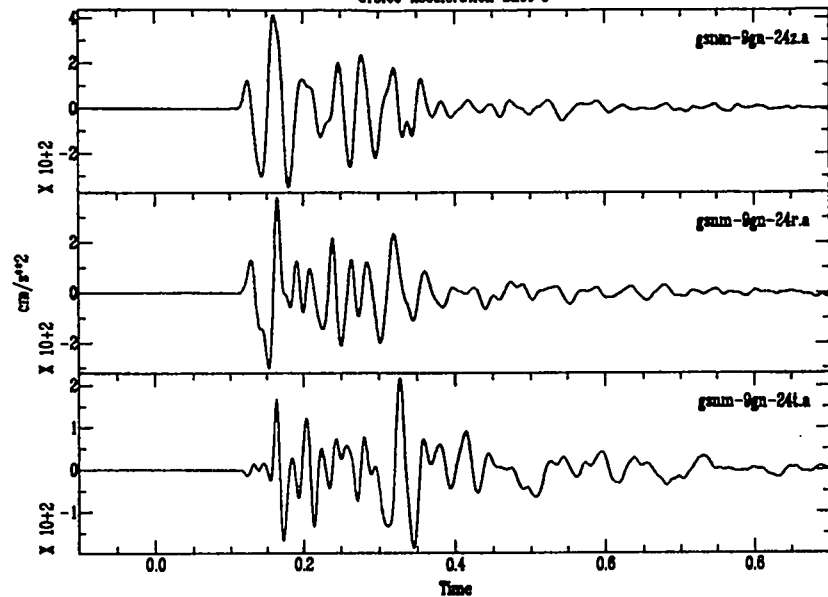


Grefco Acceleration Shot 9

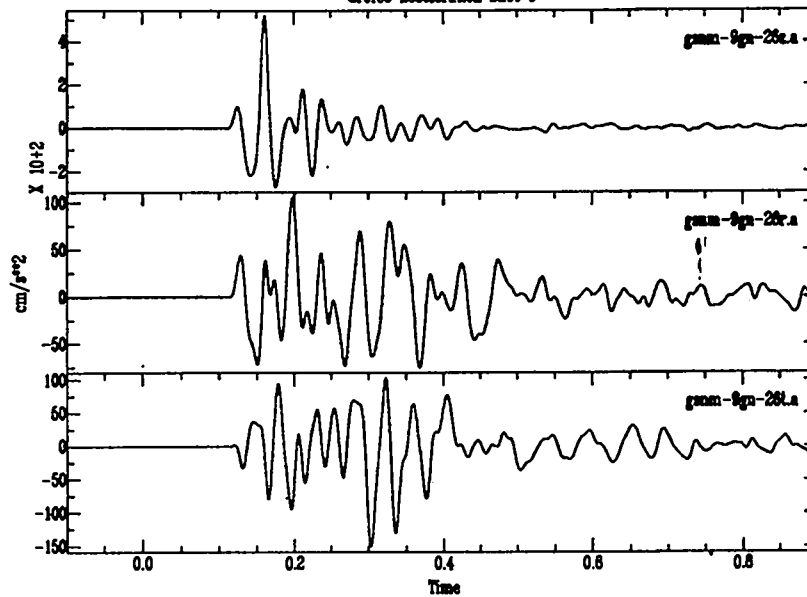




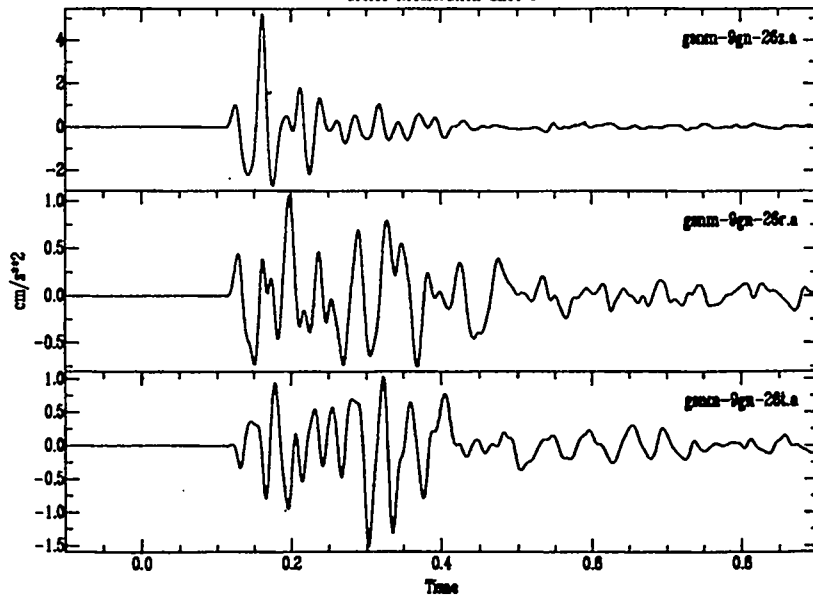
Grefco Acceleration Shot 9



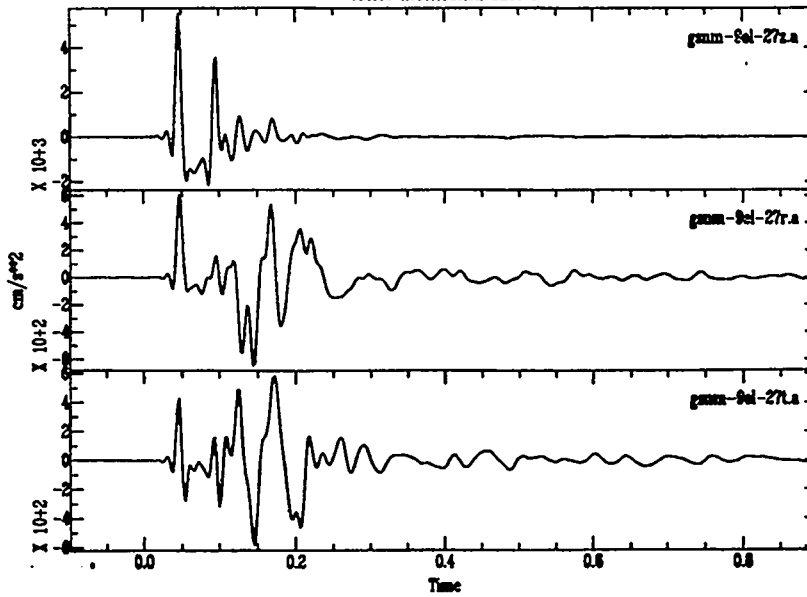
Grefco Acceleration Shot 9

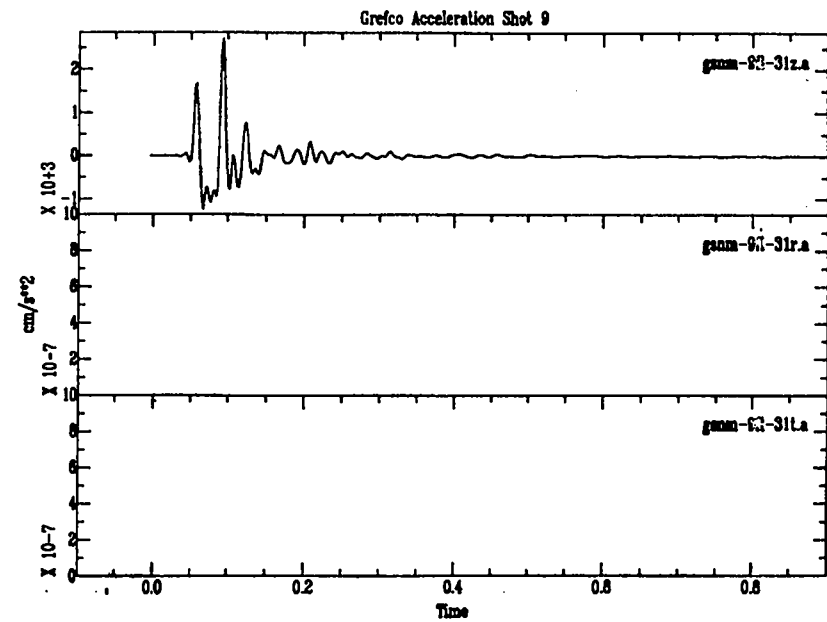
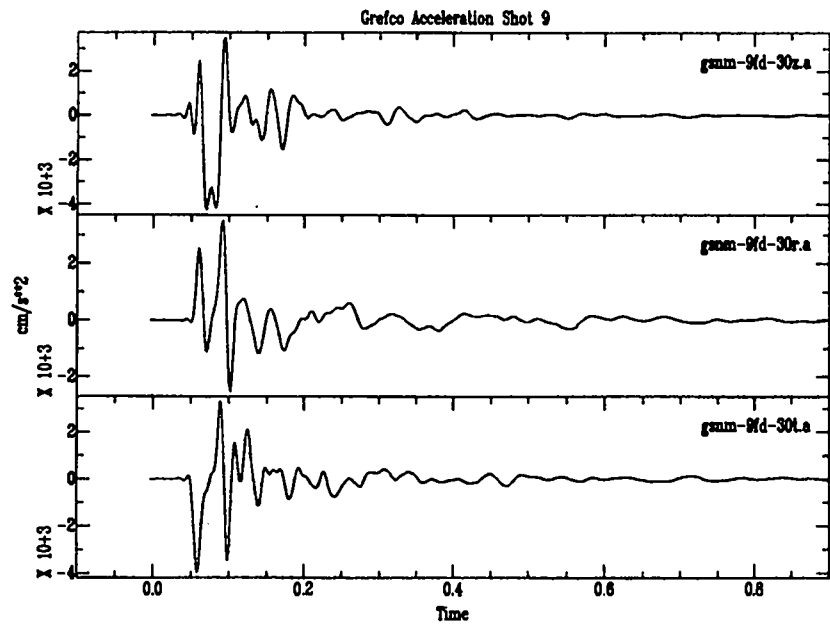
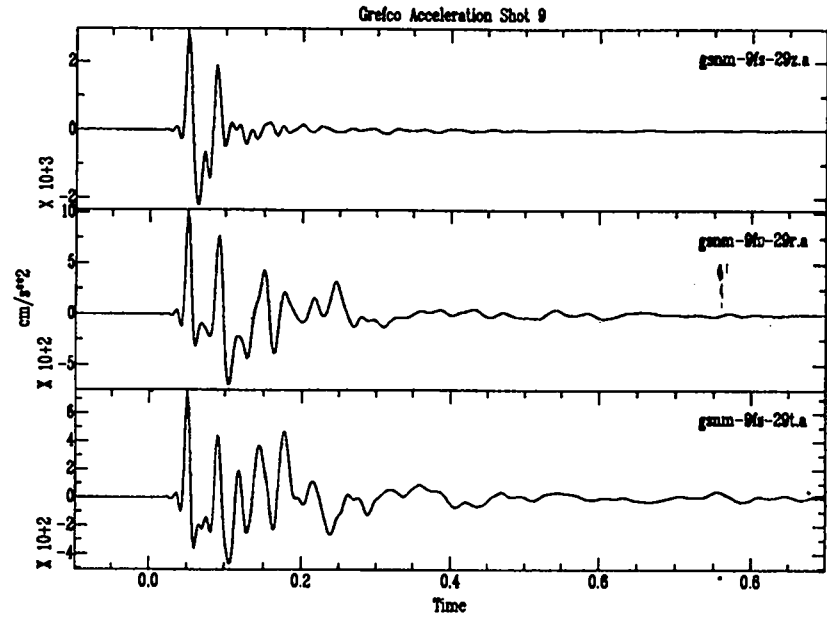
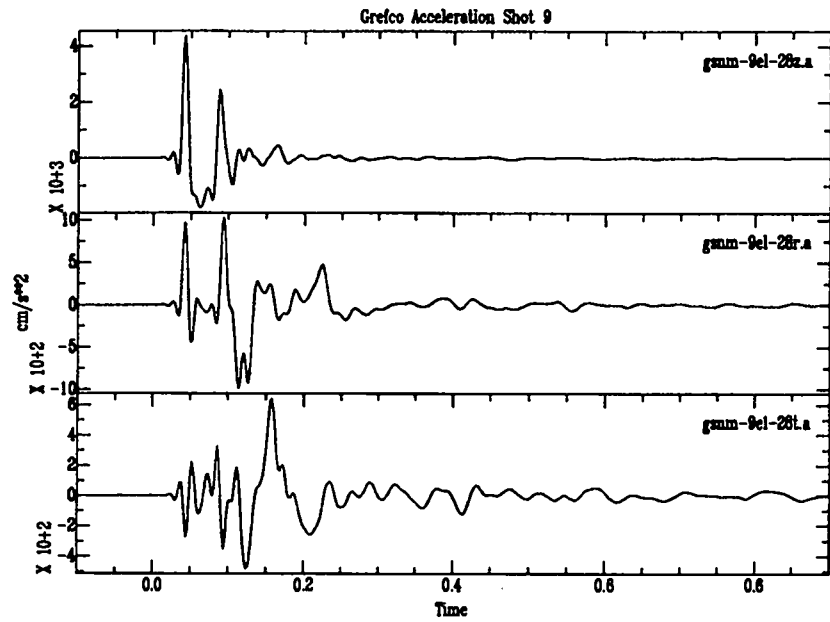


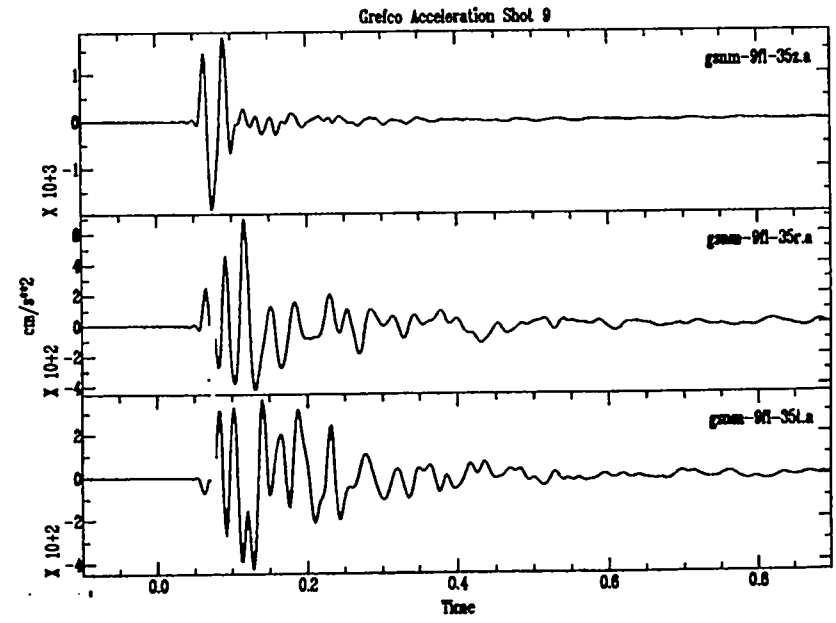
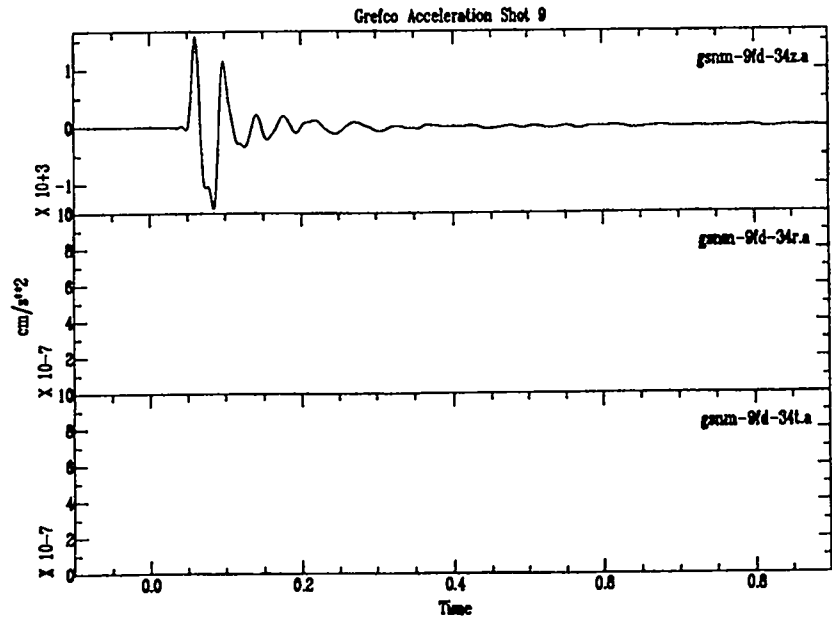
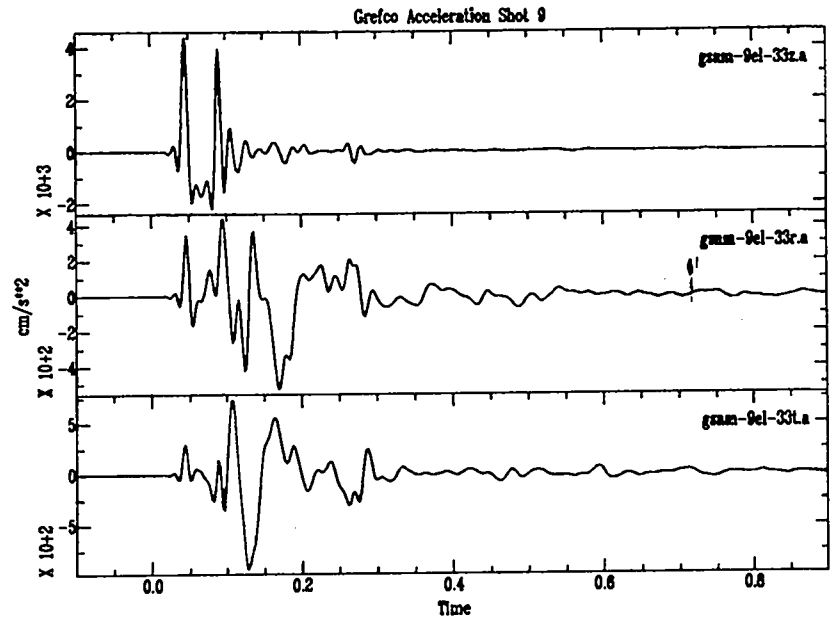
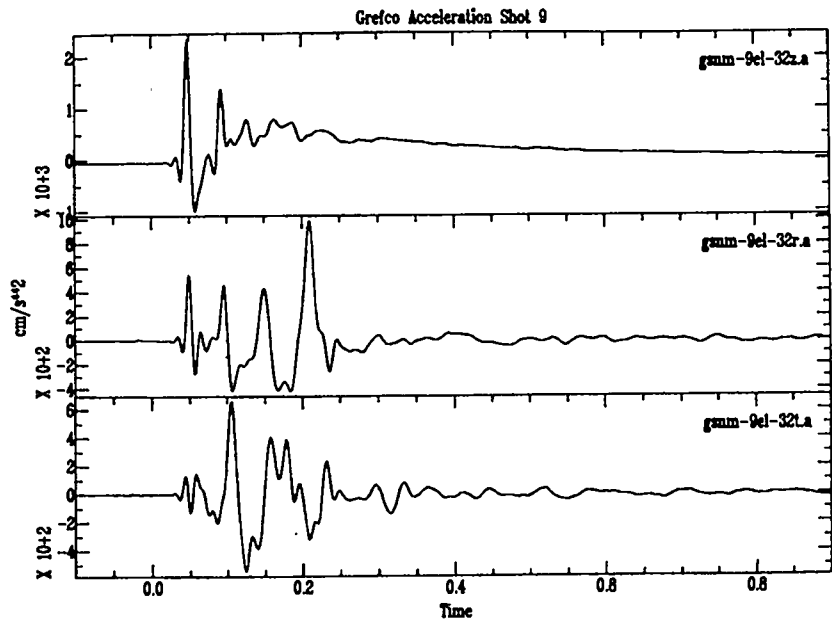
Grefco Acceleration Shot 9



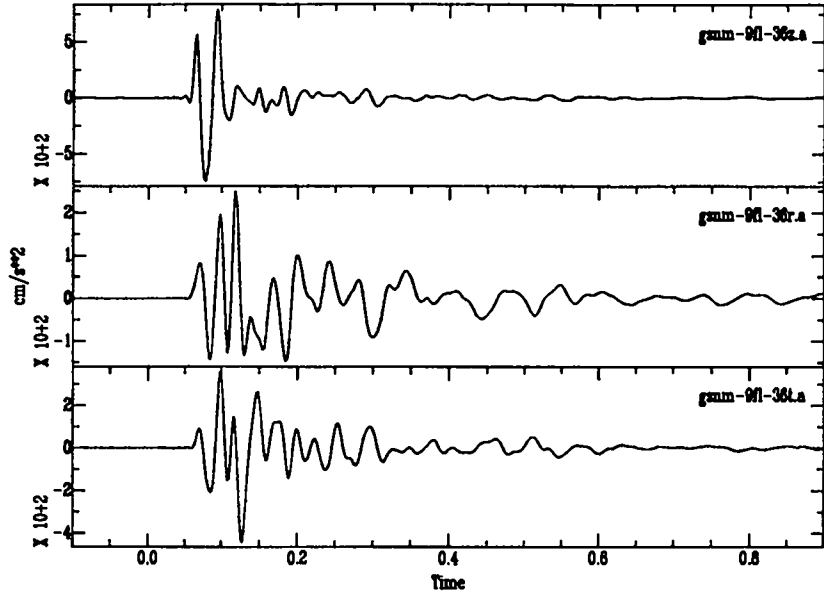
Grefco Acceleration Shot 9



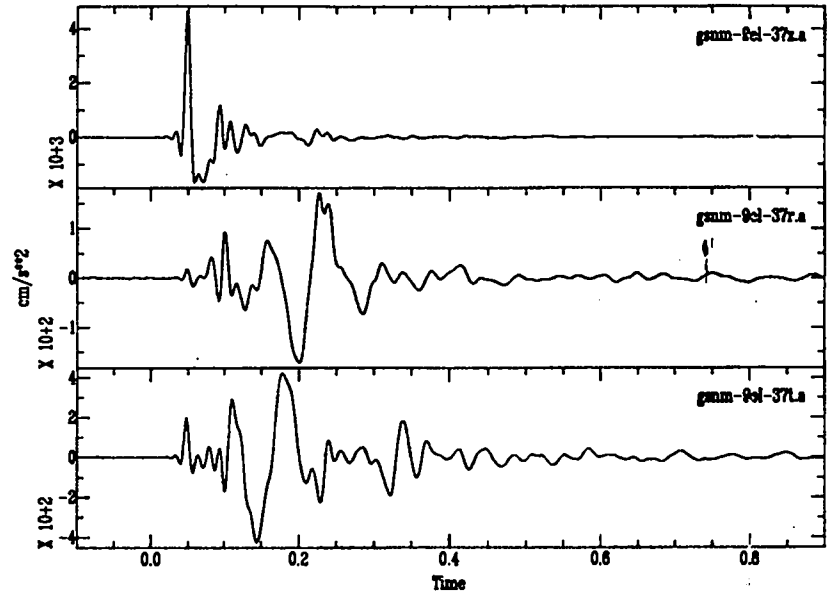




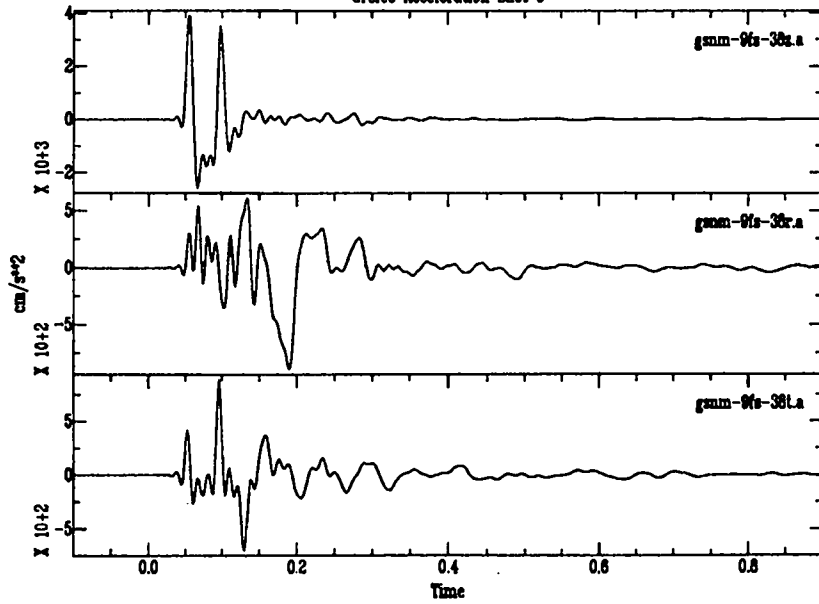
Grefco Acceleration Shot 9



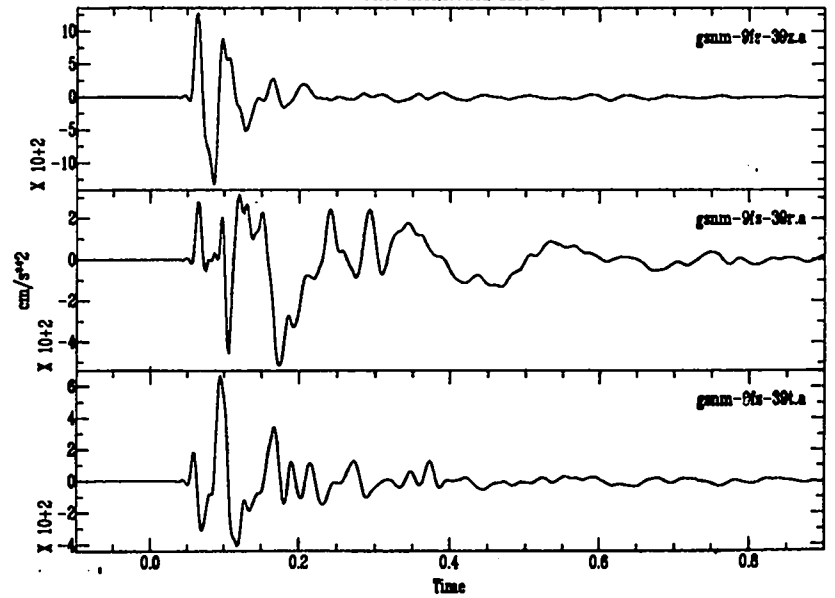
Grefco Acceleration Shot 9



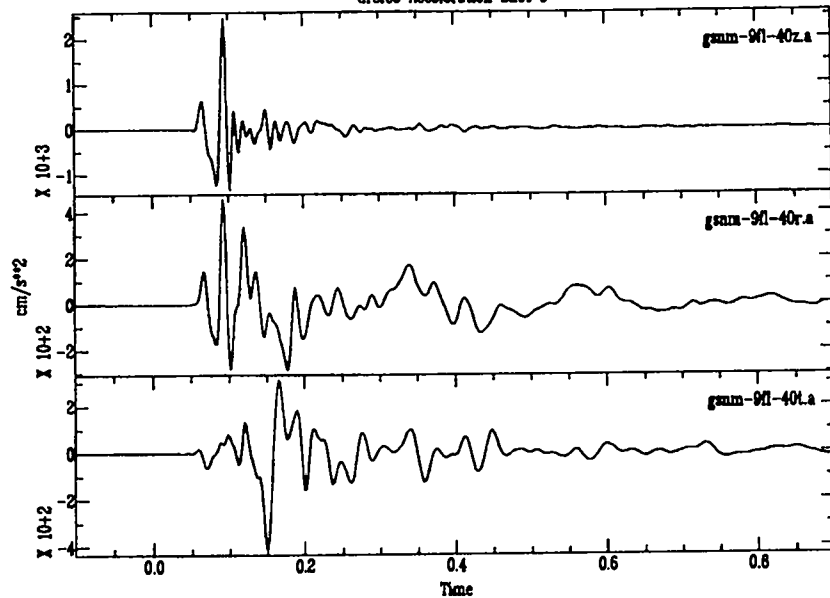
Grefco Acceleration Shot 9



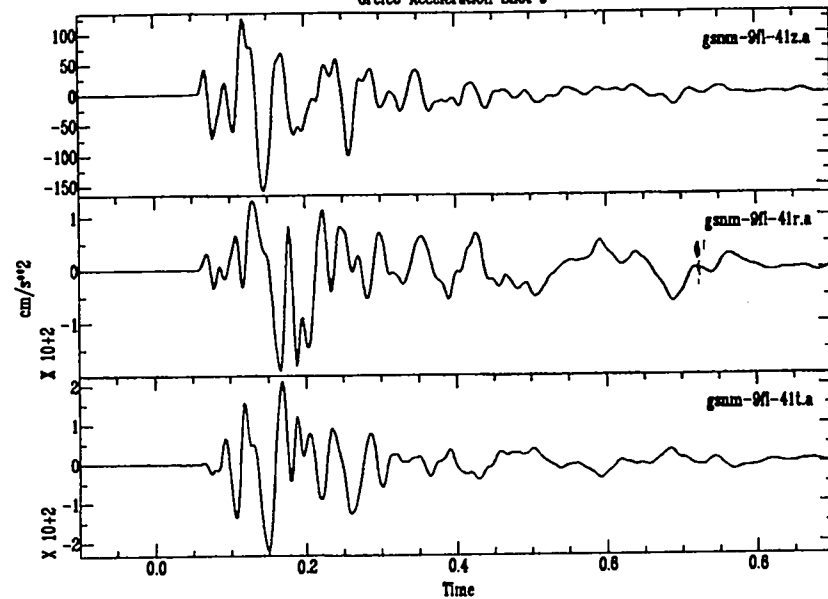
Grefco Acceleration Shot 9



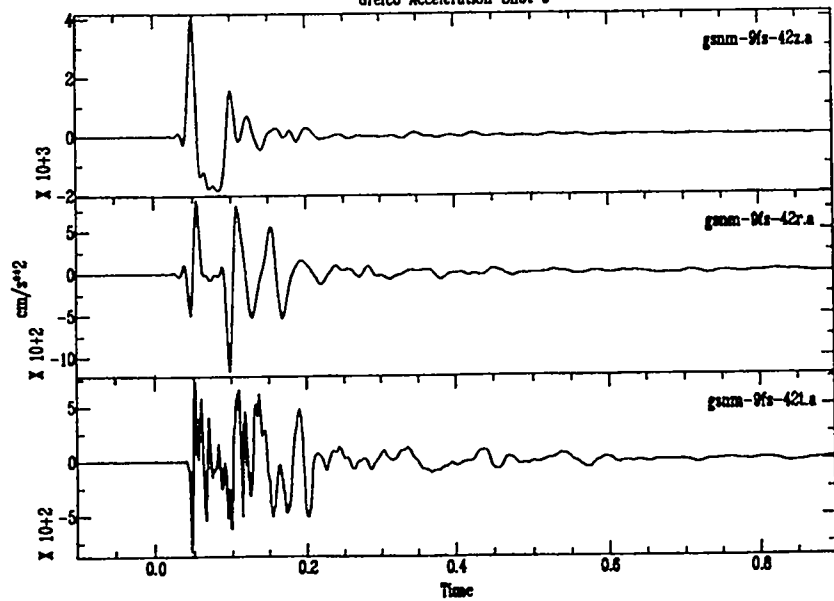
Grefco Acceleration Shot 9



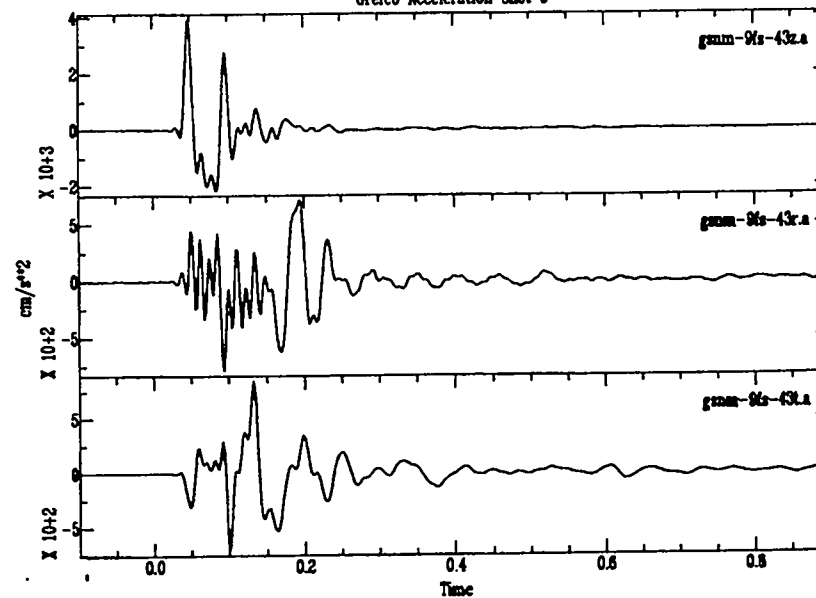
Grefco Acceleration Shot 9



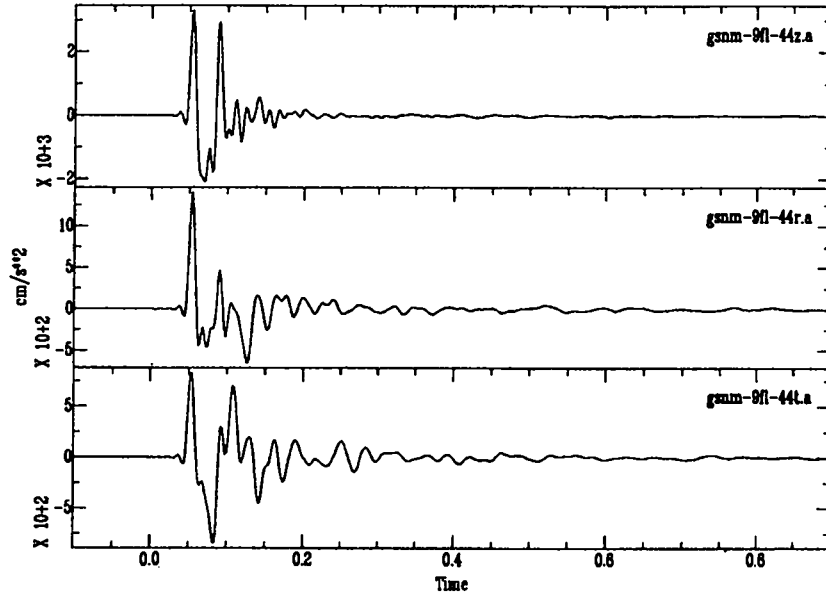
Grefco Acceleration Shot 9



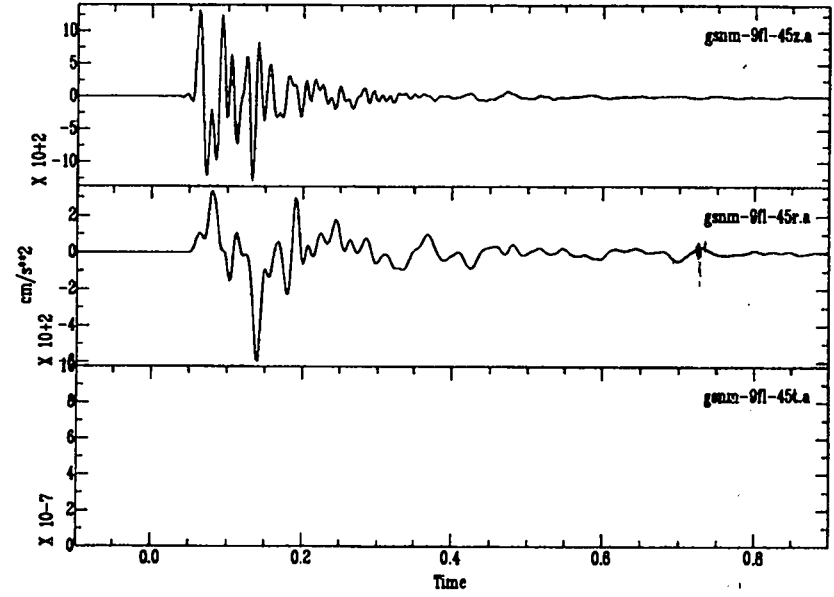
Grefco Acceleration Shot 9



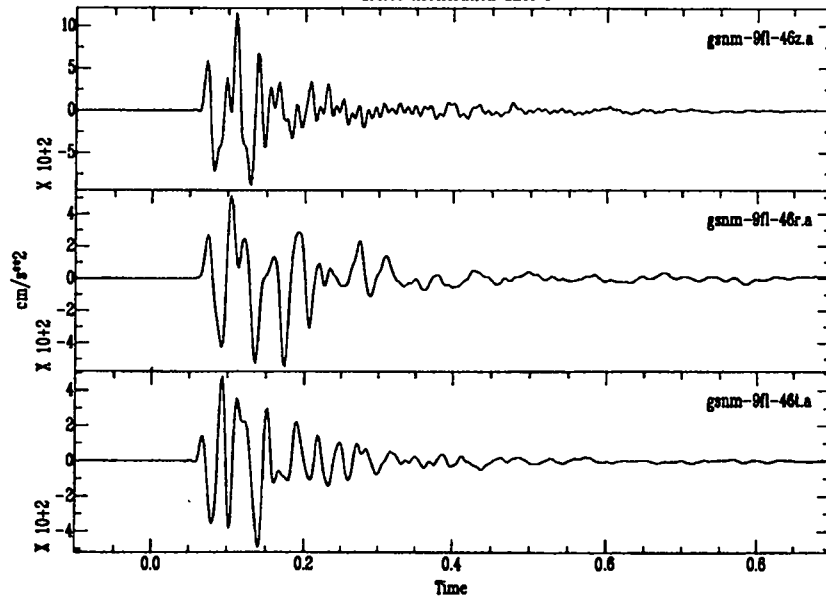
Grefco Acceleration Shot 9



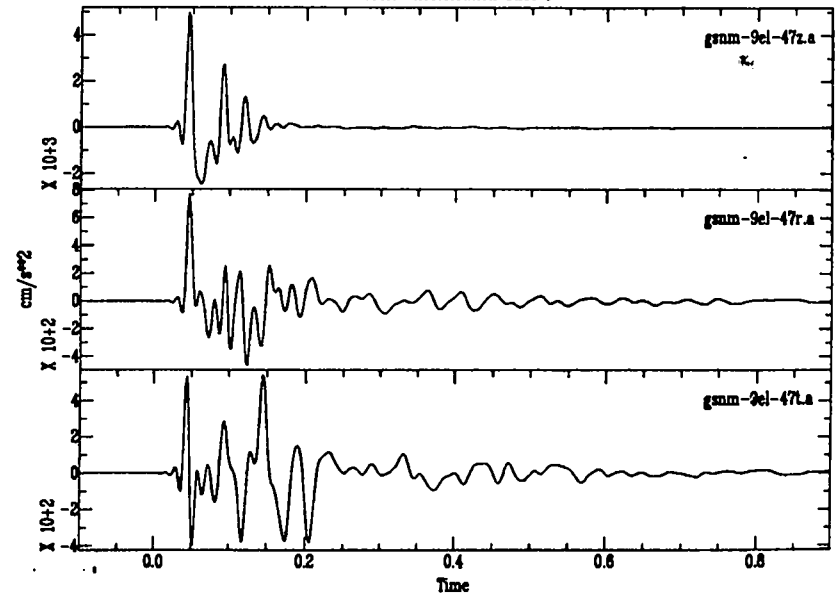
Grefco Acceleration Shot 9

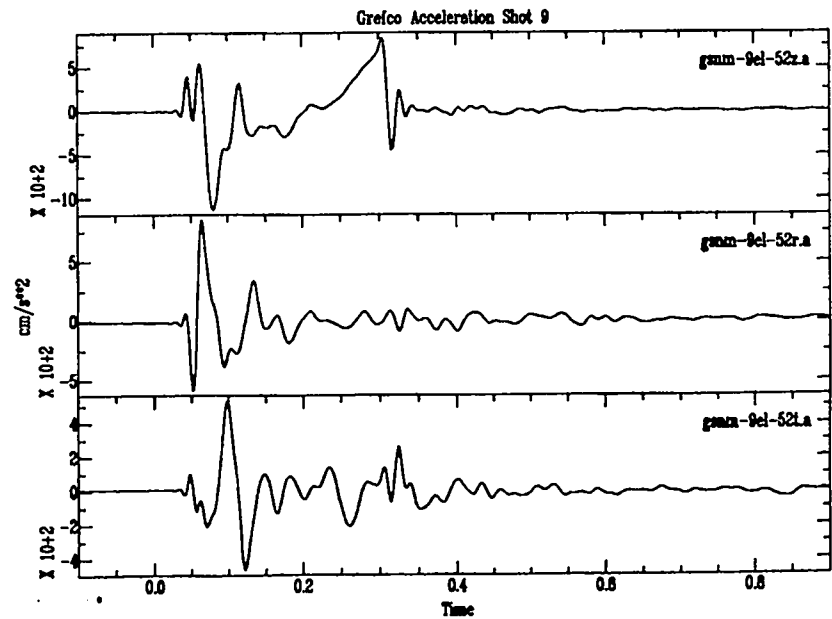
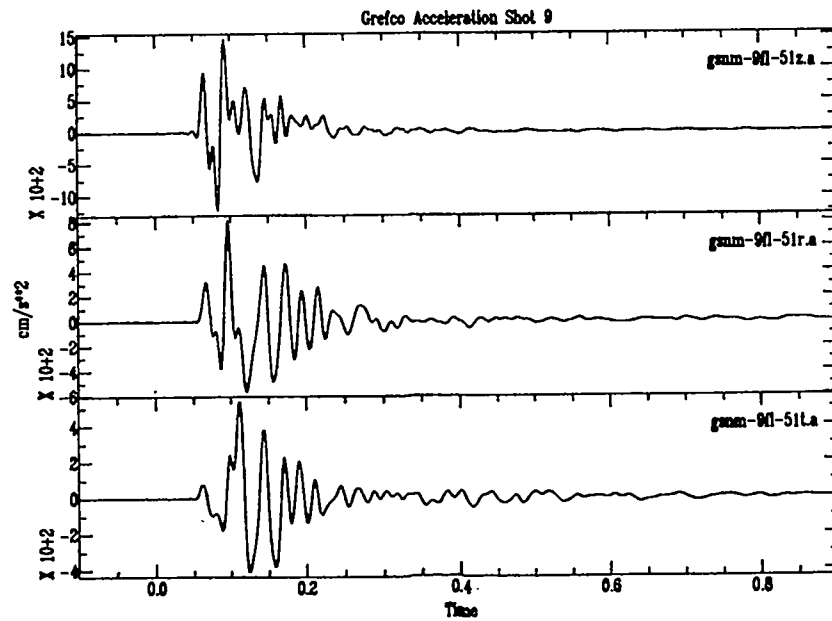
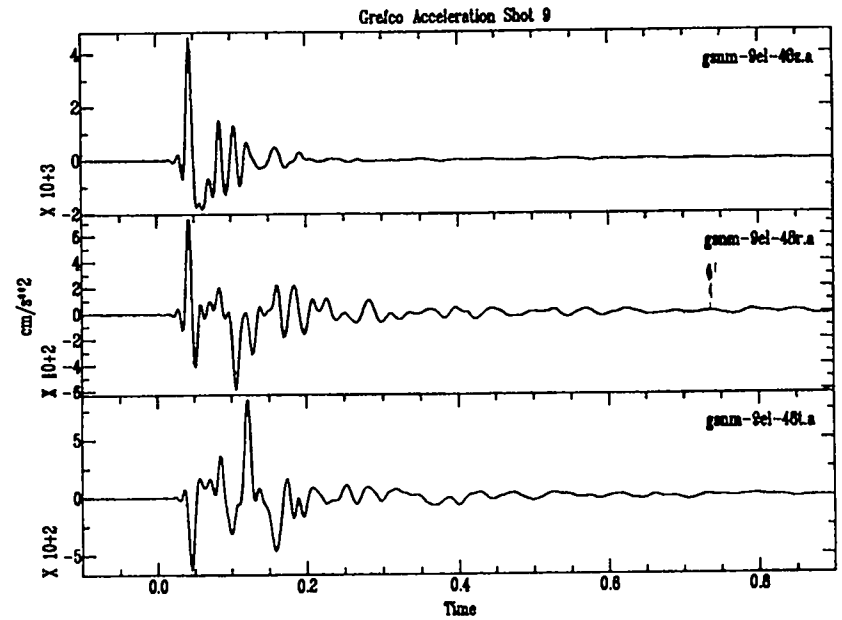
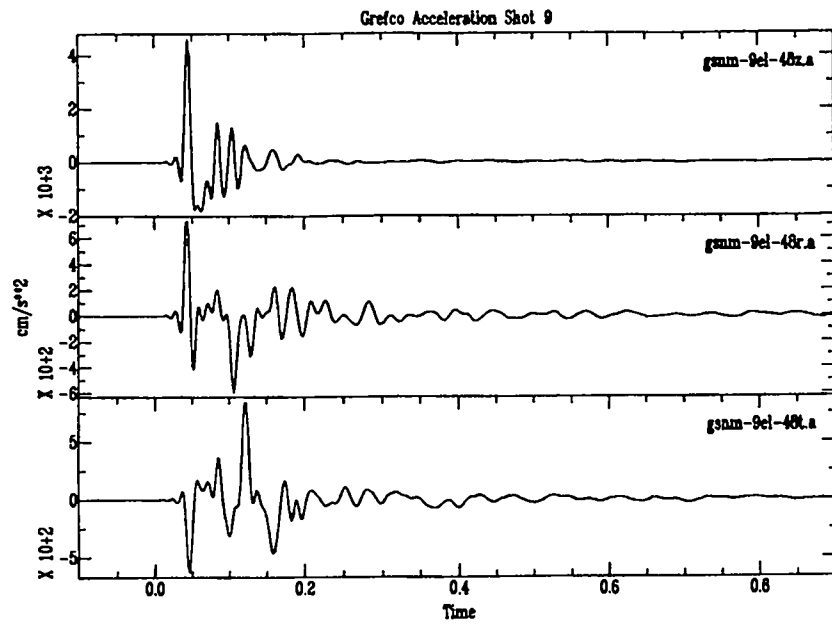


Grefco Acceleration Shot 9

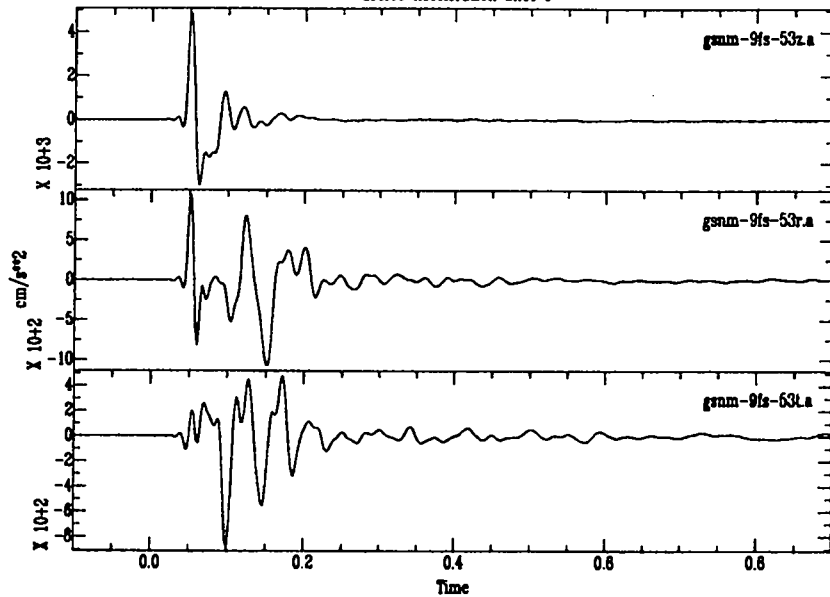


Grefco Acceleration Shot 9

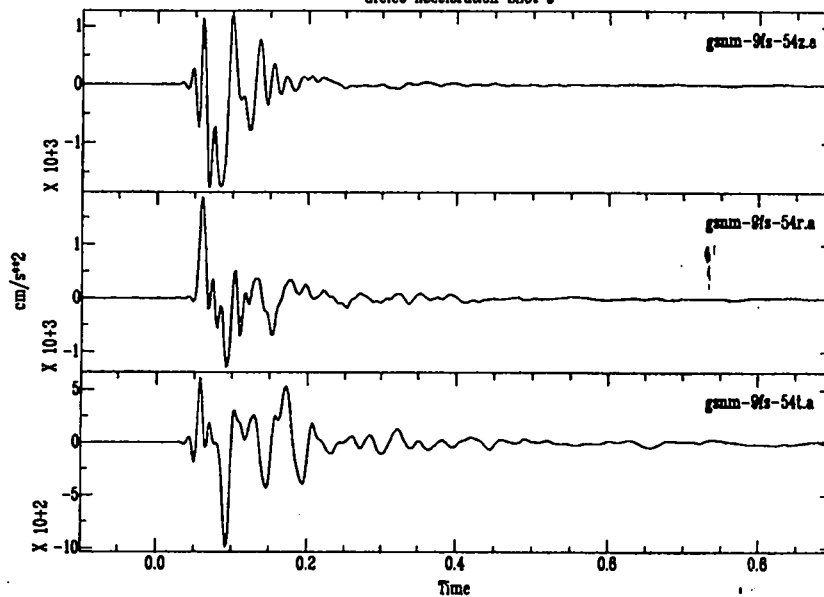




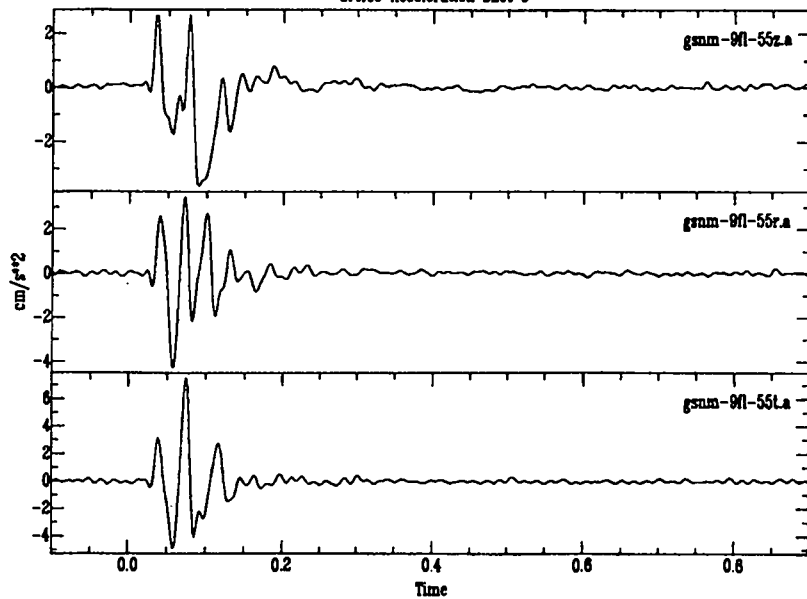
Grefco Acceleration Shot 9



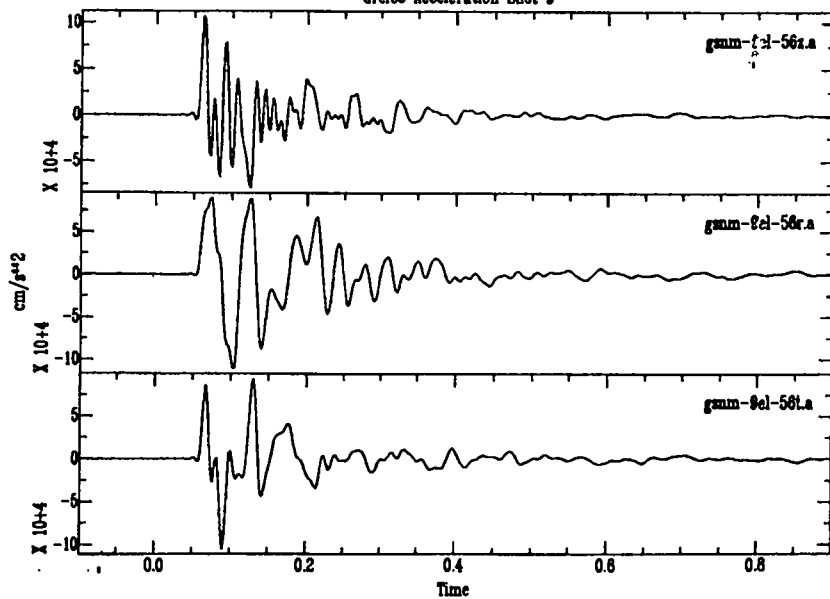
Grefco Acceleration Shot 9



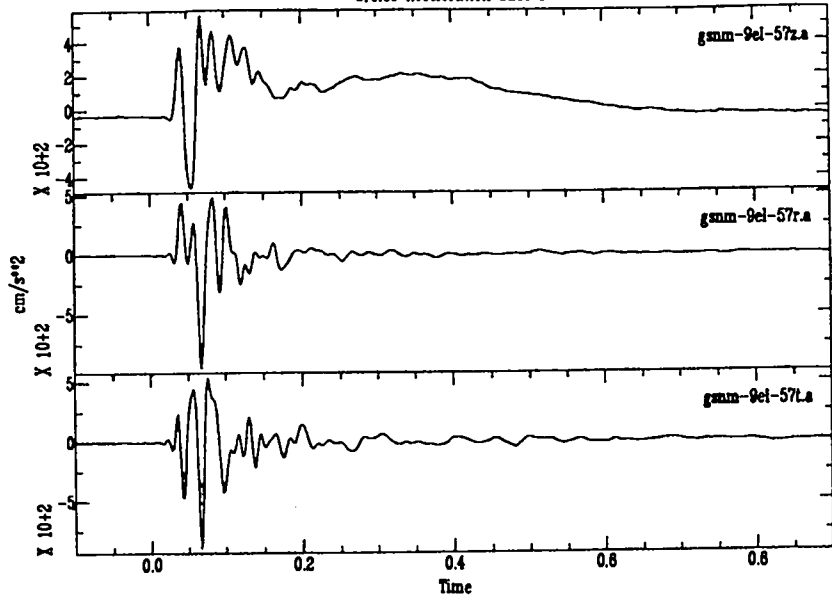
Grefco Acceleration Shot 9



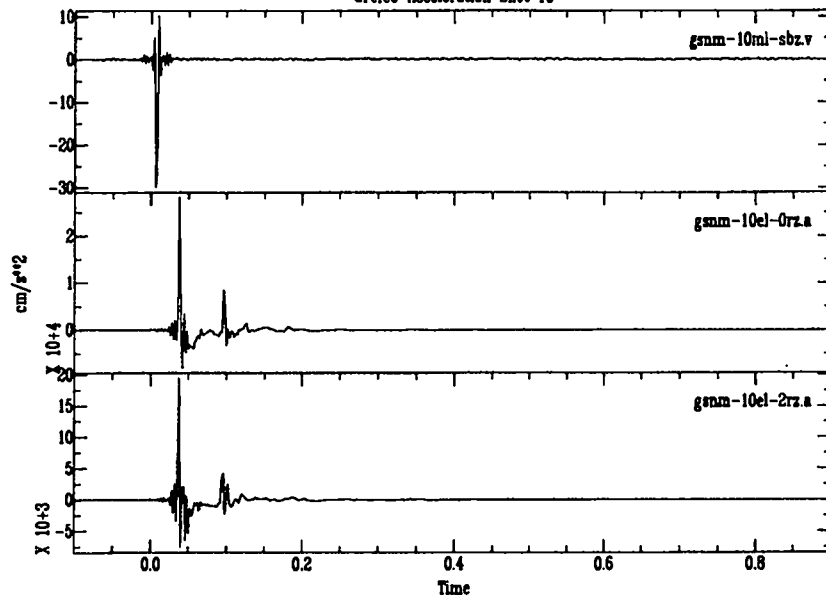
Grefco Acceleration Shot 9



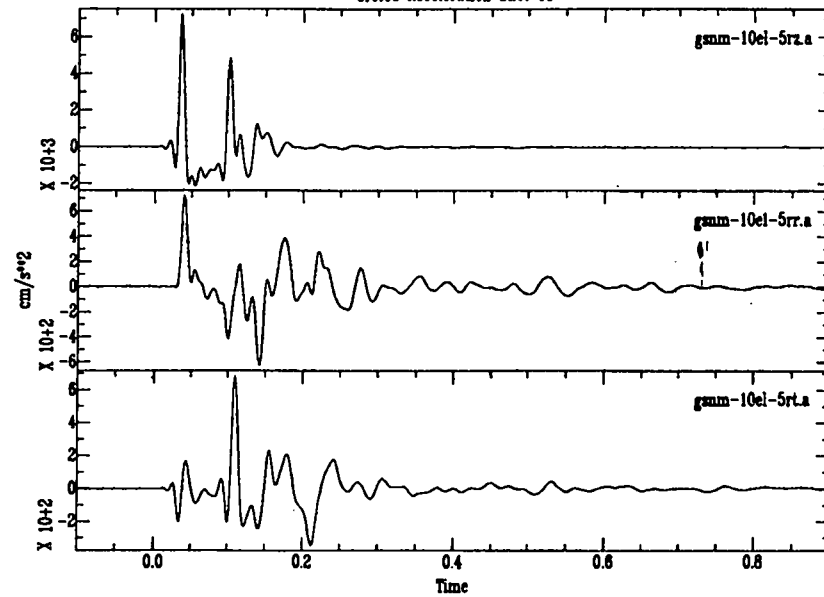
Grefco Acceleration Shot 9



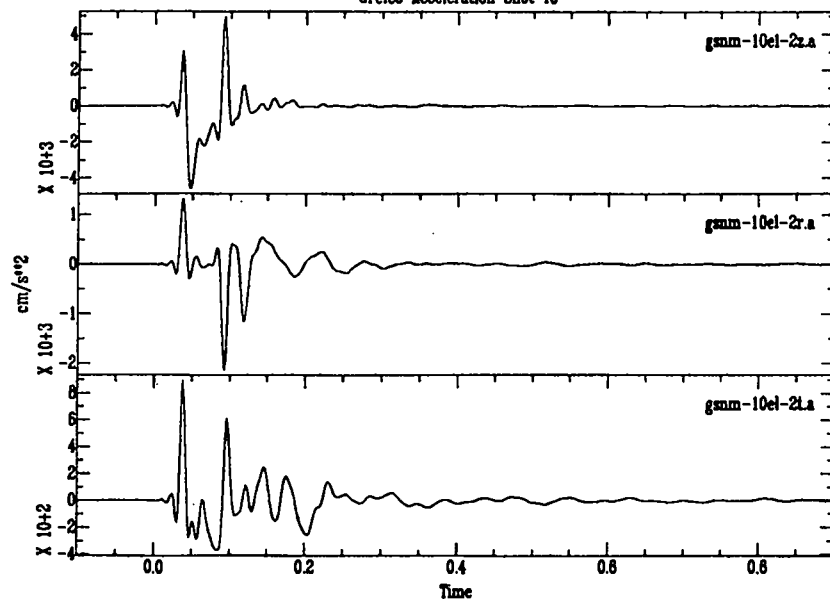
Grefco Acceleration Shot 10



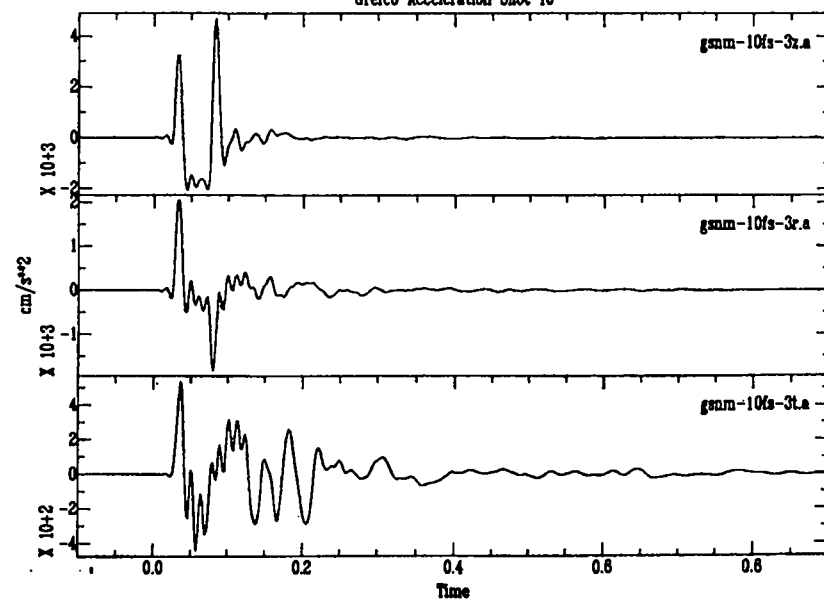
Grefco Acceleration Shot 10



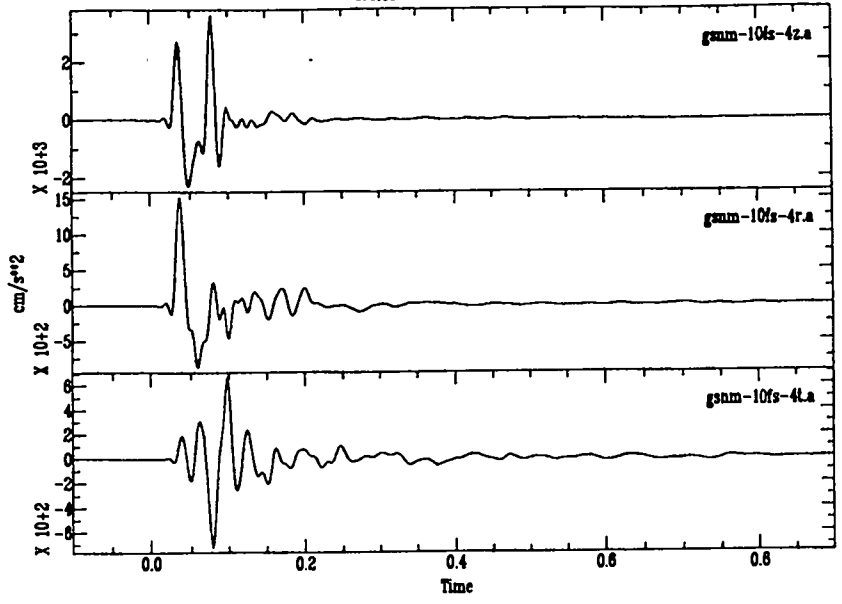
Grefco Acceleration Shot 10



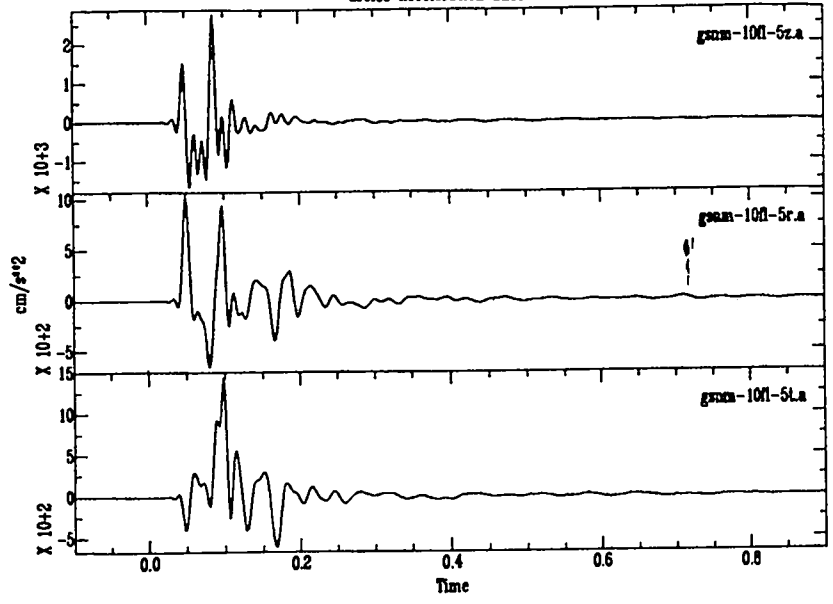
Grefco Acceleration Shot 10



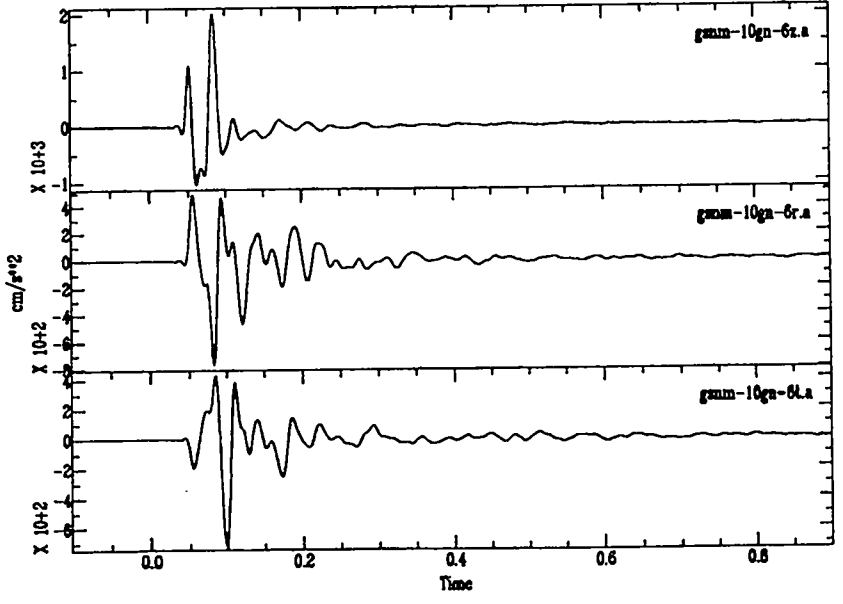
Greco Acceleration Shot 10



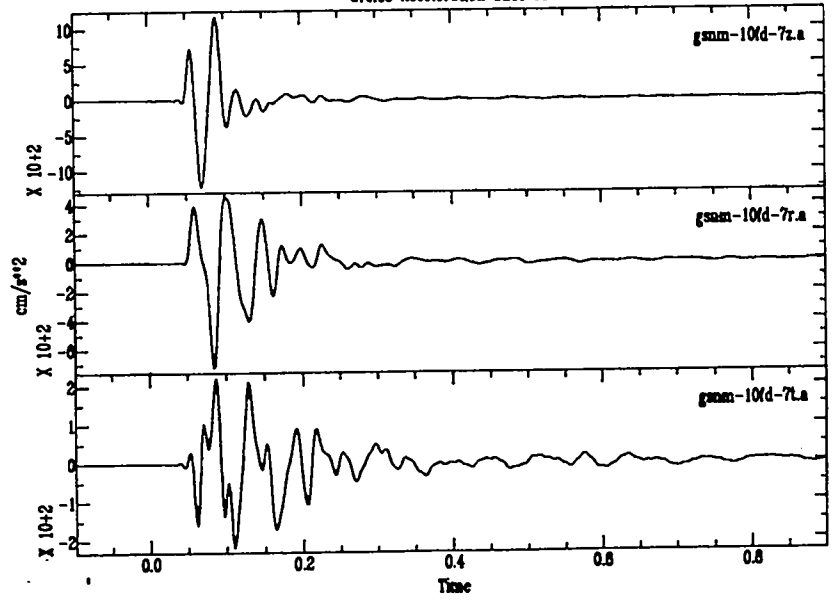
Greco Acceleration Shot 10



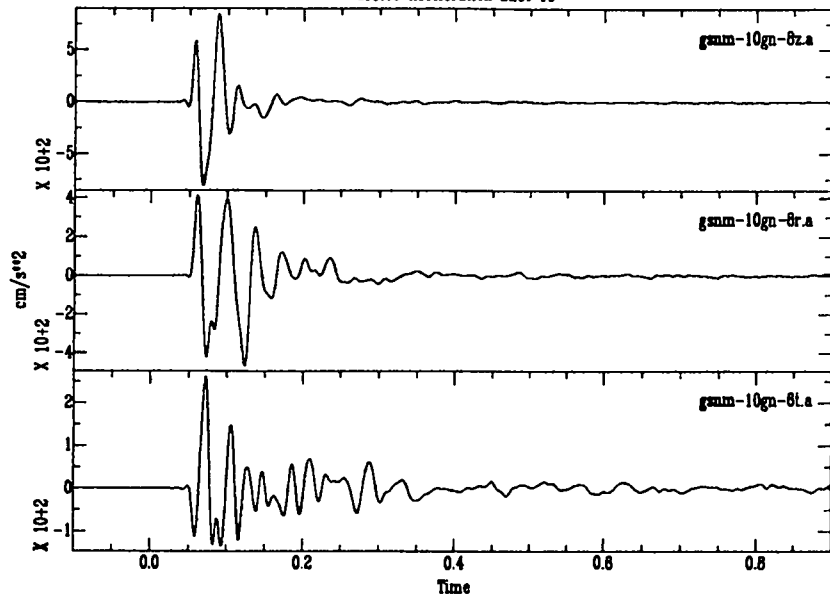
Greco Acceleration Shot 10



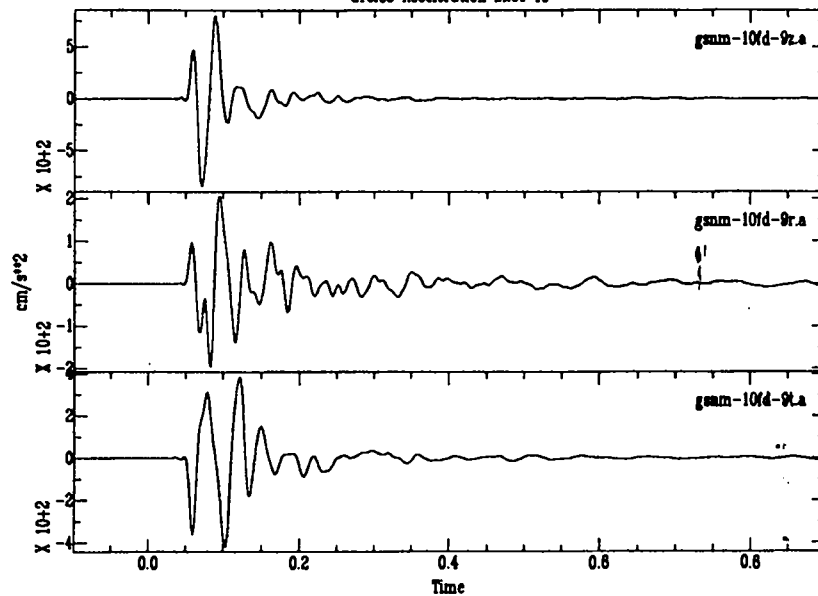
Greco Acceleration Shot 10



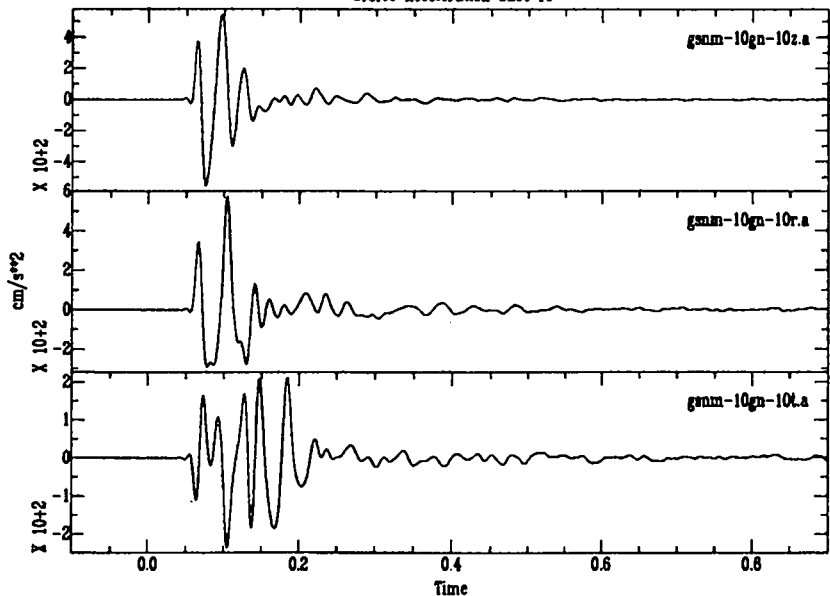
Grefco Acceleration Shot 10



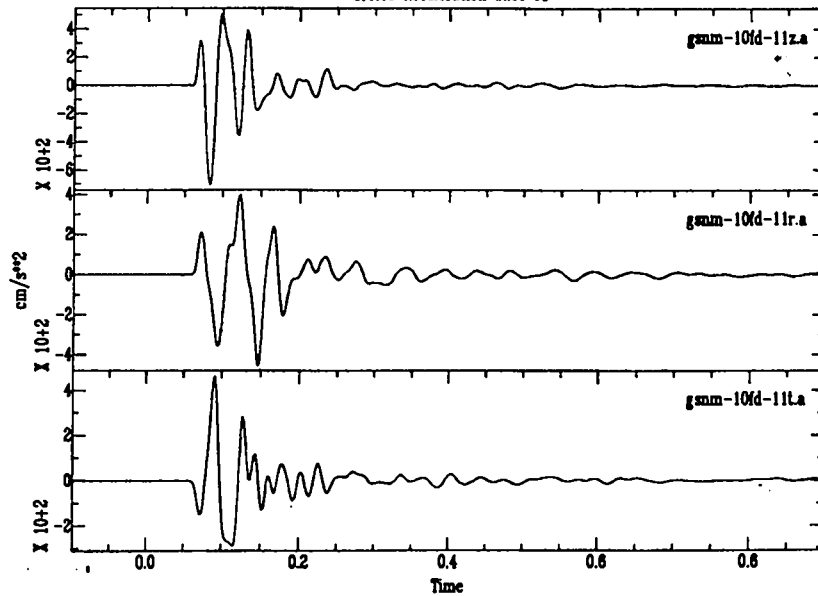
Grefco Acceleration Shot 10



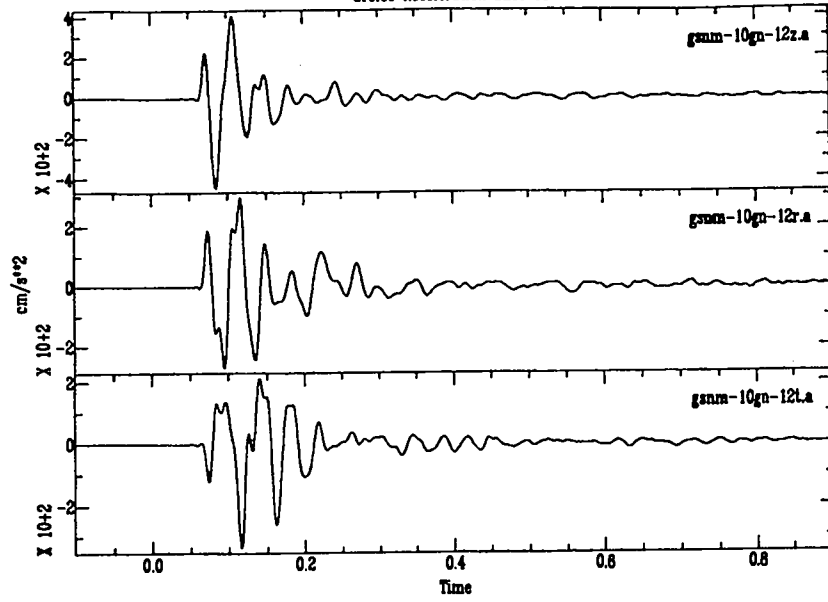
Grefco Acceleration Shot 10



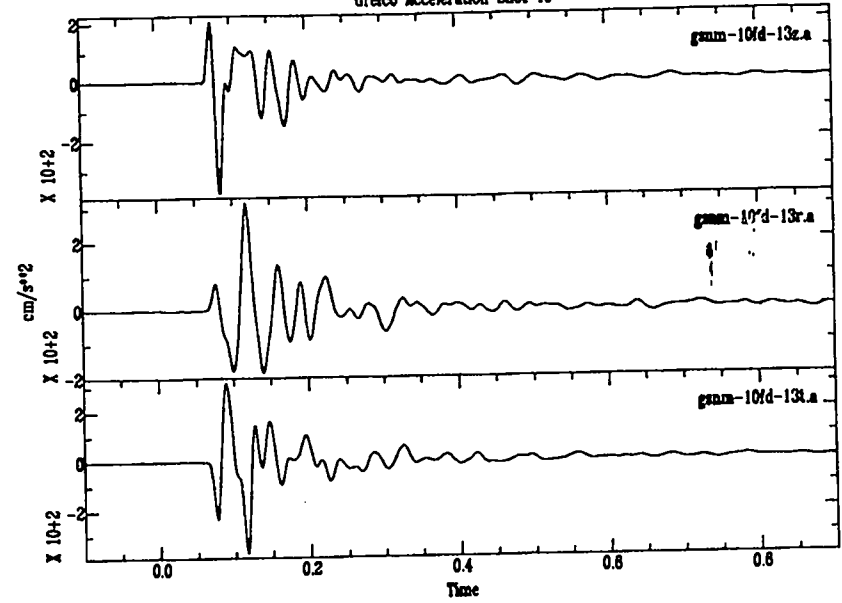
Grefco Acceleration Shot 10



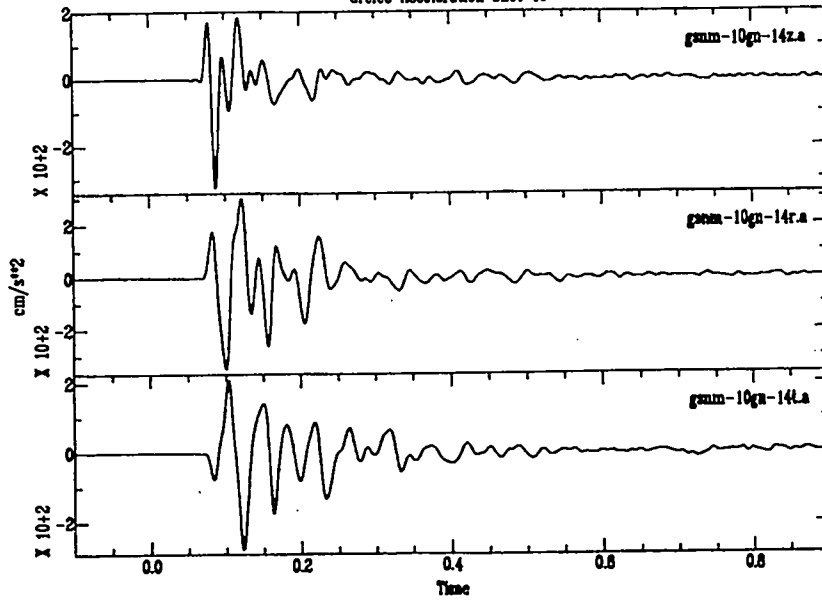
Grefco Acceleration Shot 10



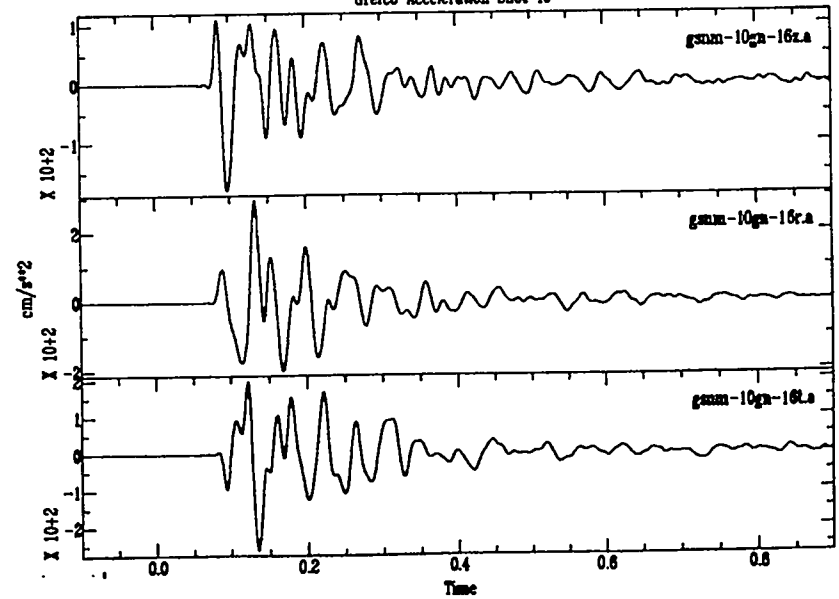
Grefco Acceleration Shot 10

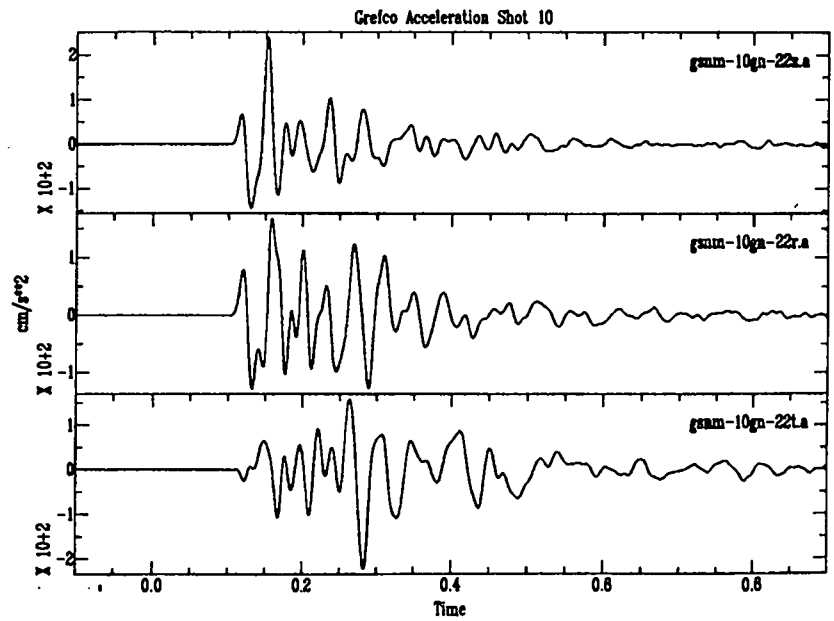
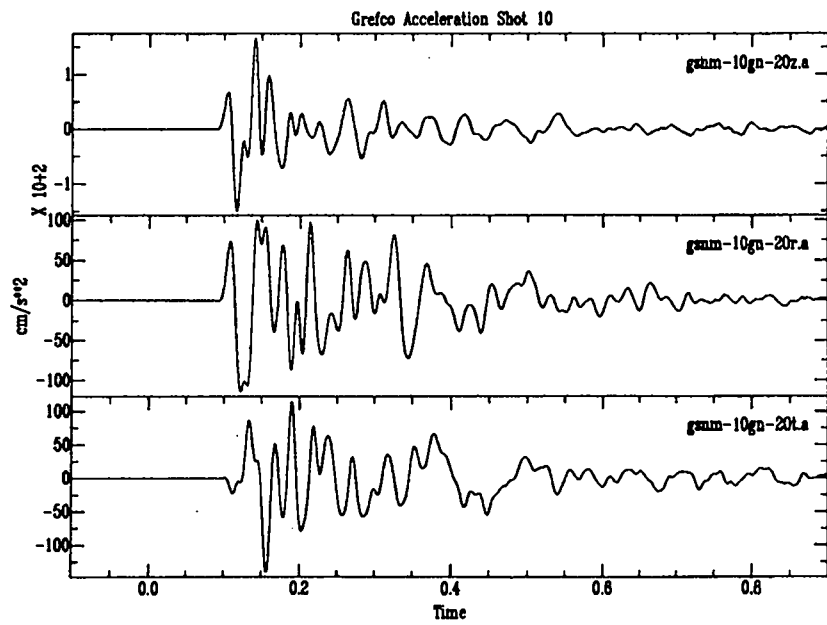
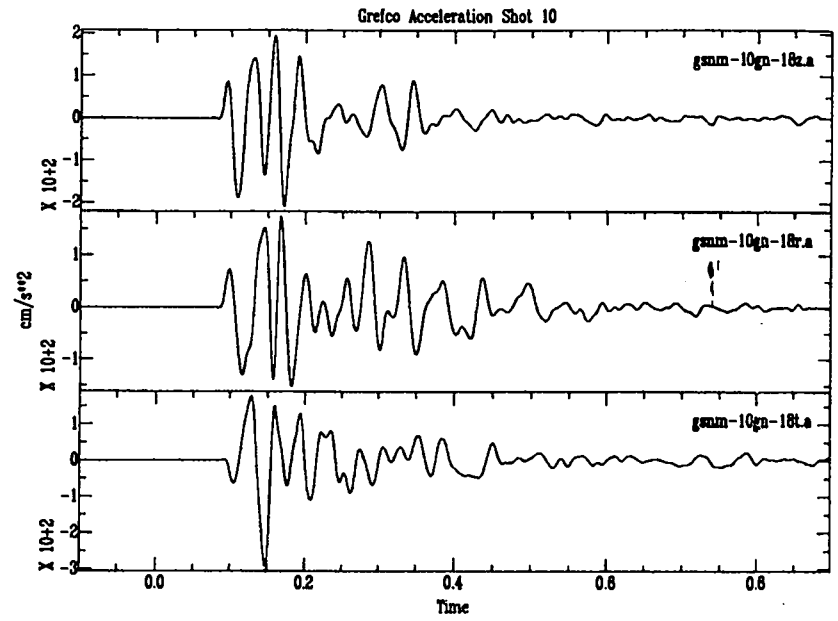
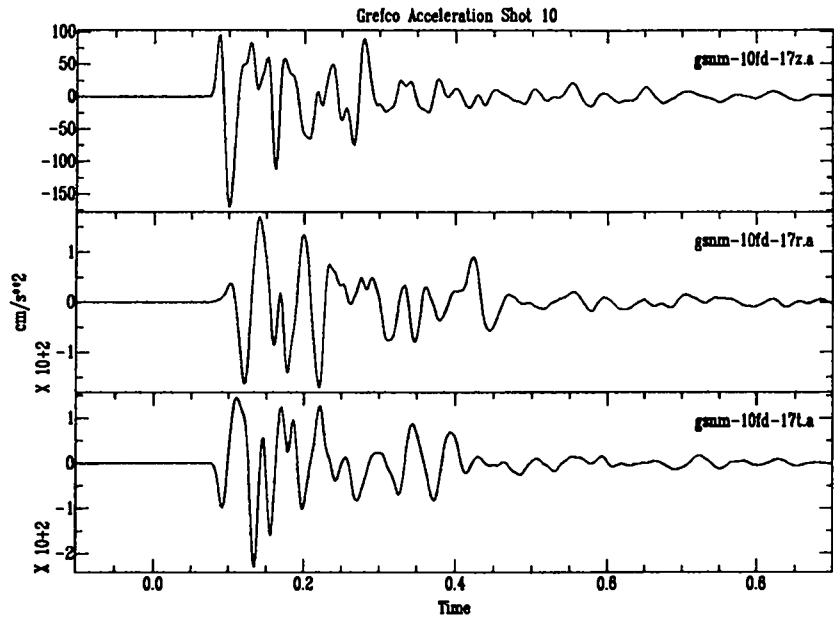


Grefco Acceleration Shot 10

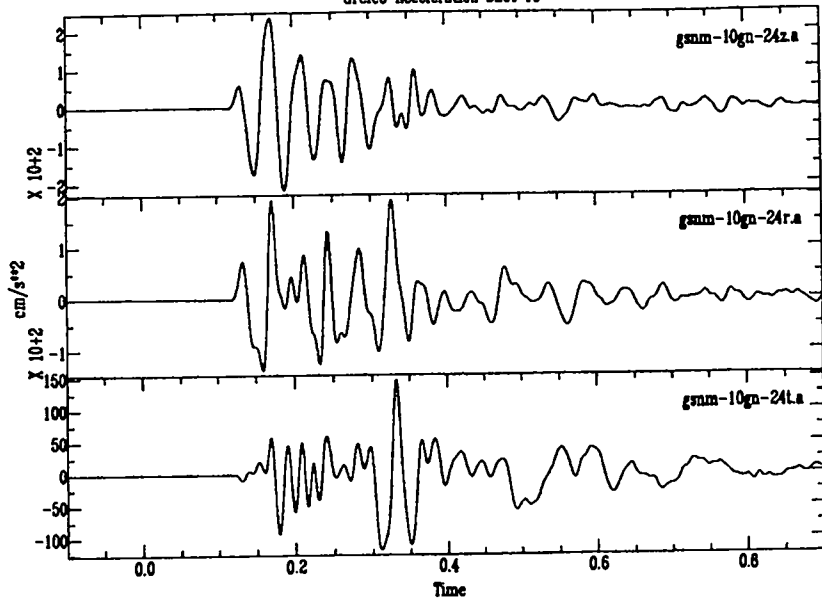


Grefco Acceleration Shot 10

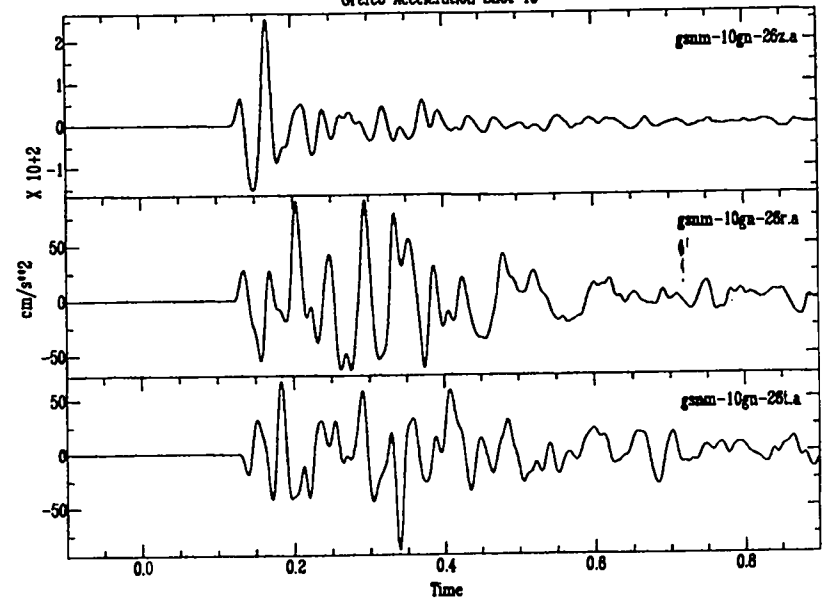




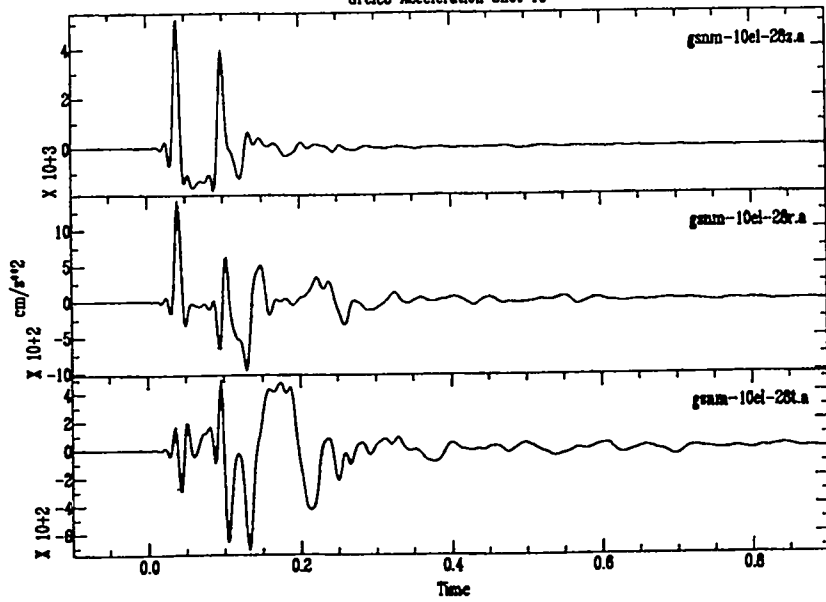
Grefco Acceleration Shot 10



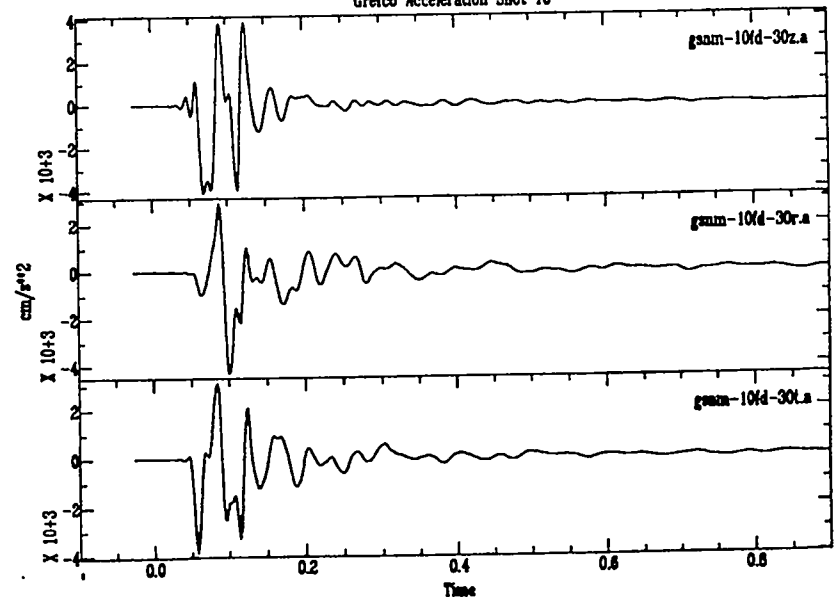
Grefco Acceleration Shot 10



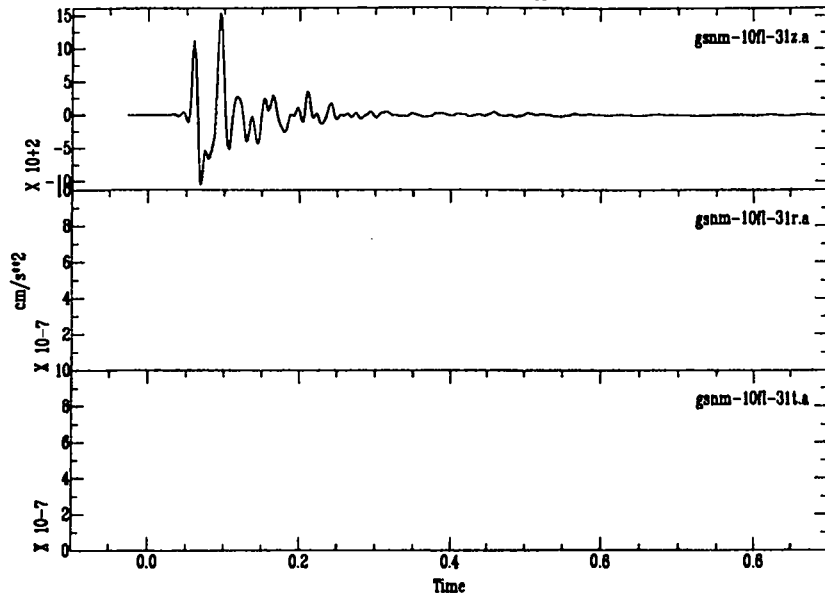
Grefco Acceleration Shot 10



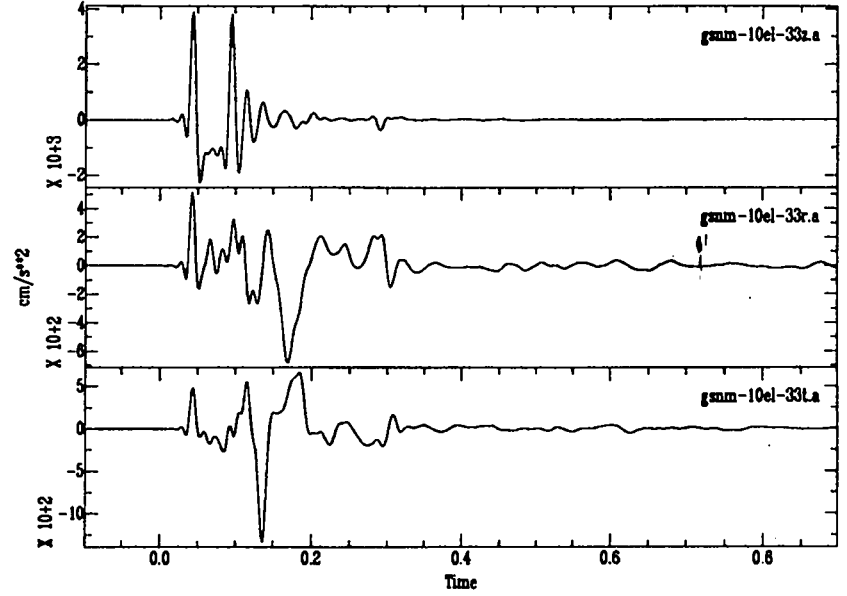
Grefco Acceleration Shot 10



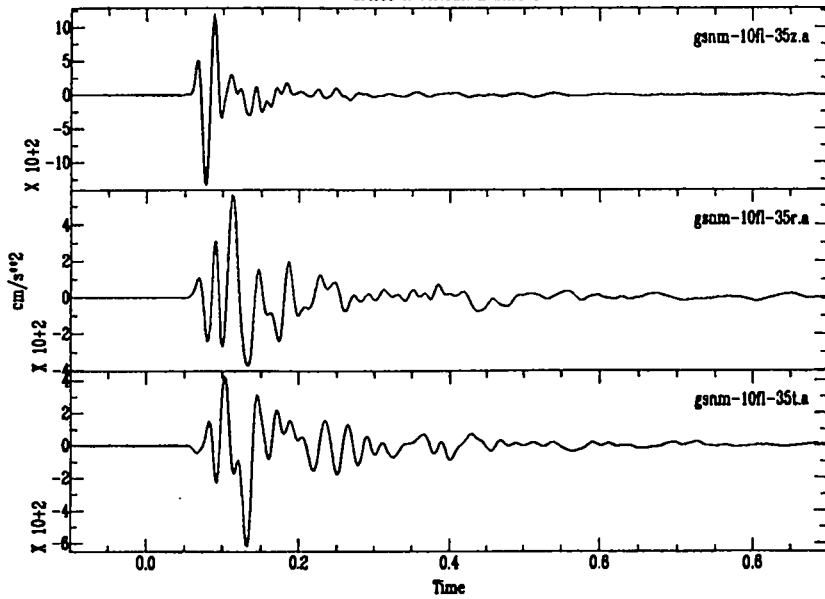
Grefco Acceleration Shot 10



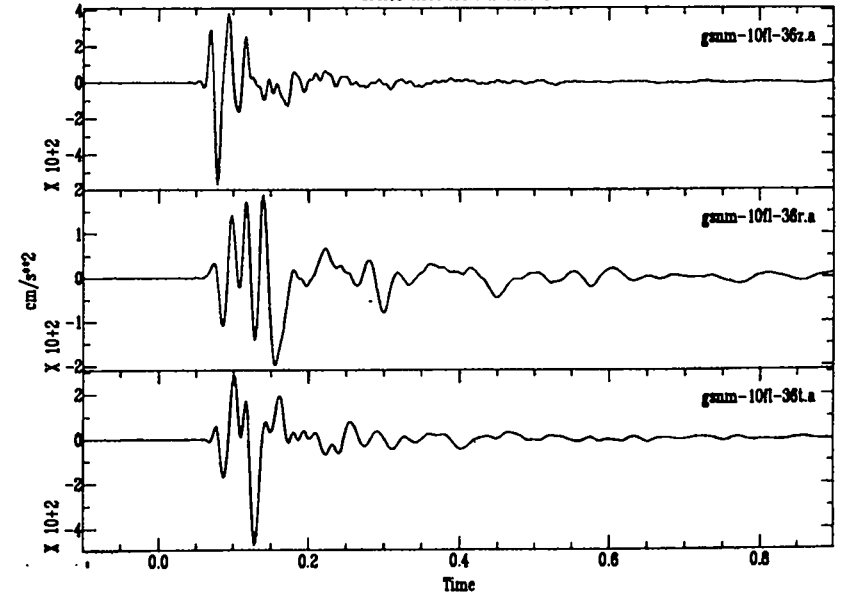
Grefco Acceleration Shot 10

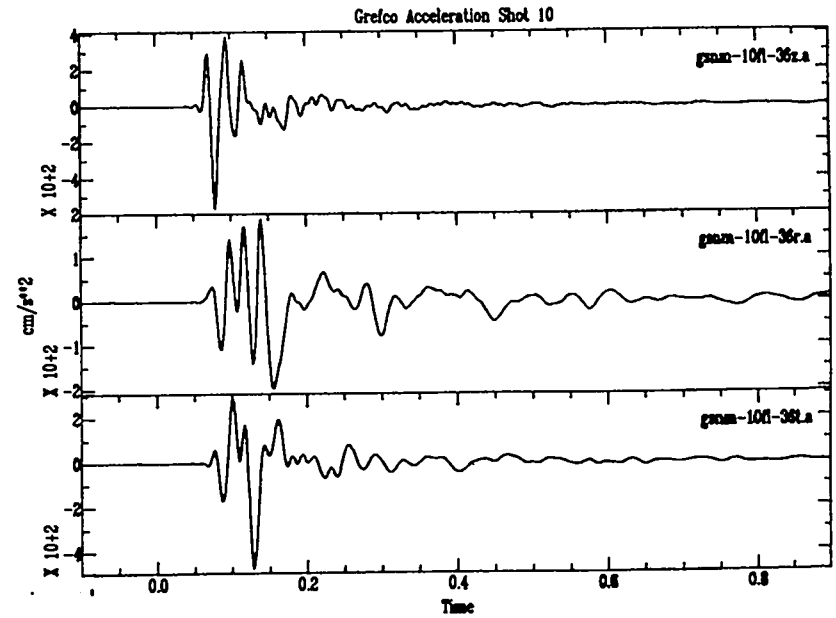
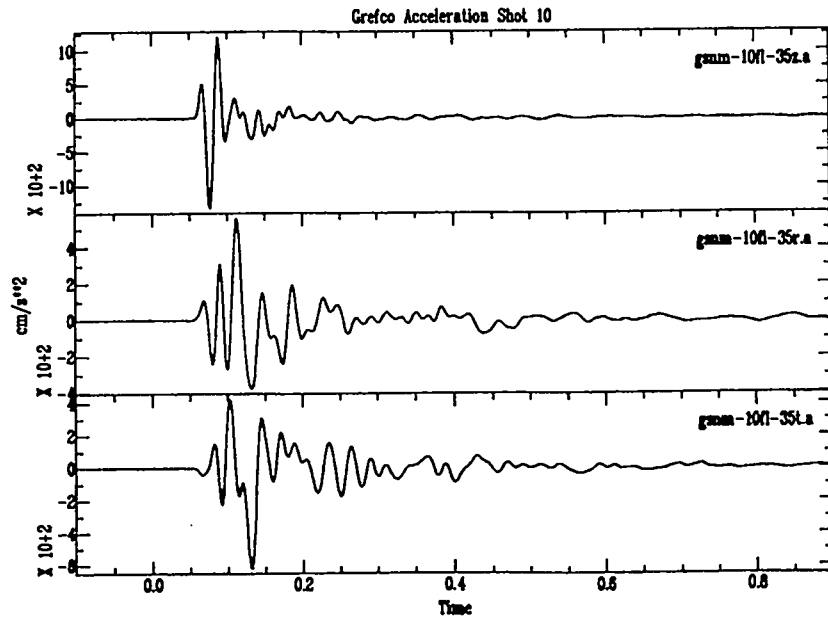
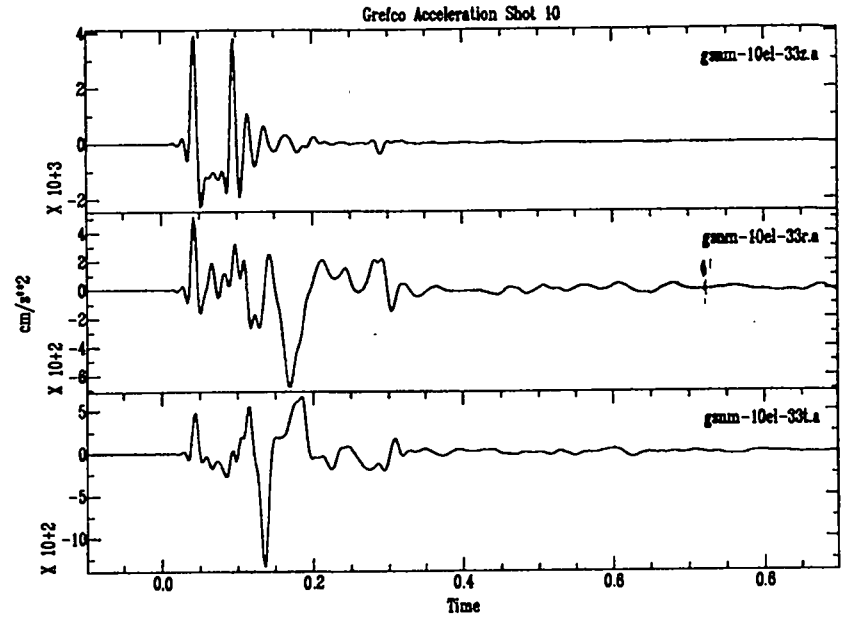
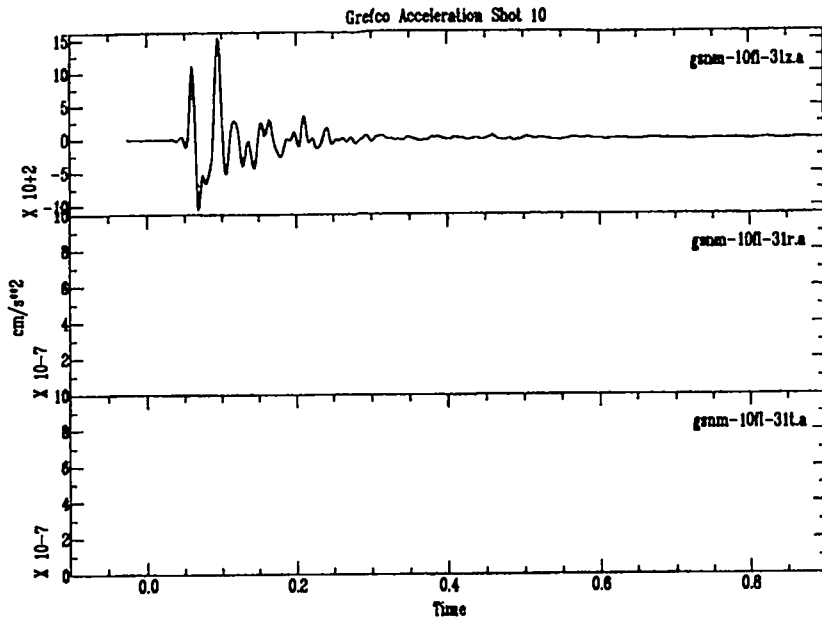


Grefco Acceleration Shot 10

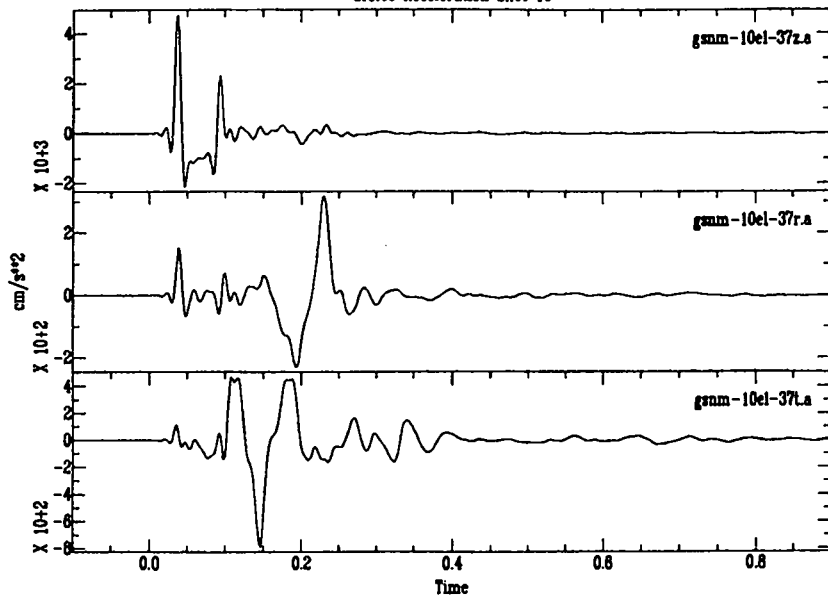


Grefco Acceleration Shot 10

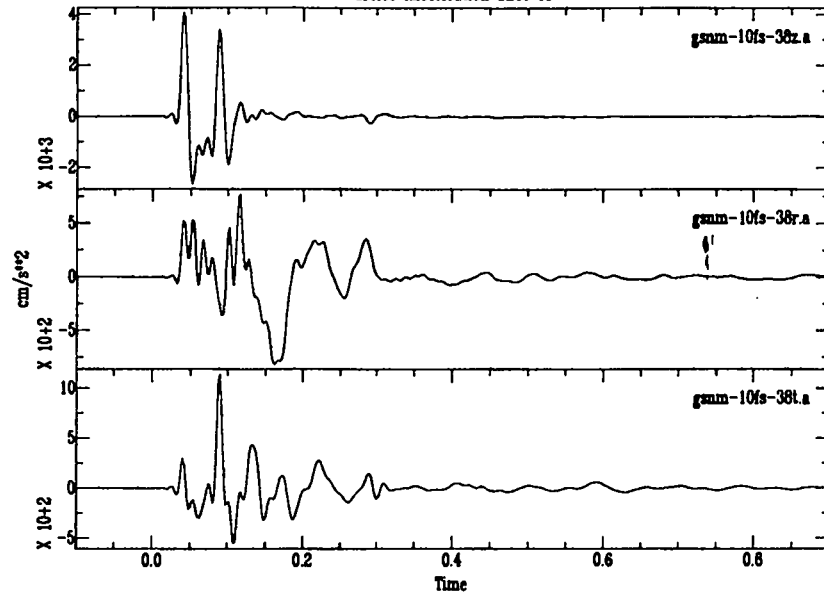




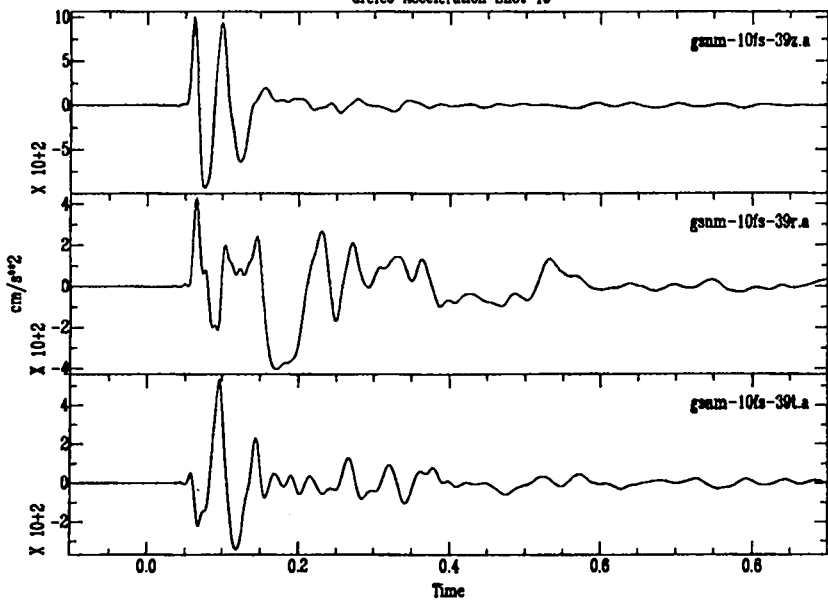
Grefco Acceleration Shot 10



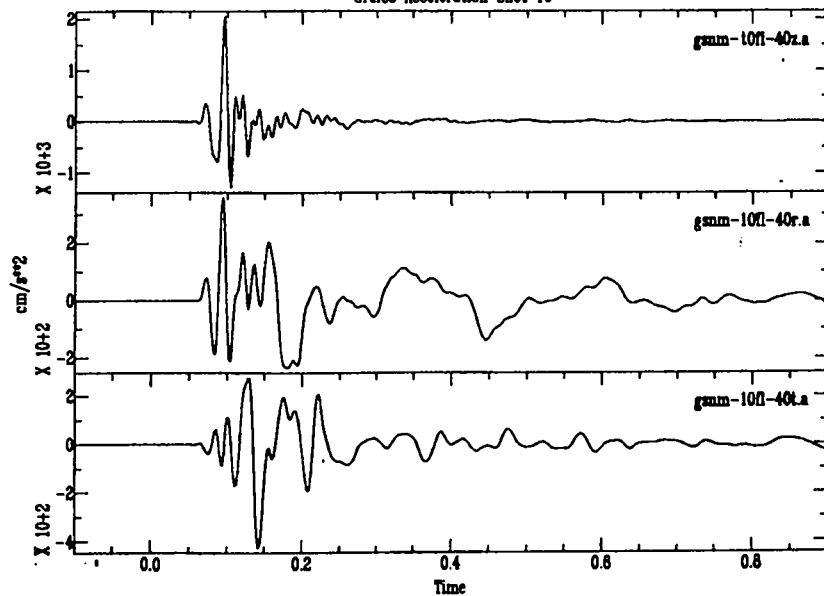
Grefco Acceleration Shot 10

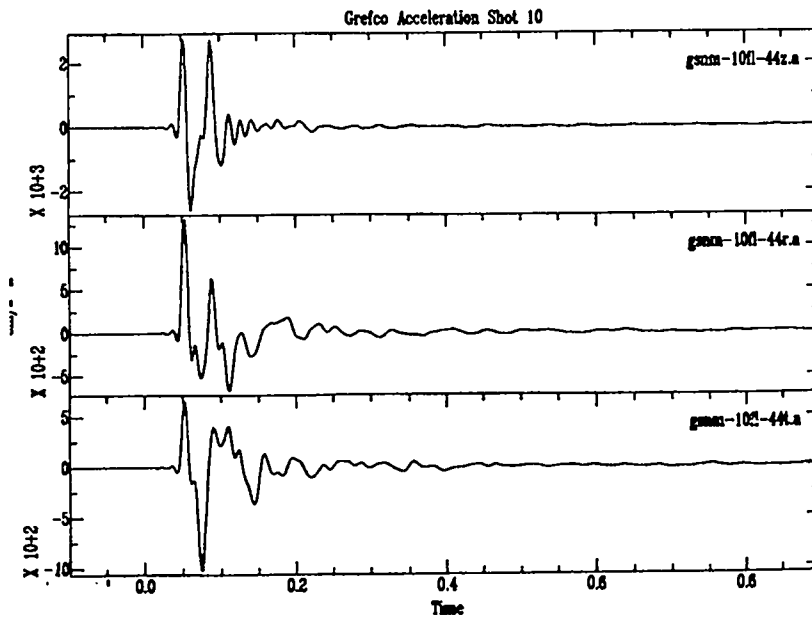
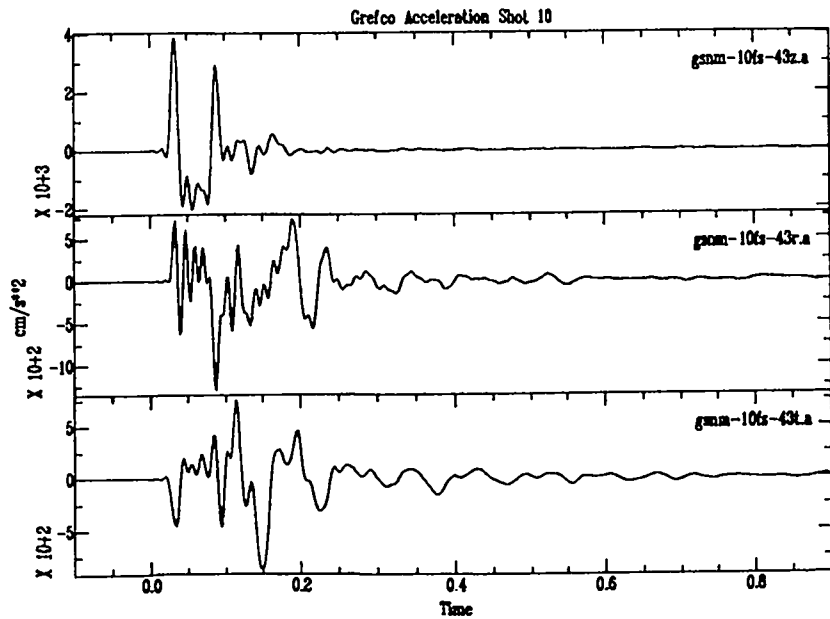
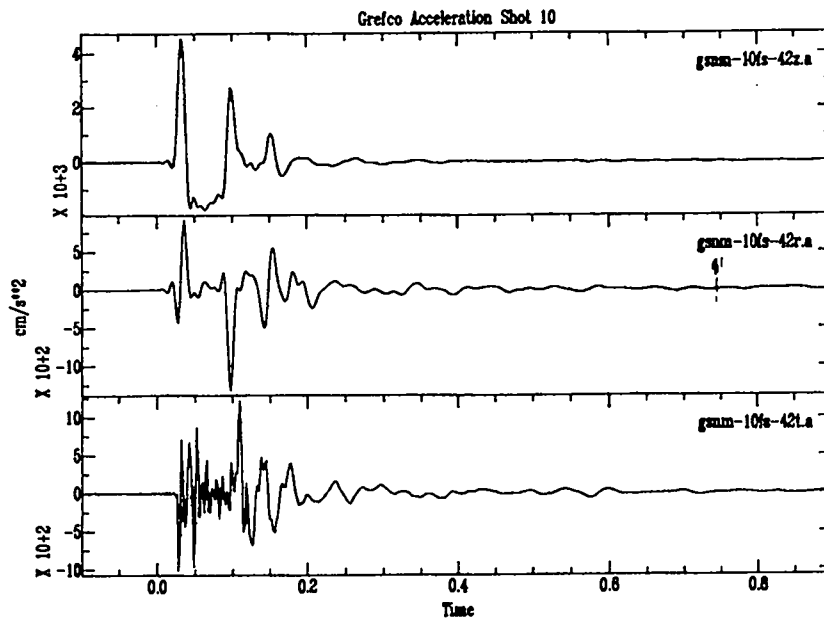
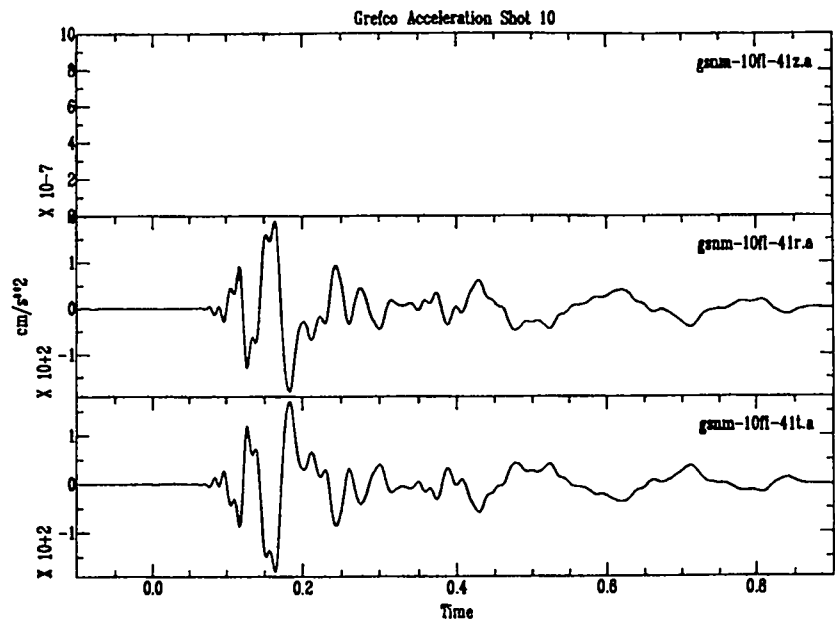


Grefco Acceleration Shot 10

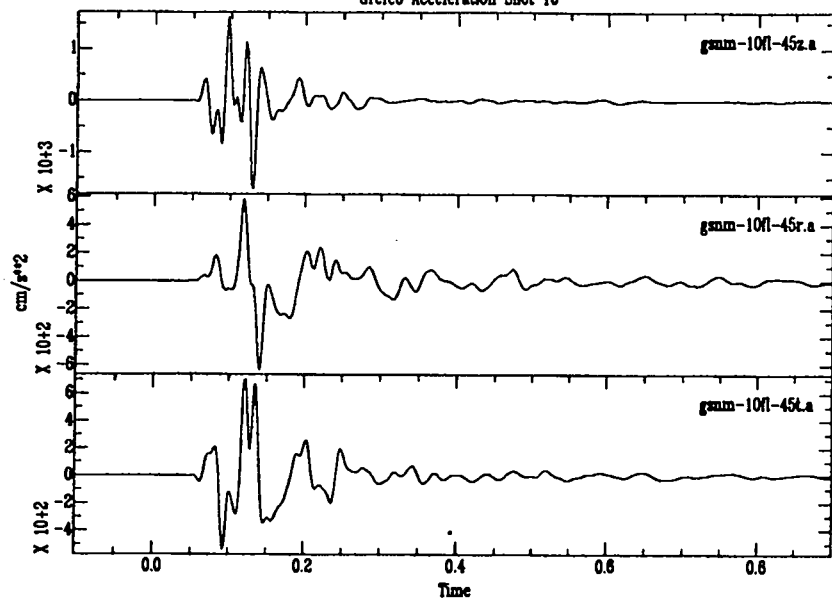


Grefco Acceleration Shot 10

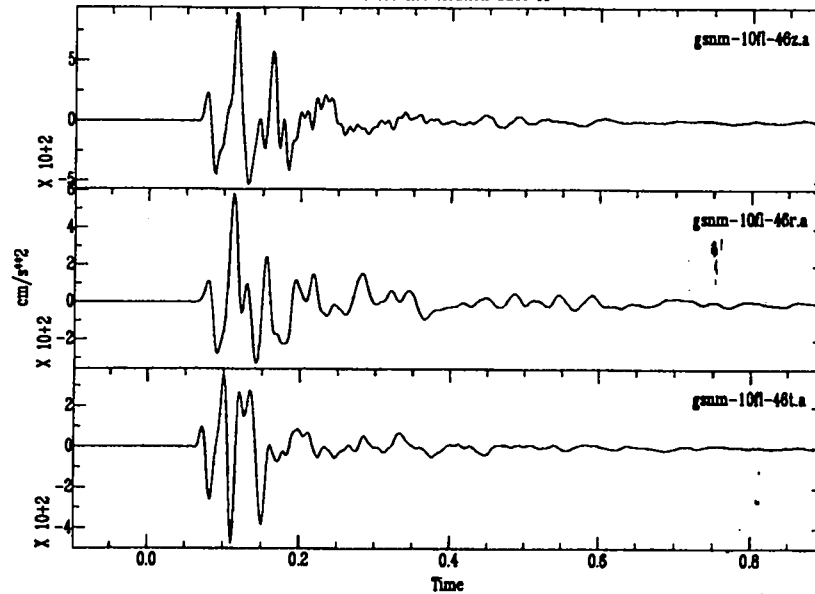




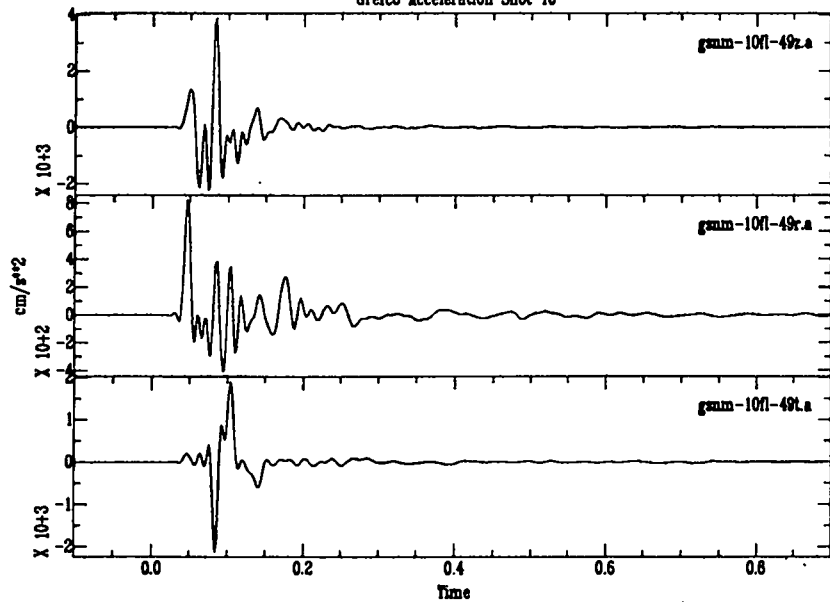
Grefco Acceleration Shot 10



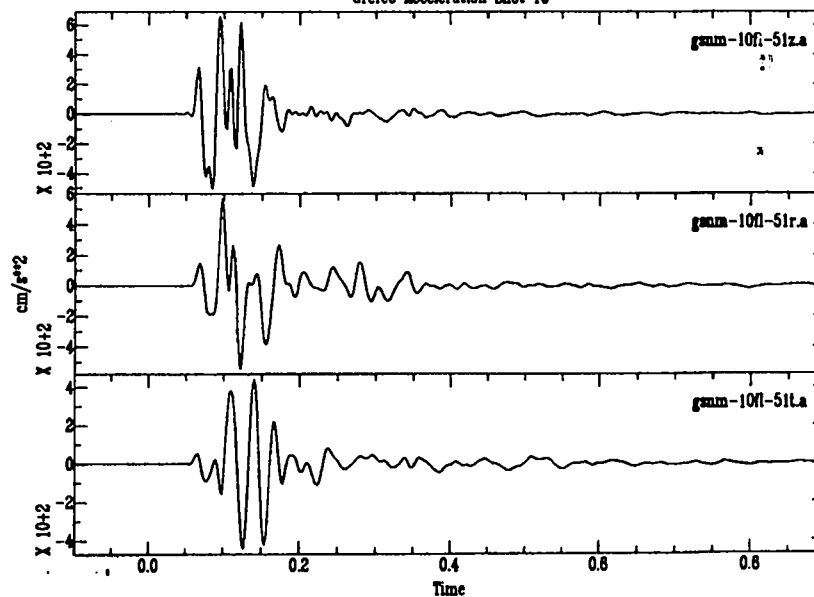
Grefco Acceleration Shot 10

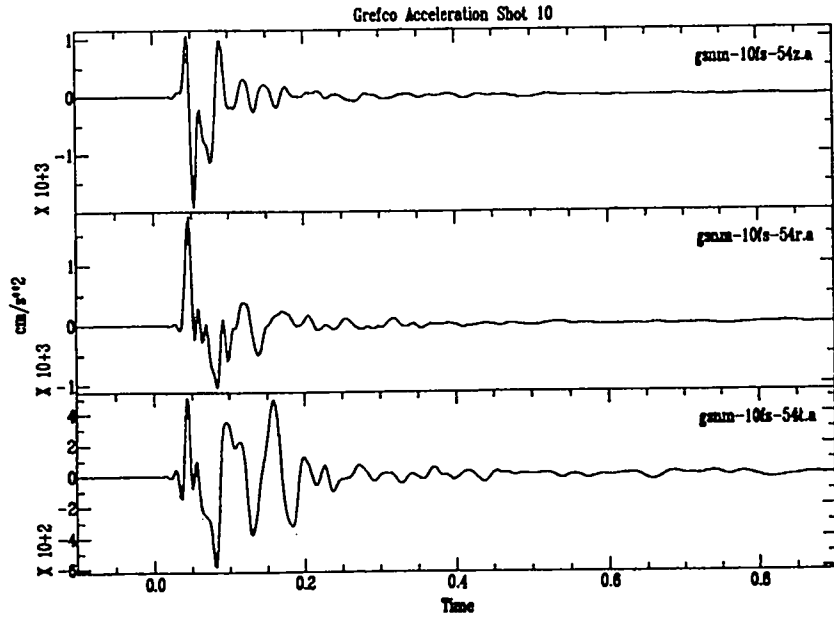
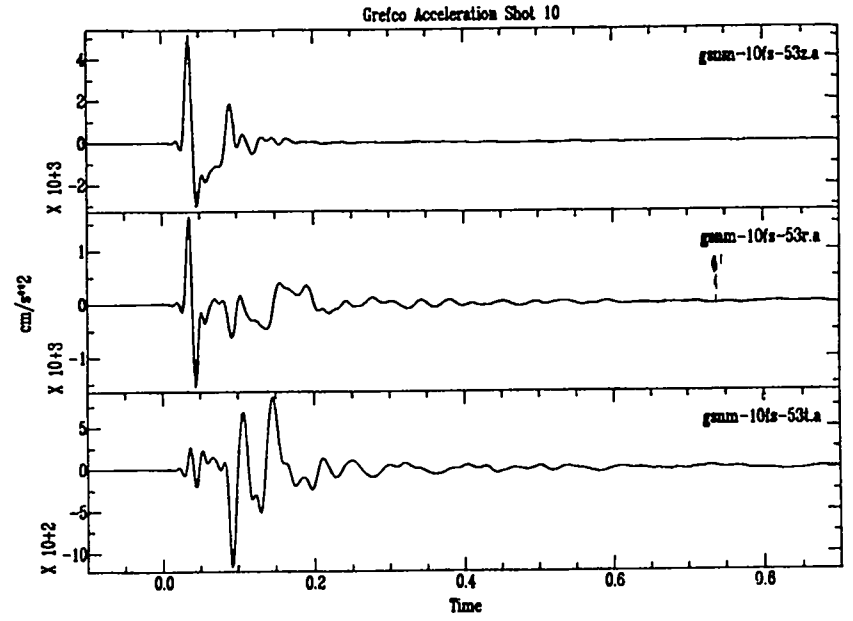
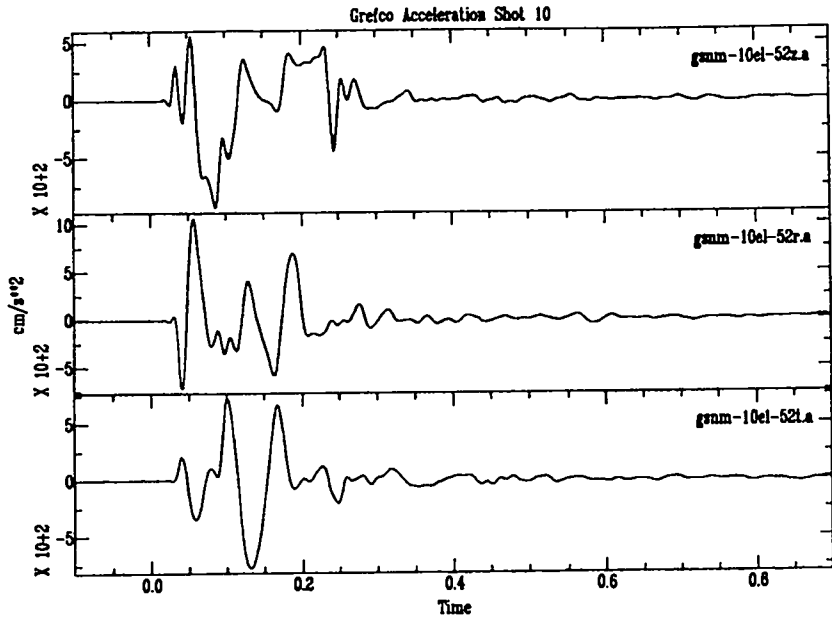


Grefco Acceleration Shot 10

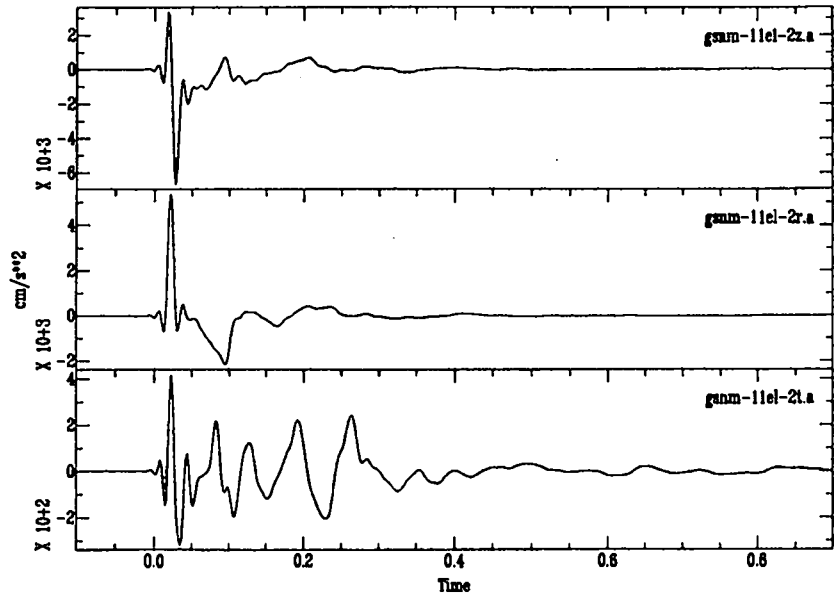


Grefco Acceleration Shot 10

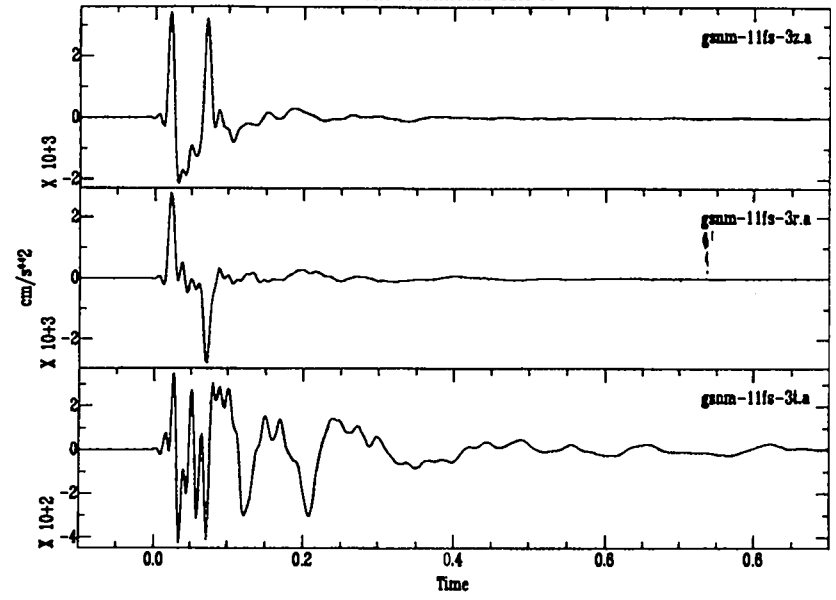




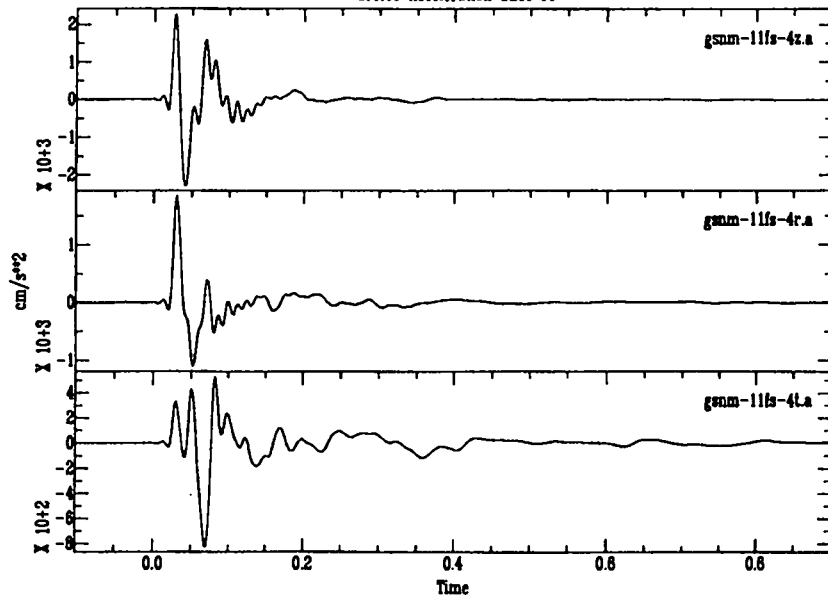
Grefco Acceleration Shot 11



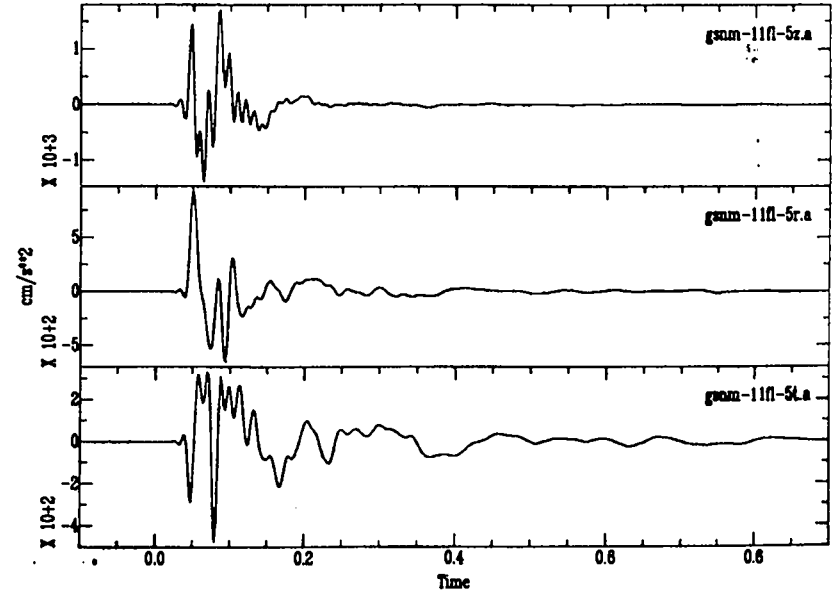
Grefco Acceleration Shot 11



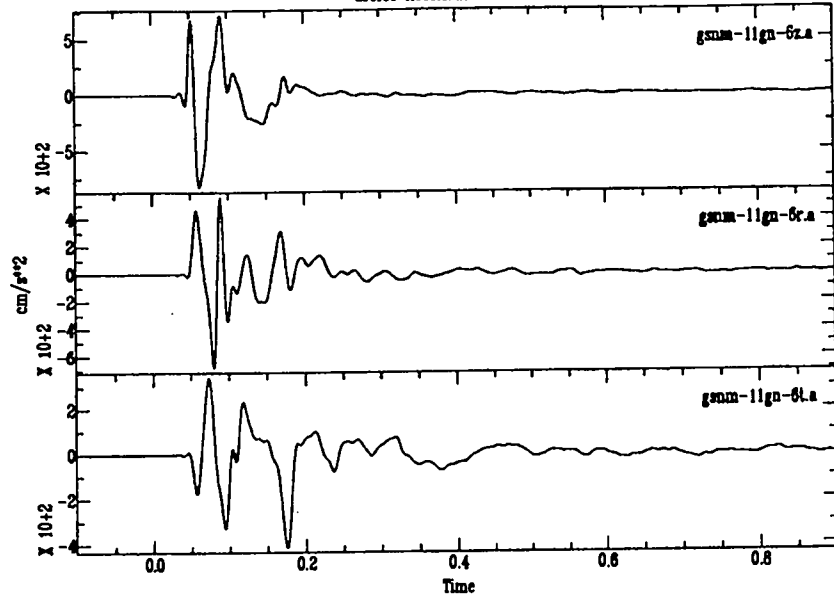
Grefco Acceleration Shot 11



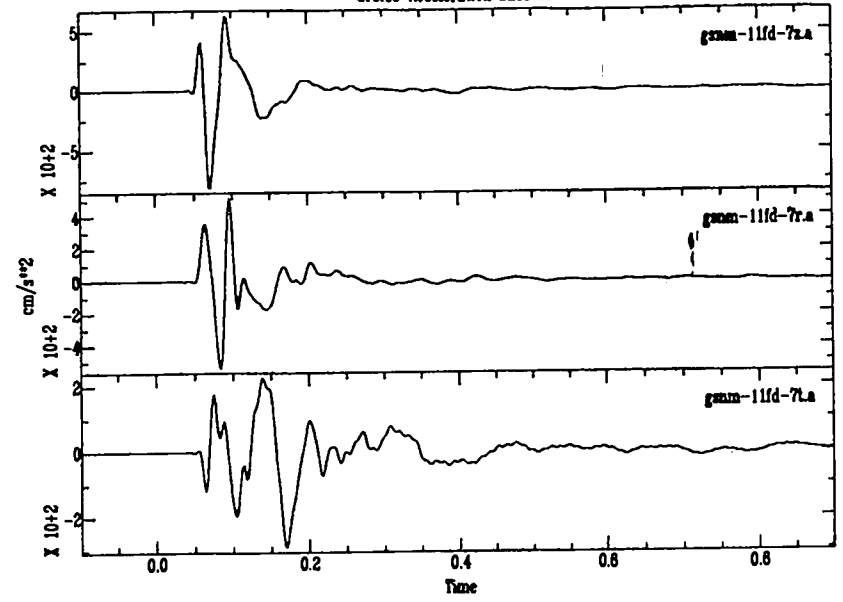
Grefco Acceleration Shot 11



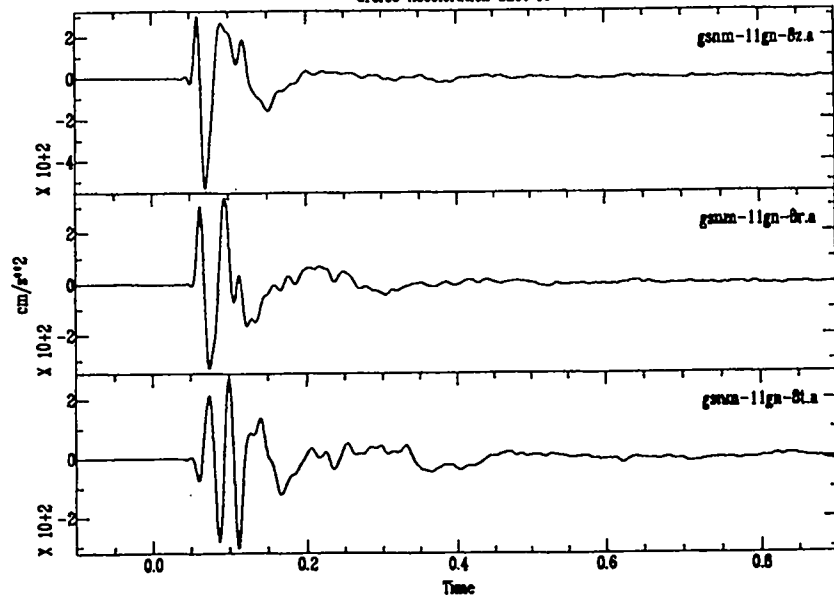
Grefco Acceleration Shot 11



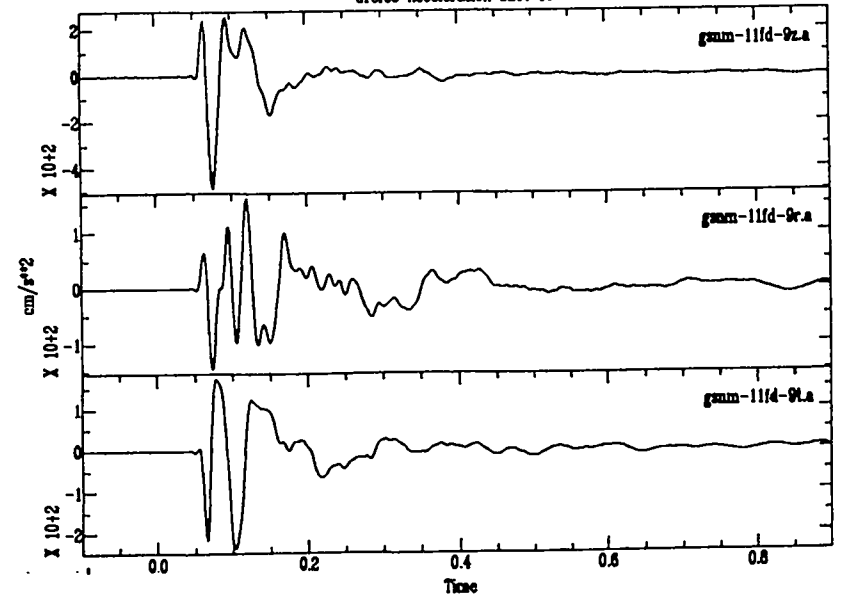
Grefco Acceleration Shot 11



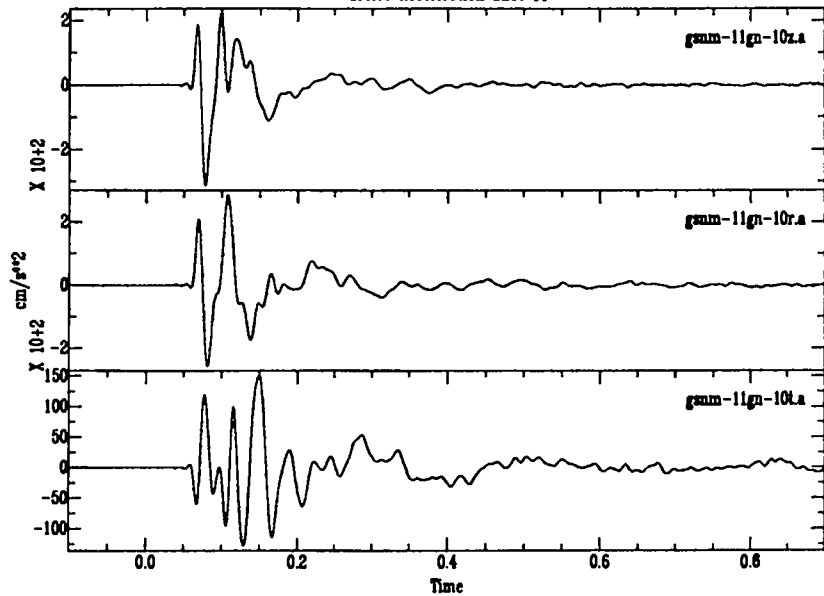
Grefco Acceleration Shot 11



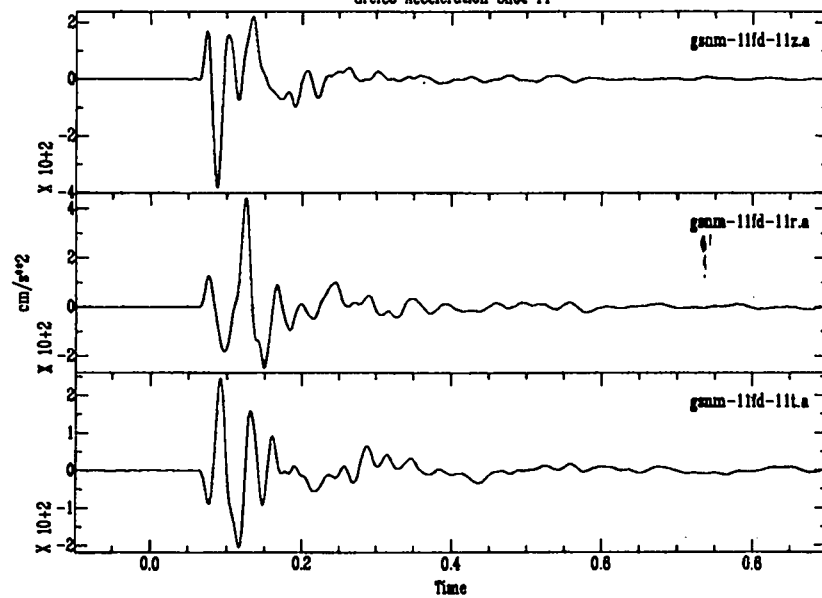
Grefco Acceleration Shot 11



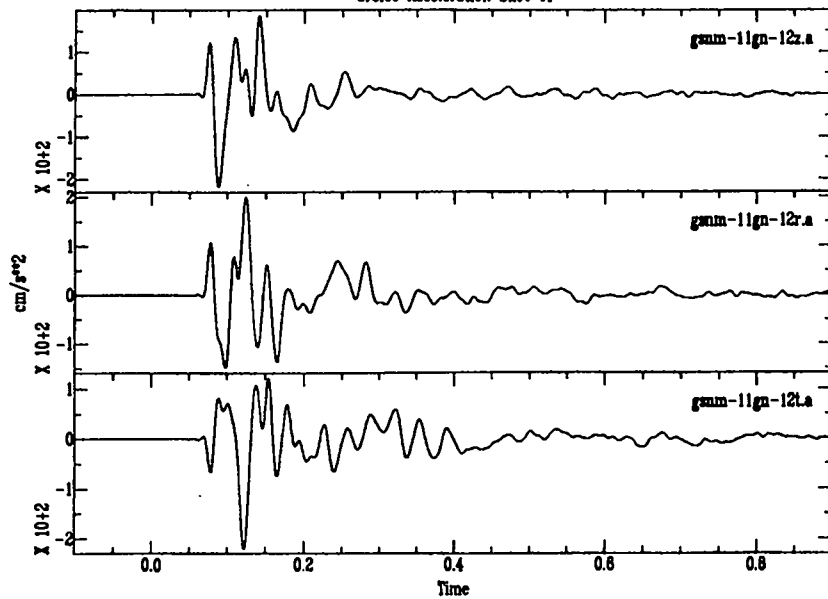
Grefco Acceleration Shot 11



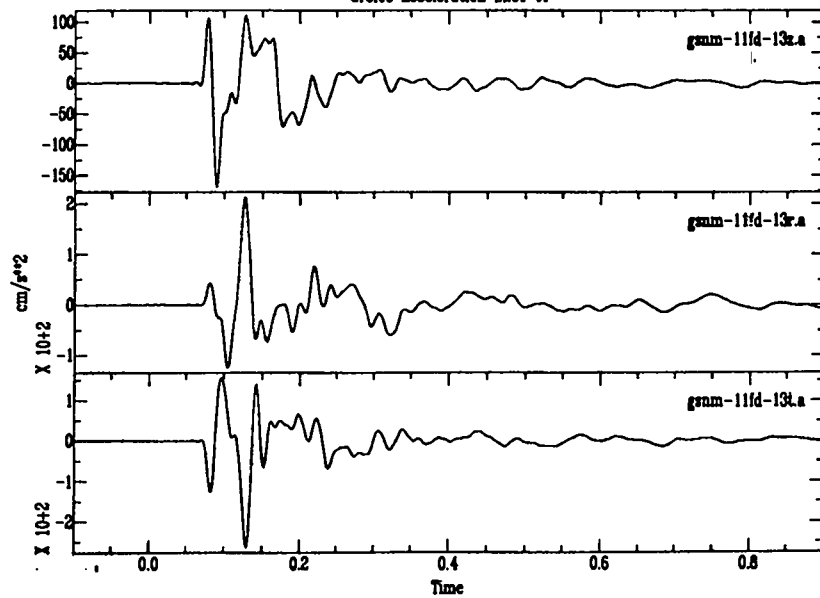
Grefco Acceleration Shot 11



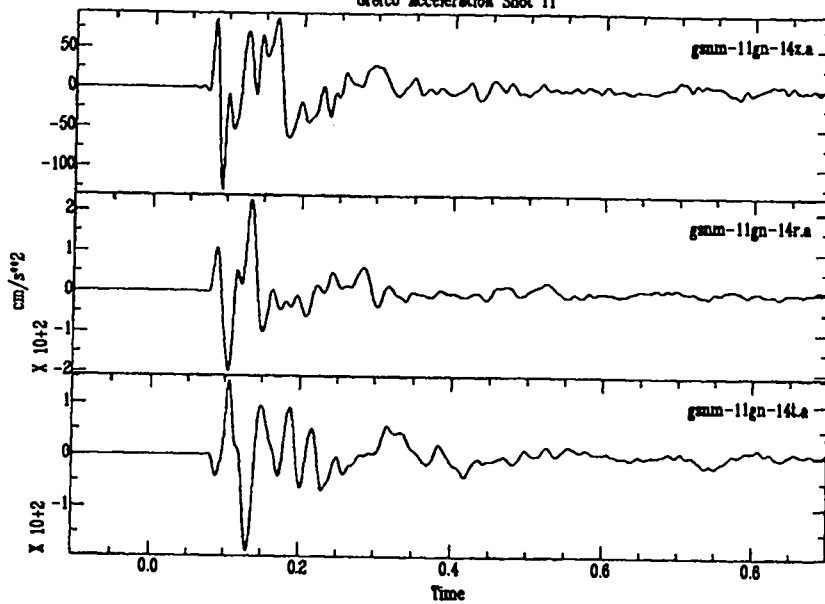
Grefco Acceleration Shot 11



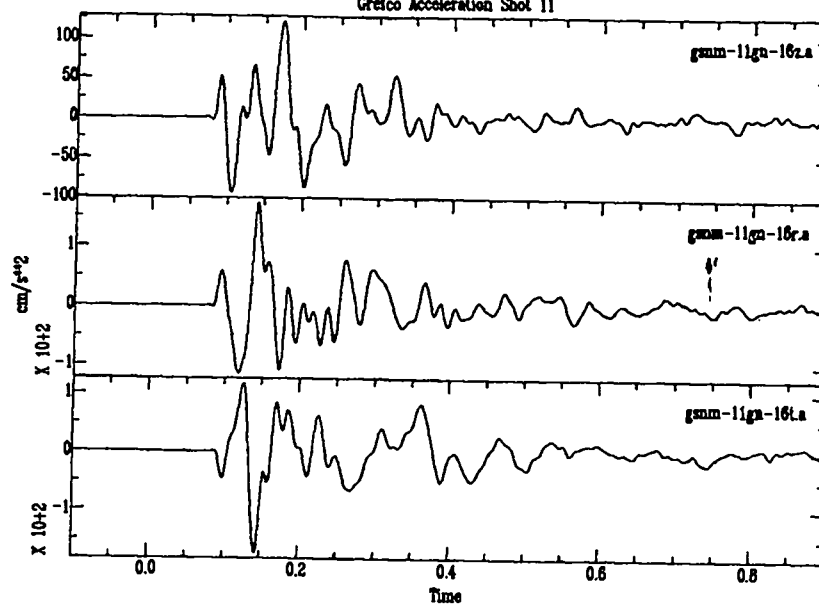
Grefco Acceleration Shot 11



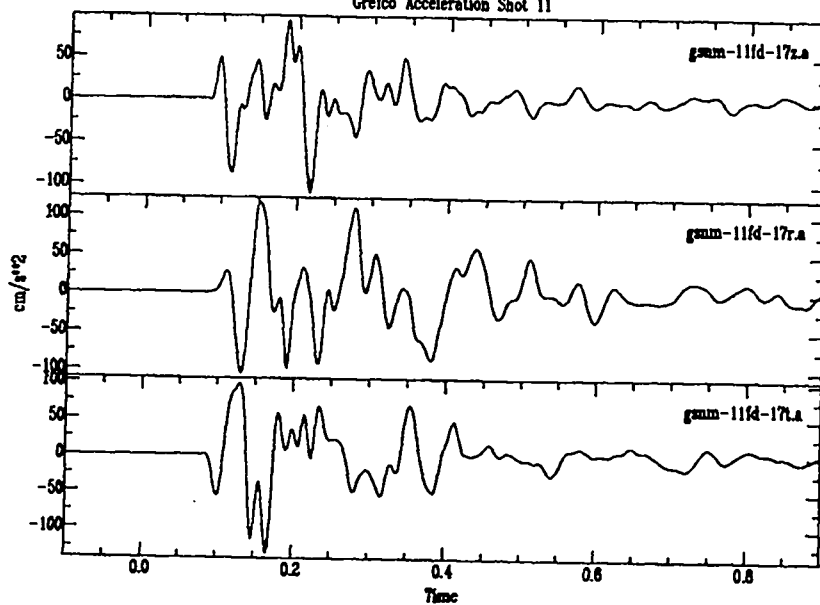
Grefco Acceleration Shot 11



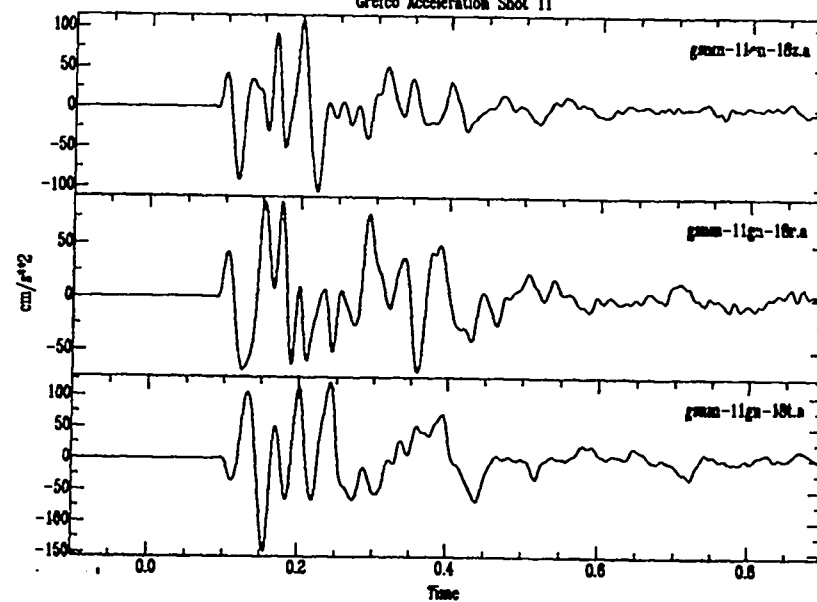
Grefco Acceleration Shot 11



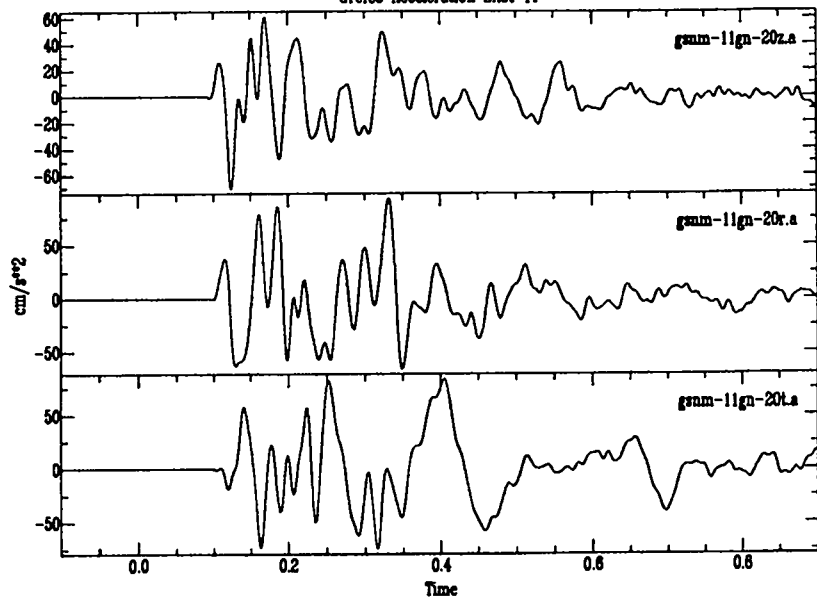
Grefco Acceleration Shot 11



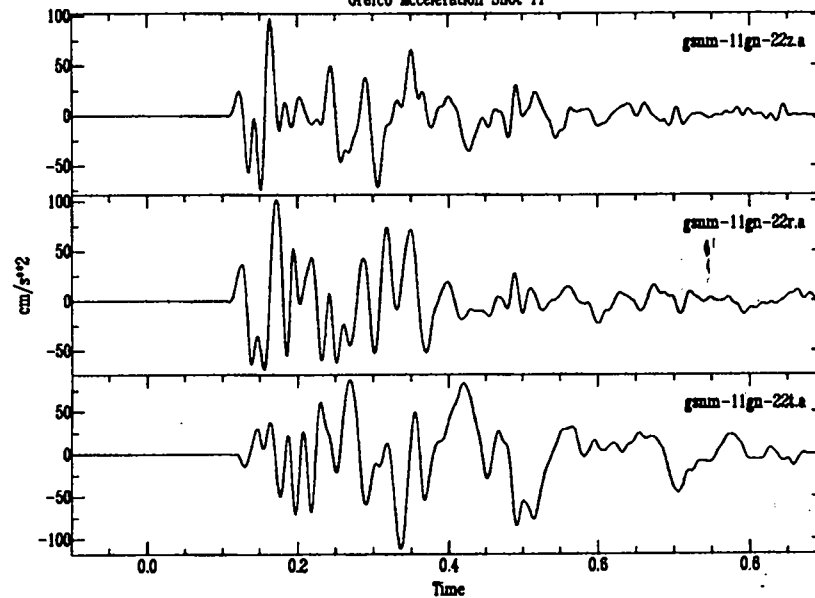
Grefco Acceleration Shot 11



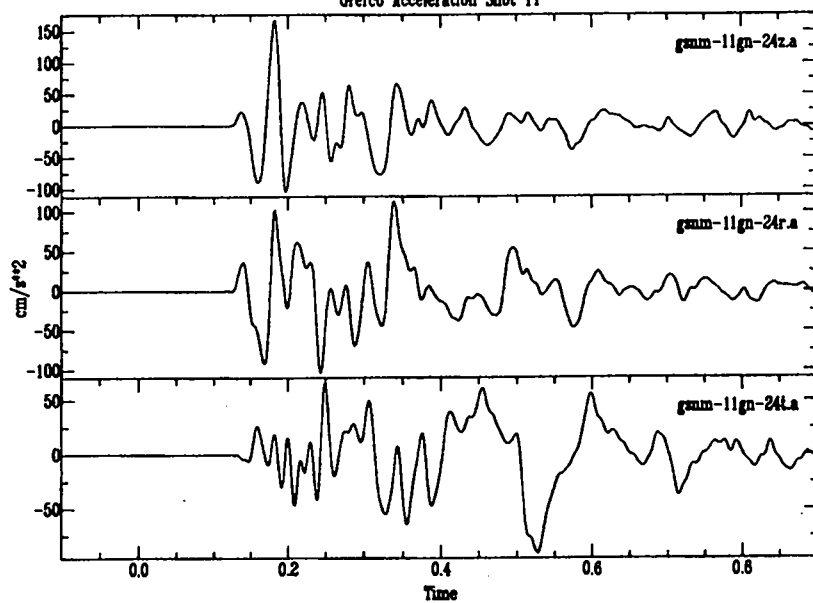
Grefco Acceleration Shot 11



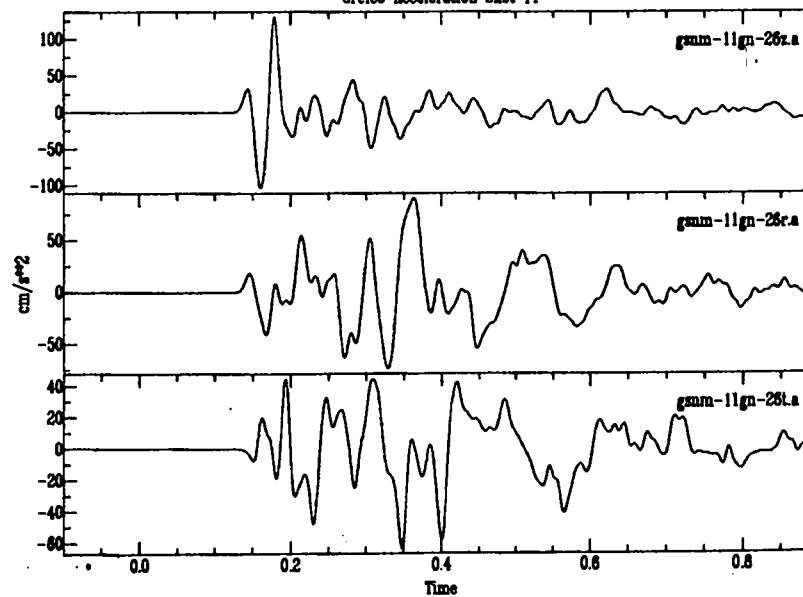
Grefco Acceleration Shot 11



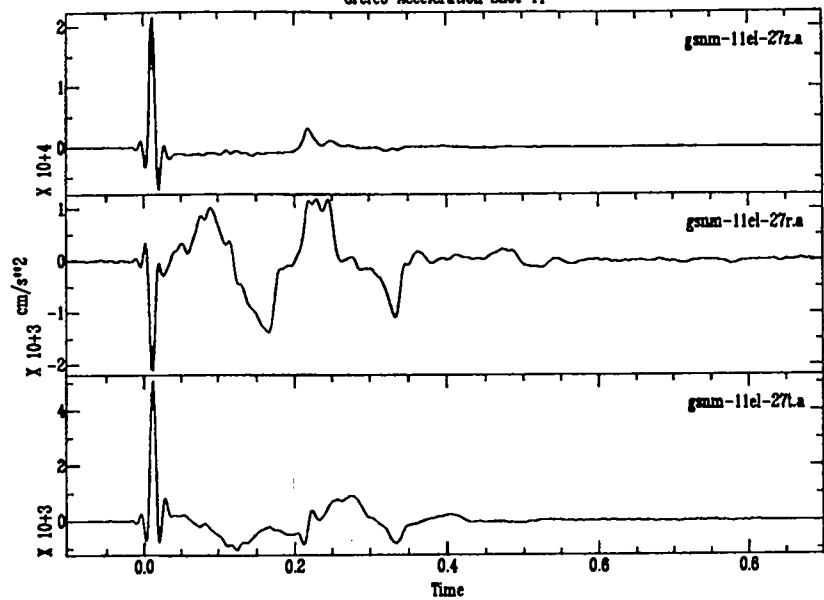
Grefco Acceleration Shot 11



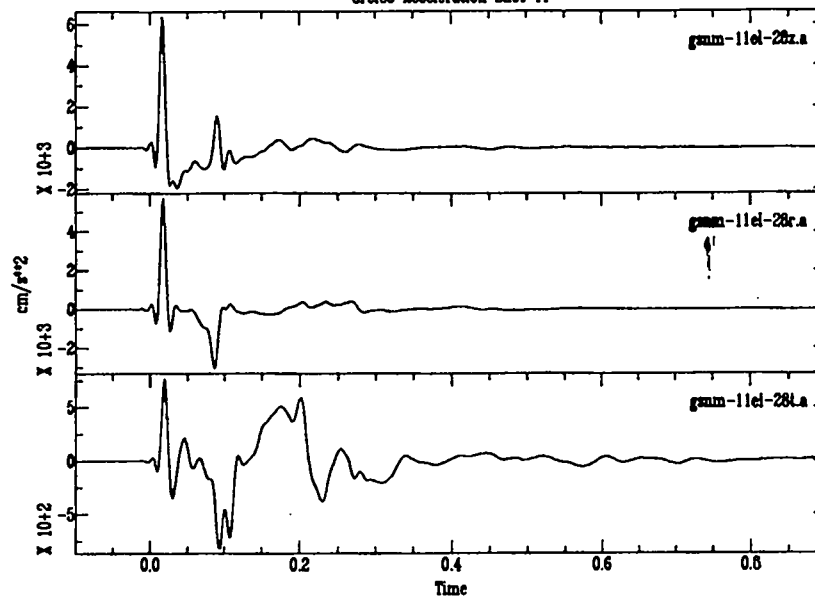
Grefco Acceleration Shot 11



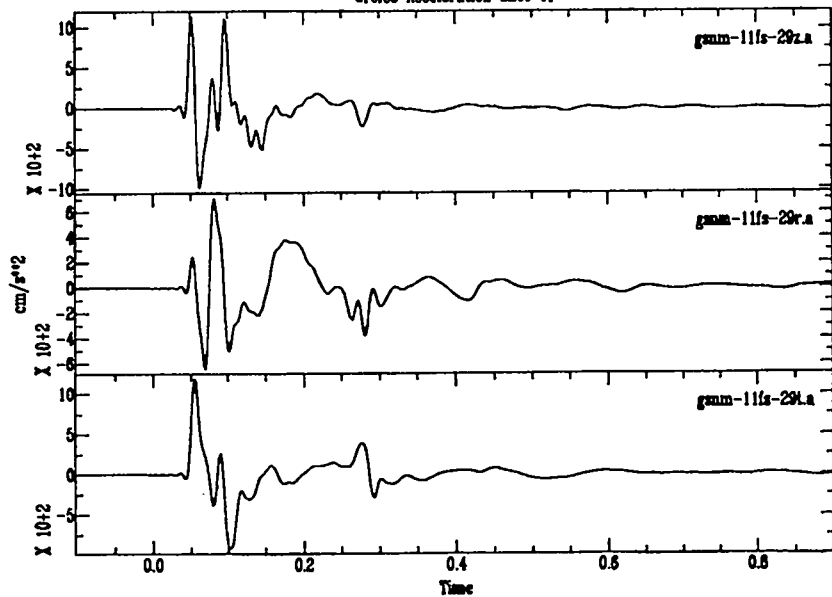
Grefco Acceleration Shot 11



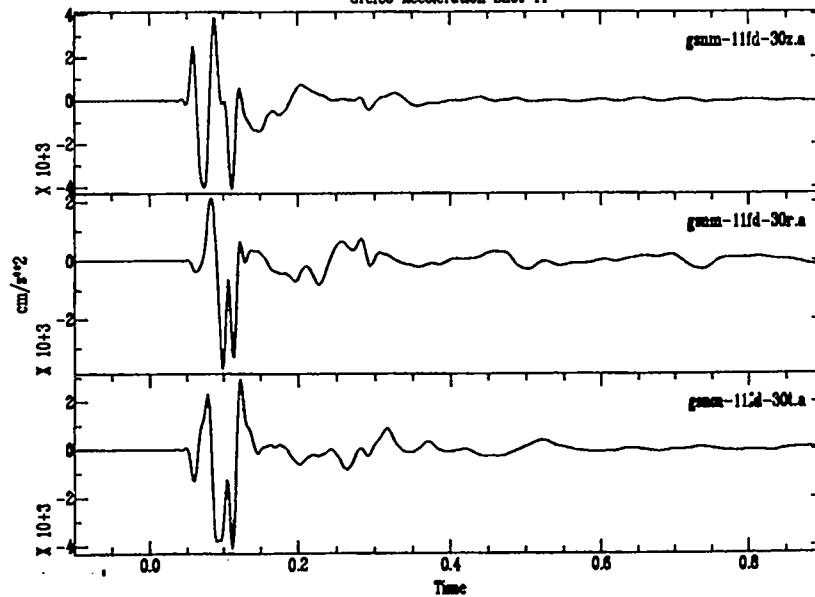
Grefco Acceleration Shot 11

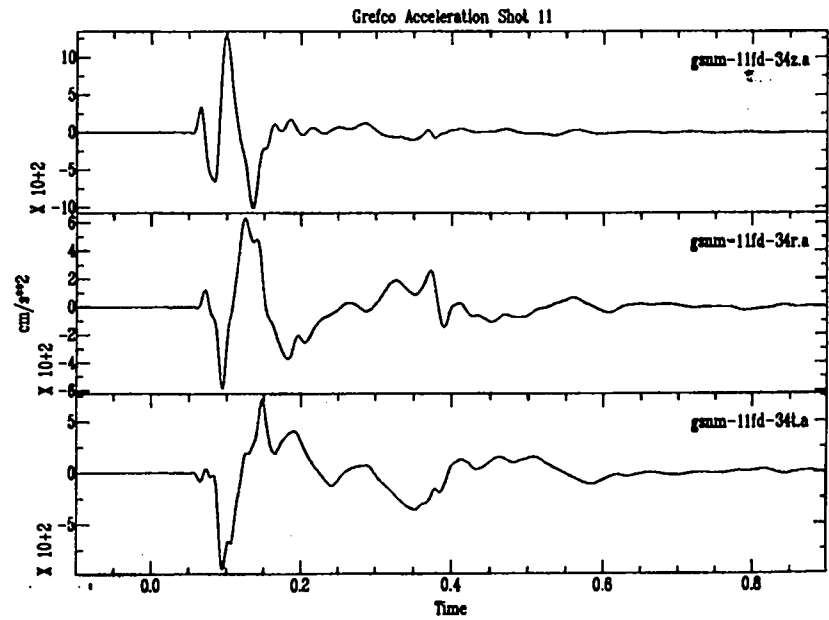
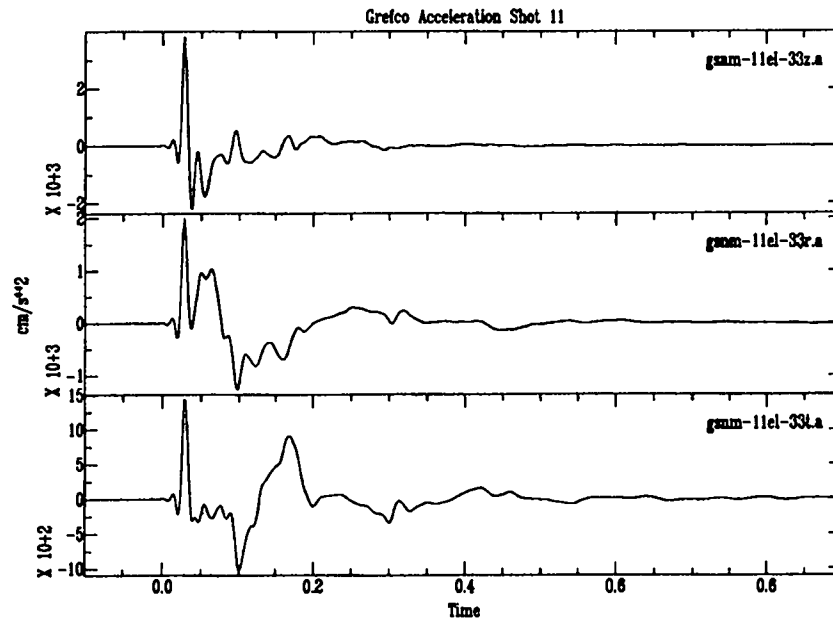
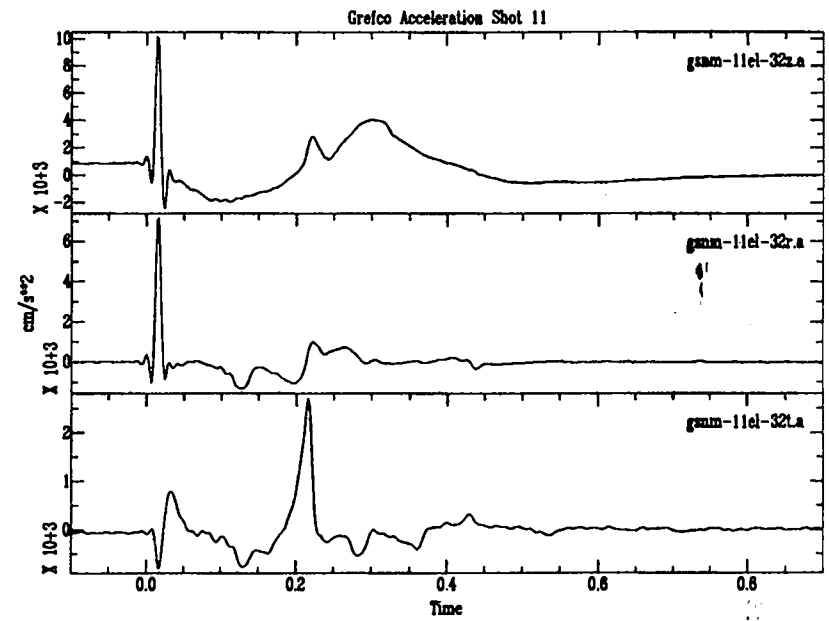
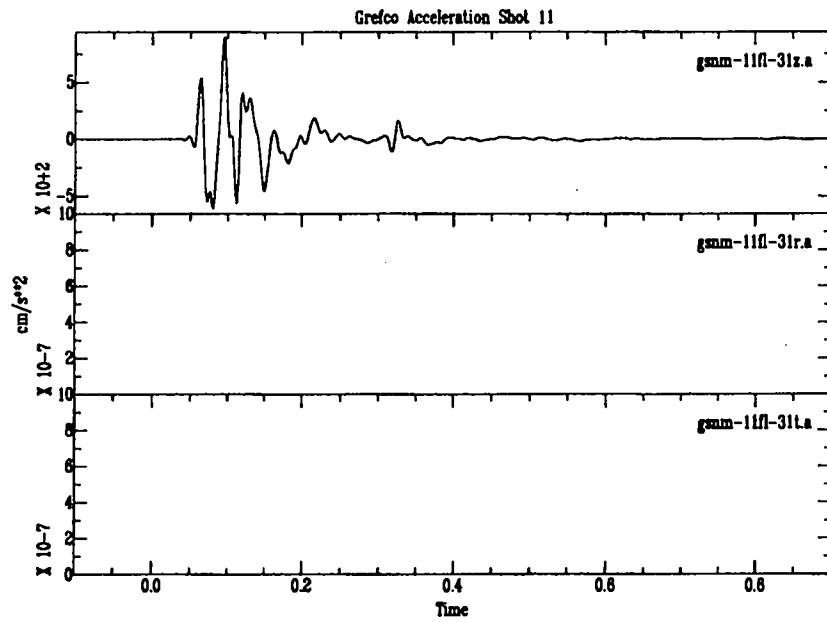


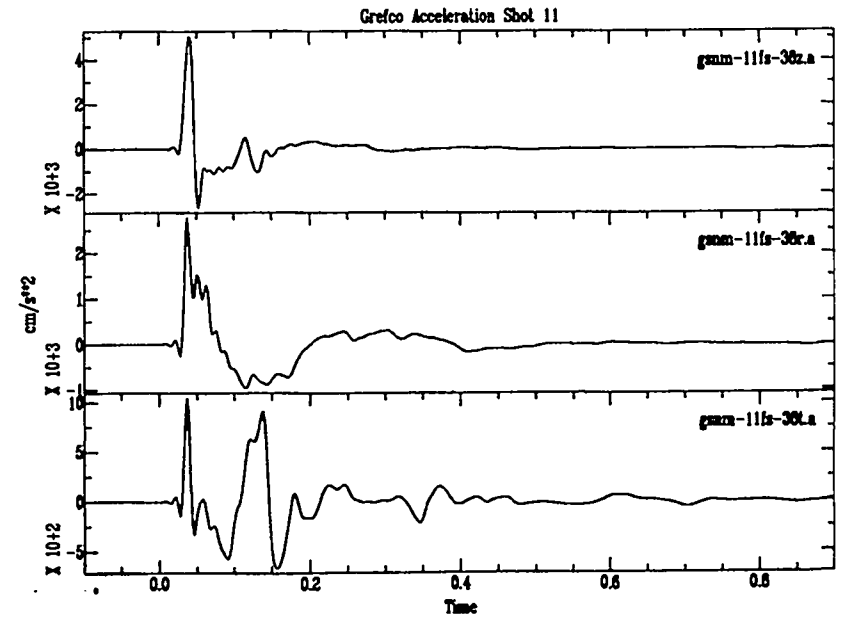
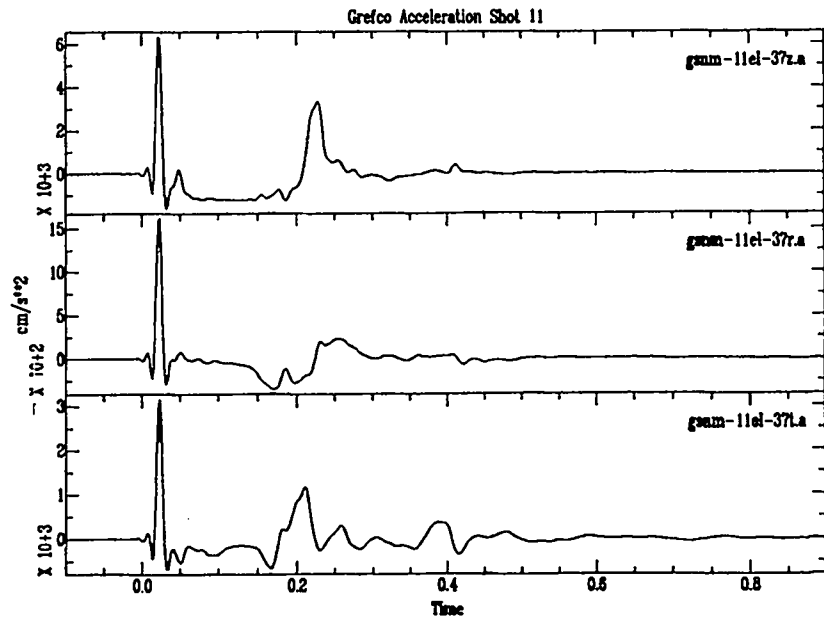
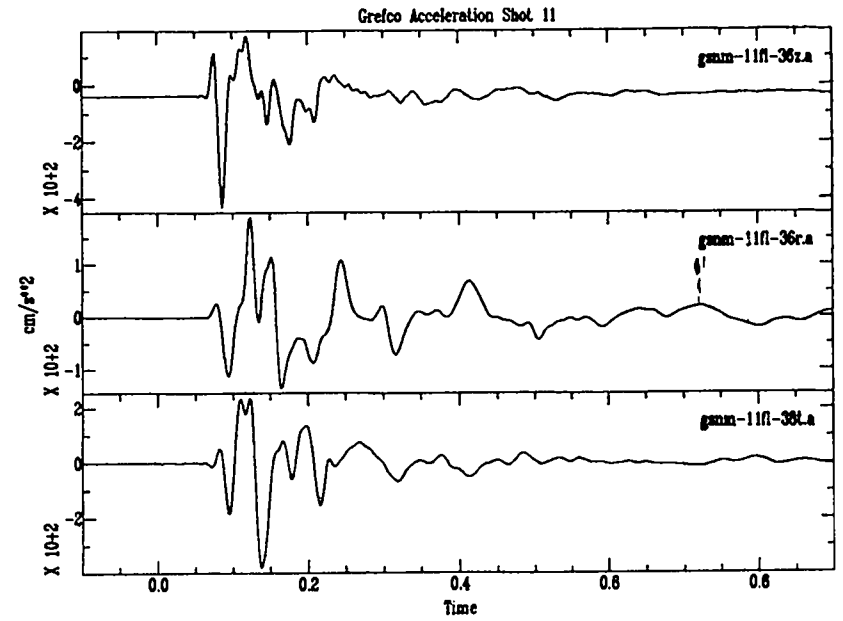
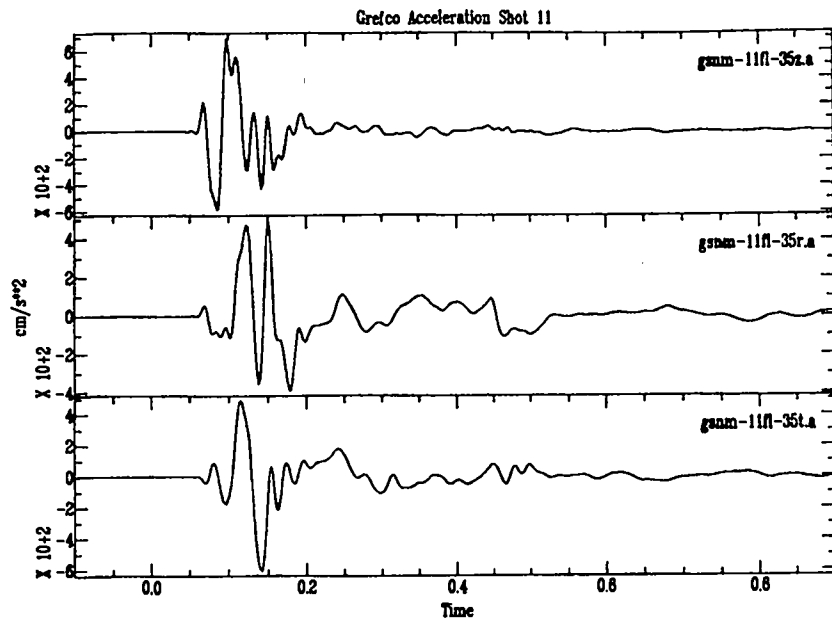
Grefco Acceleration Shot 11

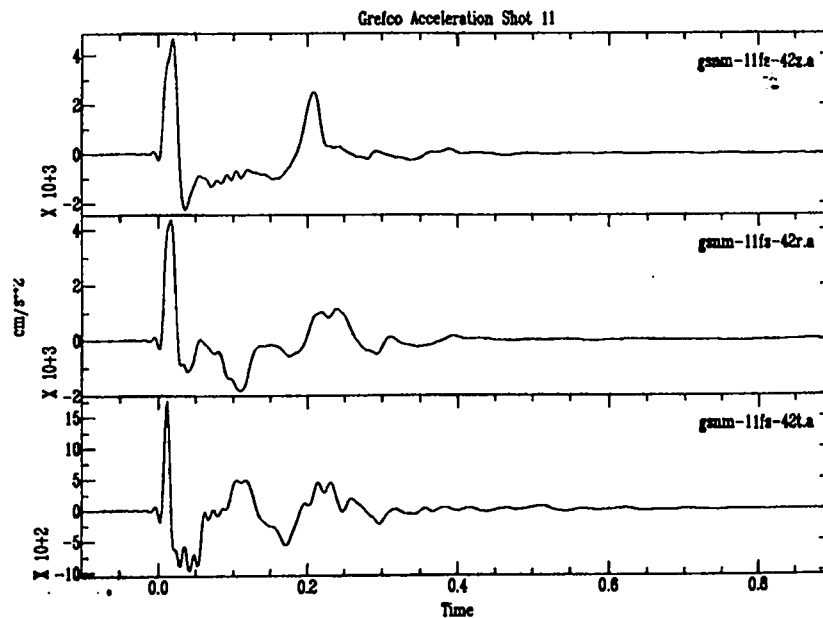
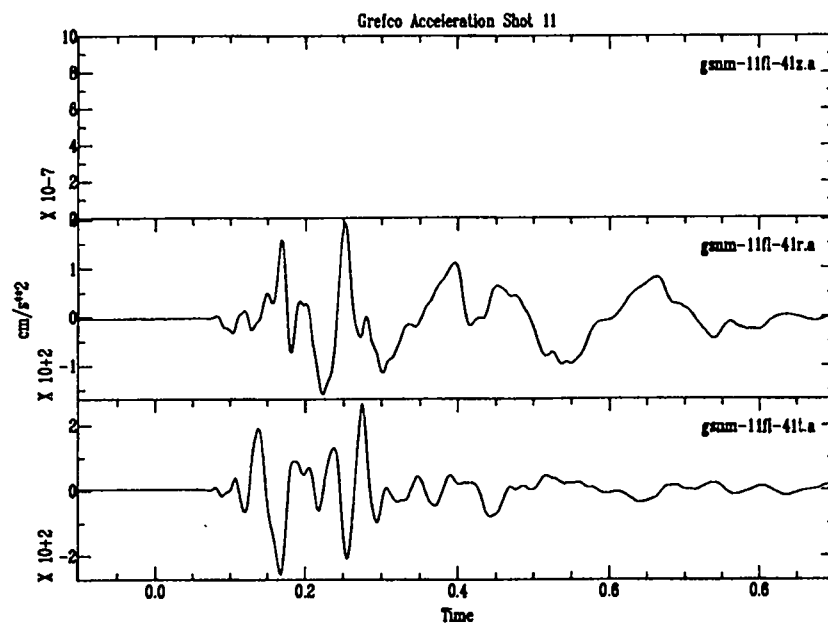
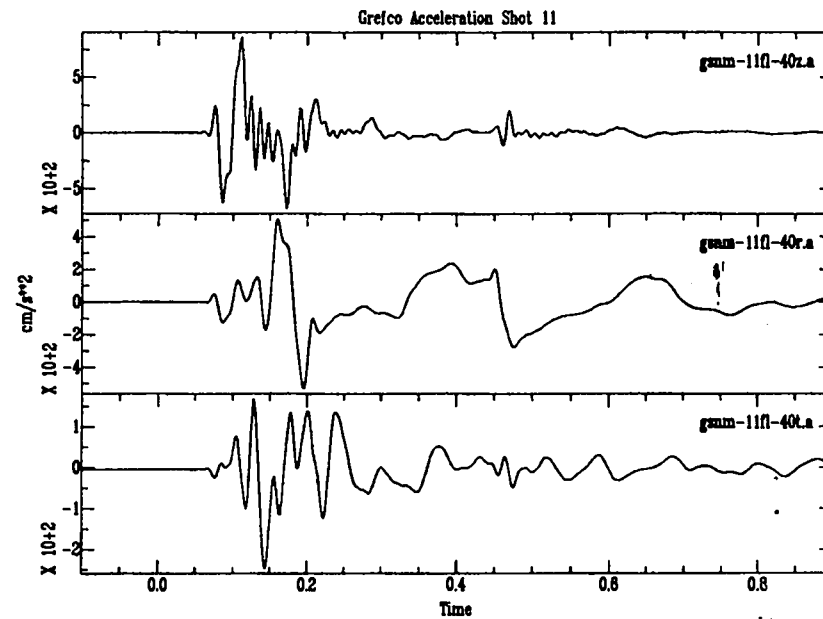
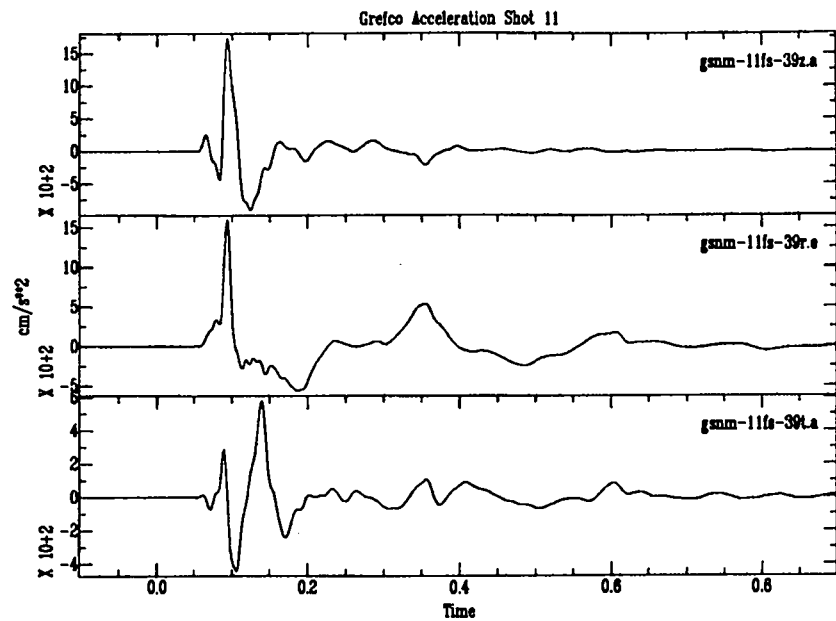


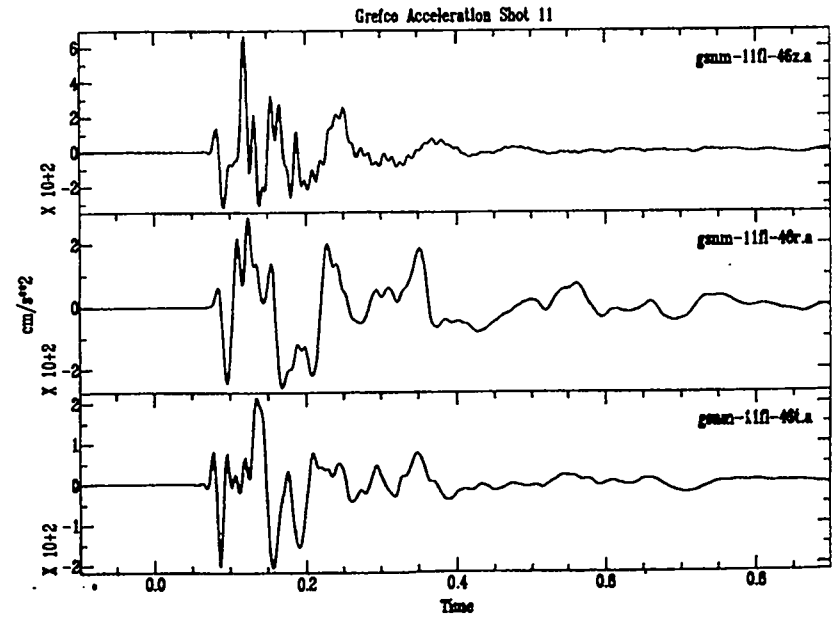
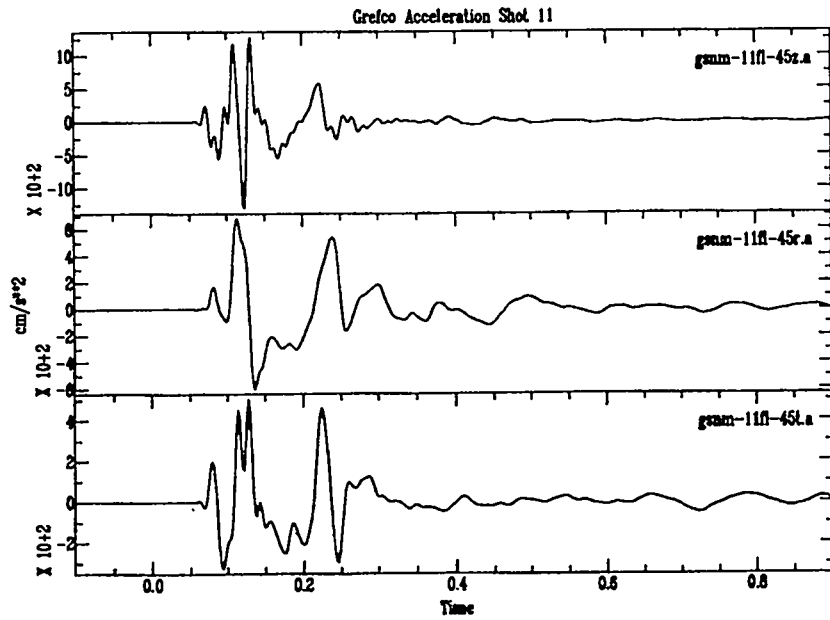
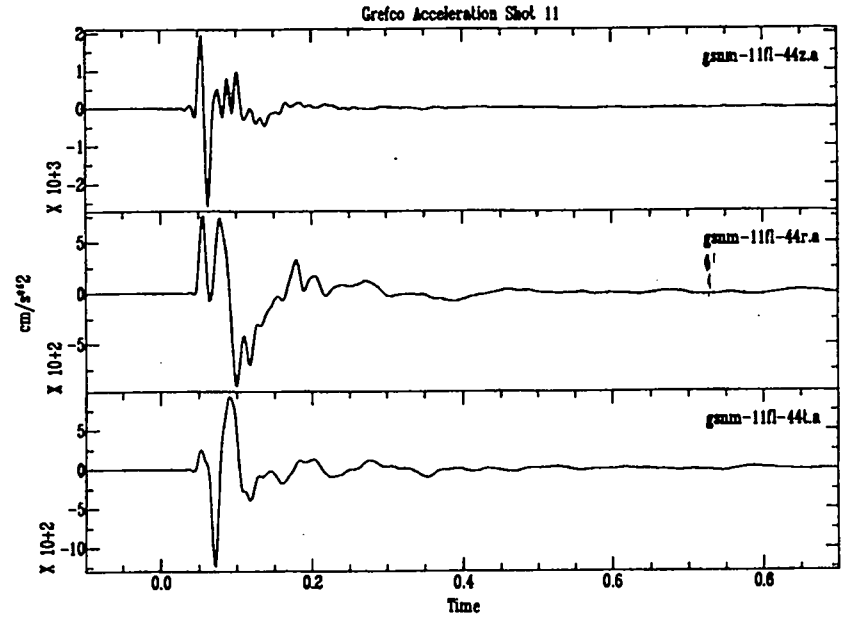
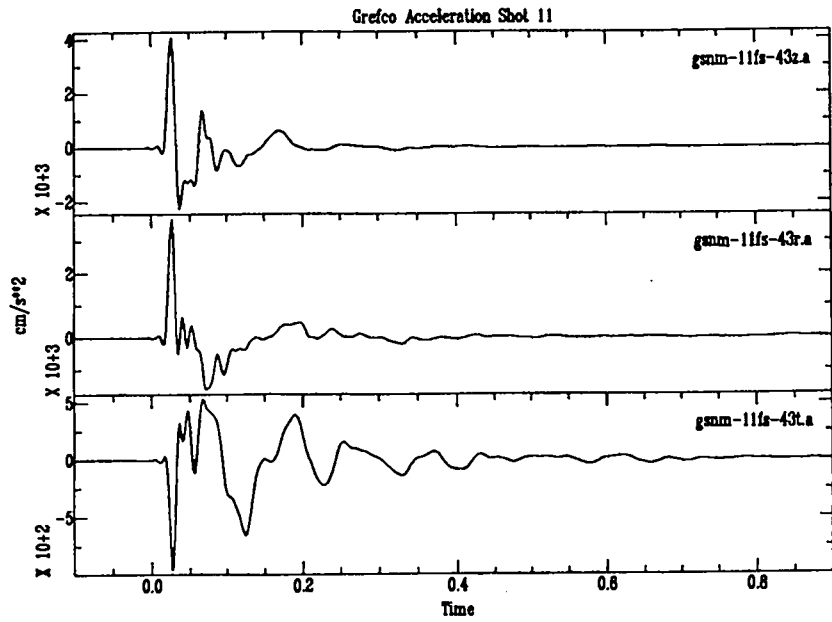
Grefco Acceleration Shot 11



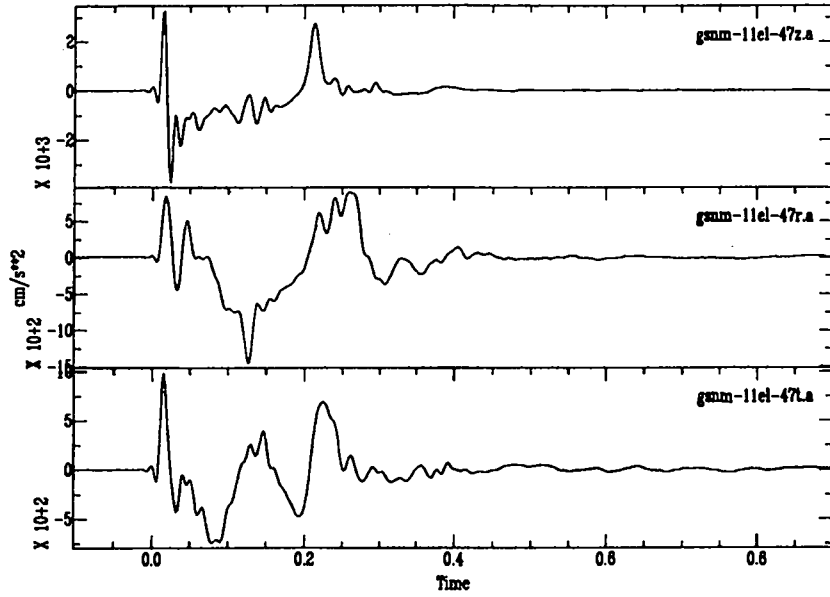




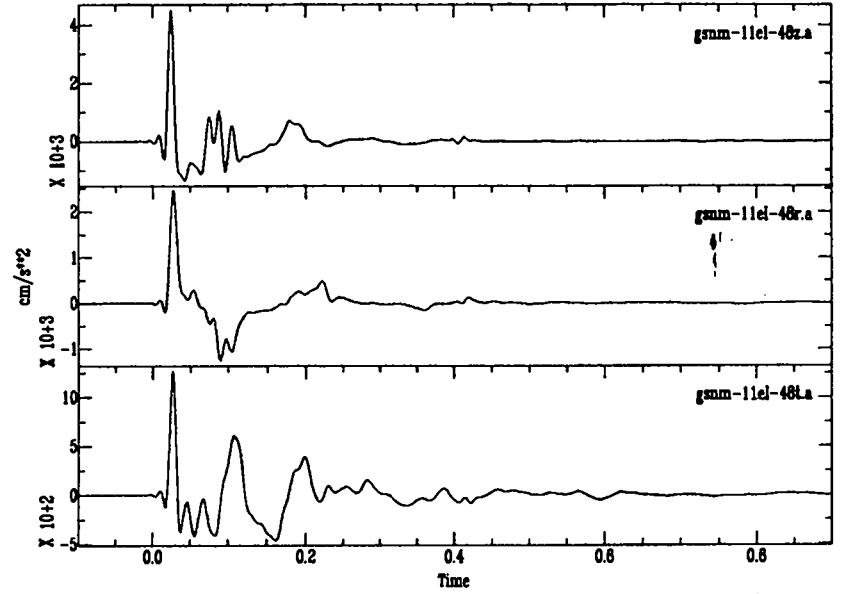




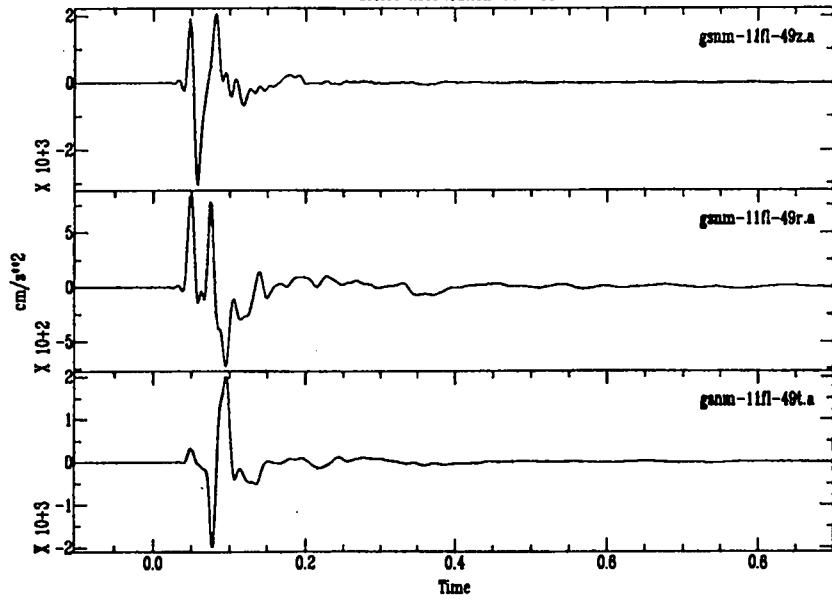
Grefco Acceleration Shot 11



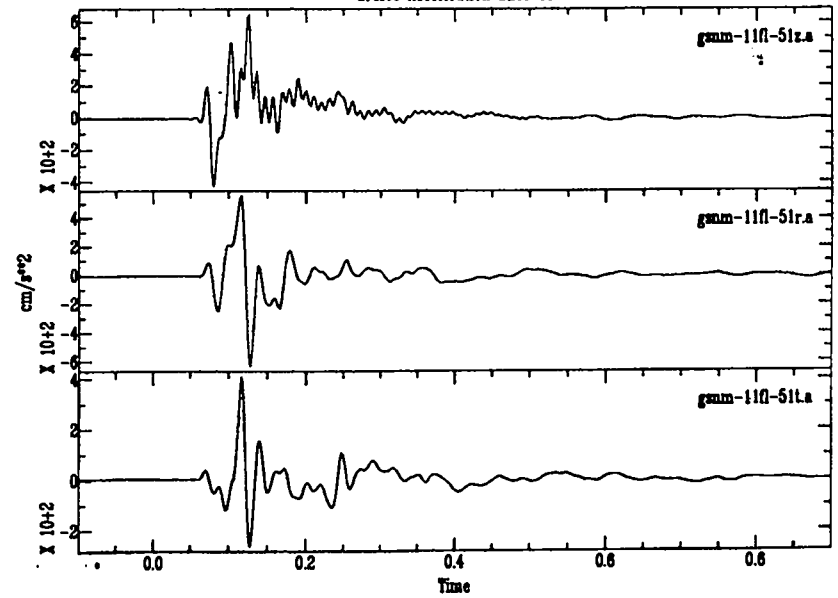
Grefco Acceleration Shot 11

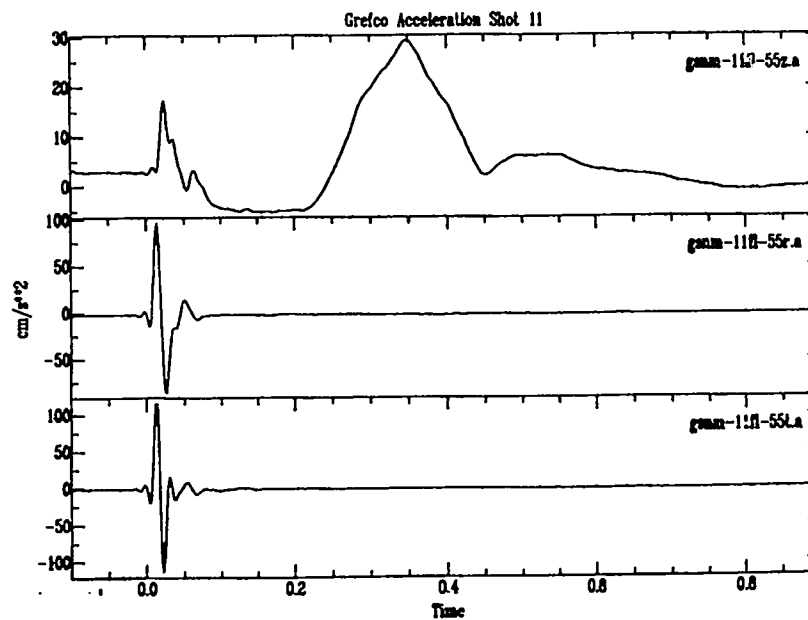
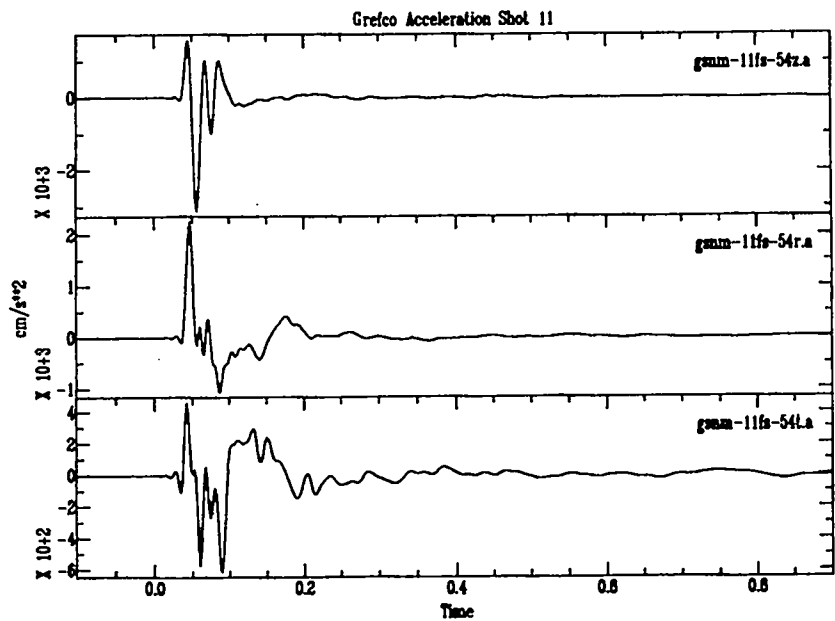
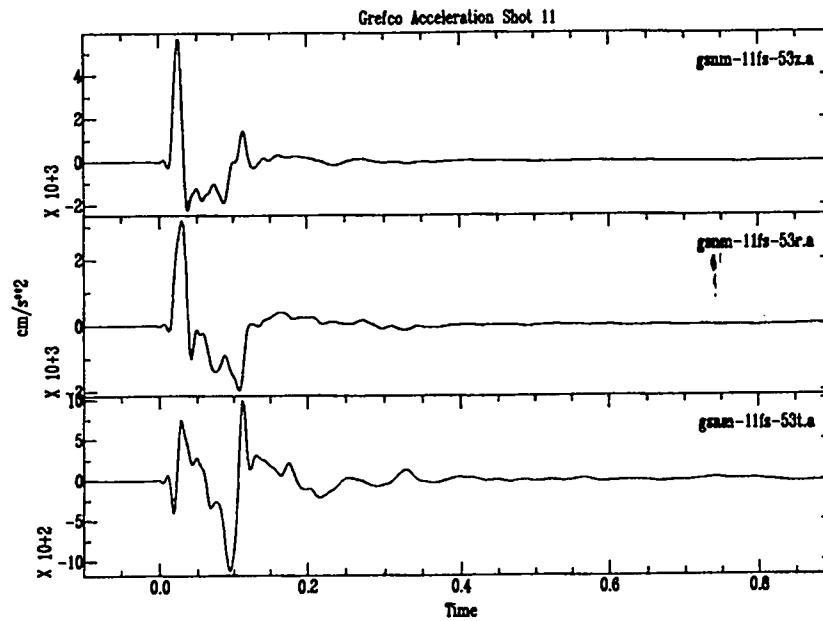
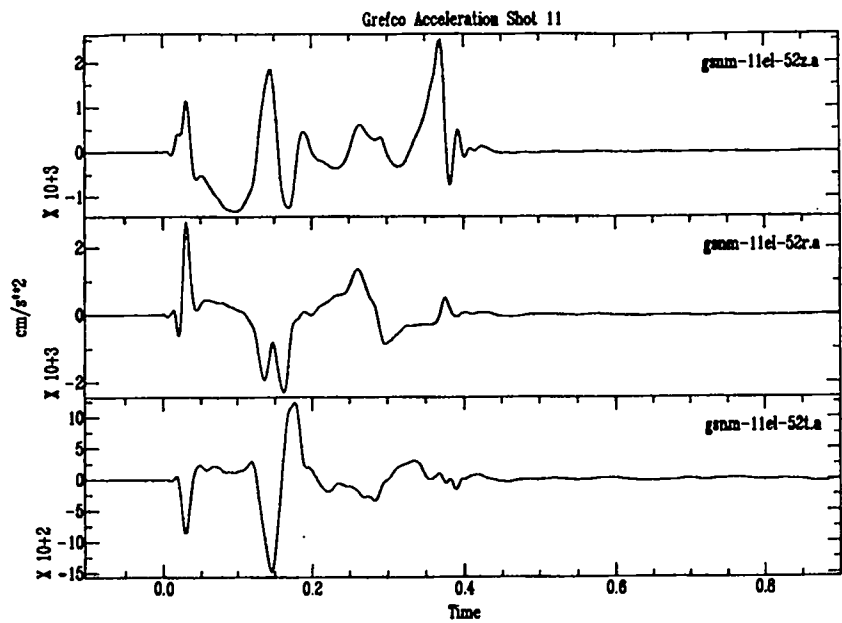


Grefco Acceleration Shot 11

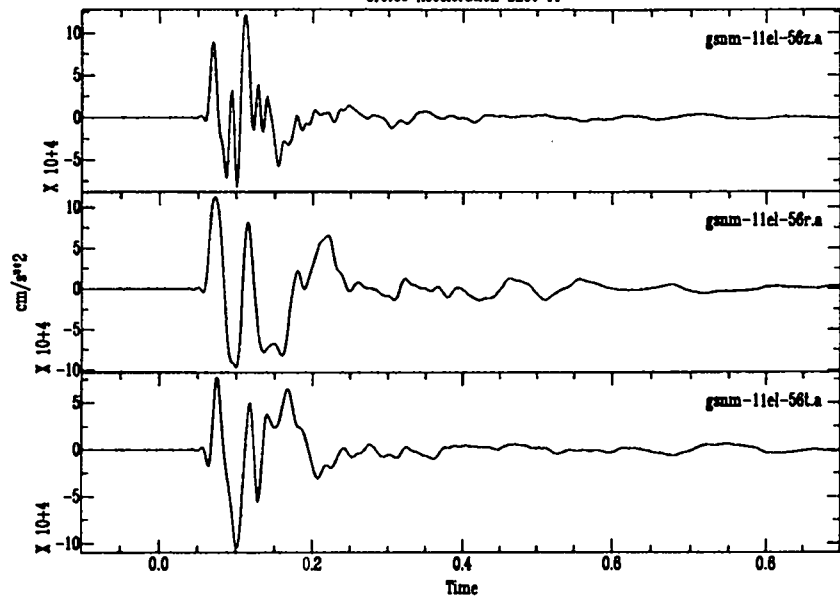


Grefco Acceleration Shot 11

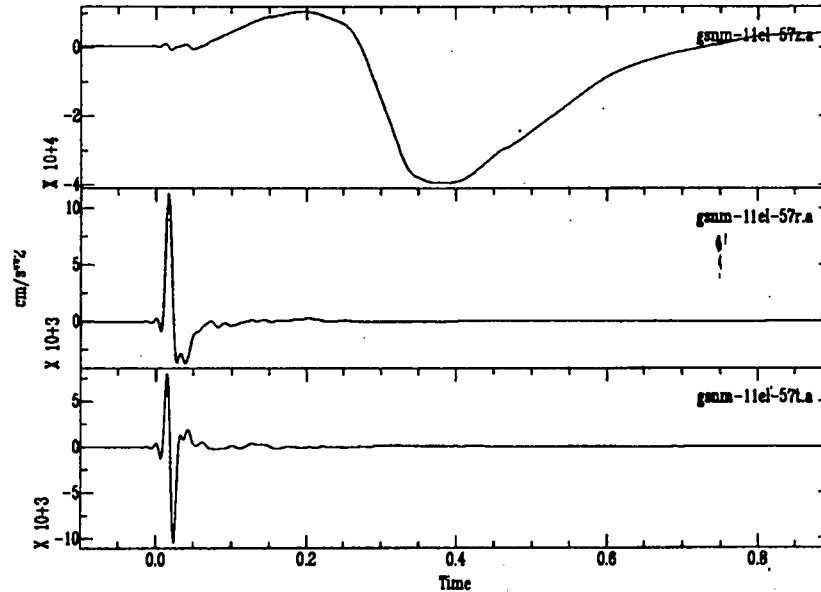




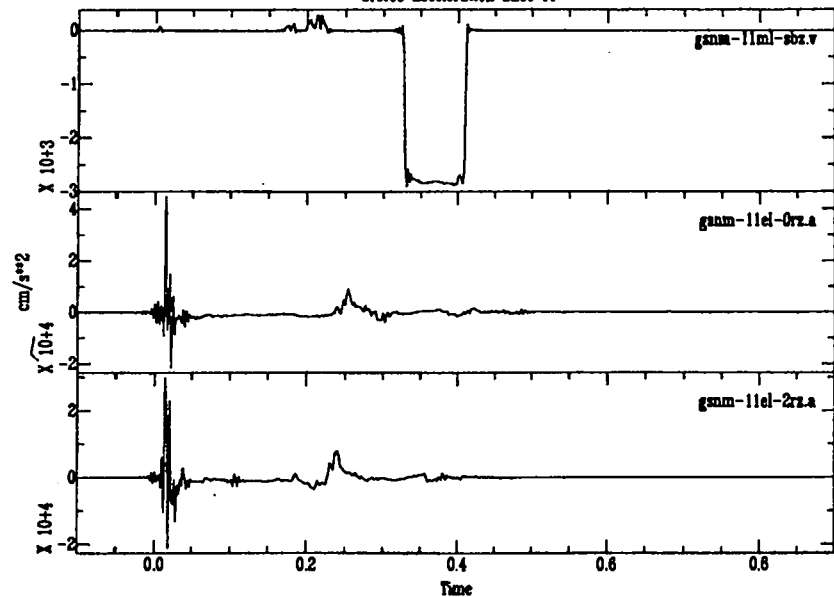
Grefco Acceleration Shot 11



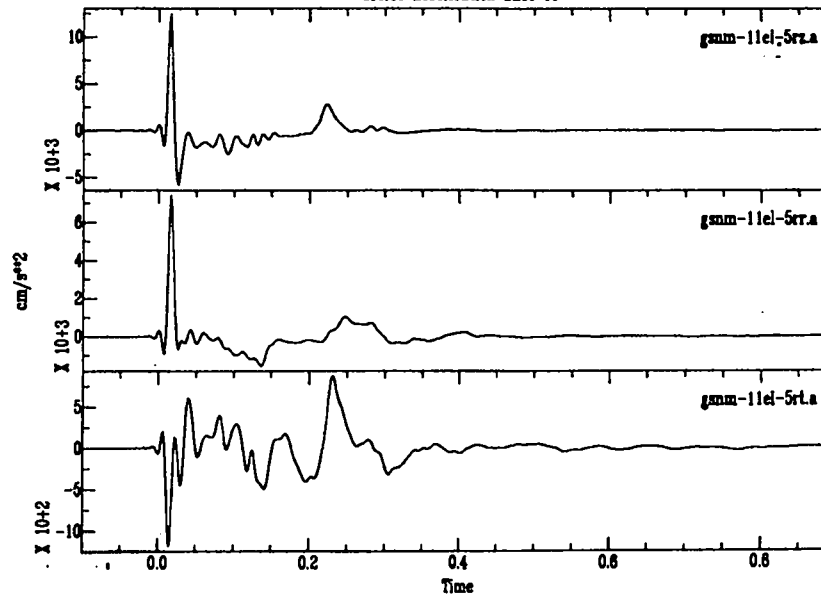
Grefco Acceleration Shot 11

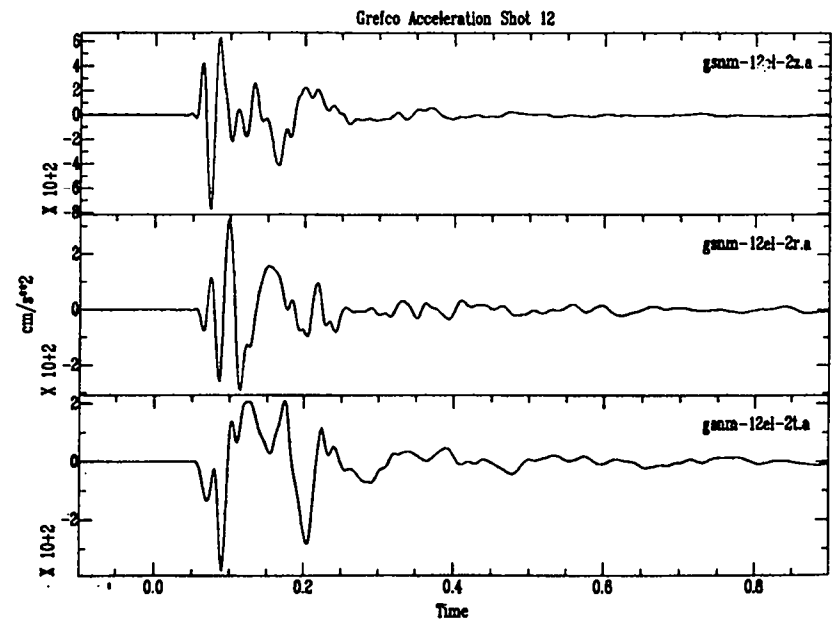
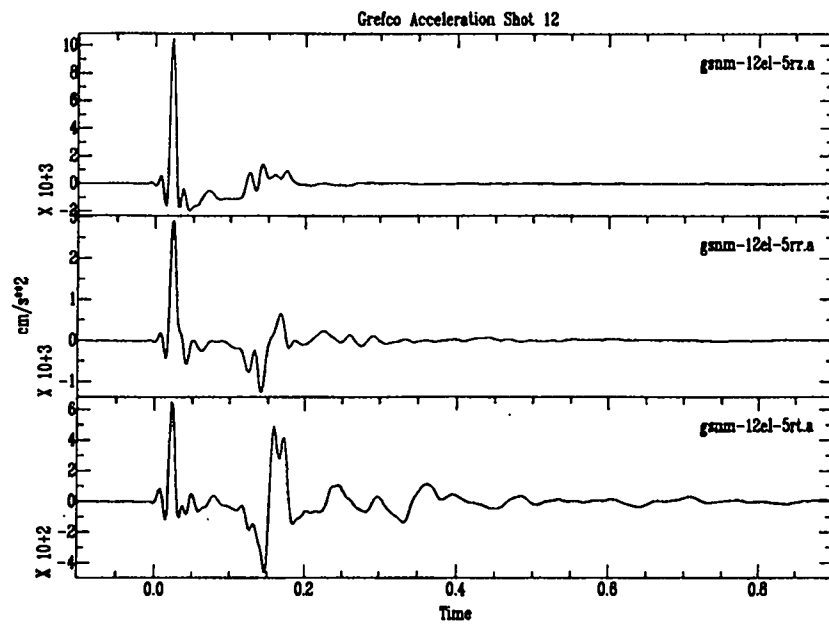
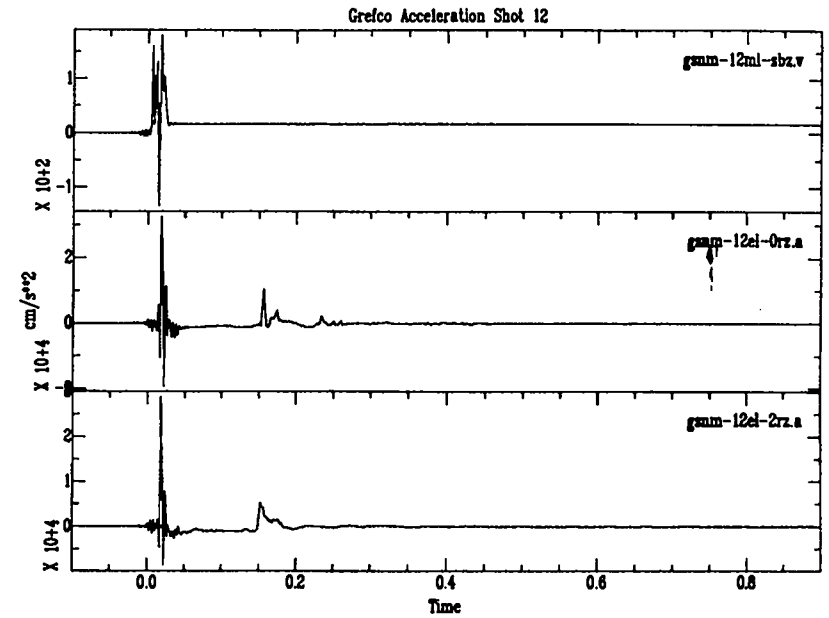
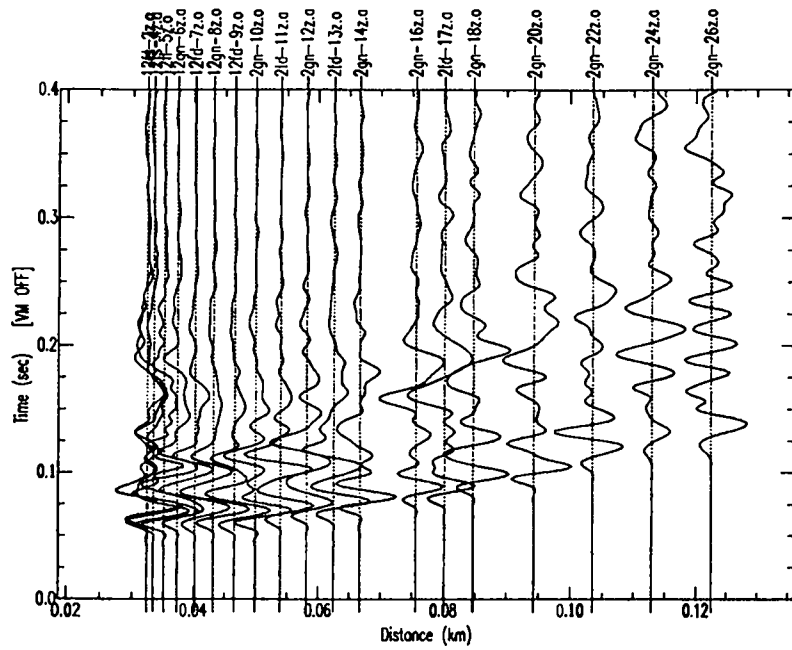


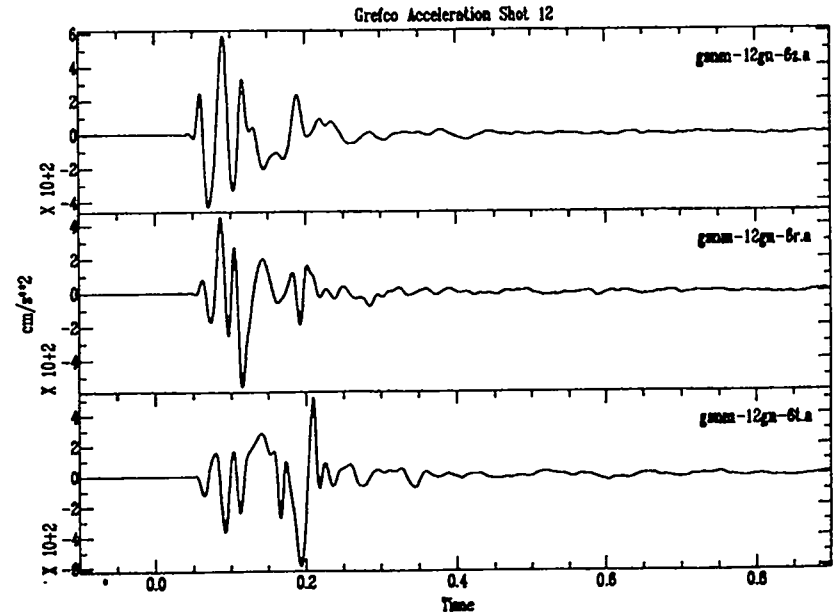
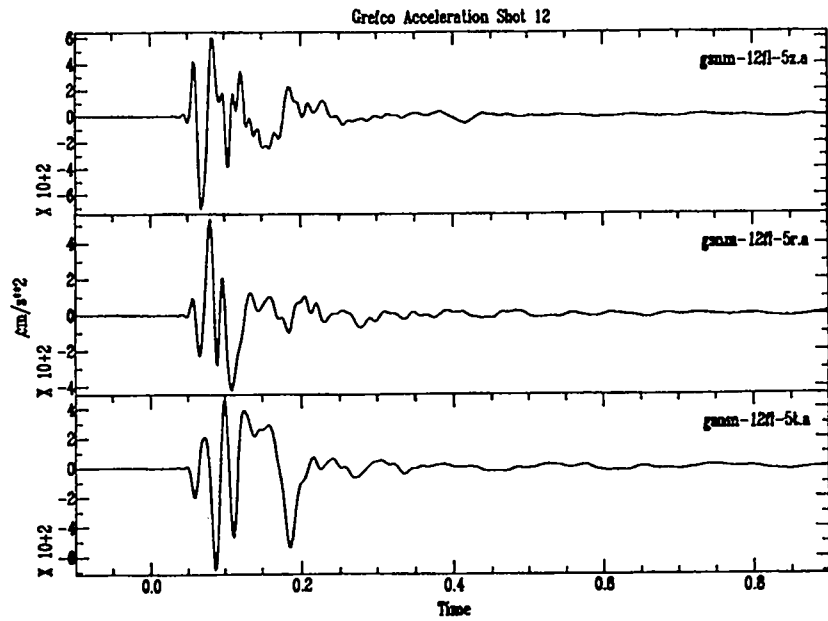
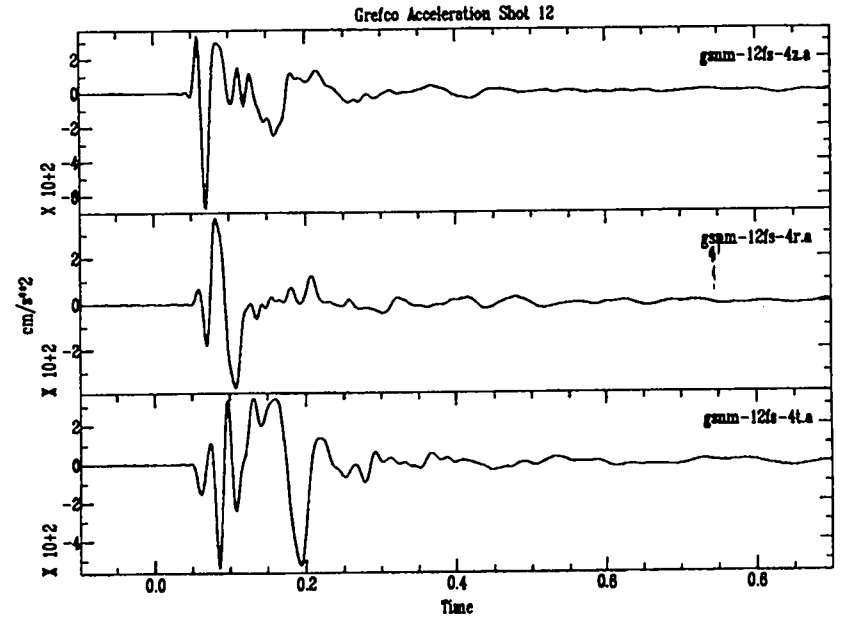
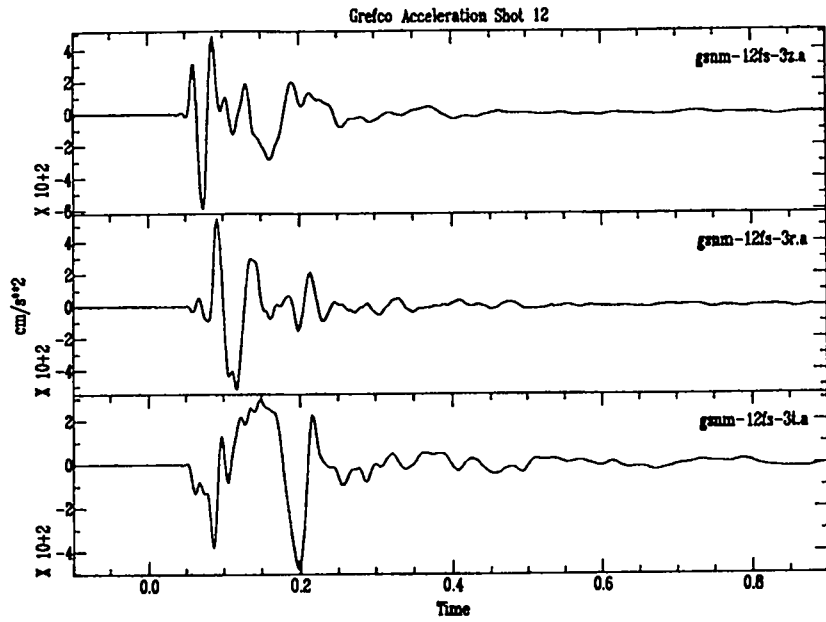
Grefco Acceleration Shot 11

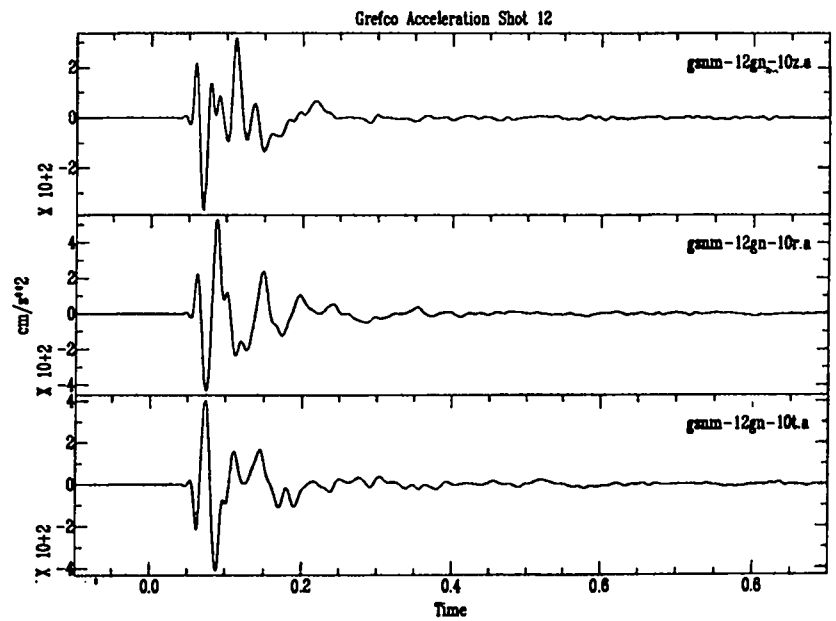
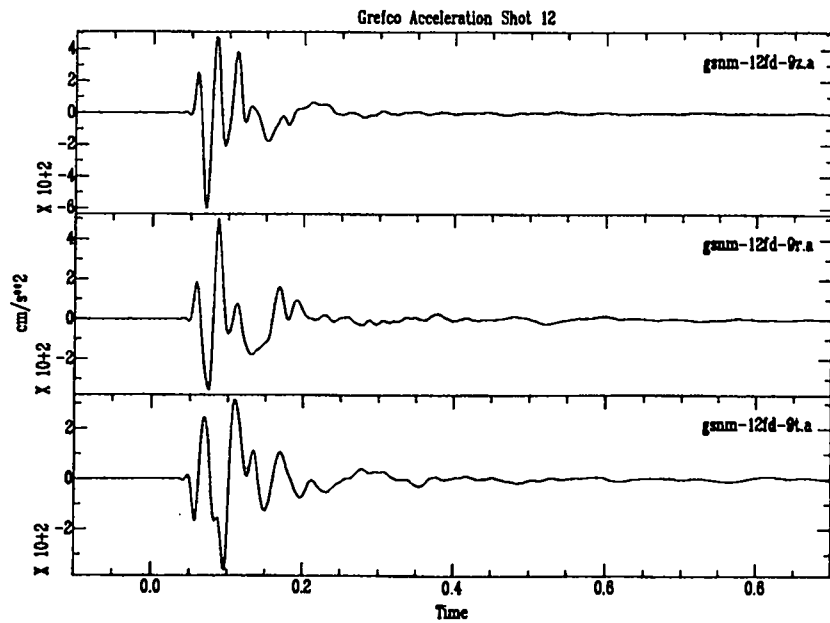
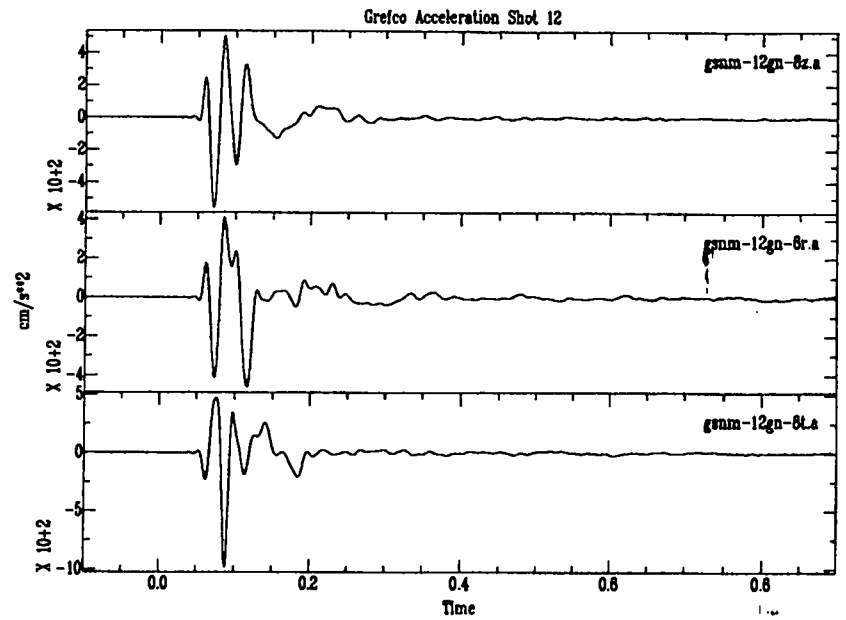
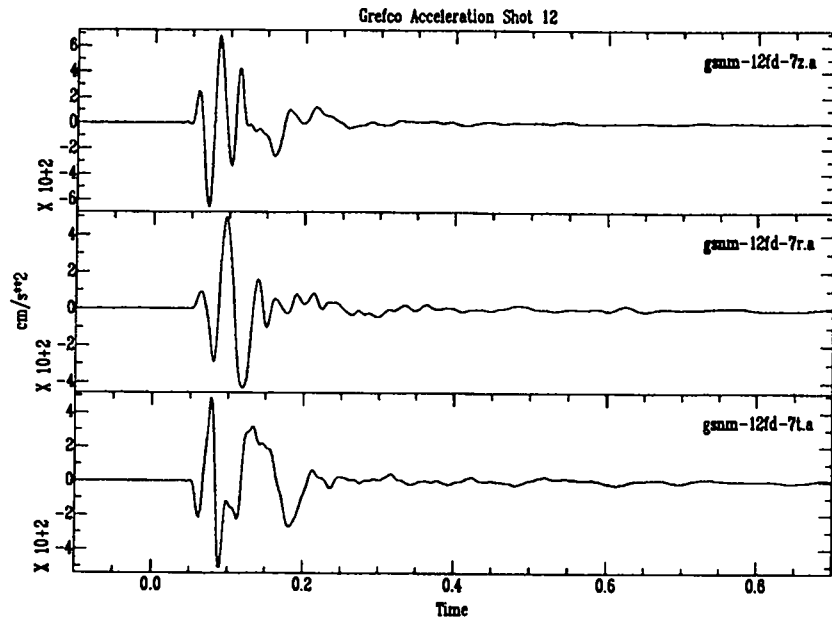


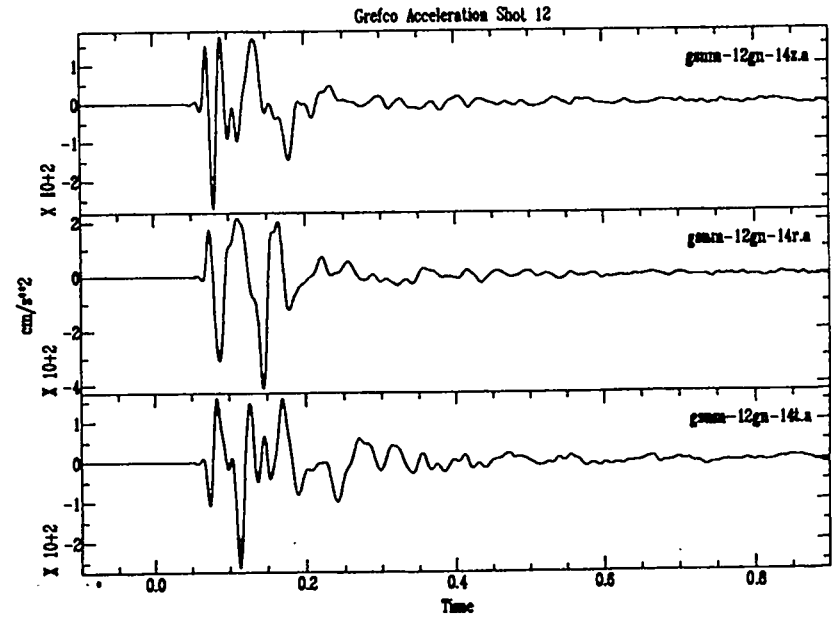
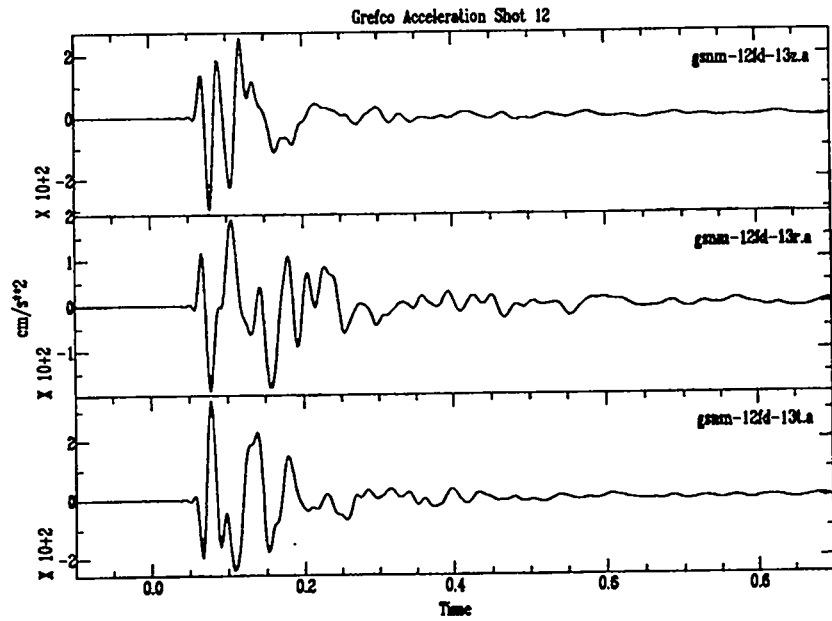
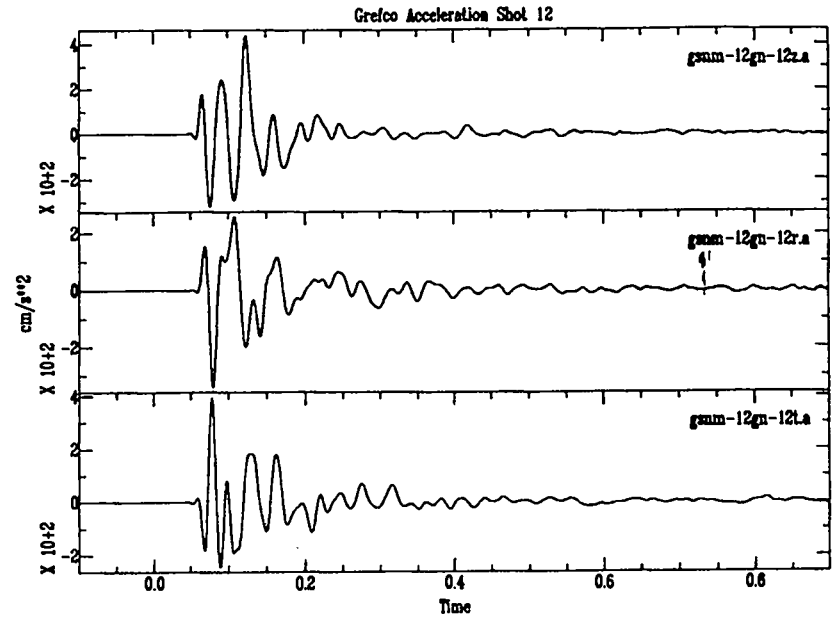
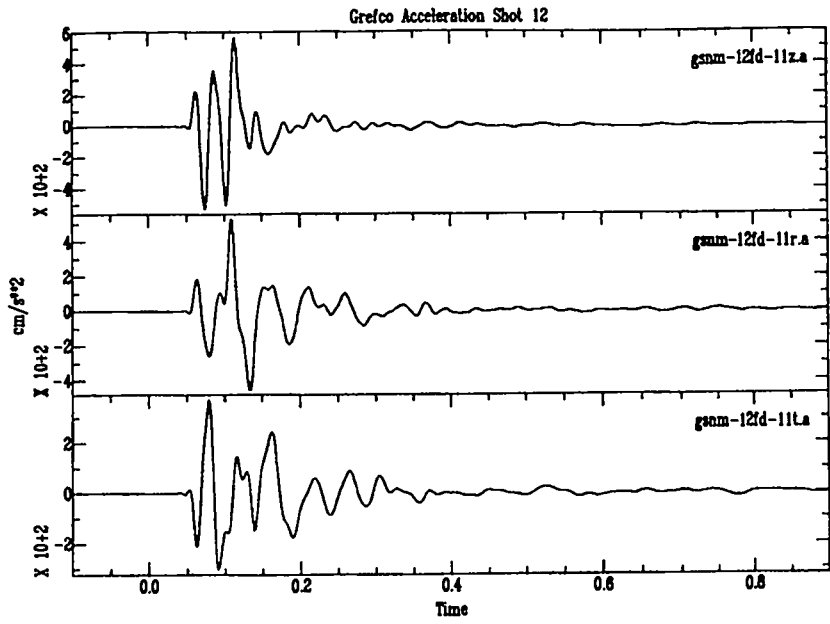
Grefco Acceleration Shot 11

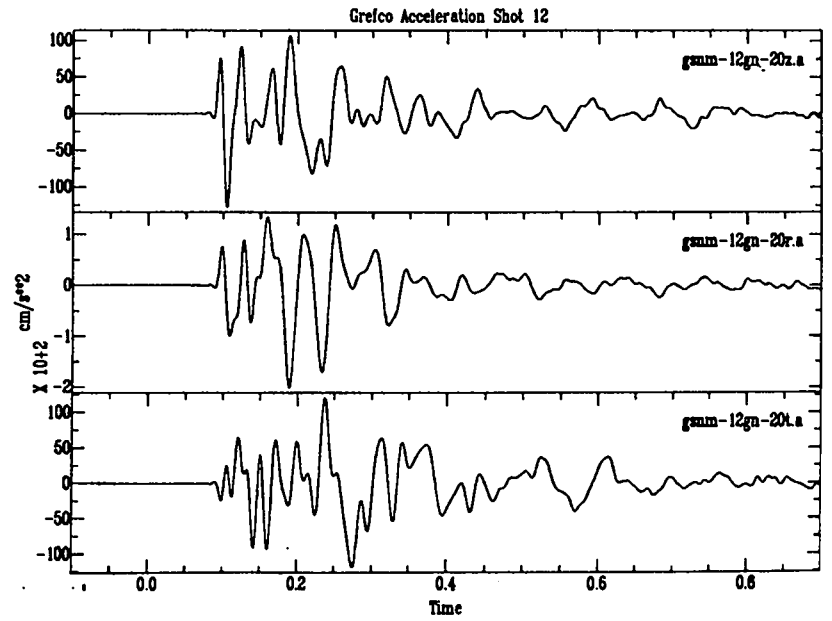
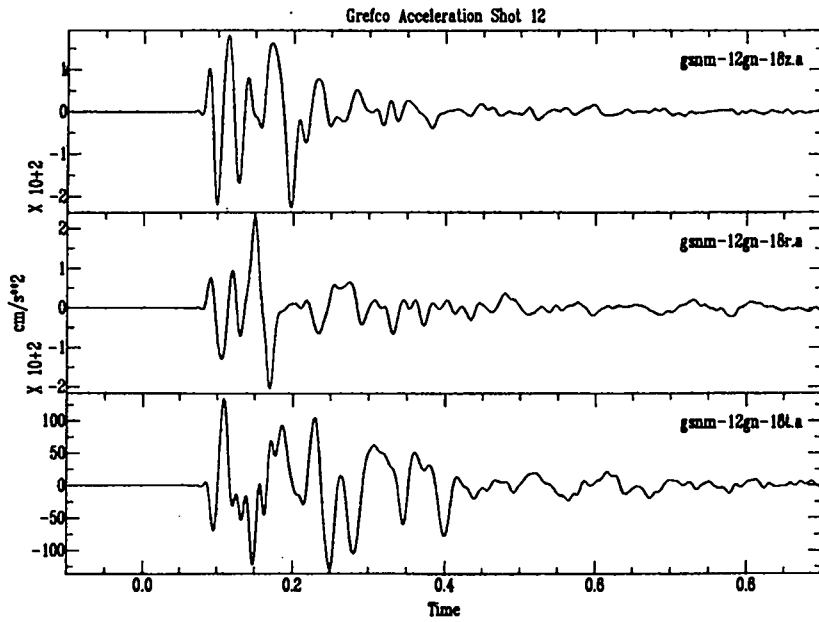
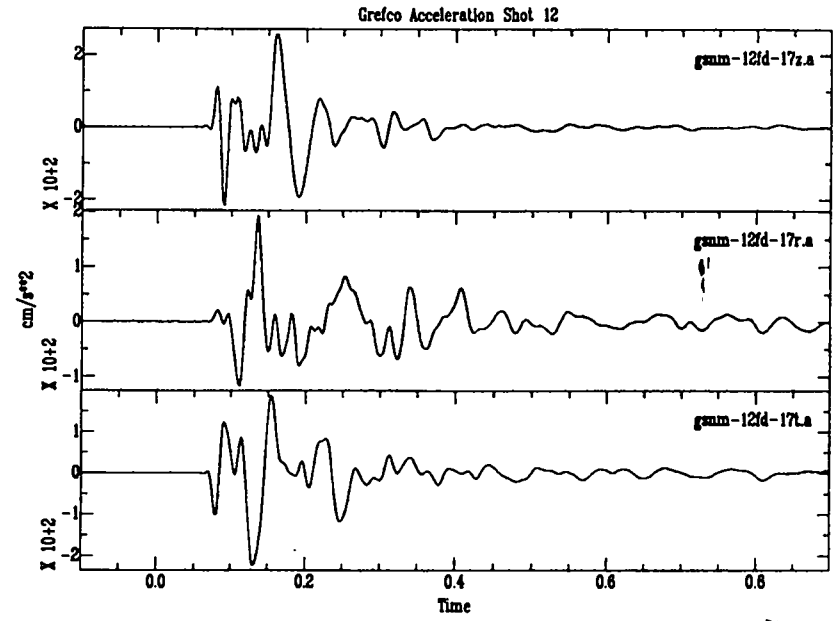
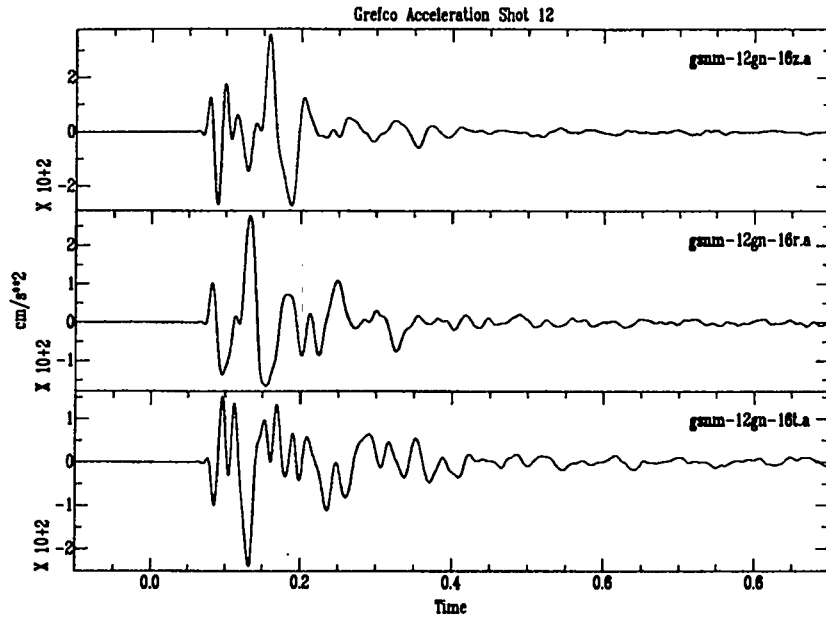


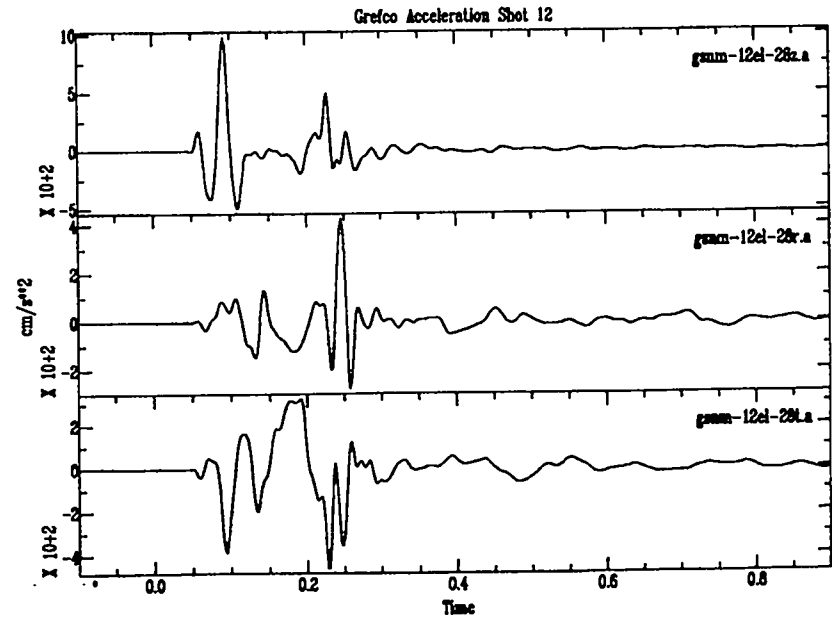
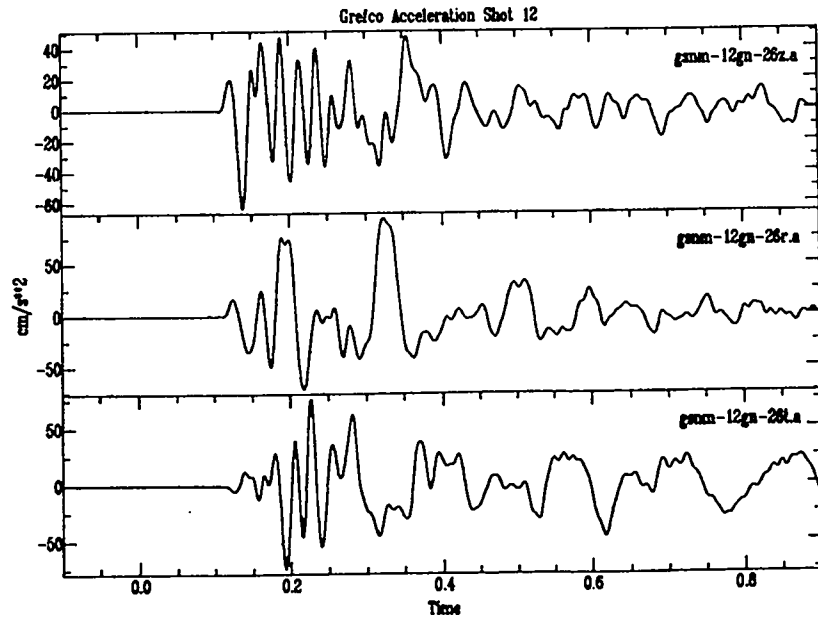
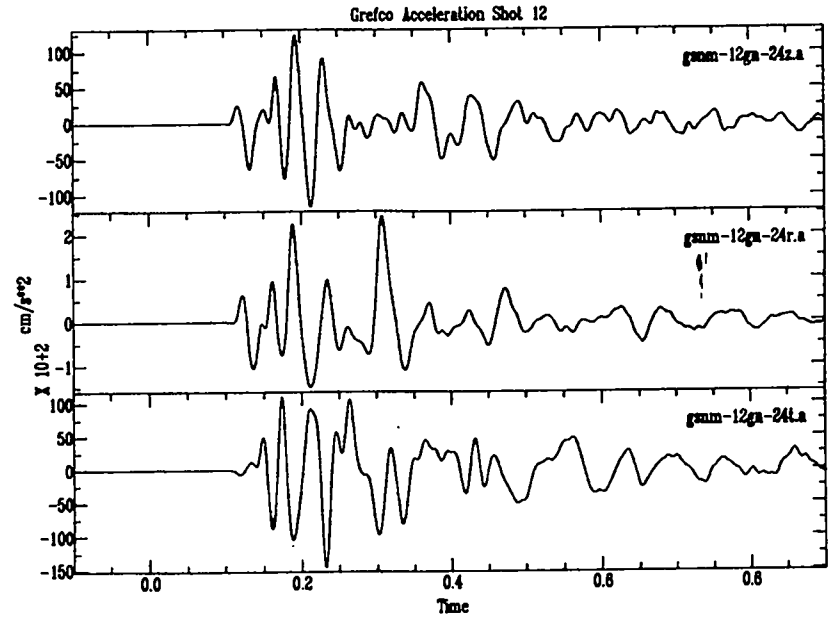
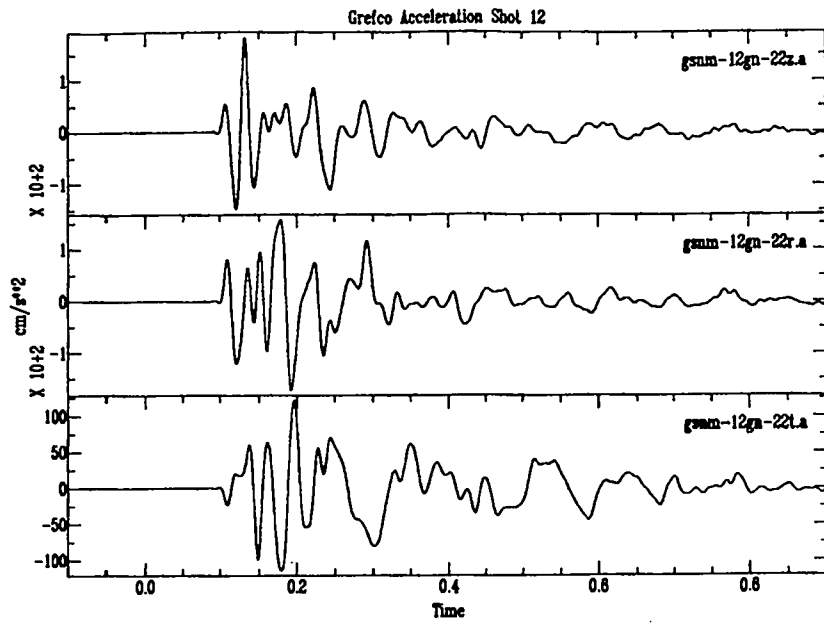




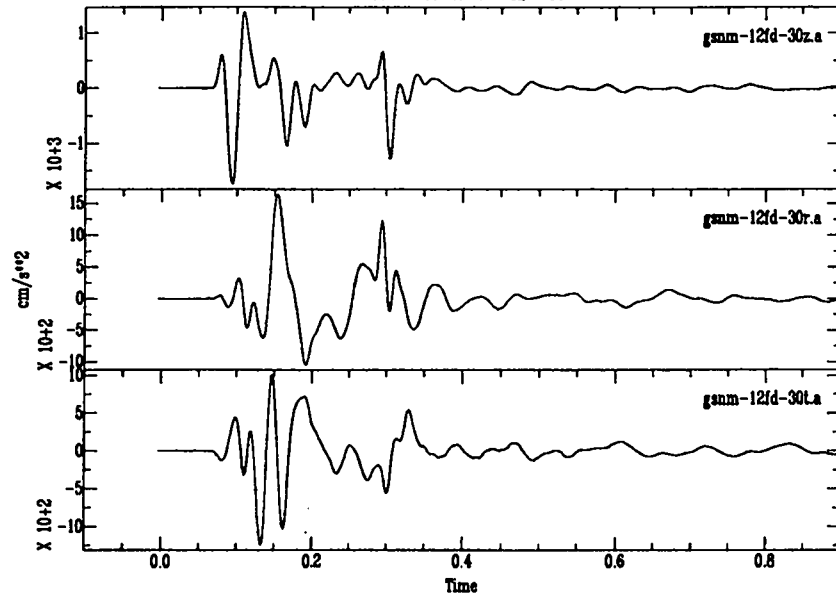




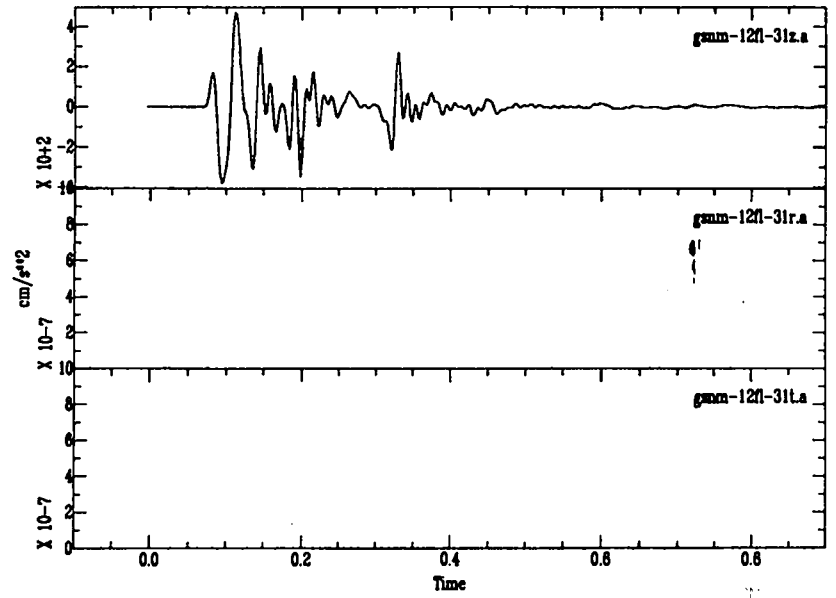




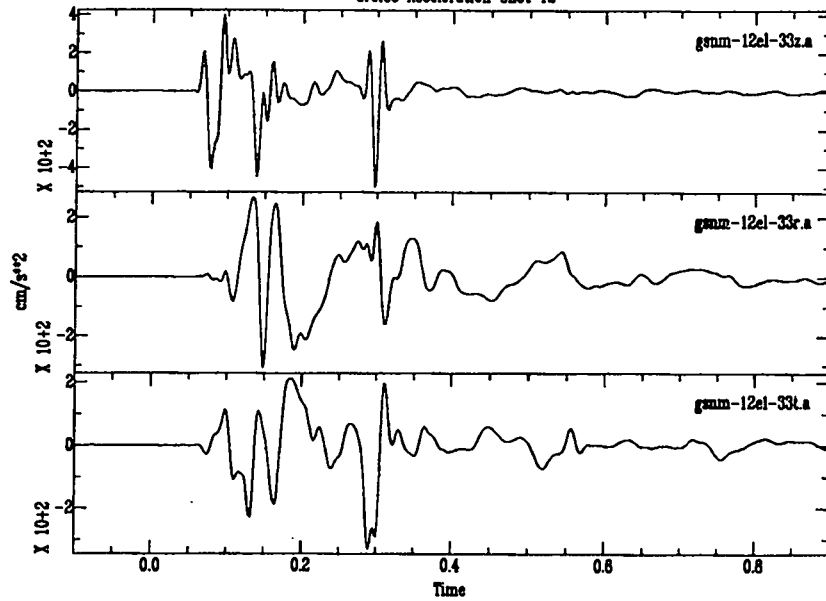
Grefco Acceleration Shot 12



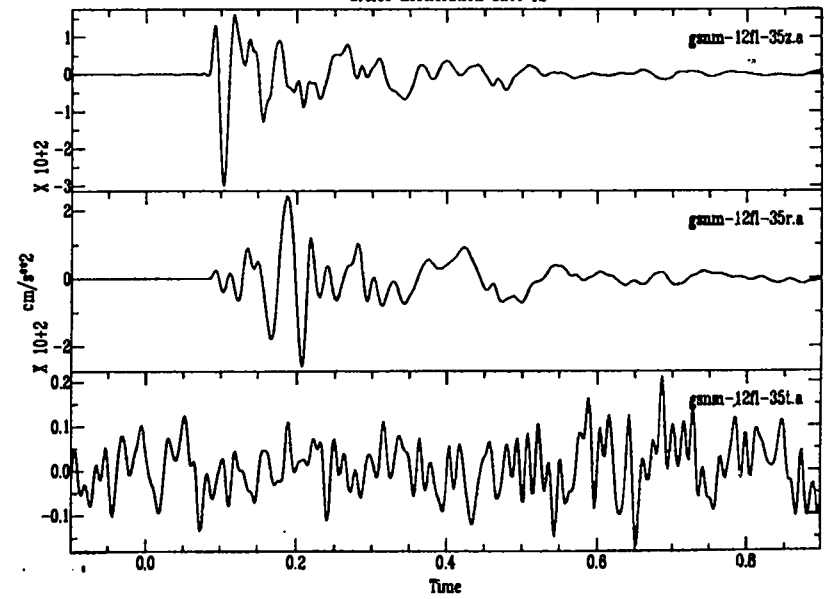
Grefco Acceleration Shot 12

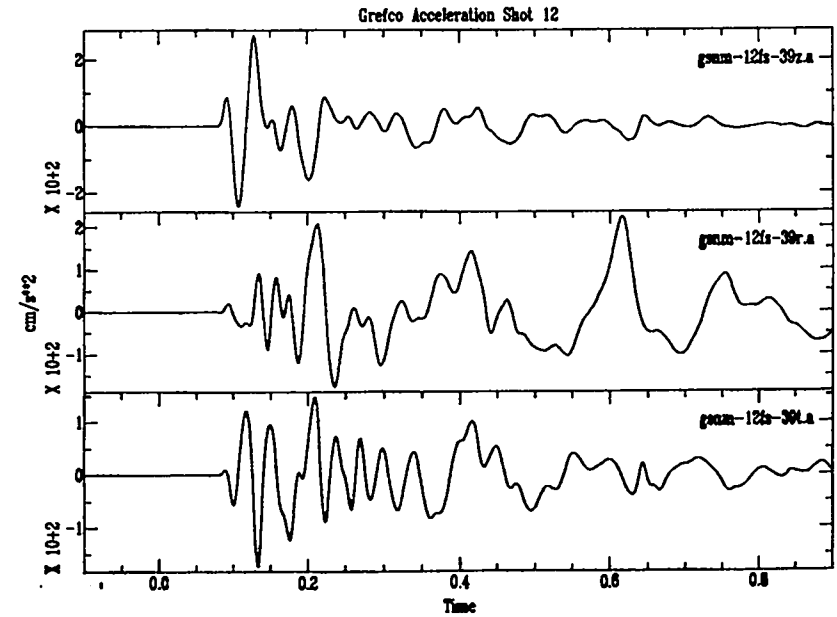
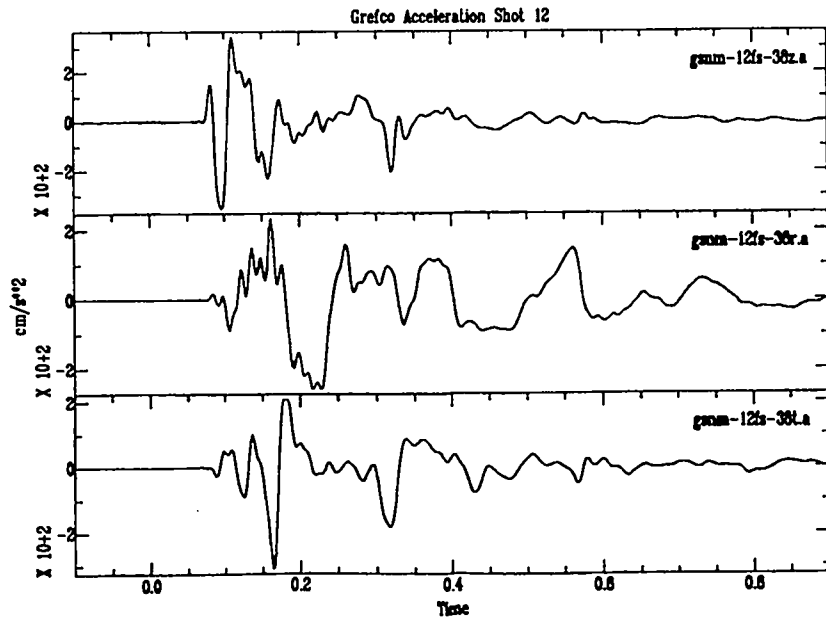
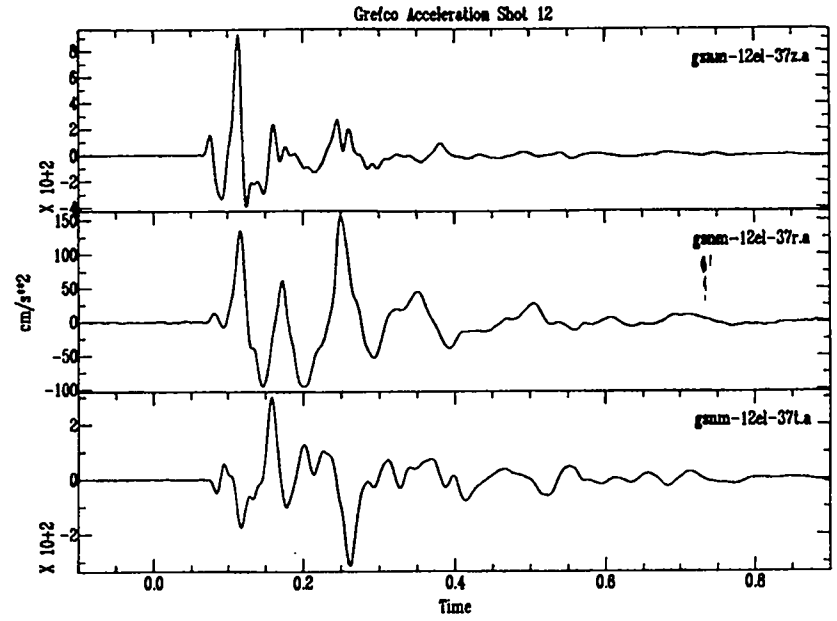
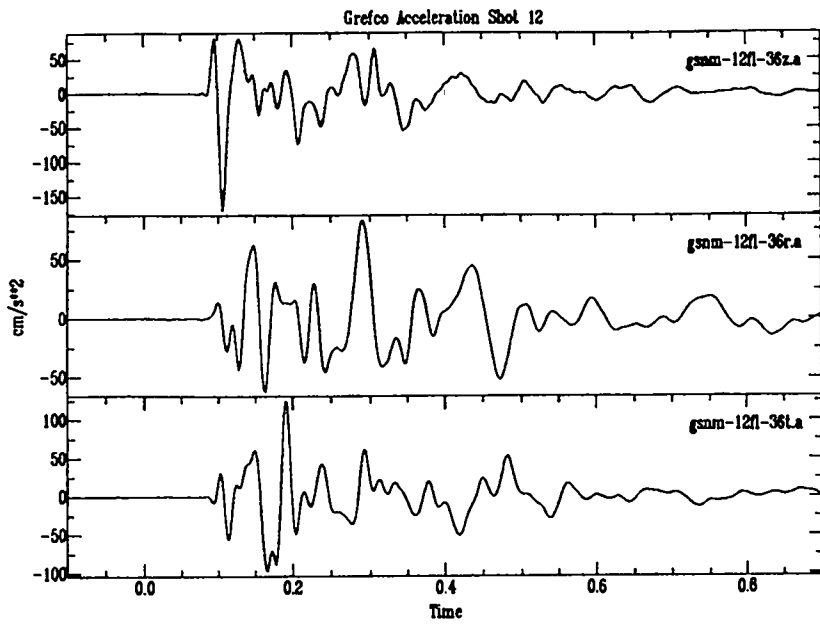


Grefco Acceleration Shot 12

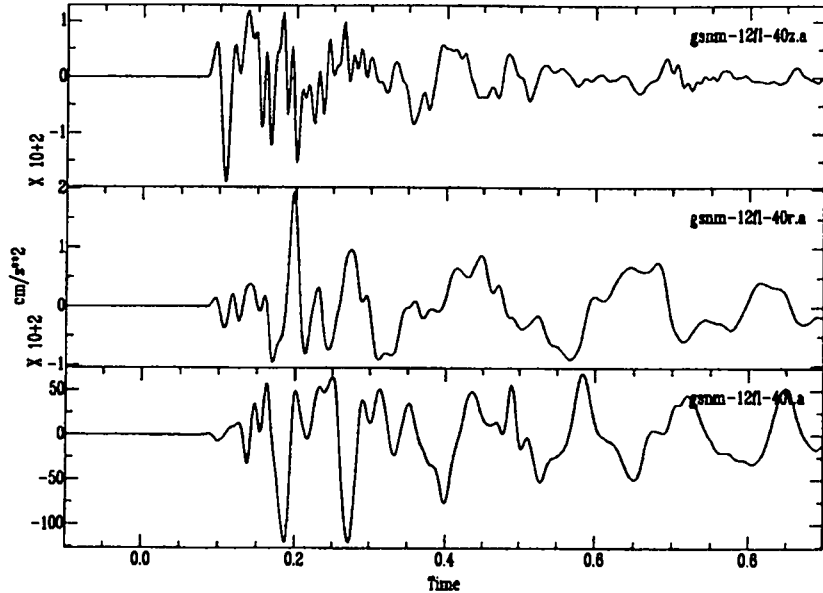


Grefco Acceleration Shot 12

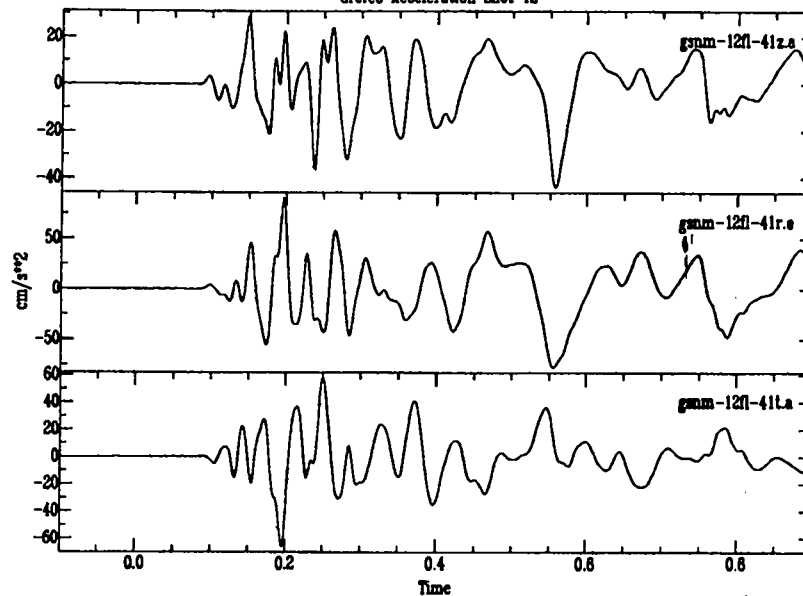




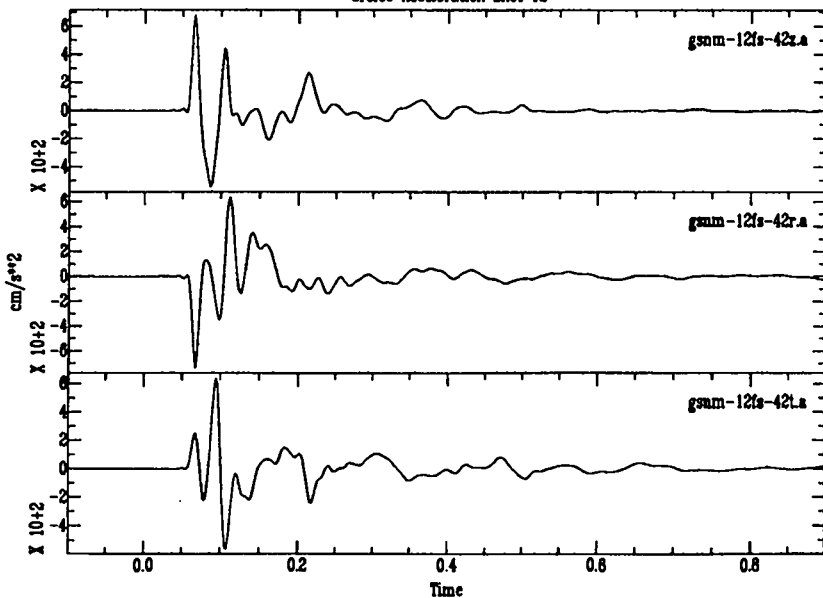
Grefco Acceleration Shot 12



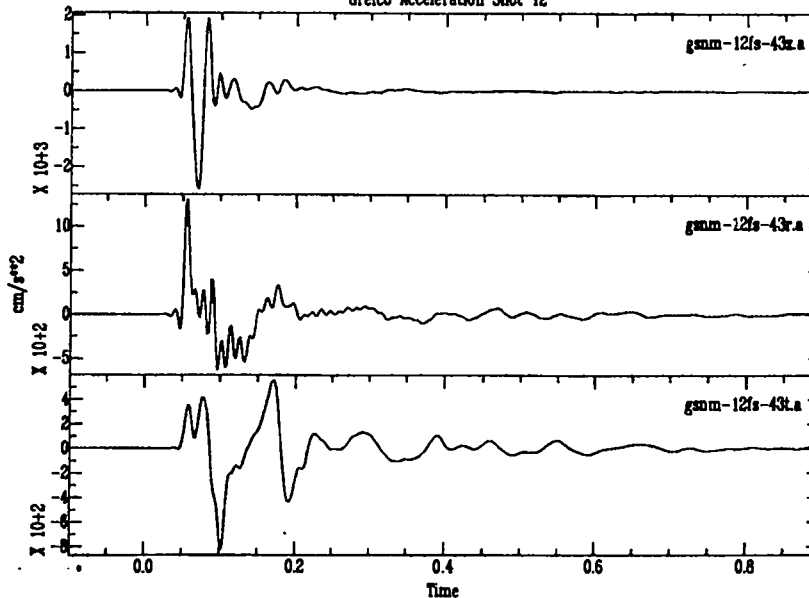
Grefco Acceleration Shot 12

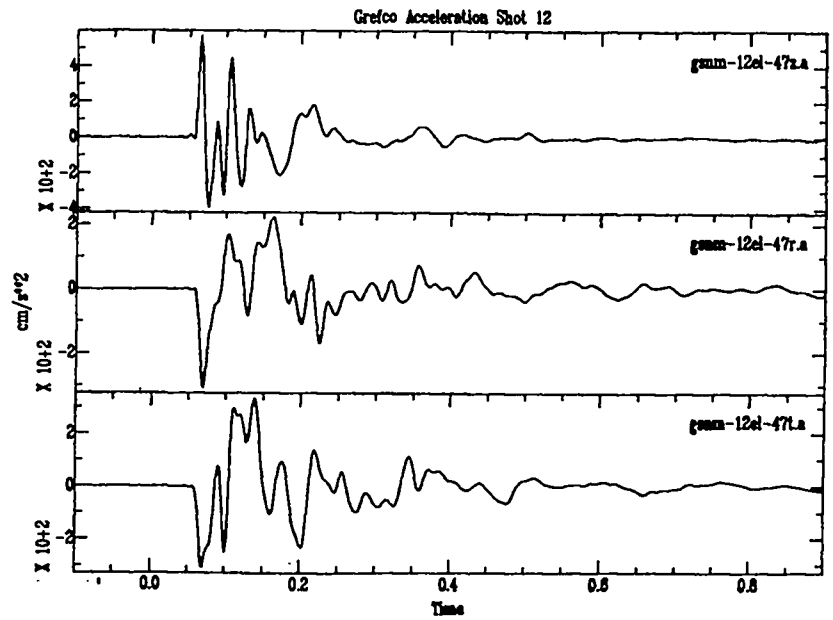
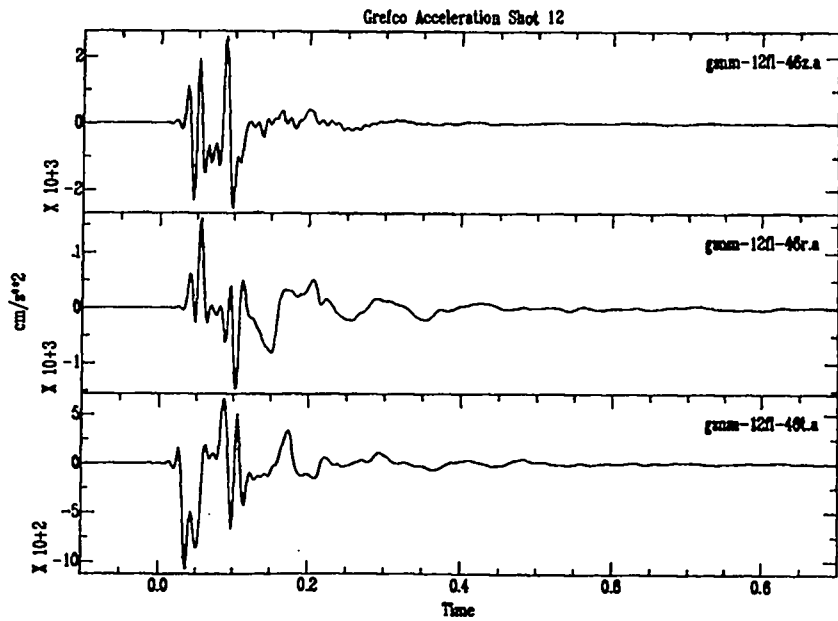
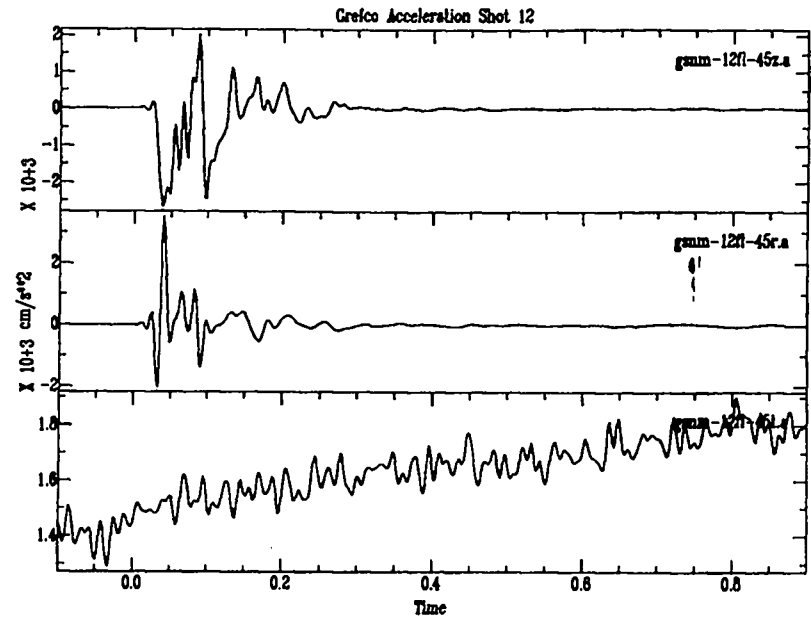
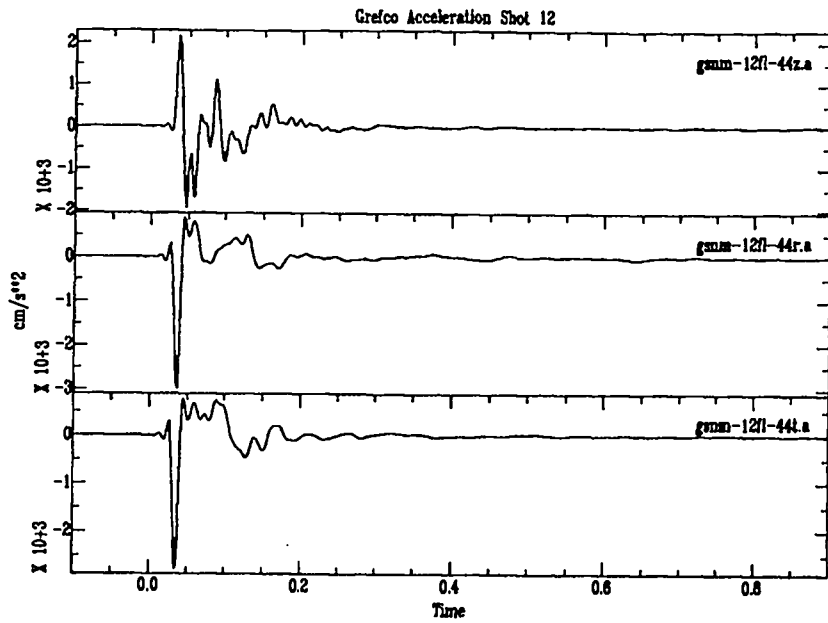


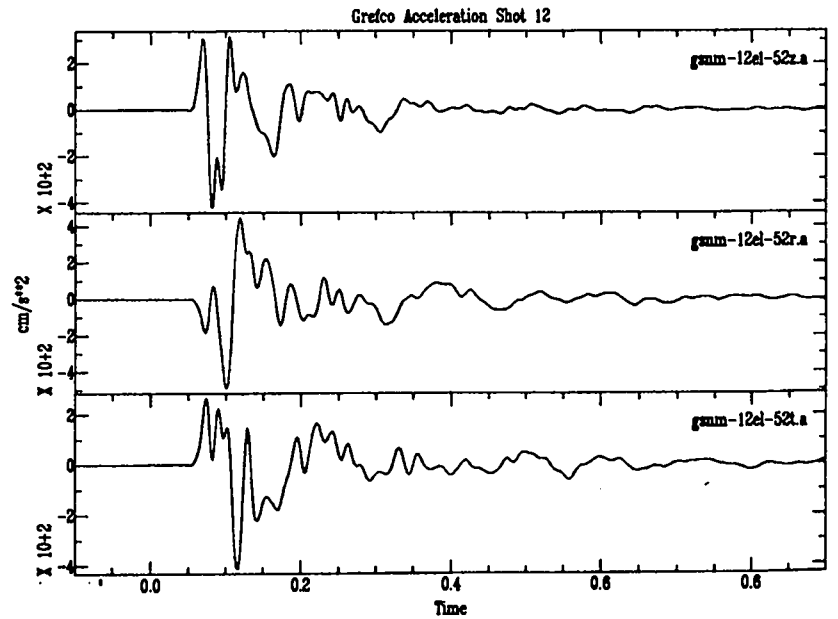
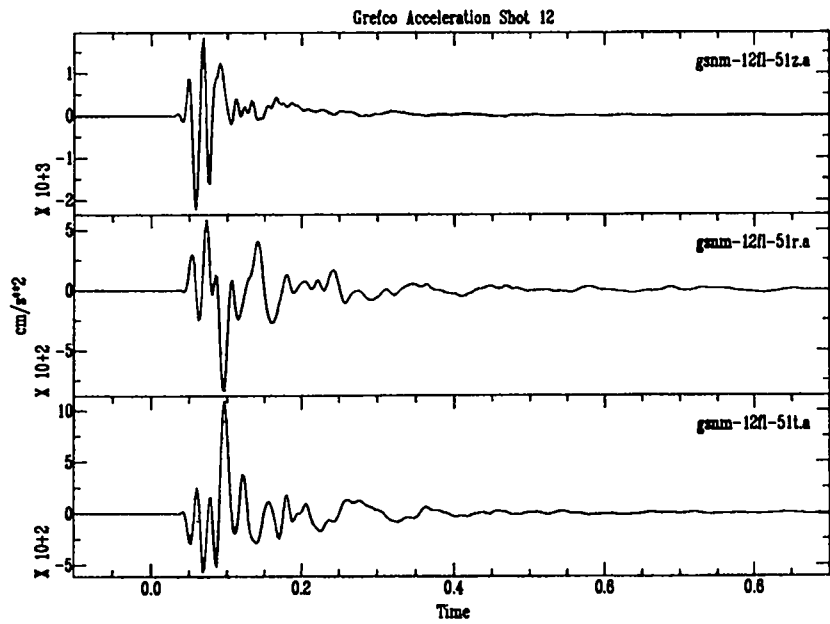
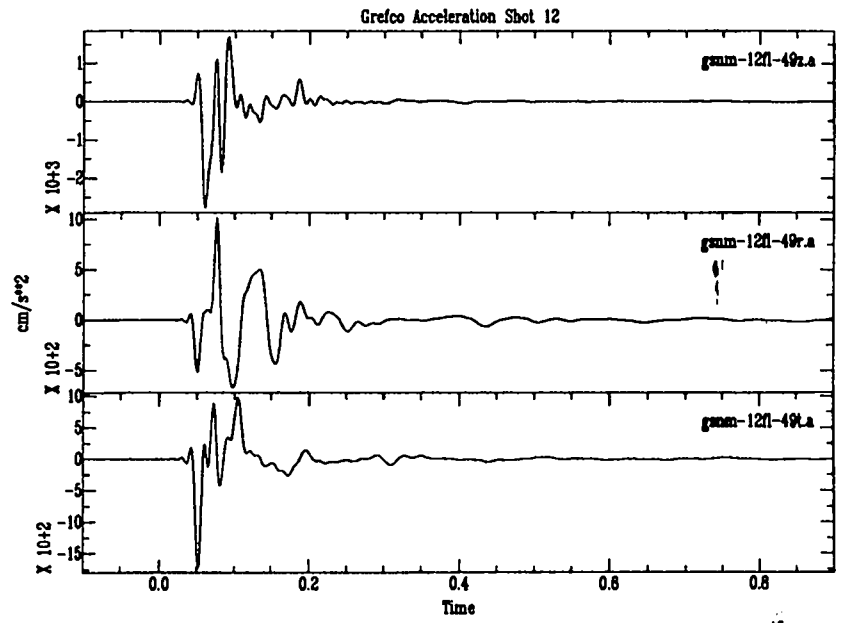
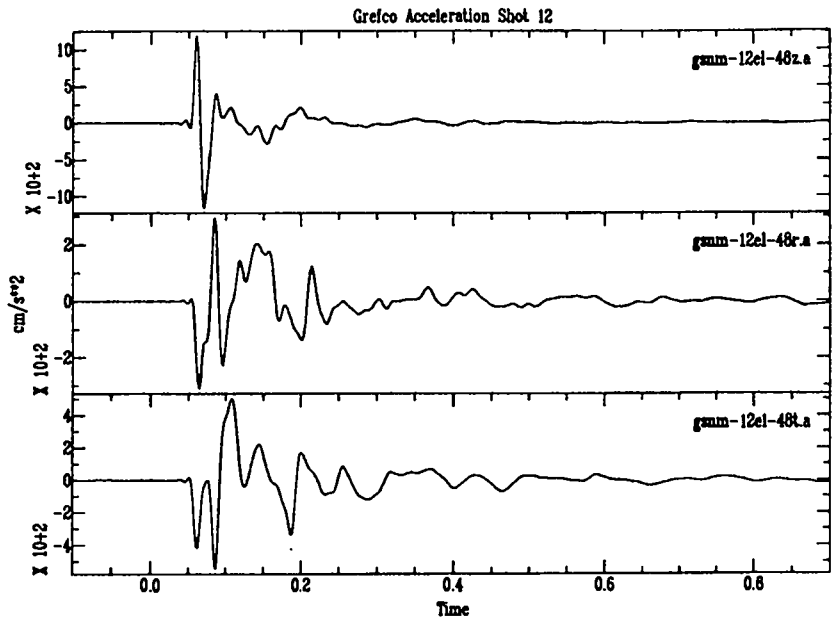
Grefco Acceleration Shot 12

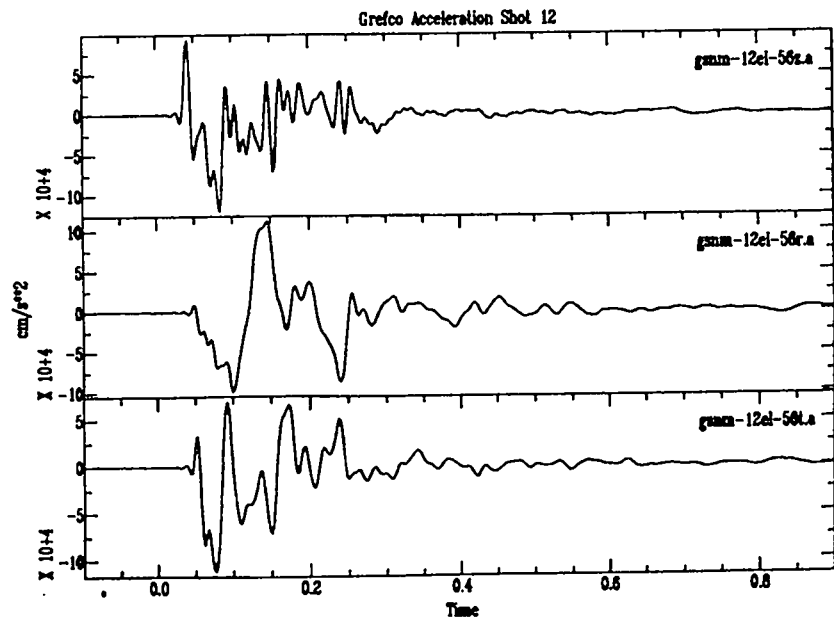
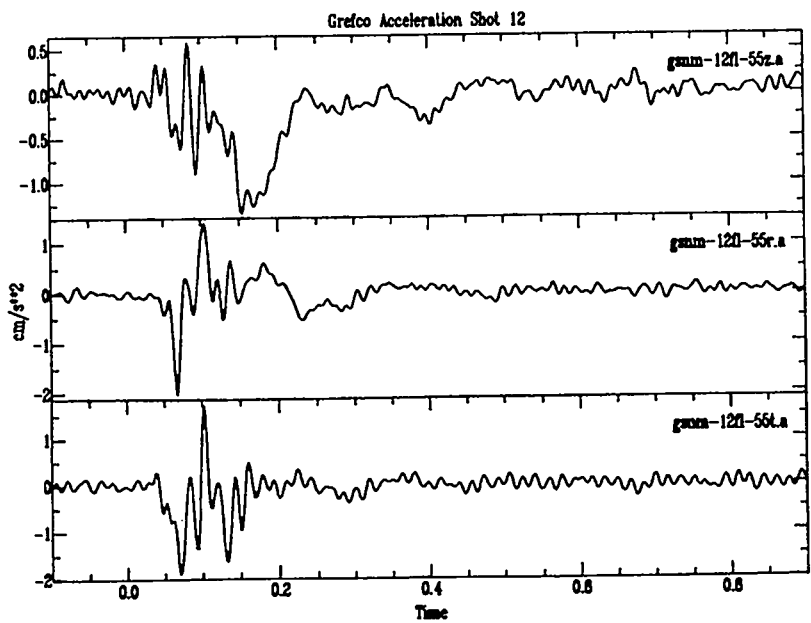
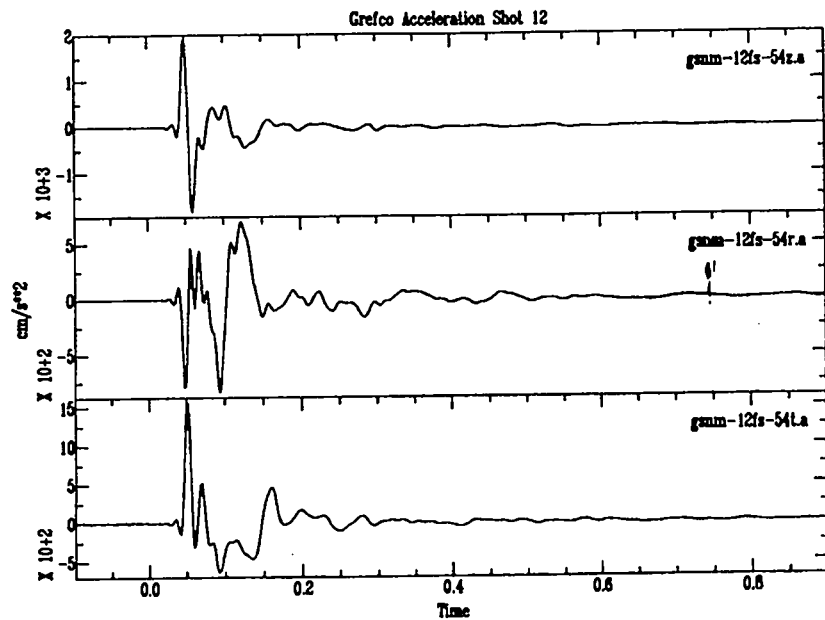
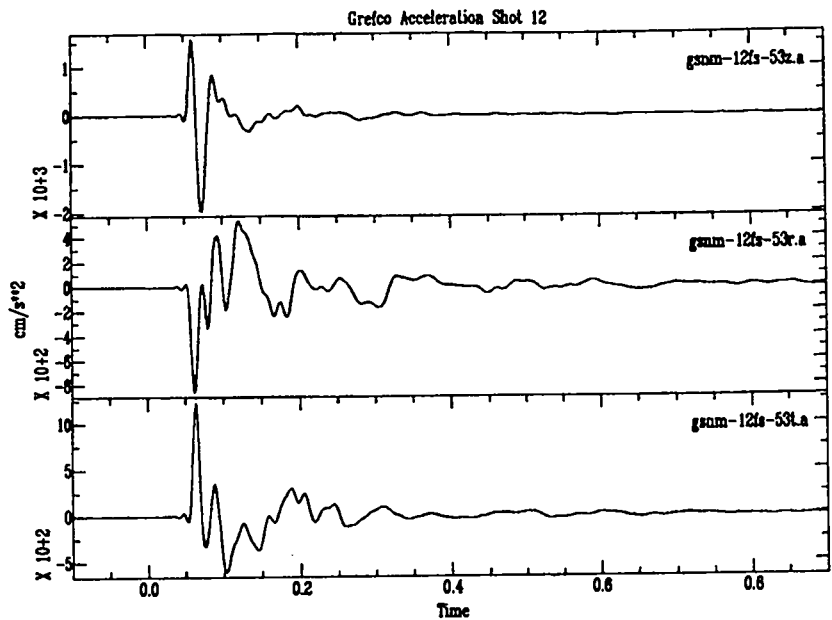


Grefco Acceleration Shot 12

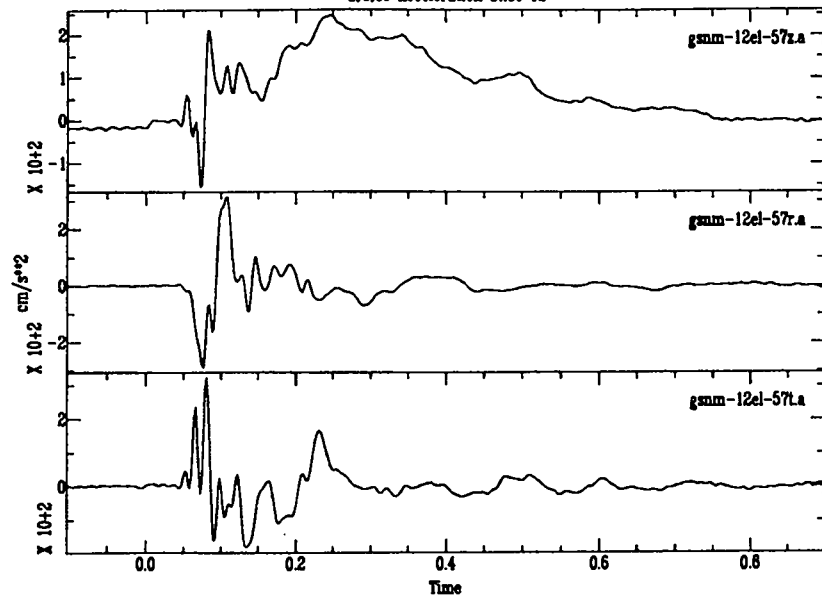


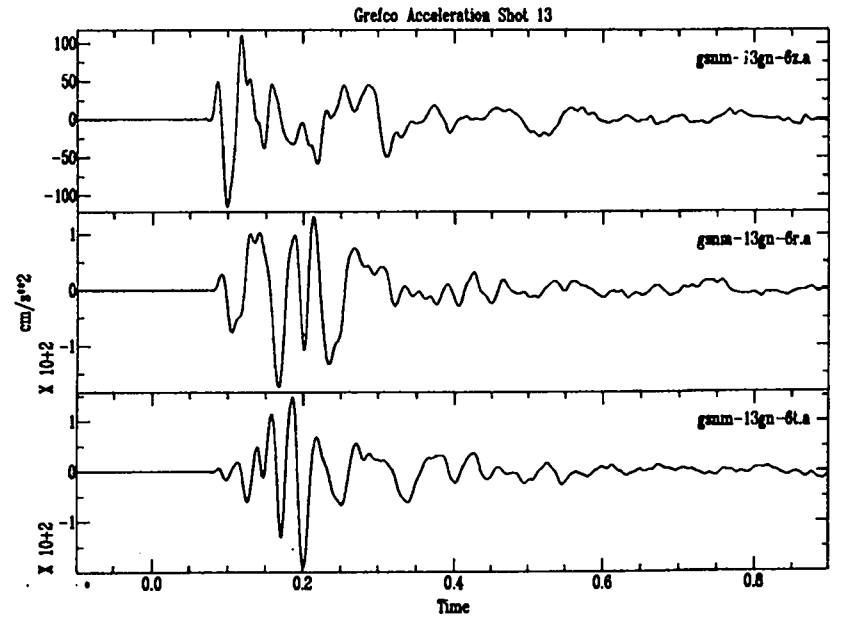
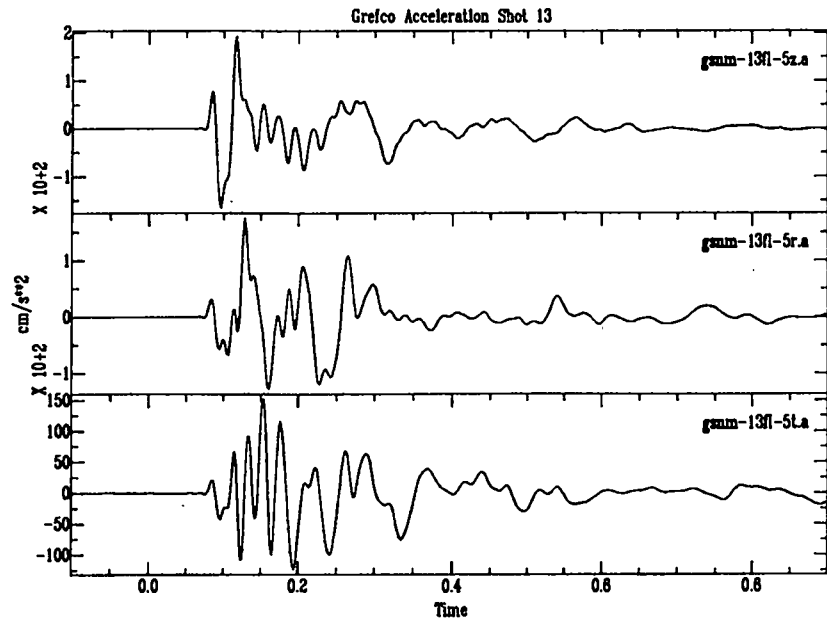
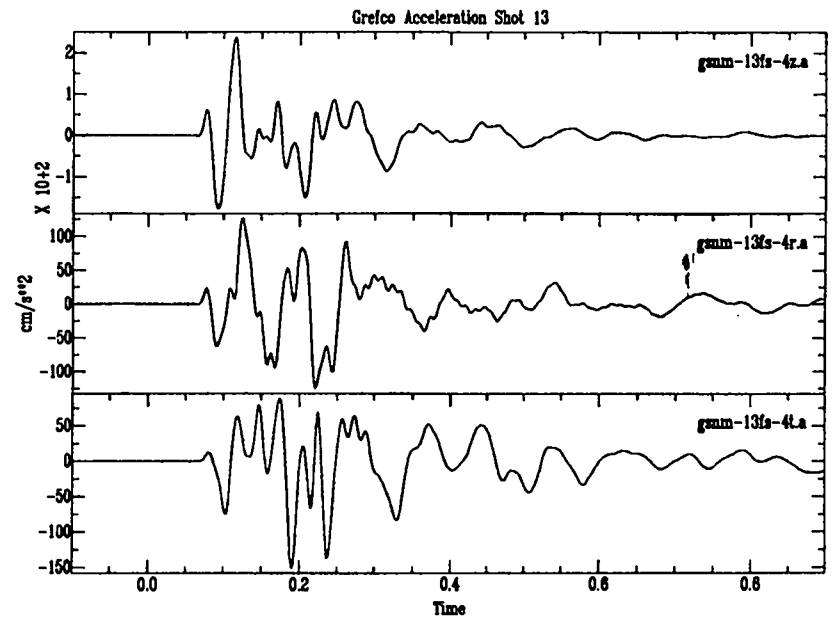
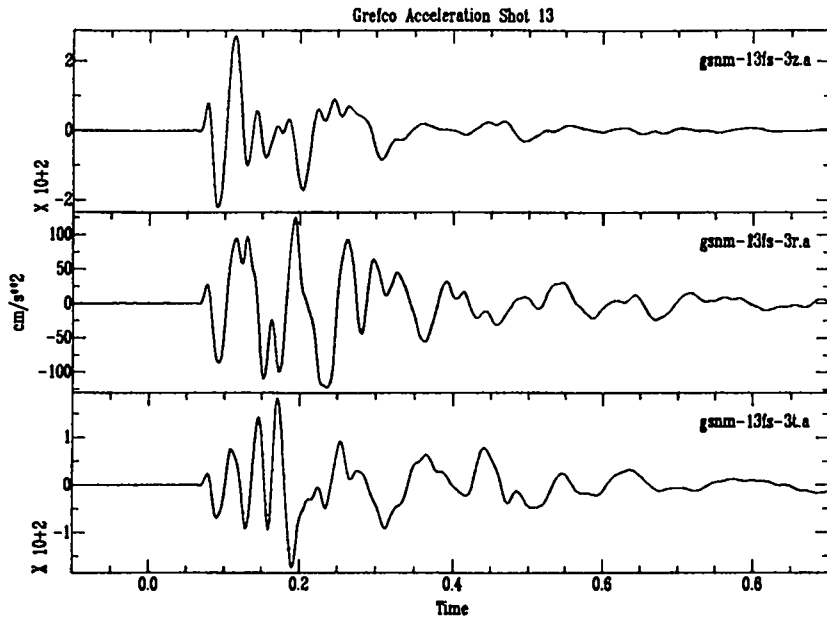




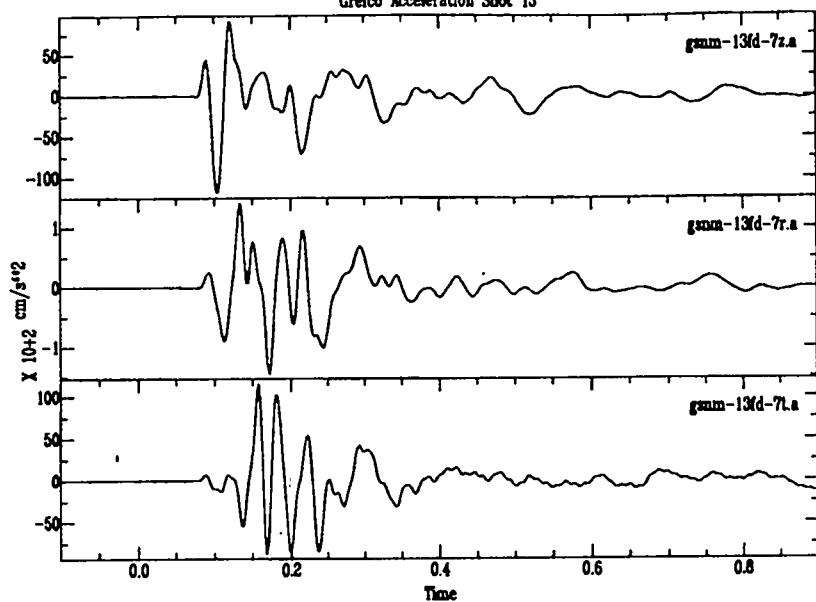


Grefco Acceleration Shot 12

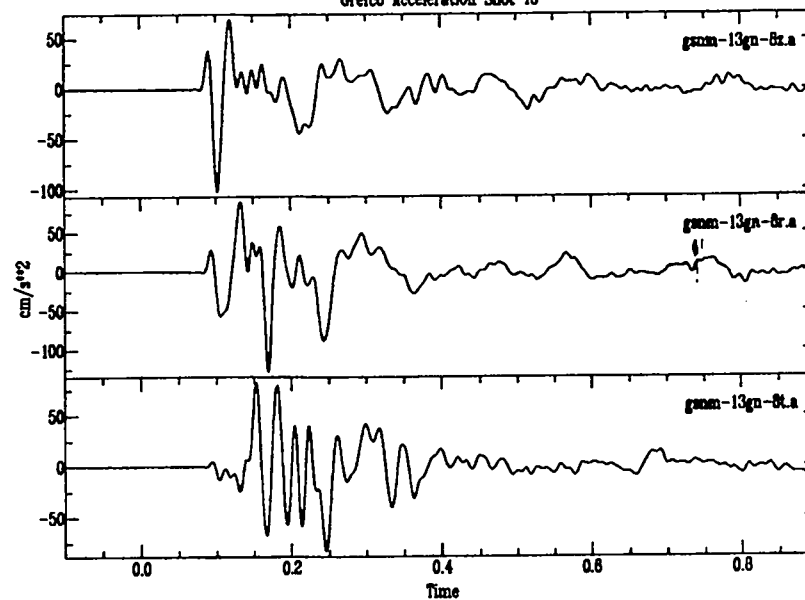




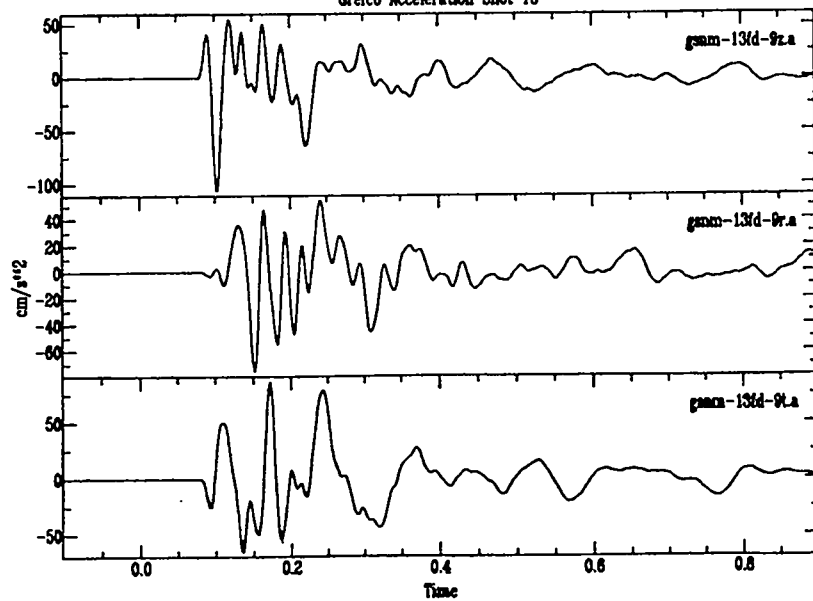
Grefco Acceleration Shot 13



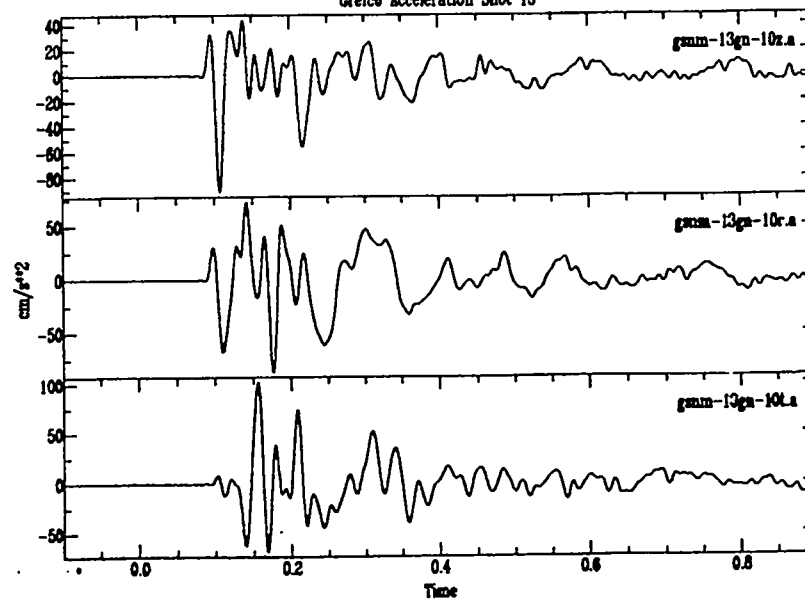
Grefco Acceleration Shot 13

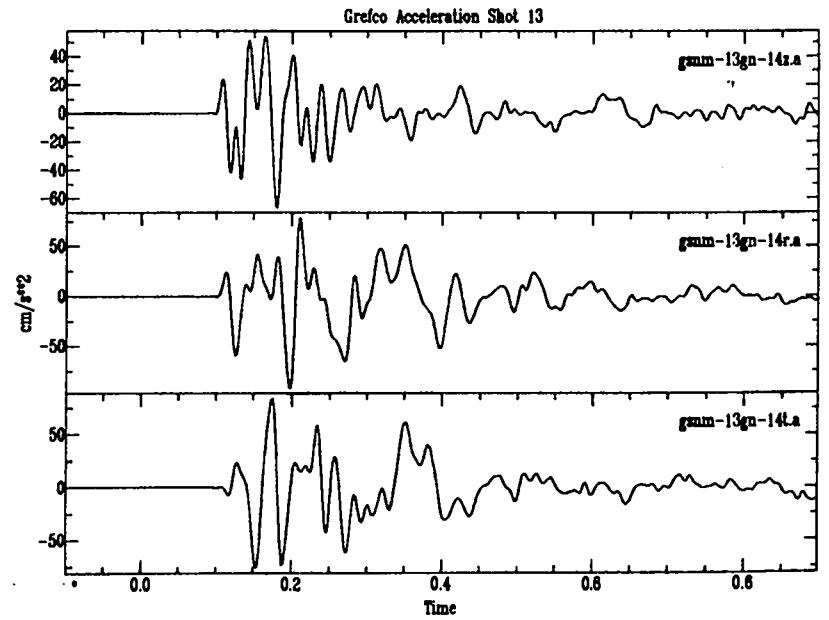
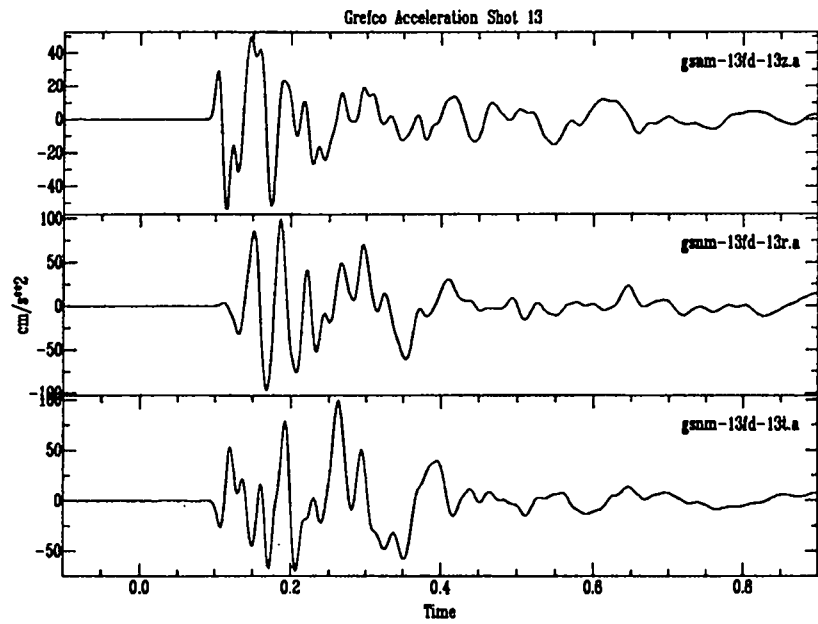
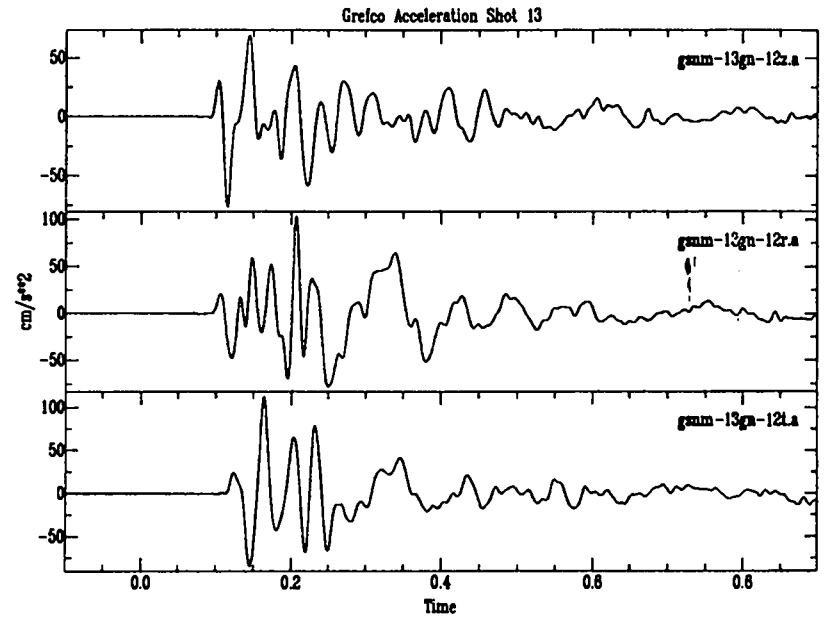
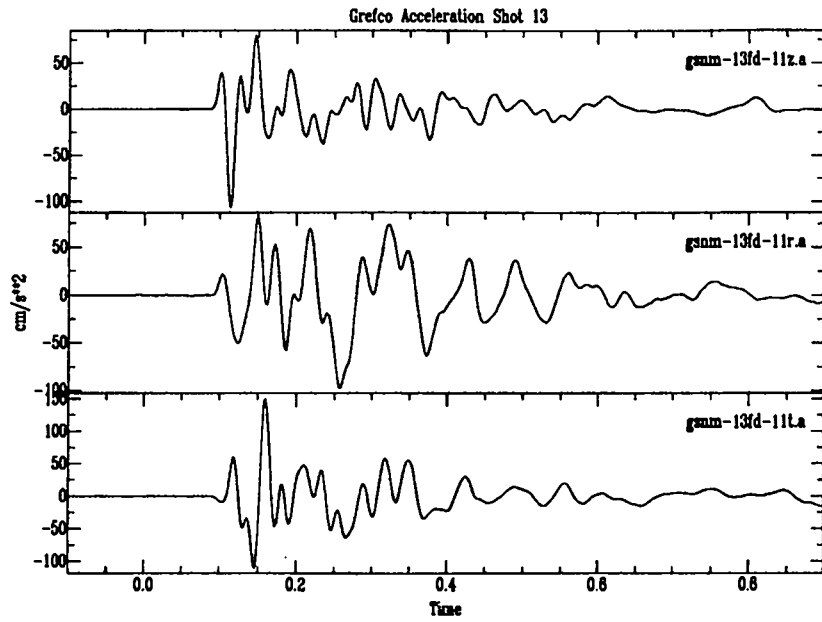


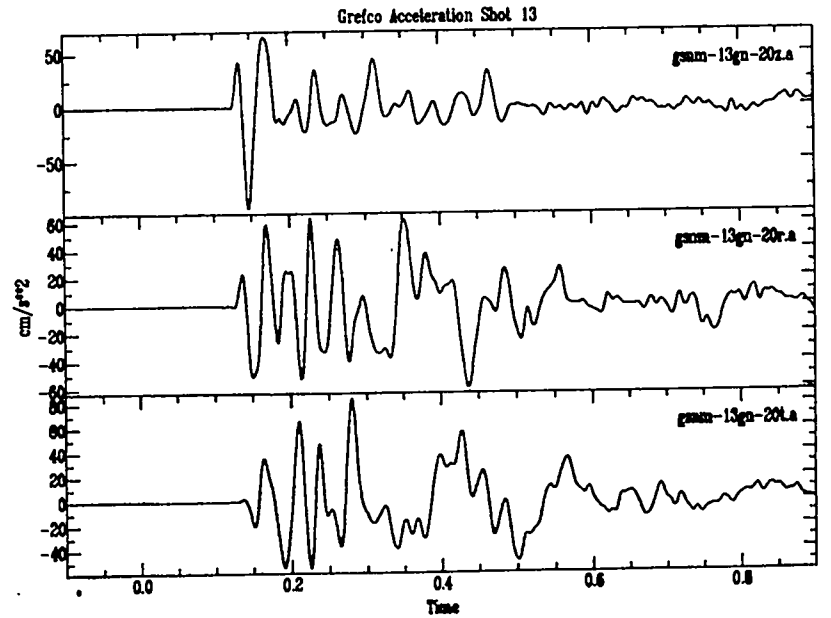
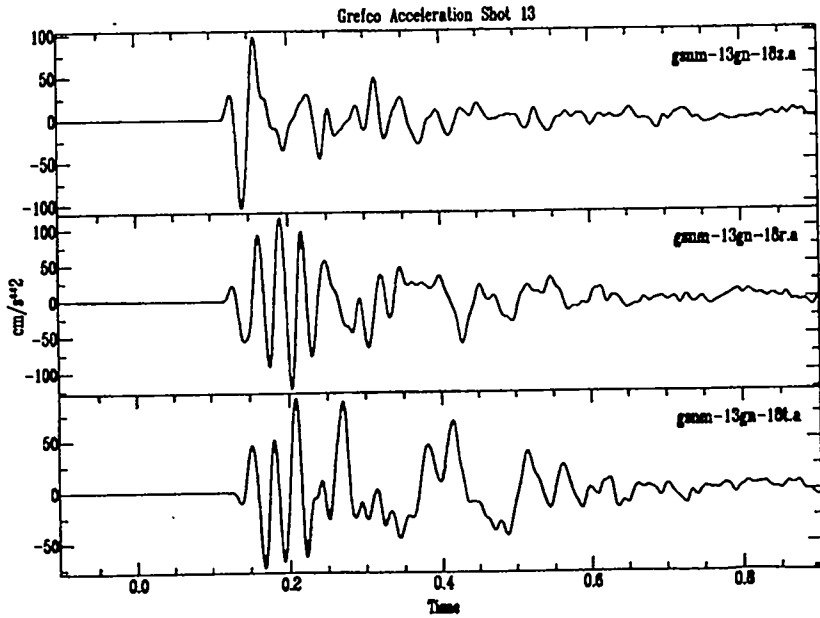
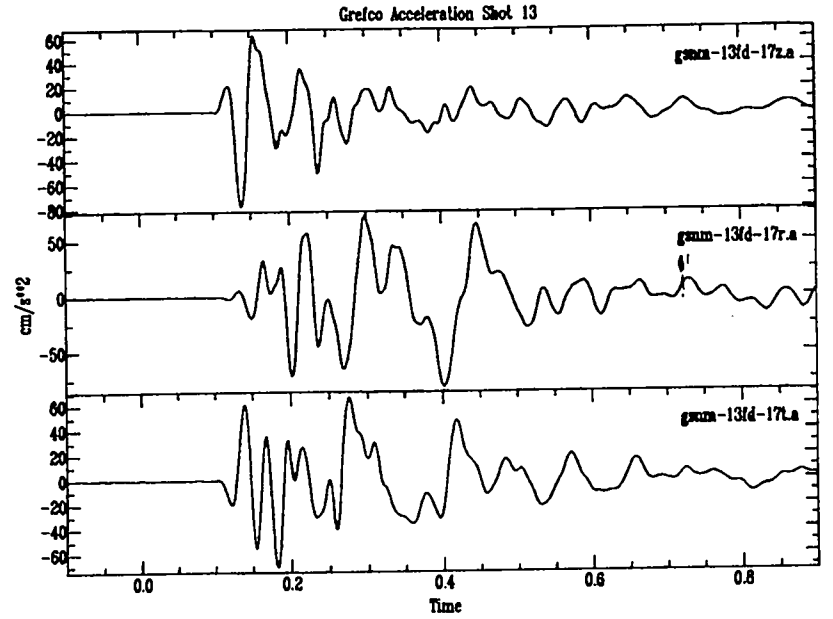
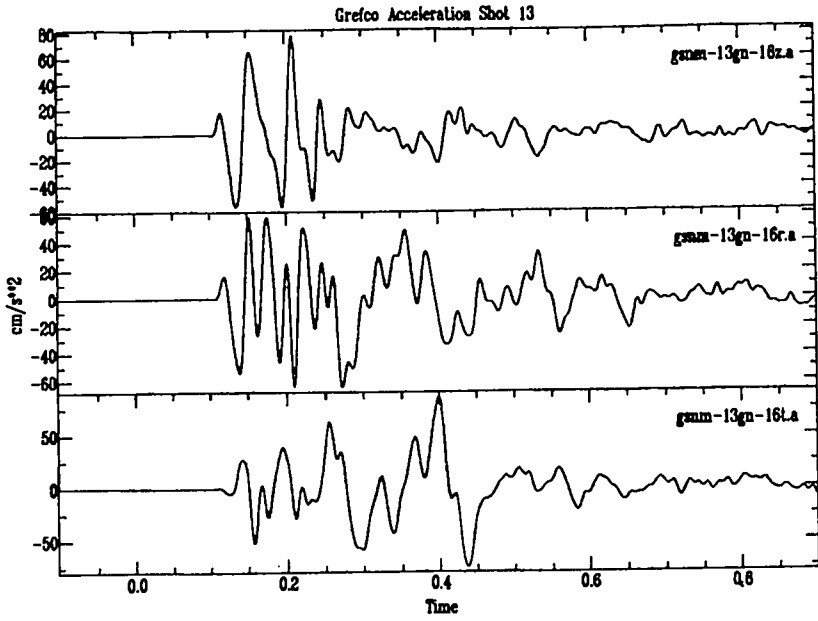
Grefco Acceleration Shot 13



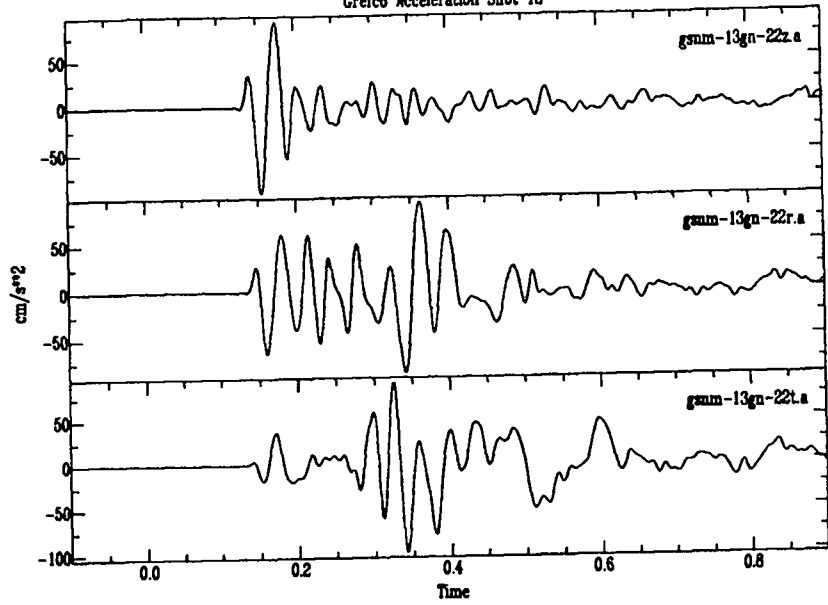
Grefco Acceleration Shot 13



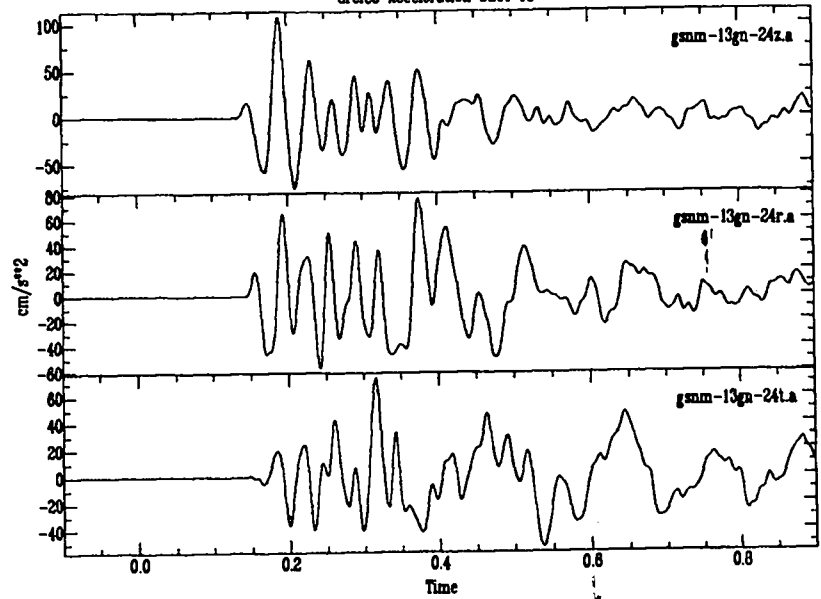




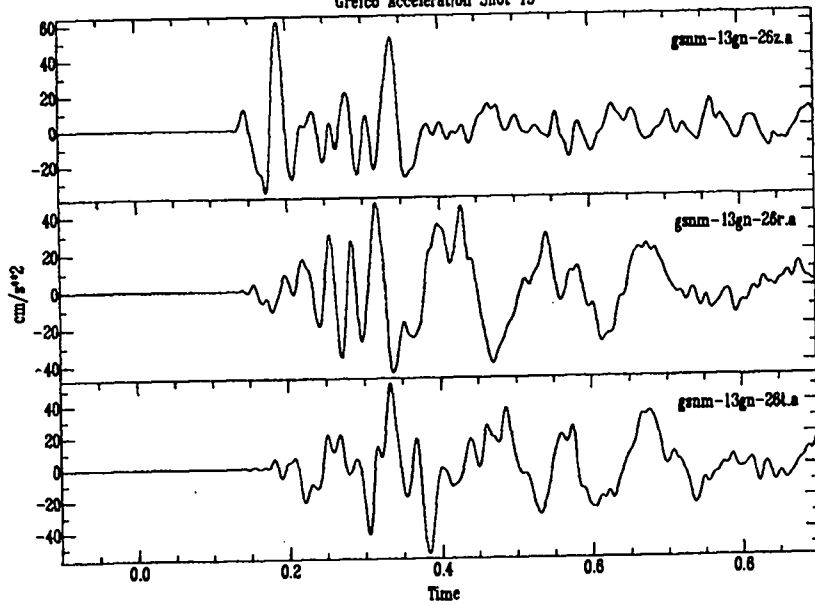
Grefco Acceleration Shot 13



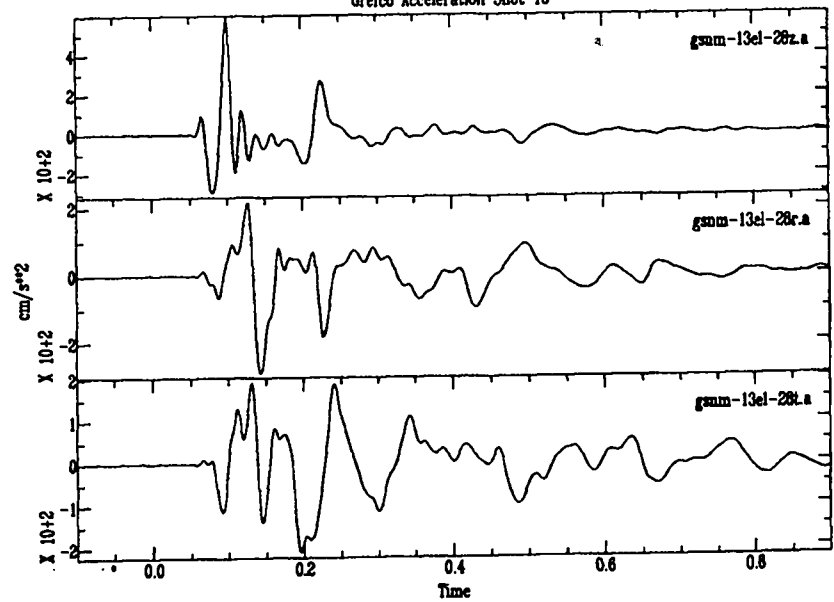
Grefco Acceleration Shot 13

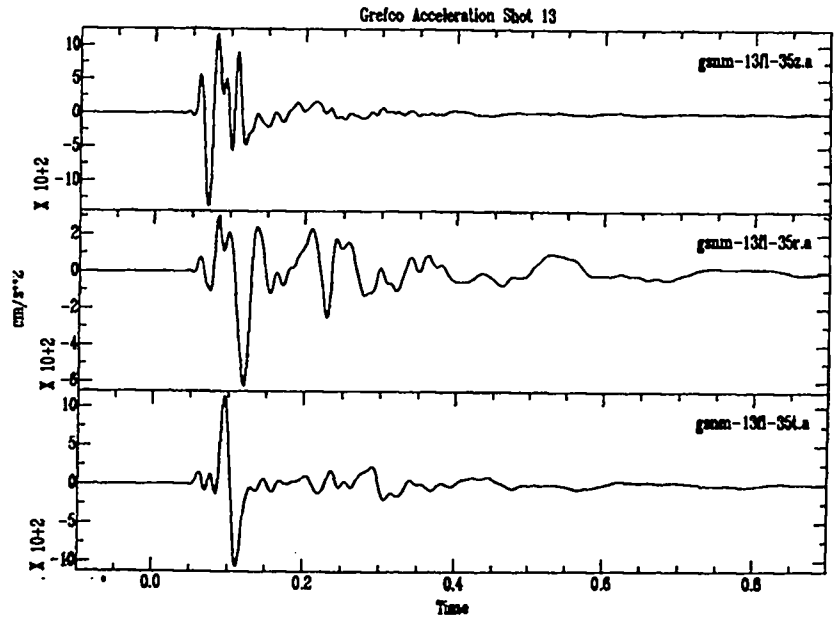
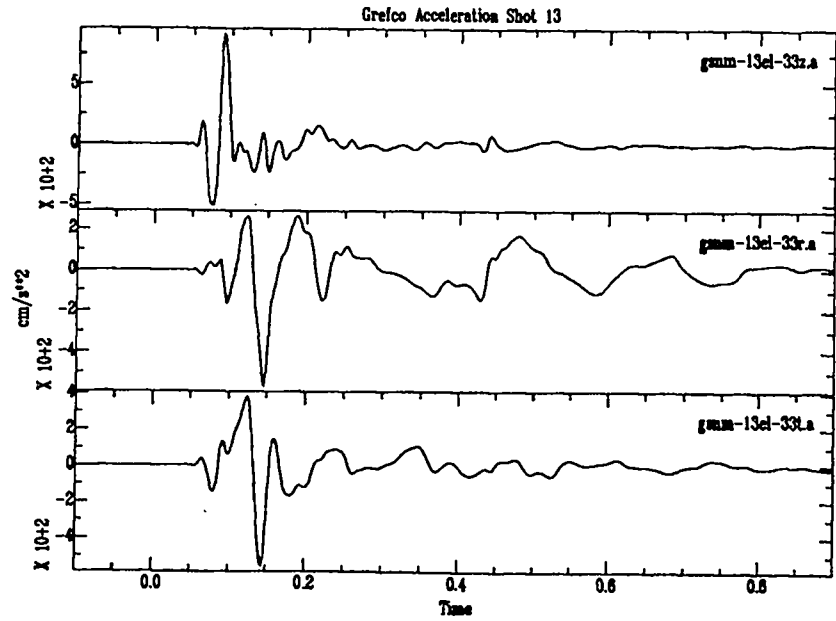
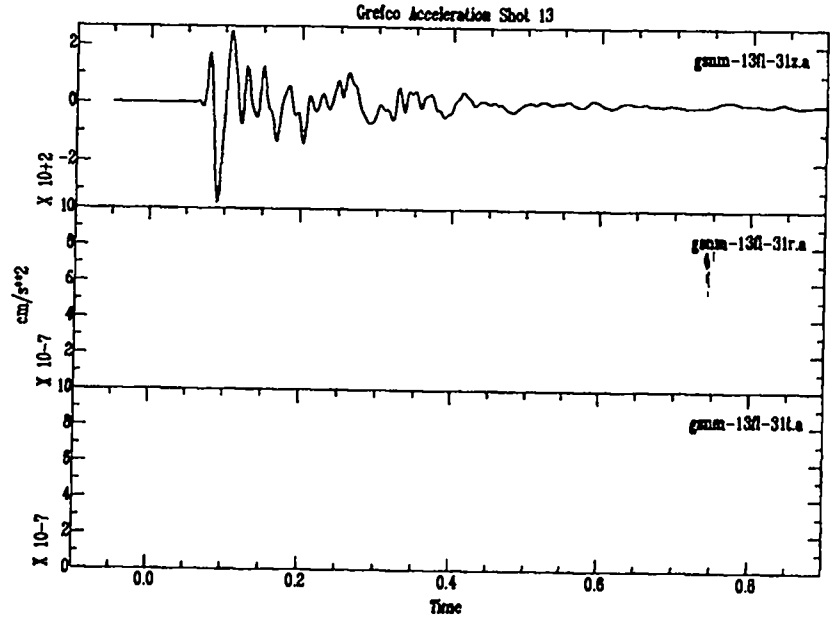
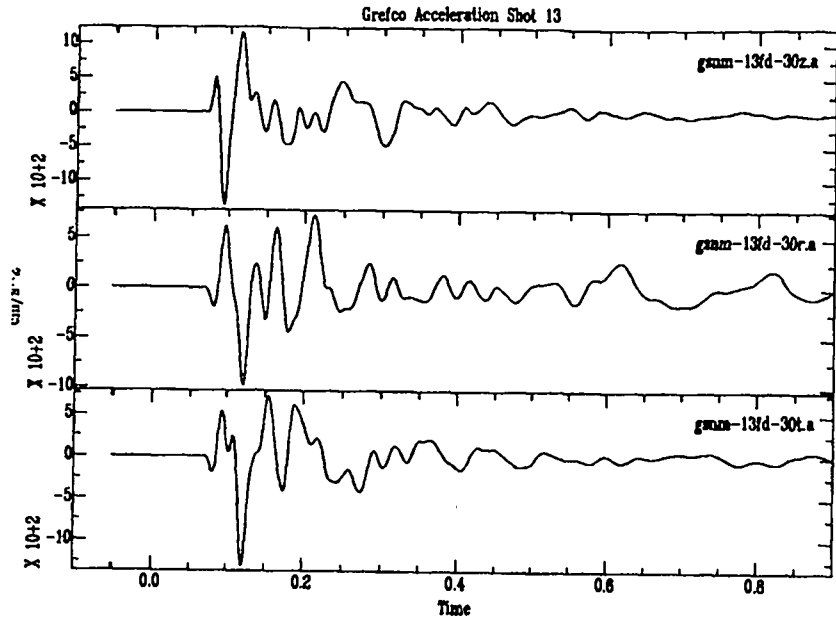


Grefco Acceleration Shot 13

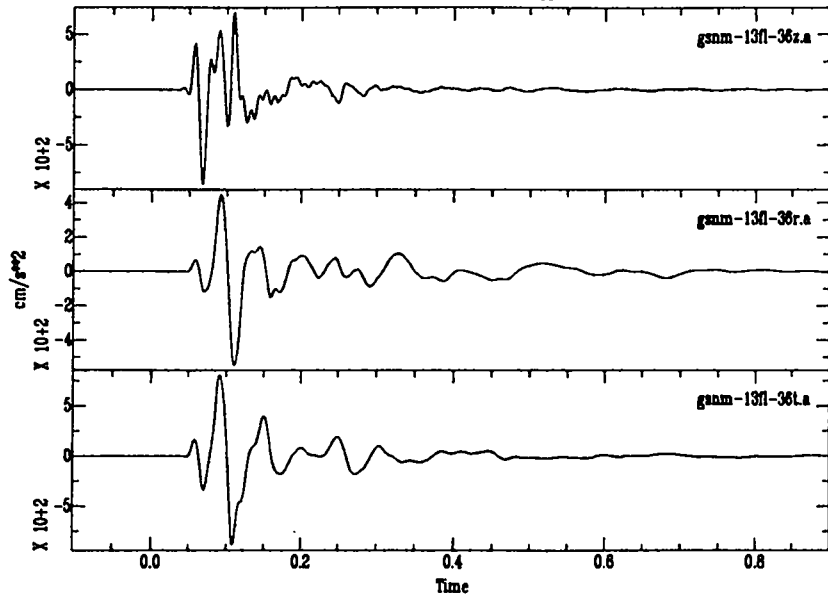


Grefco Acceleration Shot 13

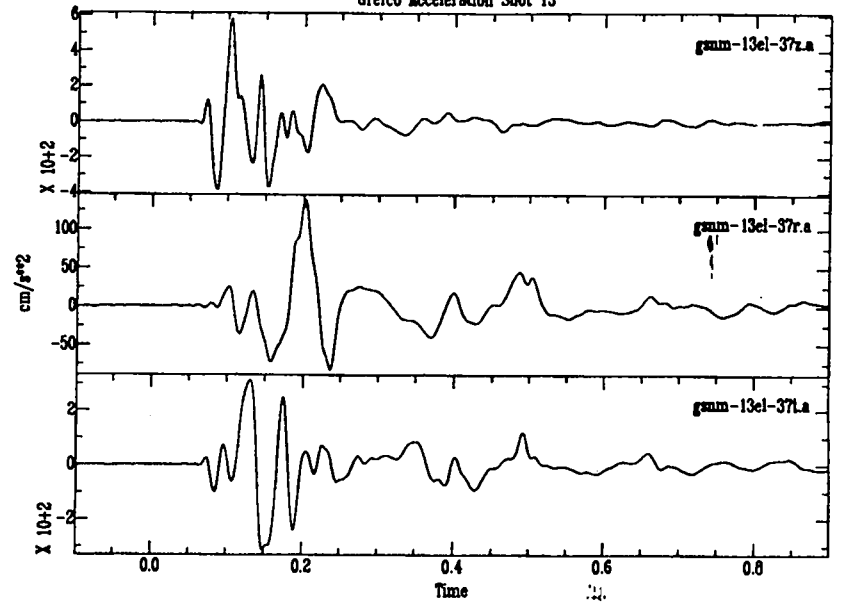




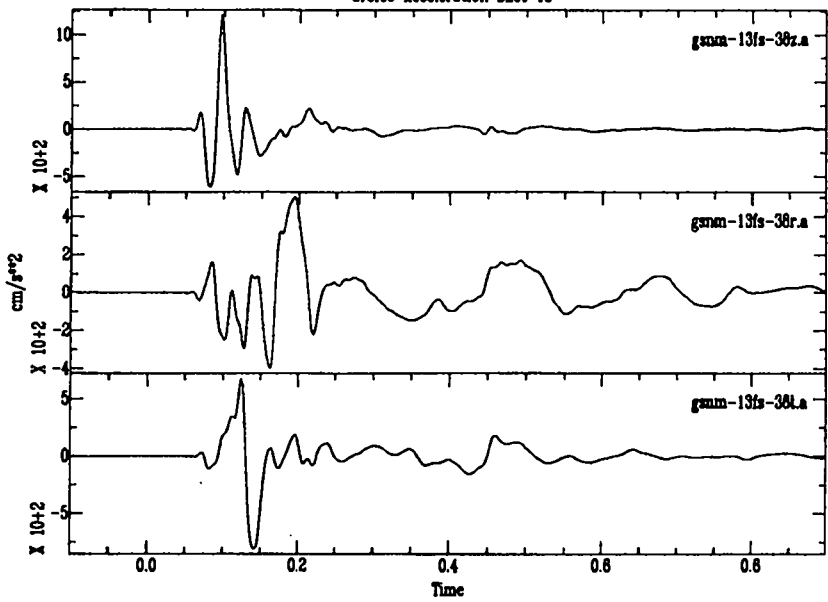
Grefco Acceleration Shot 13



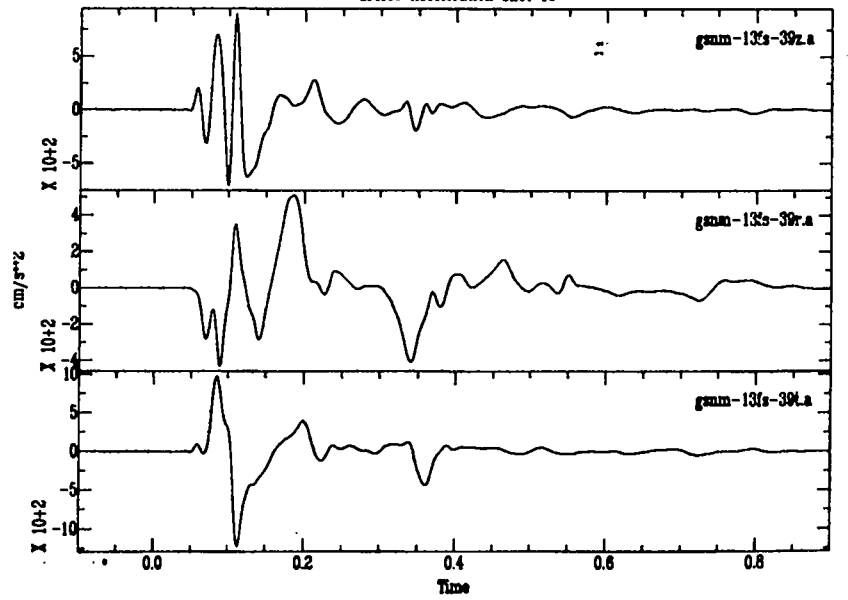
Grefco Acceleration Shot 13

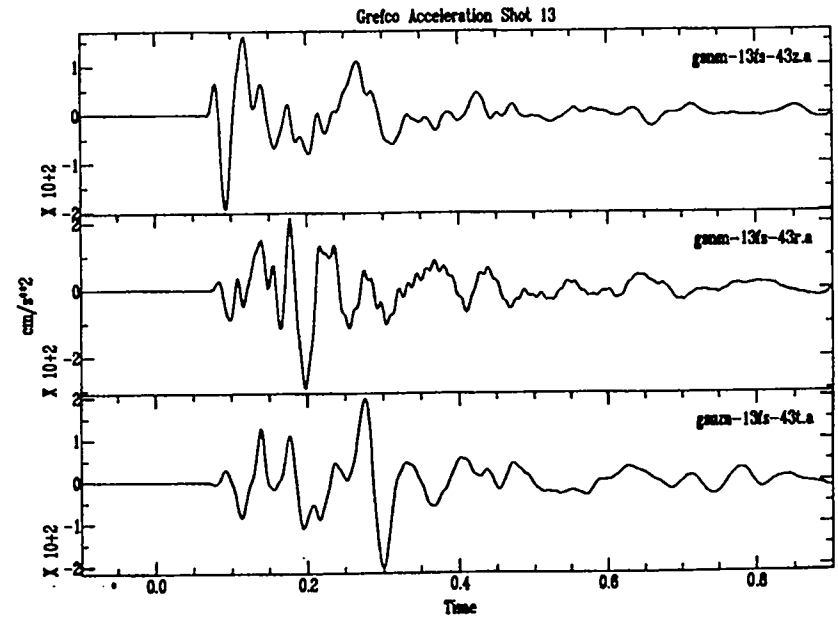
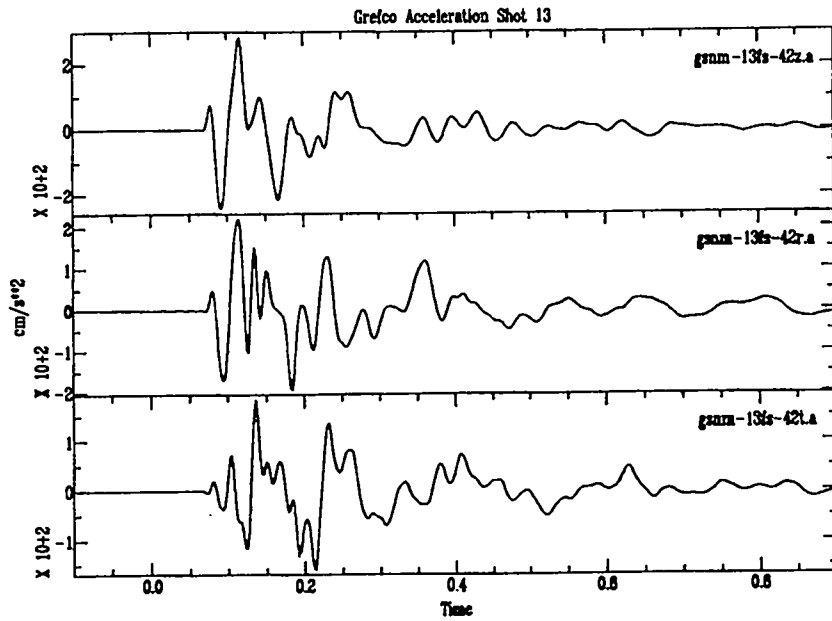
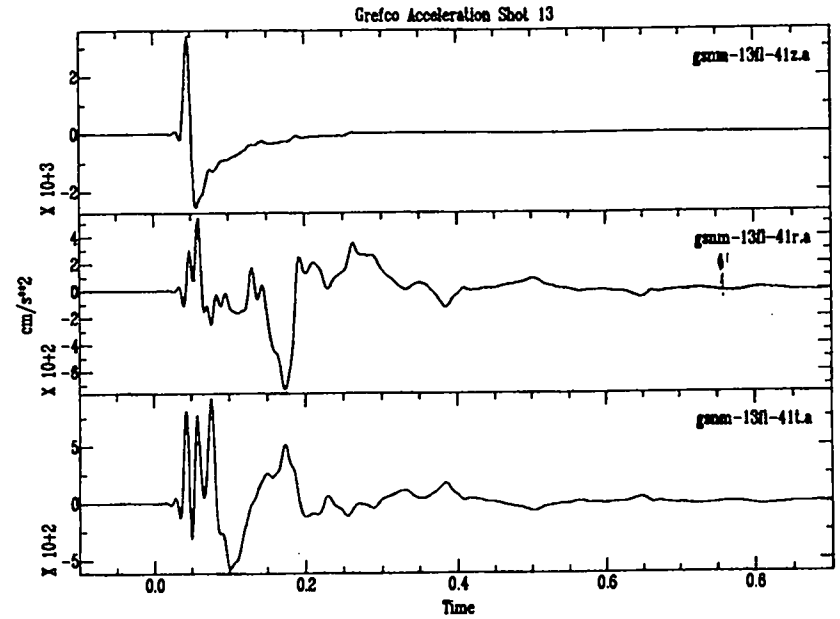
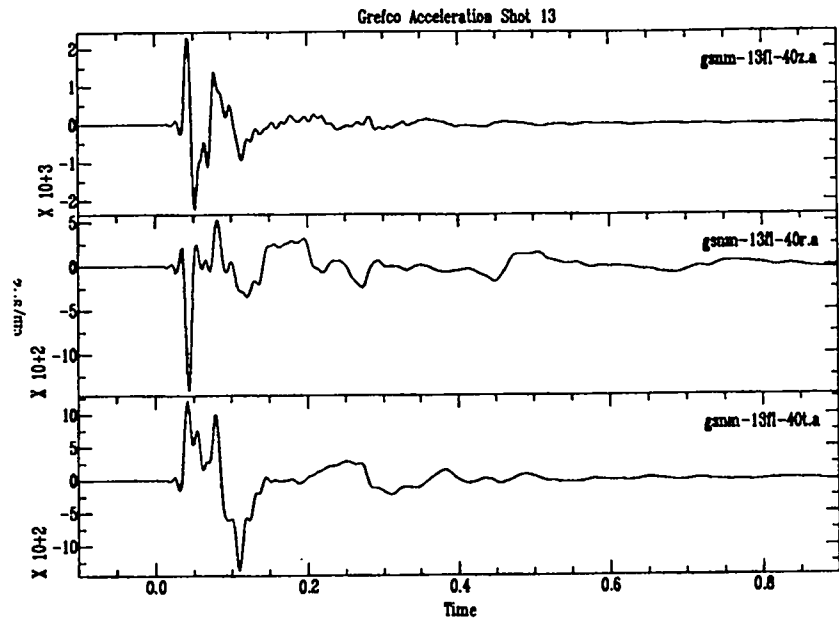


Grefco Acceleration Shot 13

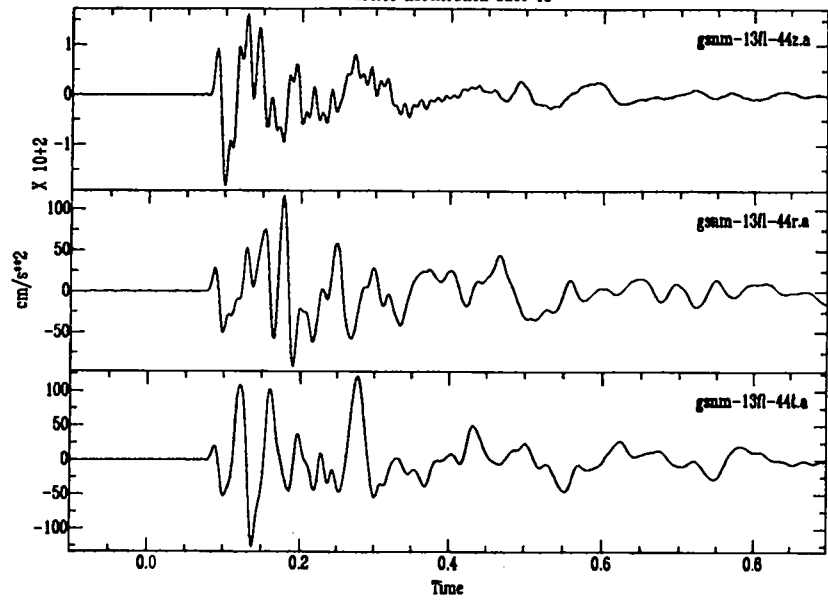


Grefco Acceleration Shot 13

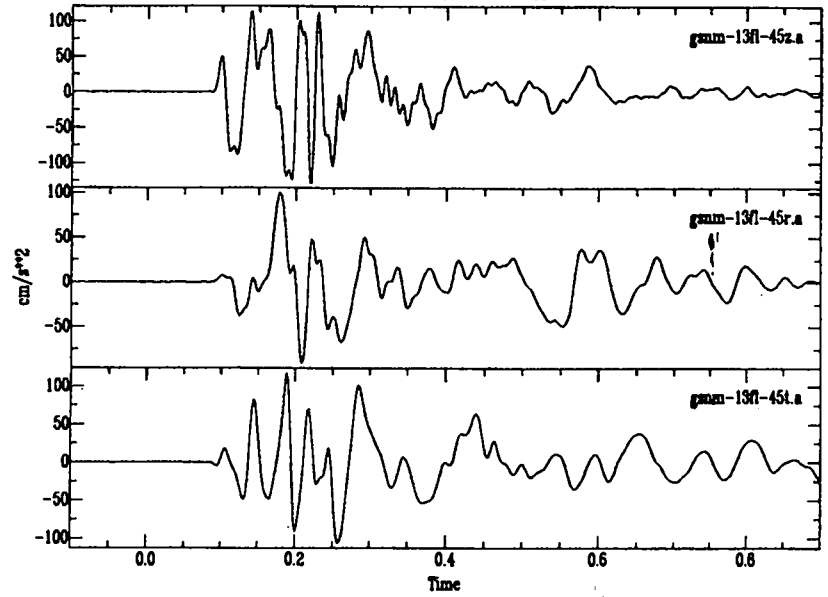




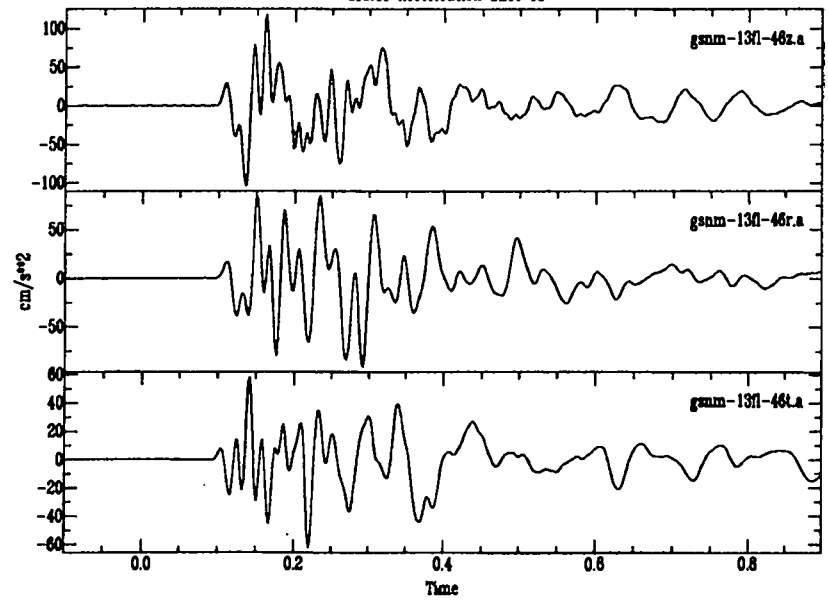
Grefco Acceleration Shot 13



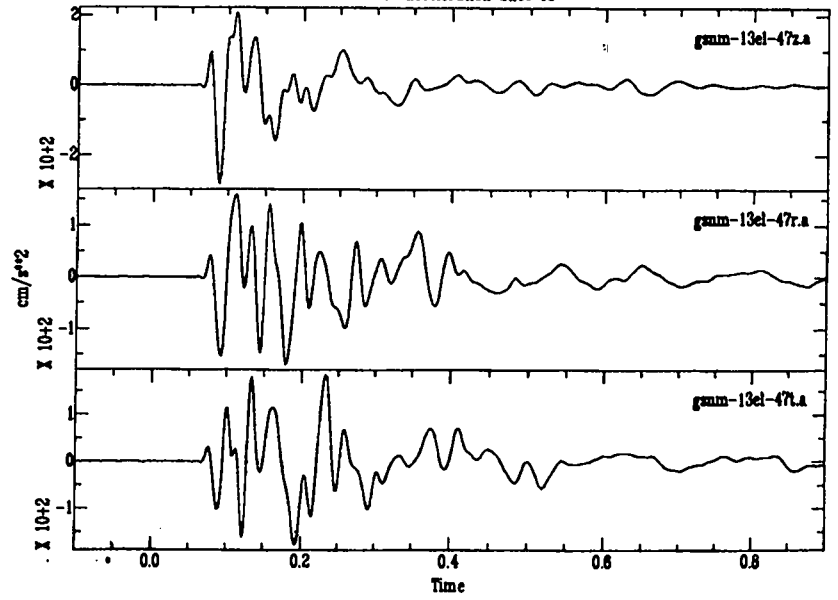
Grefco Acceleration Shot 13

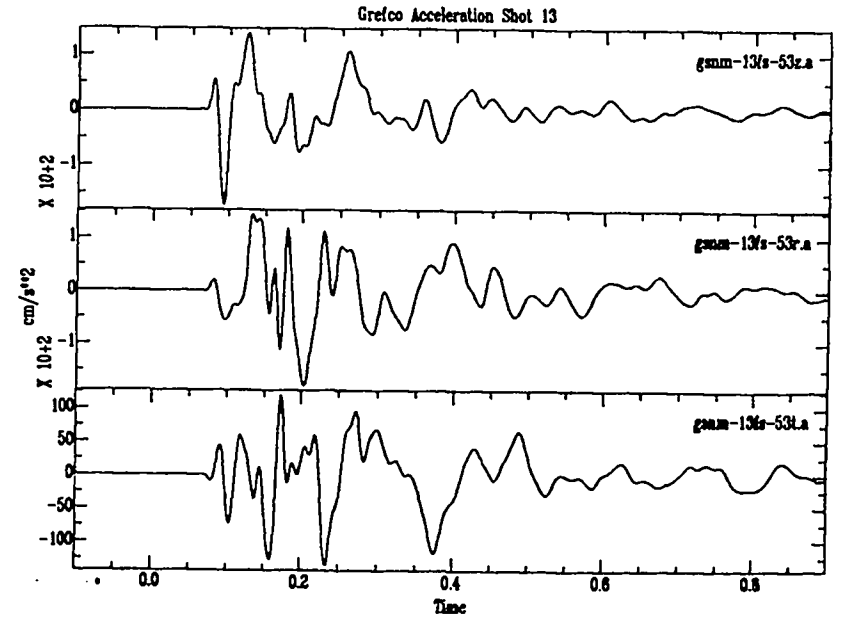
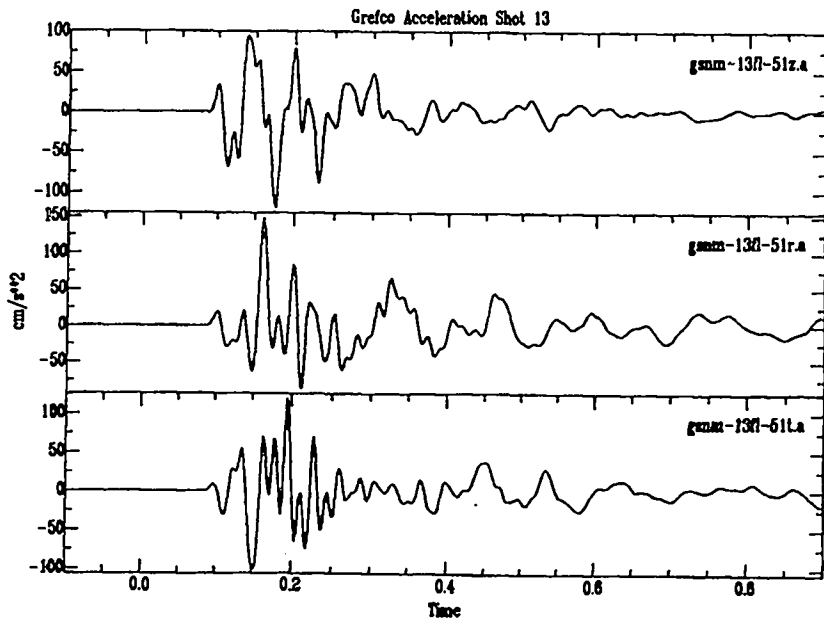
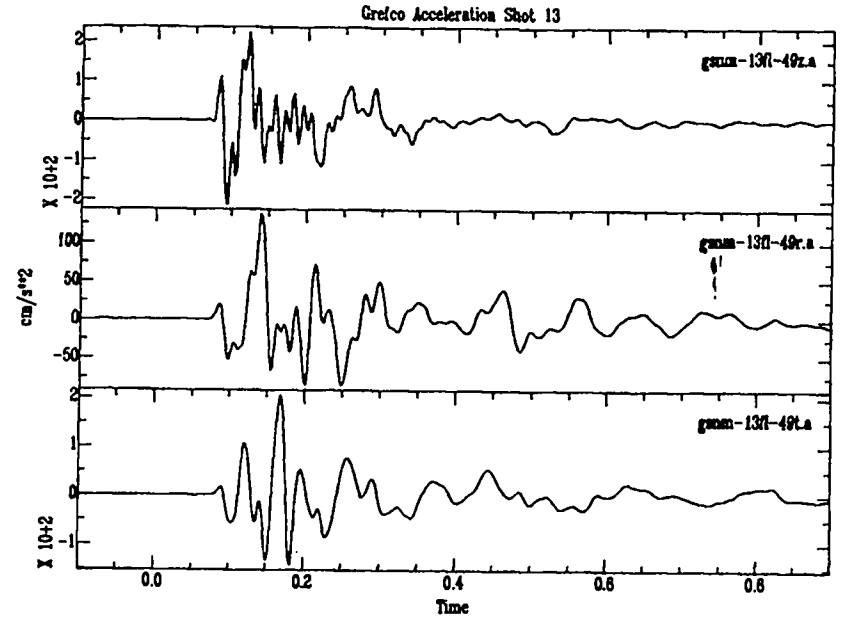
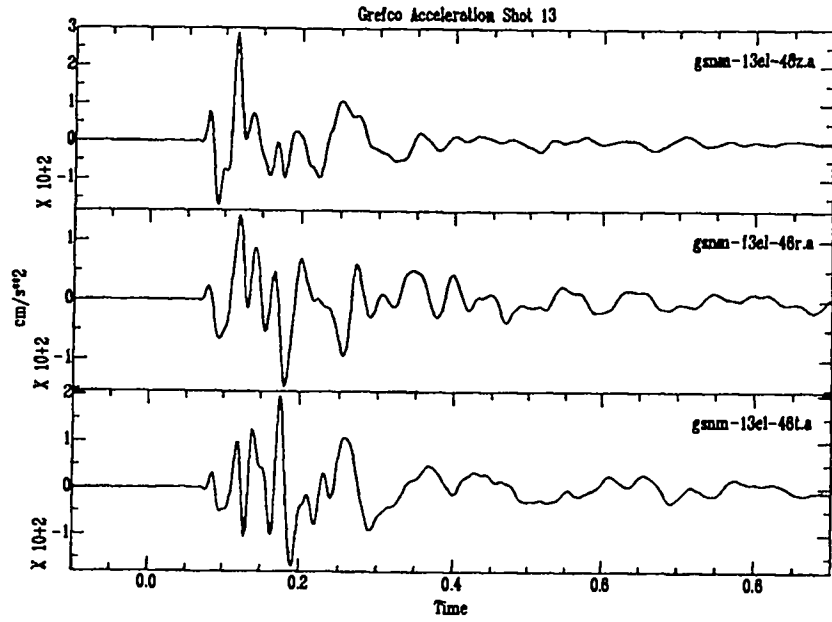


Grefco Acceleration Shot 13



Grefco Acceleration Shot 13





Grefco Acceleration Shot 13

